



HEINRICH HEINE
UNIVERSITÄT DÜSSELDORF

Diffusion in porous networks

Inaugural-Dissertation

zur

Erlangung des Doktorgrades der
Mathematisch-Naturwissenschaftlichen Fakultät
der Heinrich-Heine-Universität Düsseldorf

vorgelegt von

Dana Wagner

geboren in

Duisburg

Düsseldorf, Mai 2016

Aus dem Institut für experimentelle Physik der kondensierten Materie,
Lehrstuhl für Physik der weichen Materie
der Heinrich-Heine-Universität Düsseldorf

Gedruckt mit der Genehmigung der
Mathematisch-Naturwissenschaftlichen Fakultät der
Heinrich-Heine-Universität Düsseldorf

Referent: Prof. Dr. Stefan U. Egelhaaf
Koreferent: Prof. Dr. Peter Gilch
Tag der mündlichen Prüfung: 4.7.2016

ABSTRACT

In this Ph.D. thesis, the diffusion of macromolecules and liquids in and through porous media is described. This is relevant for a large variety of scientific areas and applications, ranging from food production, controlled drug delivery and filtration devices to fuel cells and enhanced oil recovery. Thus, diffusion in porous media has previously been the focus of numerous theoretical and experimental studies. However, the basic underlying mechanisms are still unclear, especially the interplay between solvent and solute motion, which is usually not considered.

The major goal of this work was to develop an experimental technique that allows the simultaneous but independent investigation of solvent and solute diffusion. This has been achieved through a combination of three complementary imaging techniques. While solvent diffusion was studied with neutron radiography, the movement of fluorescently labeled macromolecules was followed using fluorescence imaging. Additionally, the overall sample size and appearance were simultaneously monitored with optical brightfield transmission imaging.

In a first step, the reliability of the developed technique was successfully tested with an extensive investigation of fluorescent macromolecule diffusion through polymer hydrogels yielding results which were in good agreement with two well-established experimental techniques and Brownian dynamics simulations. The next step was a comprehensive comparison and distinction between solvent and solute diffusion into polymer hydrogels with different properties. The data were quantitatively interpreted based on different theoretical models. Even small molecules such as dyes, which are commonly used as tracer particles were shown to exhibit a significantly different diffusivity than the solvent. Compared to the influx measurements, a qualitatively different diffusion behavior was observed for the reverse process of macromolecule release from polymer hydrogels.

ZUSAMMENFASSUNG

Im Rahmen dieser Doktorarbeit wurde die Diffusion von Flüssigkeiten und Makromolekülen durch poröse Strukturen untersucht und beschrieben. In einer Vielzahl von Forschungsgebieten und Anwendungen, von der Nahrungsmittelherstellung über kontrollierten Medikamententransport im menschlichen Körper oder Filtrationsprozesse bis hin zur Erdölgewinnung, stehen Diffusionsprozesse durch poröse Medien im Vordergrund. Durch diese vielfältigen Anwendungsmöglichkeiten wurde dieses Thema bereits in zahlreichen theoretischen und experimentellen Forschungsarbeiten behandelt. Trotzdem sind bisher viele Fragen bezüglich der zu Grunde liegenden Mechanismen unbeantwortet geblieben, und besonders die Wechselwirkungen zwischen Flüssigkeiten und Makromolekülen, also dem Lösungsmittel und der gelösten Substanz, werden oftmals nicht explizit berücksichtigt.

Das Hauptziel dieser Arbeit war die Entwicklung einer experimentellen Methode zur gleichzeitigen, aber unabhängigen Untersuchung der Diffusion von Flüssigkeiten und Makromolekülen. Dies wurde mit Hilfe einer Kombination von drei einander ergänzenden bildgebenden Verfahren realisiert. Während Neutronenradiographie die Untersuchung von Flüssigkeitsbewegungen ermöglichte, wurde die Diffusion von fluoreszenzmarkierten Makromolekülen durch Fluoreszenzbildgebung visualisiert und analysiert. Zusätzlich wurde die gesamte Probe mittels optischer Bildgebung ähnlich der Hellfeldmikroskopie auf Änderungen in Größe oder Erscheinung untersucht.

Die Funktionalität und Zuverlässigkeit der entwickelten Methode wurde zunächst dadurch gezeigt, dass die Ergebnisse einer umfangreichen Studie zu der Diffusion von fluoreszierenden Makromolekülen in Polymerhydrogelen mit denen von zwei gängigen experimentellen Methoden übereinstimmten und mit Brownian Dynamics Simulationen beschrieben werden konnten. In weiterführenden Experimenten wurde die Makromolekül-Diffusion in Polymerhydrogelen dann mit der Diffusion von Lösungsmitteln verglichen. Im Vergleich zur Flüssigkeitsdiffusion konnte schon für kleine Farbstoffpartikel, welche gemeinhin als Tracer verwendet werden, ein ausgeprägter Unterschied festgestellt und gezeigt werden. Zusätzlich zu diesen Experimenten, bei denen die Diffusion in die Hydrogele hinein gemessen wurde, wurden auch der umgekehrte Fall, Diffusion aus den Hydrogelen in das umliegende Reservoir, untersucht. Dabei wurde ein qualitativ unterschiedliches Verhalten beobachtet, welches mit Hilfe von leicht unterschiedlichen theoretischen Modellen beschrieben werden konnte.

AUTHOR'S DECLARATION

I declare that the work in the dissertation was carried out autonomously and independently and without using any unauthorized help, and has not in the same or similar form been submitted at a different institution. This is my first attempt at obtaining a doctoral degree.

SIGNED: DATE:

DANKSAGUNG

Ich möchte die Gelegenheit nutzen, mich von Herzen bei all denen zu bedanken, die mich auf dem langen Weg bis hin zur Fertigstellung dieser Arbeit begleitet und unterstützt haben.

In erster Linie gilt mein Dank meinem Doktorvater, Prof. Dr. Stefan Egelhaaf – zum einen dafür, dass er mir die Möglichkeit gegeben hat, die Arbeit an seinem Lehrstuhl und unter seiner Leitung anzufertigen und zum anderen für seinen grenzenlosen Optimismus und seine Begeisterung für noch so kleine Fortschritte. Er hat mich während der gesamten Zeit unterstützt und nie in Frage gestellt, ob ich auf dem richtigen Weg bin. Außerdem möchte ich mich bei Herrn Prof. Dr. Peter Gilch für die Übernahme des Co-Referats bedanken. Besonderer Dank gilt auch Frau Dr. Helen Hermes, die mich die meiste Zeit betreut hat und die mir auch nach Verlassen der Arbeitsgruppe jederzeit mit Rat und Tat zur Seite stand. Ihr Tatendrang, ihre Energie und ihre Kreativität waren stets motivierend und stimulierend. Unsere gemeinsamen Roadtrips ans PSI und die damit verbundenen Messzeiten, bei denen wir festgestellt haben, dass wir sehr gut zusammen arbeiten können und wir uns gut ergänzen, wenn es darum geht die Messzeit optimal zu nutzen, werden mir immer in guter Erinnerung bleiben.

Jennifer Burbach hat als studentische Hilfskraft und Freundin maßgeblich zum Erfolg der Messreisen ans PSI beigetragen und mich auf der Odyssee um das Carnet A.T.A. (Passierschein A38) begleitet und vor dem Wahnsinn bewahrt. Ein großer Dank gilt in diesem Zusammenhang auch Herrn Dr. Christian Grünzweig, der von meiner Arbeit überzeugt war und sich dafür einsetzte, dass ich Messzeit außerhalb der offiziell vergebenen Messzeit bekam.

Des Weiteren möchte ich mich generell bei allen Kollegen am Lehrstuhl für Physik der weichen Materie für das nette und freundliche Arbeitsklima bedanken. Einzelne Kollegen, die für mich zu guten Freunden wurden, sollten jedoch gesondert erwähnt werden. Jörg, mit dem ich zahllose Tassen Kaffee getrunken habe und der meine Gefühlslage oftmals am besten nachvollziehen konnte. Auch wenn seine eigenen Probleme ihn an den Rand der Verzweiflung brachten, hatte er immer ein offenes Ohr für mich, hat mich unterstützt und mir Mut gemacht. Danke auch an Ronja, für Hilfe, Rat und Geduld. Mit ihr waren die regelmäßigen Fahrten nach Jülich deutlich unterhaltsamer als alleine. Christoph,

für seine stets gute Laune, übersprudelnde Begeisterung und das gründliche Lesen meines Manuskripts. Dass er mich immer wieder nach Origin-Ratschlägen gefragt hat, hat mich sehr gefreut – auch wenn ich meistens selbst keine Ahnung hatte. Richie, für die “besten” selbst erfundenen Witze und die Hilfe bei der Entwicklung meiner LabVIEW-Programme. Ein ganz besonderer Dank gilt Kevin – für das LaTeX template mit der Dokumentenklasse “kevin”, für das Korrekturlesen dieser Arbeit und die überaus hilfreichen und nicht zu vernichtenden Kommentare, für Aufmunterungen und Zuspruch und dafür, dass ich mich immer auf ihn verlassen kann.

Ich schätze mich glücklich, Freunde aus Schule, Studium, meiner Mannschaft und FF zu haben, die nicht müde geworden sind, mich zu fragen, wie es läuft und mir zu sagen, dass sie stolz auf mich sind. Auch wenn ich sie nicht alle namentlich nennen kann, sei ihnen gedankt und versichert, dass ich ihr Verständnis und ihre Unterstützung wertschätze.

Meiner Familie kann ich kaum genug danken. Tim, Natascha und Oskar für Ablenkung, Zuspruch und Hilfe bei der Steuererklärung, meinen Eltern dafür, dass sie immer an mich geglaubt haben und ich immer auf sie zählen kann und besonders meinem Vater, der nie sauer darüber war, dass ich seine Frage, wann ich denn fertig werde nicht immer freundlich beantwortet habe. Ohne euch wäre ich nicht ich selbst.

Zuletzt möchte ich mich bei meinem Freund Christian dafür bedanken, dass er mir immer Halt und Zuversicht gegeben und mir nicht ein Mal vorgeworfen hat, dass ich einen Großteil der knappen Freizeit auf dem Hockeyplatz verbracht habe. Dass wir diese schwierige Zeit so gut gemeistert haben, lässt mich optimistisch und freudig in die Zukunft blicken.

“Inmitten der Schwierigkeiten liegt die Möglichkeit.”

Albert Einstein

CONTENTS

List of Figures	xi
List of Tables	xii
1 Background	1
1.1 Soft Matter	1
1.1.1 Colloids	2
1.1.2 Polymers	3
1.1.3 Amphiphiles	5
1.2 Porous Media	6
1.3 Diffusion	8
2 Overview	13
2.1 Imaging Methods	14
2.1.1 Brightfield Imaging	16
2.1.2 Fluorescence Imaging	16
2.1.3 Neutron Radiography	19
2.2 Experimental Setup	22
2.3 Porous Systems and Intruders	25
2.3.1 Polymer Hydrogels	25
2.3.2 Mesoporous Silica	28
2.3.3 Fluorescent Dyes and Macromolecules	30
2.4 Diffusion in Porous Media	30
3 Publications	39
3.1 Neutron, Fluorescence and Optical Imaging: An in-situ Combination of Complementary Techniques	39
3.2 Diffusion of macromolecules in a polymer hydrogel: from macroscopic to microscopic scales	51

Contents

3.3	Solvent and solute ingress into a polymer hydrogel resolved by a combination of imaging techniques	97
3.4	Release of macromolecules from polyacrylamide hydrogels	119
Appendices		127
A Software		127
A.1	Display and save images of two cameras	127
A.2	Choose color plane, calculate average intensity in region of interest and export results to Origin	130
A.3	SubVI: Display color image and choose color plane	134
A.4	Choose color plane and subtract background in area of interest in fluorescence images	135
A.5	Normalize and scale neutron images	138
A.6	Convert image to binary image	142
A.7	Find contour of the hydrogel	145
A.8	Calculate intensity profile	148
B Publications: Protein Phase Behavior		153
B.1	Effect of glycerol and dimethyl sulfoxide on the phase behavior of lysozyme: Theory and experiments	155
B.2	Additivity of the Specific Effects of Additives on Protein Phase Behavior . .	157
B.3	Tuning protein-protein interactions by cosolvents: specific effects of ionic and non-ionic additives on protein phase behavior	159
B.4	Cosolvent-Induced Changes of Protein-Protein Interactions: From Phase Behavior to Second Virial Coefficient	161

LIST OF FIGURES

1.1	The colloidal length scale	1
1.2	Exemplary polymer architectures	3
1.3	Amphiphiles and the formation of micelles	5
1.4	Scanning electron micrographs of natural hierarchical structured porous materials	7
2.1	Resolving power of the human eye, optical light and electron microscopes	15
2.2	Schematic illumination path in a brightfield imaging device	16
2.3	Schematic representation of a Jablonski diagram	17
2.4	Schematic illumination path in a fluorescence imaging device	18
2.5	Spectra of two neutron radiography beamlines at the Paul Scherrer Insitute	21
2.6	Neutron transmission of H ₂ O-D ₂ O mixtures	22
2.7	Schematic representation and photographs of the experimental setup	23
2.8	Exemplary optical, fluorescence, and neutron images of a polymer hydrogel in a reservoir of fluorescein solution	24
2.9	Schematic representation of a hydrogel sample constrained in a sampe cell	29
2.10	Synthesis pathway of mesoporous silica	29
2.11	Comparison of experimentally determined diffusion coefficients of dextran molecules with Brownian dynamics simulations	31
2.12	Solvent volume fraction profiles obtained from neutron radiography measurements	33
2.13	Normalized H ₂ O volume fraction in the center of D ₂ O-hydrogels after contact with H ₂ O solutions containing fluorescent molecules	34
2.14	Fluorescent (macro)molecule influx into and release out of hydrogel discs	35

LIST OF TABLES

1.1	Colloidal Dispersions	2
1.2	Size regimes in porous media	8
2.1	Overview of investigated polymer hydrogels	27
2.2	Overview of dyes and dextran molecules used in the experiments	30

BACKGROUND 1

1.1 Soft Matter

Colloids, polymers, and amphiphiles were traditionally independent research fields until being joined under the new umbrella '*soft matter*' in the 1980s [1]. Soft matter represents a subfield of condensed matter which connects diverse research areas such as physics, chemistry, biology, and material sciences. This diversity is also manifested in various technological applications of soft materials, ranging from paint to lubricants, adhesives, detergents and food. Soft matter comprises a variety of physical states and systems which span the mesoscopic size regime between a nanometer and a micrometer (Fig. 1.1) and which are mechanically soft and hence easily deformable by external stresses and electric or magnetic fields [2–6].

The mesoscopic size of soft matter entities leads to two essential characteristics. Firstly,

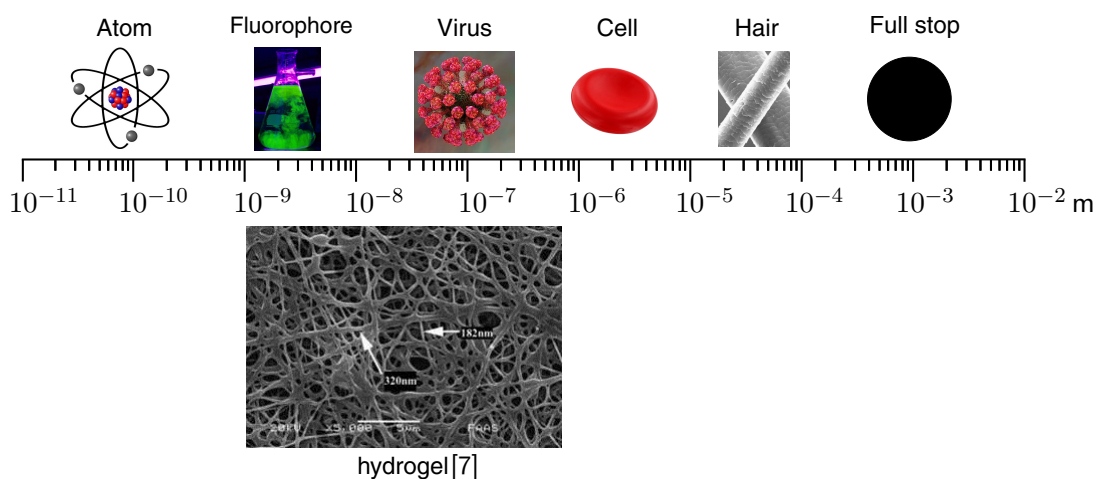


Figure 1.1 Illustration of exemplary systems spanning different length scales. The scanning electron microscopy image of a hydrogel represents the mesoscopic size range relevant for soft matter systems; adapted from [8].

1.1 Soft Matter

effects on the atomic scale do not have to be considered but rather coarse-grained models are suitable to describe soft matter physics. Secondly, particles are small enough to undergo thermal fluctuations, so-called Brownian motion, which is based on the observation of randomly moving pollen grains in water by the botanist Robert Brown in 1827 [9]. Almost 80 years later, in 1905, Albert Einstein developed a theoretical model which successfully described Brown's findings. He proved that the pollen grains moved due to stochastic collisions with water molecules, which also served as verification of the existence of atoms and molecules [10].

1.1.1 Colloids

A colloidal dispersion consists of two phases: a dispersed phase ('particle') and a dispersing medium ('solvent'). All possible combinations of solid, liquid and gas are possible with the exception of gas-gas. Examples are found in everyday life, as shown in Table 1.1. The mesoscopic size of the dispersed particles is much larger than the size of the molecules forming the dispersion medium which can hence be treated as a structureless continuum. This ensures a well-defined and distinguishable interface between particles and medium. A mixture of two gases represents a homogeneous system where the two original phases are not distinguishable any more and is hence not a colloidal dispersion.

dispersed phase	dispersion medium	type of colloidal dispersion	examples
gas	liquid	foam	soap, beer froth, sparkling drinks
gas	solid	solid foam	pumice stone, marshmallow
gas	gas	does not exist	–
liquid	gas	liquid aerosol	fog, mist, hair spray
liquid	liquid	emulsion	milk, mayonnaise
liquid	solid	solid emulsion, gel	cheese, ice cream
solid	gas	solid aerosol	smoke, dust
solid	liquid	sol, colloidal suspension	paint, ink, clay
solid	solid	solid suspension	plastic, glass

Table 1.1 Types of colloidal dispersions [11].

1.1.2 Polymers

Polymers are molecules consisting of repeating units (monomers) and also belong to the world of soft matter. Indeed, the name *polymer* itself gives an indication of the nature of these materials. It is derived from the Greek words 'poly' and 'mer', meaning many and segment, respectively. A number of monomers are covalently bound together to form a macromolecule. Homopolymers are built up by one single monomer species, whilst copolymers consist of different monomers. Polymers are ubiquitous in nature and industrial products and occur in vast numbers of architectures with highly diverse properties and applications [12]. Examples of synthetic polymers are polyethylene, nylon, polyester or Teflon, while natural polymers like silk, wool or DNA are widely known. The simplest case is a long linear polymer chain, but in principle all conceivable shapes exist, e.g. stars, combs, brushes, rings, or three-dimensional polymer networks (Fig. 1.2). These can be custom-tailored by the use of appropriate monomers in the polymerization process.

Rotations around the bond axis are generally not restricted by the covalent bonds between individual monomers. Long polymer chains thus have a large number of internal degrees of freedom resulting in many possible spatial arrangements of the monomeric building blocks. The conformation of one isolated, single polymer chain can thus only be usefully described statistically. The entropically favored configuration of a polymer chain is a random coil which constantly dynamically changes its actual shape. Stretching out of the chain is en-

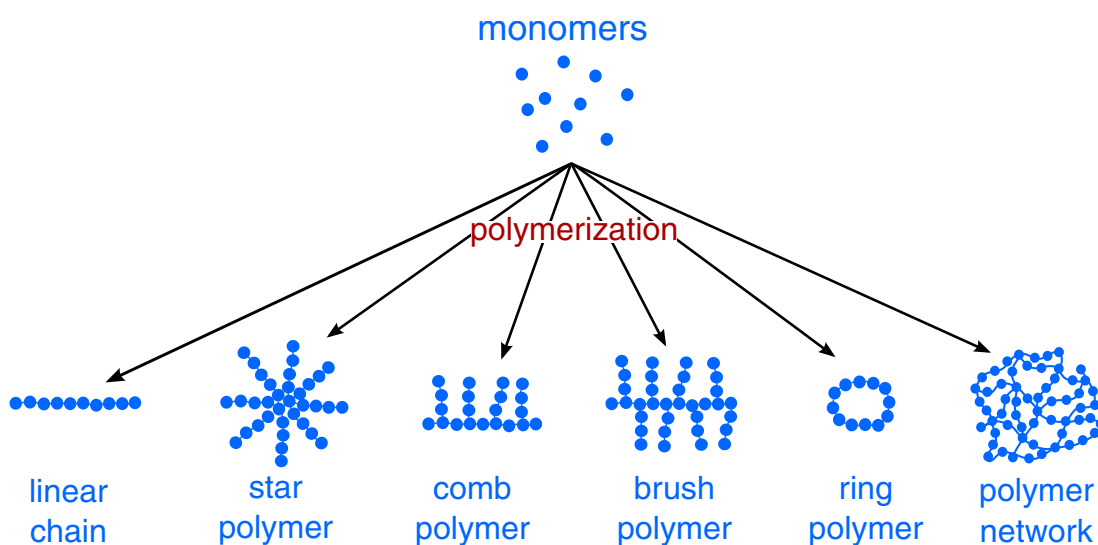


Figure 1.2 Schematic representation of generic polymer types.

1.1 Soft Matter

tropically unfavorable. This entropic force is responsible for the elasticity of rubber and also polymer networks [2].

The simplest model to describe the ideal polymer chain configuration is the *freely-jointed chain* model, where N monomers with a fixed bond length, l , are freely jointed such that all angles between individual segments are equally likely. The configuration can thus be described as a random walk in three dimensions, yielding an average end-to-end distance, $R_{ee} = lN^{1/2}$. An extension of this model, the *freely-rotating chain* model, takes into account that two consecutive bonds enclose a fixed bond angle while rotation around the bond is still possible [13, 14]. Despite the fixed bond angle, a monomer can be placed at any direction relative to a monomer far enough away along the chain. The length over which the orientational correlation is lost is called 'Kuhn statistical length'. Thus, the polymer can again be represented by a freely-jointed chain.

This model lacks an important restriction. While it is possible to revisit a location in a classical random walk, two monomers cannot occupy the same position. Thus, a self-avoiding random walk is more appropriate to describe real polymer configurations, as introduced by the chemist Paul Flory [15]. A rigorous solution of the self-avoiding random walk is not yet available, but approximate solutions and computer simulations suggest $R_{ee} = lN^{3/5}$. The radius of gyration, R_g , is frequently used instead of the end-to-end distance as a measure of the extension of the chain. It is the mean distance of all monomers to the center of mass of the molecule.

Polymer networks will be discussed in more detail in Chapter 2.3.1. These are defined as networks in which each monomer is connected to all other monomers and also to the macroscopic surrounding via numerous continuous paths through the macromolecule [16]. Whilst one can distinguish between chemical and physical networks, the naming refers to the nature of the so-called crosslinking points. According to IUPAC nomenclature, a crosslink is defined as a region in a macromolecule which connects at least four polymer chains. If less than four polymers are connected, it is called a branch point [16]. In a chemical polymer network, separate chains are joined by covalent bonds which are formed by chemical reactions that can be initiated by a change in pH , heat, pressure, or radiation [15, 17]. These bonds are mechanically and thermally stable and difficult to break up, hence complicating the recycling of crosslinked materials such as car tires. Physical crosslinks on the other

hand are based on entanglements and attractive interactions between polymer chains and are thus not permanent.

1.1.3 Amphiphiles

Like polymers, the third main species of soft matter – *amphiphiles* – take their name from Greek ‘amphis’ meaning both and ‘philia’ meaning love; it describes substances comprising a hydrophilic (water-loving) polar head and a hydrophobic (water-hating) tail. The hydrophilic head can either be charged or uncharged and the hydrophobic tail typically consists of one or more long hydrocarbon chains. Common amphiphiles are soaps or phospholipids, a major component of all cell membranes [2, 18].

The amphiphilic character influences how these molecules behave in solution. In pure water for example, they preferentially situate themselves at the surface with their polar heads in and their non-polar tails outside the water phase. That is why they are also referred to as *surfactants*, short for surface-active-agents. If they are forced to enter the water phase – for instance by increasing the amphiphile concentration – the hydrophobic parts will try to avoid contact with water through the formation of micelles. These amphiphile aggregates are held together by weak physical interactions in the order of $1 k_B T$, with the Boltzmann constant k_B and the temperature T (Fig. 1.3). Besides the spherical micelle shown in Fig. 1.3, cylindrical micelles, planar double layers or inverted structures are possible. The concentration which is needed for this spontaneous self-assembly into micelles to occur, is called the critical micelle concentration (cmc).

Basic laws of statistical mechanics postulate that all thermodynamic systems minimize their free energy, $F = U - TS$, by reducing the internal energy, U , or maximizing the entropy, S . A balance between entropy and energy decides the number, shape, and size of the aggregates.

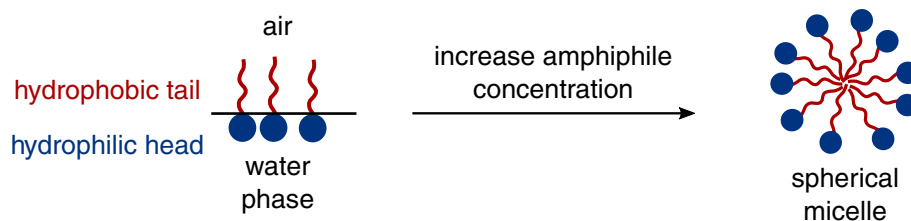


Figure 1.3 Schematic representation of amphiphiles and the formation of micelles.

1.2 Porous Media

Another factor, determining the aggregate geometry is the shape of the single amphiphile molecules, more precisely the headgroup cross-section, the volume taken up by the hydrophobic chain and its length.

One of the main uses of amphiphiles is to stabilize mixtures of two, normally immiscible, liquids such as oil and water. When an amphiphile is added to the mixture, the molecules preferentially adsorb at the interface, thus reducing the interfacial tension. Oil droplets will be encapsulated by the amphiphilic micelles and a stable emulsion is formed. This is also how amphiphiles work in detergents and soaps and why they are widely called surfactants.

1.2 Porous Media

Porous media consist of two phases: the network, often called the matrix or frame, is usually a solid while the pores or voids are filled with a fluid (gas or liquid). Apart from metals, some dense rocks and some plastics, most solid materials can be classified as porous media with the pore structure enabling fluid transport through the materials [19]. Natural materials such as rocks, bones or wood as well as manufactured materials such as cements or ceramics exhibit a porous structure which often significantly influences the material's properties and functionality. Porous building materials for instance are better thermal insulators as they can enclose large amounts of air. Another example is soil and sand, which causes natural filtration of ground water and also traps water in the voids which can successively be absorbed by plants. A selection of scanning electron microscopy and optical microscopy images of natural porous media is shown in Figure 1.4 [20].

Generally, porous media serve to store fluids or gases, separate different substance or catalyze chemical reactions. Physical properties of porous materials are mainly governed by the texture and stiffness of the matrix, the pore sizes and their distribution as well as the resultant specific surface area. According to the IUPAC, there are three different pore size regimes: micropores, mesopores and macropores (Table 1.2) [21].

There are several experimental ways to determine the pore size distribution. The most direct approach is to take an image of the material and measure the dimensions of the pores [22]. Depending on the pore sizes and the required resolution, optical, electron or atomic force microscopy can be used. Additionally, three-dimensional X-ray imaging, computer tomography, is a commonly used technique in geology to reconstruct the internal structure

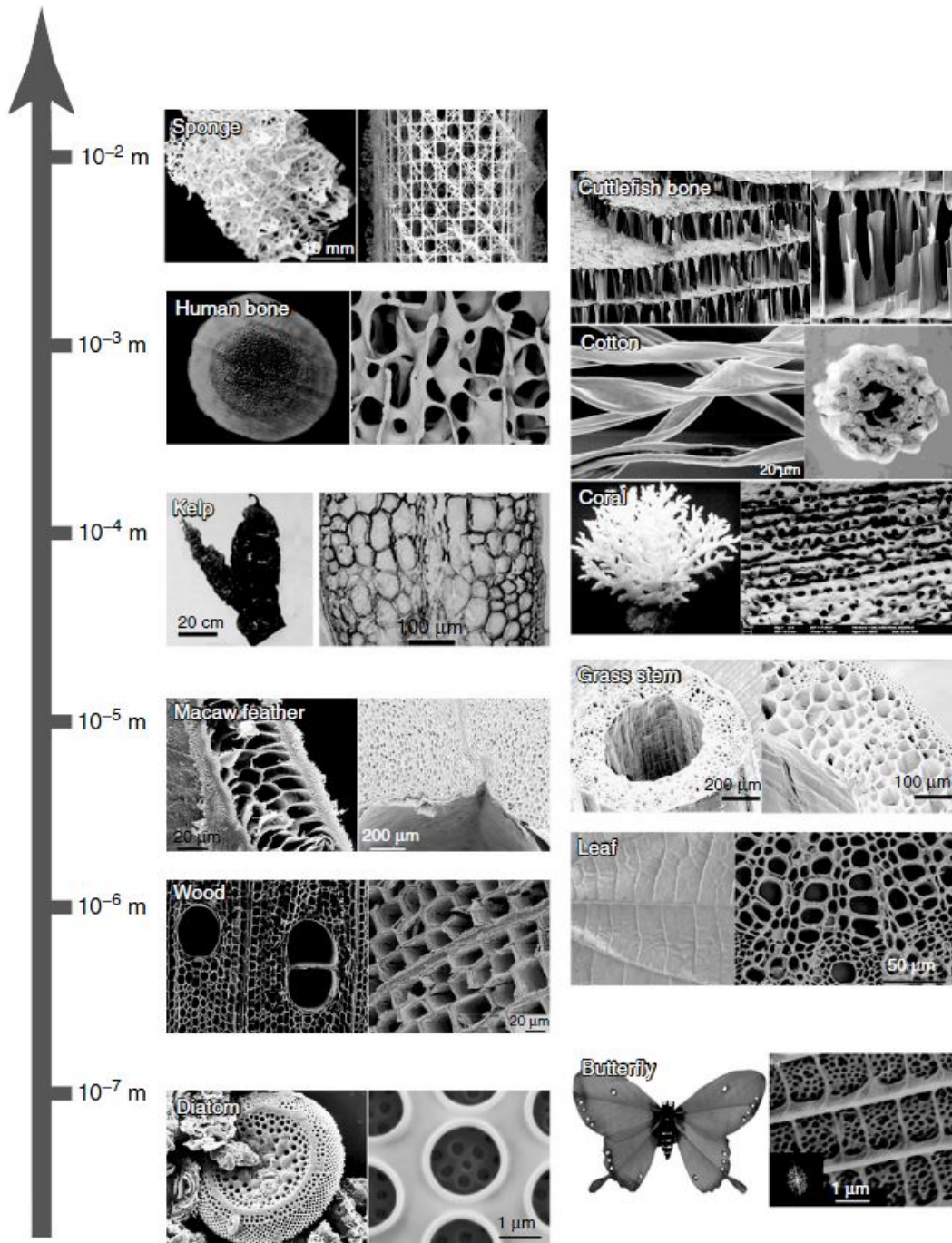


Figure 1.4 Examples of scanning electron and optical microscopy images of natural porous materials; adapted from [20].

of rocks non-destructively. However, these techniques are only useful for certain samples. It might be necessary to cut the sample into thin sections or to treat the sample in order to enhance contrast, which might also change the sample properties or the pore sizes [22, 23].

1.3 Diffusion

pore diameter	IUPAC nomenclature	examples
0–2 nm	micropores	activated carbons, zeolites, metal-organic frameworks
2–50 nm	mesopores	silica, alumina, polymer hydrogels
>50 nm	macropores	plant roots, soil

Table 1.2 Pore size regimes in porous media according to the IUPAC [21].

Very common porosity measurement techniques for solid materials are gas sorption and liquid intrusion measurements. In gas sorption experiments, the change in pressure is measured when an inert gas, typically nitrogen, is absorbed by the sample [24, 25]. For liquid intrusion measurements, a non-wetting liquid, often mercury, needs to be forced into the porous material under high pressure. The porosity can then be calculated based on the volume of liquid and the pressure needed to fill the voids.

However, these techniques are all only applicable for dry samples with a stiff, self-supporting matrix. Another class of porous materials which is of particular importance for the work described in this thesis, are polymer hydrogels (Chapter 2.3.1). In this case, scattering techniques can be applied to investigate the porosity. The sample is irradiated with a monochromatic beam of light, neutrons, or X-rays and the scattered intensity as a function of scattering angle is measured. Information about the pore structure can usually be derived by analyzing the small angle scattering data based on appropriate models and assumptions. The interpretation of scattering data often requires prior knowledge about the expected pore structures [22].

1.3 Diffusion

Diffusion is a spontaneously occurring process that leads to the complete mixing of two or more components. The origin of this process is the Brownian motion of the diffusing substances paired with a concentration gradient [26]. This can be intuitively explained: whilst Brownian motion alone only results in a fluctuating random motion without preferred direction and frequent collisions between molecules, the concentration gradient induces a macroscopically directed movement due to a higher collision probability in regions of a

higher concentration.

First extensively documented experiments about diffusion of gases were conducted from 1828 to 1833 by Thomas Graham. Although he already postulated that diffusion in solutions depends on both the concentration gradient and temperature [27], it was Adolf Fick who developed the laws of diffusion in 1855, which are based on the analogy to heat conduction and can be used to describe fundamentally all diffusion problems.

In one dimension, x , Fick's first law postulates that the diffusive flux, J , which is the rate of transfer of a diffusing substance per unit area is proportional to the concentration gradient, $\partial c/\partial x$, whereas the diffusion coefficient D , is the constant of proportionality:

$$J = -D \frac{\partial c}{\partial x} . \quad (1.1)$$

The negative sign indicates the diffusion direction from high to low concentrations. A combination of Eq. 1.1 with the conservation equation yields Fick's second law, the most fundamental diffusion equation. It describes the temporal change in concentration, c , during a diffusion process. If the diffusion coefficient, D , is independent of position, x , and concentration, c :

$$\frac{\partial c}{\partial t} = -\frac{\partial J}{\partial x} = D \frac{\partial^2 c}{\partial x^2} . \quad (1.2)$$

Note that the dependence of the concentration on position and time, $c(x, t)$, is omitted in this representation. In the case of radial diffusion in a sphere or an infinitely long cylinder, the surface of diffusion is position dependent and has to be considered. For radial diffusion in a sphere, Eq. 1.2 can be expressed as:

$$\frac{\partial c}{\partial t} = D \left(\frac{\partial^2 c}{\partial r^2} + \frac{2}{r} \frac{\partial c}{\partial r} \right) , \quad (1.3)$$

and similarly for diffusion in a cylinder as:

$$\frac{\partial c}{\partial t} = \frac{1}{r} \frac{\partial}{\partial r} \left(r D \frac{\partial c}{\partial r} \right) , \quad (1.4)$$

where r is the radial position inside the sphere or cylinder and $r = 0$ in the center.

With an adequate consideration of the geometry and the boundary conditions of a given system, the diffusion equation can be solved. Many theoretical scenarios were extensively covered by Crank [28] and picked up by many authors [29–33].

Bibliography

Fick's laws are based on a macroscopic approach to describe diffusion processes which does not explicitly take the motion of individual diffusing particles into account. On this microscopic level, Brownian motion can be described by a theory independently developed by Albert Einstein and Marian Smoluchowski in 1905 and 1906, respectively. They derived a relation between the diffusion coefficient, D , and the mean square displacement, $\langle \Delta r^2 \rangle$, which is a measure for the average distance a particle travels in a certain delay time, τ :

$$\langle \Delta r^2(\tau) \rangle = \frac{1}{N} \sum_{i=1}^N (r_i(t + \tau) - r_i(t))^2 = 2dD\tau . \quad (1.5)$$

The mean square displacement is an ensemble average over N particles and d denotes the dimensionality of the diffusion process. Equation 1.5 describes free diffusion and becomes much more complicated if external obstructions are introduced.

These two approaches on different length scales also point towards fundamentally different experimental methods to study diffusion. The first one is to monitor the change in concentration of the diffusing substance and then apply the Fickian diffusion equations and the second is to study how the system evolves on the molecular level.

Bibliography

- [1] de Gennes, P.-G. *Angewandte Chemie International Edition in English* **1992**, *31*, 842–845.
- [2] Dhont, J. K. G.; Gompper, G. *Lecture Notes of the 42nd IFF Springschool*; Forschungszentrum Jülich, 2011.
- [3] Evans, D. F.; Wennerström, H. *The colloidal domain: where physics, chemistry, biology, and technology meet*; Wiley-VCH: New York, 1999.
- [4] Jones, R. A. *Soft condensed matter*; Oxford University Press, 2002; Vol. 6.
- [5] Vincent, B. *Colloid Science: Principles, Methods and Applications* **2005**, 1–13.
- [6] Hirst, L. S. *Fundamentals of soft matter science*; CRC Press, 2012.
- [7] Liu, H.; Zhen, M.; Wu, R. *Macromol. Chem. Phys.* **2007**, *208*, 874–880.
- [8] Hanes, R. D. L. Colloids in controlled energy landscapes. Ph.D. thesis, Heinrich-Heine-Universität Düsseldorf, 2012.
- [9] Brown, R. *The Philosophical Magazine, or Annals of Chemistry, Mathematics, Astronomy, Natural History and General Science* **1828**, *4*, 161–173.
- [10] Einstein, A. *Annalen der Physik* **1905**, *322*, 549–560.
- [11] Shaw, D. J. *Introduction to colloid and surface chemistry*.
- [12] Brandrup, J.; Immergut, E. H.; Grulke, E. A.; Abe, A.; Bloch, D. R. *Polymer handbook*; Wiley New York, 1999; Vol. 89.
- [13] Friedlinghaus, H. *Lecture Notes of the 35th IFF Springschool*; Forschungszentrum Jülich, 2004.

- [14] Piazza, R. *Soft matter: the stuff that dreams are made of*; Springer Science & Business Media, 2011.
- [15] Flory, P. J. *Principles of Polymer Chemistry*; Baker lectures 1948; Cornell University Press, 1953.
- [16] Jenkins, A.; Kratochvil, P.; Stepto, R.; Suter, U. *Pure Appl. Chem.* **1996**, *68*, 2287–2311.
- [17] Elias, H.-G. *An introduction to polymer science*; VCH, 1997.
- [18] Chen, X.; Fuchs, H. *Soft Matter Nanotechnology: From Structure to Function*; John Wiley & Sons, 2015.
- [19] Dullien, F. A. *Porous media: fluid transport and pore structure*; Academic press, 2012.
- [20] Su, B.-L.; Sanchez, C.; Yang, X.-Y. *Hierarchically structured porous materials: from nanoscience to catalysis, separation, optics, energy, and life science*; John Wiley & Sons, 2012.
- [21] Everett, D. *International Union of Pure and Applied Chemistry (IUPAC)* **1972**, *31*, 577–638.
- [22] Espinal, L. *Characterization of Materials* **2012**,
- [23] Klobes, P.; Meyer, K.; Munro, R. G. *Porosity and specific surface area measurements for solid materials*; US Department of Commerce, Technology Administration, National Institute of Standards and Technology, 2006.
- [24] Allen, T. *Particle size measurement*; Powder technology series; Chapman and Hall, 1990.
- [25] Rouquerol, J.; Rouquerol, F.; Llewellyn, P.; Maurin, G.; Sing, K. S. *Adsorption by powders and porous solids: principles, methodology and applications*; Academic press, 2013.
- [26] Cussler, E. L. *Diffusion: mass transfer in fluid systems*; Cambridge university press, 2009.
- [27] Graham, T. *Philosophical Transactions of the Royal Society of London* **1850**, *140*, 1–46.
- [28] Crank, J. *The Mathematics of Diffusion*; Oxford University Press: New York, 1979.
- [29] Haggerty, L.; Sugarman, J.; Prudhomme, R. *Polymer* **1988**, *29*, 1058–1063.
- [30] Samprovalaki, K.; Robbins, P.; Fryer, P. *J. Food Eng.* **2012**, *111*, 537–545.
- [31] Chen, Y.; Flanagan, D. *Theory of diffusion and pharmaceutical applications, developing solid oral dosage forms*. 2009.
- [32] Huang, I.; Yen, S. *Mater. Chem. Phys.* **2002**, *74*, 289–299.
- [33] Zhang, X.; Hirota, N.; Narita, T.; Gong, J. P.; Osada, Y.; Chen, K. *J. Phys. Chem. B* **1999**, *103*, 6069–6074.

This page has been left intentionally blank.

OVERVIEW 2

In this chapter, an overview of the work performed for this thesis and which is presented in more detail in Chapter 3 is provided. A central part of the work described in this thesis was the design, construction and optimization of an experimental setup that allows the simultaneous application of three complementary imaging techniques: optical transmission or reflection imaging, fluorescence imaging, and neutron radiography (Chapters 2.2 and 3.1). This experimental setup was used to investigate diffusion into, through, and out of porous media (Chapter 2.2).

In a first step, the diffusion of fluorescent macromolecules into a water-swollen polymer hydrogel was studied using optical and fluorescence imaging. The results were compared to those obtained from two different experimental techniques (fluorescence correlation spectroscopy and nuclear magnetic resonance spectroscopy) and from Brownian dynamics simulations (Chapter 3.2). A good agreement between the results from these fundamentally different experimental and theoretical techniques proves the reliability and functionality of the developed experimental setup and the associated measuring and analysis techniques.

In the next step, similar measurements were performed using additionally the third imaging method, neutron radiography, in order to distinguish between solvent and solute diffusion. This allowed the separate but simultaneous study of the influx of solvent and solute into polymer hydrogels (Chapter 3.3) as well as the release of fluorescent macromolecules from the hydrogels (Chapter 3.4). Even though the diffusion of molecules through porous networks such as polymer hydrogels is crucial for a number of applications and hence the focus of numerous experimental and theoretical studies [1–11] there are few studies explicitly addressing the solvent motion and its interplay with the solute motion [12, 13].

2.1 Imaging Methods

A central part of the work described in this thesis was the development of an experimental technique that combines three complementary imaging methods to simultaneously and independently investigate various features of a system. Thus, a general overview of common imaging techniques is given in this chapter and the three techniques used in the experimental part of this thesis (brightfield, fluorescence and neutron imaging) are discussed in more detail.

Imaging in science is applied in multidisciplinary research areas with numerous applications. It is a very popular experimental approach as it satisfies the human desire to see what is occurring even if it is not visible to the eye. In the modern smartphone era, the practice of taking a photograph has become a daily occurrence and photography can be conveniently used to explain the underlying principle of all imaging techniques.

Light emitted or reflected from an object is focused by an optical system onto an image sensor or a light-sensitive material, forming an image of the object. Light intensities, and in the case of a color sensitive image detector, wavelengths are measured and visualized via spatially resolved gray levels or a color code. Image quality is determined by both the spatial resolution, i.e. the minimal distance between two points in the image that can be distinguished from each other, and the image contrast, i.e. the difference in brightness and color between different points in the image. The limits of resolution paired with the obtained magnification have been continuously improved. While the human eye is limited to resolving objects that are a fraction of a millimeter apart, light microscopes allow micrometer sized objects to be seen. As the resolution is determined by the wavelength of the radiation, the use of an electron beam with a much shorter wavelength yields a resolution down to 0.1 nm (Fig. 2.1). Two types of optical imaging, brightfield and fluorescence imaging, will be discussed in more detail in Chapters 2.1.1 and 2.1.2.

In a few applications, the sample automatically emits the radiation which is to be detected. Examples are thermal imaging, where radiation in the long-infrared range of the electromagnetic spectrum is measured to generate a heat map, or the detection of radioactive radiation used in positron emission tomography in nuclear medicine. In most cases, the sample needs to be irradiated with some kind of radiation first. This can be compared to using a flash when taking a photograph in dark environments. The radiation interacts with

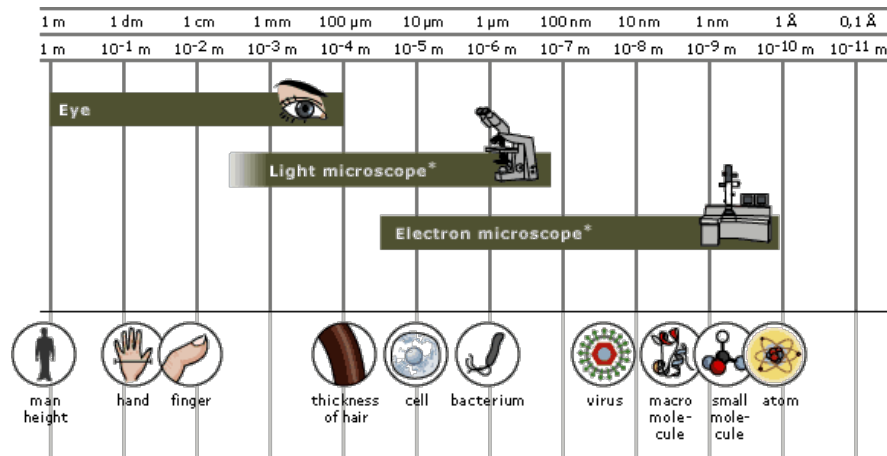


Figure 2.1 Schematic representation of the resolving power of the human eye compared to light and electron microscopes; from [14].

*Light microscope includes brightfield, dark field, phase contrast and fluorescence microscopes. Electron microscope includes scanning electron and transmission electron microscope.

the sample, is absorbed, transmitted or scattered and thus contains information about the sample, which is recorded using a suitable detector. Depending on the radiation, contrast in the image is generated by different features of the sample. This can be understood by comparing two common medical imaging techniques: X-ray and magnetic resonance imaging.

In 1895, Wilhelm Röntgen discovered X-rays, a radiation with a wavelength between 0.01 and 10 nm, which can be used to identify bone structure. X-ray imaging in medicine is often called radiography, even though technically speaking the term 'radiograph' describes only a shadow image produced by any kind of radiation after passing through an object. In the case of X-rays, human tissue and liquids are basically transparent while the minerals in bones, especially calcium, efficiently absorb X-rays due to their high electron density. This results in a reduction of X-rays reaching the detector and hence contrast in the image.

Magnetic resonance imaging (MRI), also called nuclear magnetic resonance imaging (NMRI), is achieved by placing the sample in a strong and uniform magnetic field (typically about 1.5 T). This results in a polarization of the protons and thus alignment of their spins parallel to the magnetic field. Protons are the nuclei of hydrogen atoms and thus present in H₂O molecules in human tissue. Then, an additional weaker magnetic field, that oscillates at the resonance frequency of the hydrogen atoms is applied. This causes the spins to tilt

2.1 Imaging Methods

and precess. After turning of the oscillating field, the spins will relax again and orient in the direction of the static magnetic field. The time constant for this relaxation process is measured. As it strongly depends on the molecular environment of the hydrogen molecules, different tissues and organs result in a characteristic signal and contrast in the image.

For the sake of completeness, it should be noted that imaging with all other types of radiation such as ultrasound or radar is also possible. Imaging with particle radiation is discussed in more detail in Chapter 2.1.3 using the example of neutron radiography.

2.1.1 Brightfield Imaging

Brightfield imaging is the simplest optical imaging method. Light, typically from a halogen or a LED lamp, is directed onto the sample either transmitted or reflected and subsequently focused onto a detector. The light path through a brightfield transmission imaging device is schematically depicted in Figure 2.2. The collimator lens collects light from the light source and collimates it in order to be able to efficiently use the provided illumination. The collimated light beam is then focused onto the sample plane by a condenser lens before it reaches the objective. The objective can be a single lens or consist of several optical components and serves to magnify the image of the sample and to focus it onto the detector, which can be a camera or the human eye. In most microscopes, an additional lens, called the ocular or eye piece, is placed near the focal point of the objective to further magnify the image. The obtained magnification depends on the individual lenses in the objective and contrast in the image results from absorption of light in the sample.

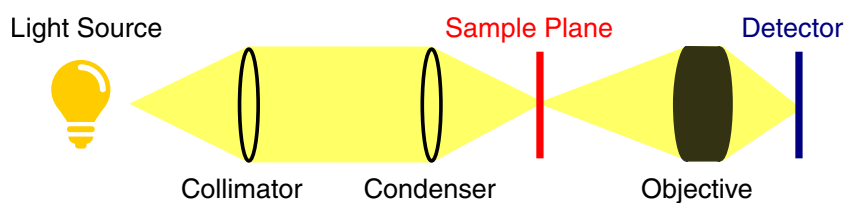


Figure 2.2 Schematic illustration of the light path through a brightfield transmission imaging device.

2.1.2 Fluorescence Imaging

Luminescence is the emission of light from substances which either transfer external energy not at all or not entirely into thermal energy but get electronically excited. There are many

different types of luminescence depending on the nature of the excitation. Examples are chemiluminescence which is the result of a chemical reaction, electroluminescence, resulting from an electric current passing through a material or photoluminescence which is a consequence of the absorption of photons. Photoluminescence can be divided into fluorescence and phosphorescence, which is the emission of light from excited singlet or triplet states [15, 16].

The absorption and emission of light can be illustrated by Jablonski diagrams, as seen in Figure 2.3, where S_0 , S_1 , and S_2 represent the ground, first, and second excited states, respectively. These states can be further divided into different energy levels corresponding to different vibrationally excited states. Fluorescence typically occurs from aromatic molecules and fluorescent substances are commonly known as fluorophores. Important characteristics of a fluorophore are its fluorescence lifetime and its quantum yield. The fluorescence life time, τ , is the average time between excitation and emission and is typically in the order of nanoseconds. In contrast to the instantaneous absorption of light, the time span the fluorescent molecule remains in the excited state allows it to interact with other molecules. Thus, absorption spectroscopy can only yield information about the energy ground state of the molecules while the fluorescence signal contains information about the molecular environment and dynamics of a fluorescent molecule [15]. The quantum yield is the ratio of the

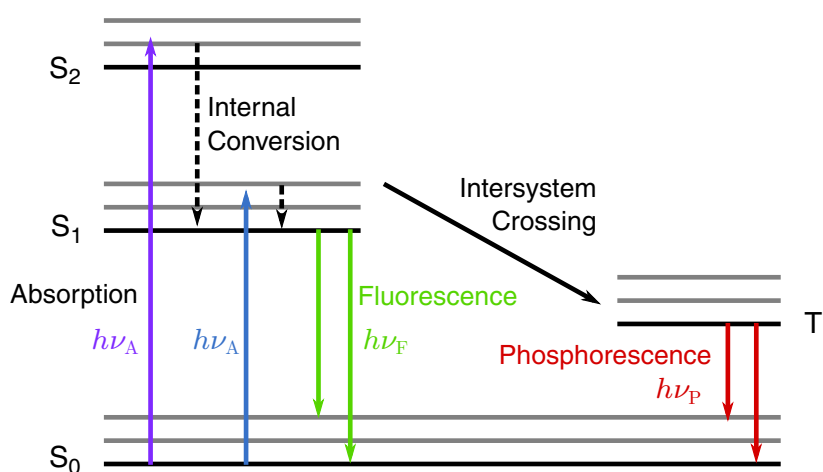


Figure 2.3 The *Jablonski diagram* schematically shows the excitation of a fluorophore from its ground state, S_0 , to an excited state, S_1 or S_2 , followed by either an internal conversion to a lower excited state or an intersystem crossing to the first triplet state, T_1 . Fluorescence and phosphorescence are emitted upon relaxation to the ground state from the S_1 or T_1 state, respectively; redrawn from [15].

2.1 Imaging Methods

number of emitted photons to the number of absorbed photons and hence determines the brightness and the necessary excitation energy to generate a sufficient fluorescence signal [15]. The emission spectrum is characteristic for the respective fluorophore and independent of the excitation wavelength [17].

In addition to fluorescing, molecules can also undergo a spin conversion from the excited singlet state to the first triplet state, T_1 . The phosphorescence emitted from this energy state occurs on considerably slower emission rates of $10^3 - 10^0 \text{ s}^{-1}$, corresponding to lifetimes in the range of milliseconds to seconds or even longer. As displayed in Figure 2.3, the emitted light usually has a lower energy and thus longer wavelength, λ , compared to the excitation light. This difference in wavelength is named 'Stokes shift' after the Irish physicist Sir George G. Stokes, who first observed this phenomenon in 1852 [18]. It enables the separation of excitation and emission light with optical filters necessary for fluorescence imaging techniques, as illustrated in Figure 2.4 for the fluorophore fluorescein isothiocyanate (FITC). The excitation filter (EX) is usually a band pass filter that only transmits a narrow wavelength range around the excitation maximum of the fluorophores in the fluorescent specimen (Fig. 2.4). FITC displays its maximum absorption at 495 nm and an emission peak at about 519 nm. After interacting with the sample, the light beam contains both the excitation light and the emitted fluorescence light. A dichroic mirror (DM) is used to separate these two contributions. If it is placed at an angle of 45° to the incident beams, it

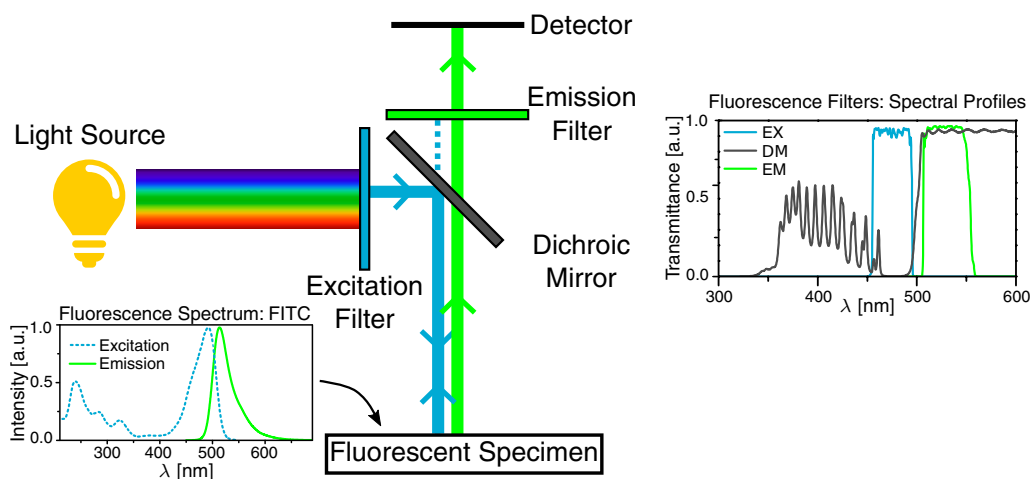


Figure 2.4 Schematic representation of the light path and the use of optical filters in epi-fluorescence imaging devices. The fluorescence spectrum of fluorescein isothiocyanate (FITC) and spectral profiles of filters optimized for this fluorophore are presented.

reflects wavelength below a certain cut-off value while higher wavelengths are transmitted. The DM is chosen such that the cut-off value lies between the excitation and the emission wavelengths. In the case of FITC, wavelengths below 500 nm are reflected and higher wavelengths are transmitted. As seen in the spectral profiles of a commercially available fluorescence filter set optimized for FITC in Figure 2.4, it is still possible that some fraction of the excitation light is transmitted by the dichroic mirror. Thus a third filter, the emission filter (EM), which is typically a band pass or a longpass filter that only transmits wavelengths well above the excitation wavelengths is used. Thus, only fluorescence generated in the specimen reaches the detector. The high sensitivity of fluorescence detection, even allowing single-molecule observation together with a vast number of fluorescence technologies and applications render it a dominant and extensively used methodology. Prominent examples of additional fluorescence techniques are fluorescence correlation spectroscopy (FCS), fluorescence anisotropy, Förster energy transfer (FRET) or fluorescence recovery after photobleaching (FRAP).

2.1.3 Neutron Radiography

In contrast to the optical imaging methods discussed in the previous sections, neutron imaging uses a neutron beam instead of light to irradiate the object of interest and hence to form the image. Neutrons are the electrically neutral constituents of atoms with a mass of 1.675×10^{-27} kg, which were discovered by James Chadwick in 1932 [19, 20]. An important requirement for neutron radiography experiments is access to a neutron source providing a sufficient neutron flux at a large scale facility for science. There are two classes of neutron sources, nuclear fission reactors and spallation sources. In a reactor, the fission of the uranium isotope ^{235}U after capturing a slow neutron is used. The uranium nucleus is deformed and split up into two lighter nuclei instantly releasing two to three neutrons. Each of these neutrons can again initiate the fission of another uranium nucleus, leading to a chain reaction of fission events. The amount of available fissile material is very important for a stable neutron flux and a safe reactor operation. While too much fissile material would quickly lead to an uncontrollable chain reaction with an exponential increase of generated neutrons accompanied by a huge energy release, a certain critical mass of uranium is necessary to sustain the chain reaction.

For the second nuclear reaction used for neutron production, the spallation reaction, highly

2.1 Imaging Methods

energetic protons produced by a particle accelerator are directed onto a target containing heavy nuclei such as lead or tantalum. The protons collide with individual nucleons (i.e. neutrons or protons) in the nuclei. As a result of these collisions, nucleons are either ejected or experience further intra nuclear collisions leading to a highly excited nucleus, which consequently releases further nucleons.

An important property of neutrons relating to their use in soft matter experimentation is their dual wave-particle nature, which allows their energy, E , to be related to their wavelength, λ . The de Broglie equation is:

$$\lambda = \frac{h}{p} = \frac{h}{m_n v} = \frac{h}{\sqrt{2Em_n}}, \quad (2.1)$$

with the Planck constant, $h = 6.626 \times 10^{-34}$ Js, momentum, p , and speed, v , and allows suitable wavelengths to be chosen to match the energy required.

The energy of neutrons produced with one of the explained nuclear reactions is typically in the range of 1 MeV. However, for scientific purposes and condensed matter investigations, neutron wavelengths in the order of a few Angstroms are required. This corresponds to the meV energy range and hence the generated neutrons have to be cooled or in other words slowed down before they can be used for the experiments. This is achieved with a moderator which is typically graphite, heavy water or light water, where the speed of the neutrons is reduced by elastic collisions with the moderator molecules. The different energy and thus wavelength regimes are classified roughly according to the respective moderator temperature into hot, thermal, cold, and ultracold neutrons. Figure 2.5 shows exemplary neutron wavelength spectra of two neutron radiography beamlines available at the Paul Scherrer Institute in Villigen, Switzerland. Whilst NEUTRA is a thermal neutron imaging facility, the experiments described in Chapter 3.3 were performed at the cold neutron imaging beamline ICON.

As its name states, neutron radiography is a radiographic technique, meaning that shadow images of the objects are recorded. Neutron tomography, a three-dimensional reconstruction of several radiographs taken in different orientations is possible as well but will not be discussed further. Contrast in the radiographs is generated when neutrons interact with the object, get absorbed or change their direction, resulting in a reduction of transmitted neutrons. As neutrons only interact weakly and mainly with the atomic nuclei, they are

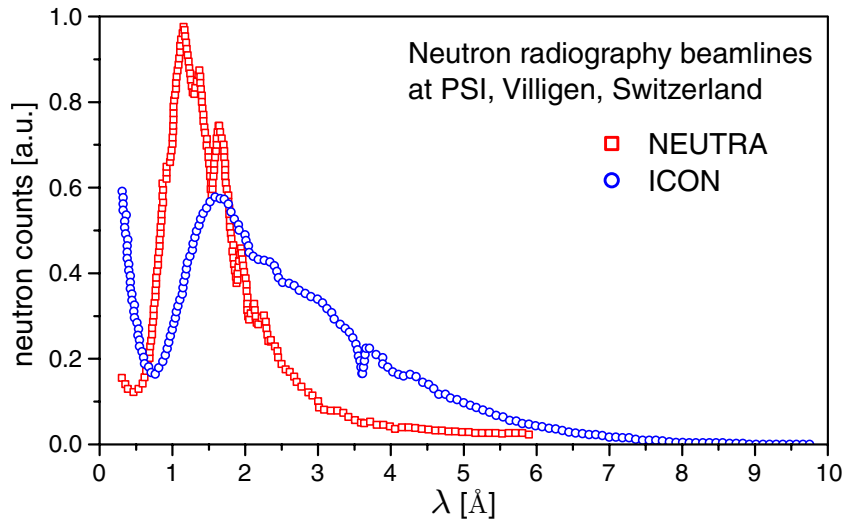


Figure 2.5 Neutron wavelength spectra of two neutron radiography beamlines at the Paul Scherrer Institute in Switzerland; redrawn from [21].

highly penetrating into most materials and suitable to internally image large objects and structures in a non-destructive fashion [22]. A particularly useful property of neutrons is that their interaction cross-section varies randomly throughout the periodic table. This is in distinct contrast to X-rays, where the attenuation coefficient of an element increases with increasing atomic number due to their interaction with electrons. Neutrons interact strongly with some light atoms such as hydrogen, lithium or boron while they barely interact with metals such as aluminum [22, 23]. Even isotopes of the same element can have markedly different neutron attenuation coefficients. This has particular relevance for neutron radiography in soft matter applications as isotope exchange can be used to induce contrast in the images and thus highlight certain parts of the sample. A prominent example, which was also exploited for the experiments described in Chapter 3.3, is the difference in neutron attenuation of ^1H and ^2H , hydrogen and deuterium, respectively. Even though these isotopes only distinguish themselves by one neutron, hydrogen has a total neutron cross-section $\sigma_{\text{H}} = 82.36 \text{ b}$ (whereas $1 \text{ b} = 10^{-28} \text{ m}^2$) while that of deuterium is only $\sigma_{\text{D}} = 7.64 \text{ b}$ for a neutron wavelength of $\lambda = 0.1798 \text{ nm}$ [24, 25]. The cross-section is an intrinsic measure for the likelihood of an interaction between neutron and nucleus. The larger neutron cross-section of H_2O compared to that of D_2O thus translates into a lower neutron transmission of H_2O in a neutron imaging experiment. This is illustrated in Figure 2.6, where the neutron transmission, T , of H_2O - D_2O mixtures as a function of the respective

2.2 Experimental Setup

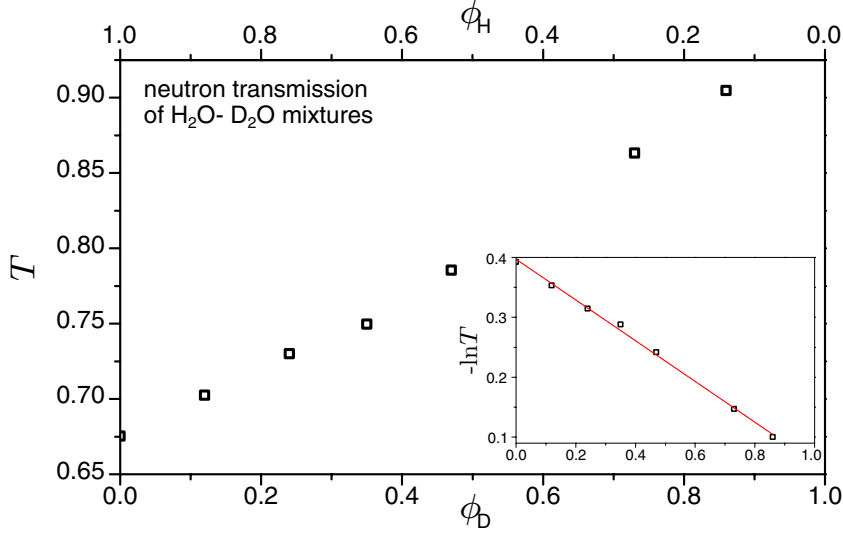


Figure 2.6 Neutron transmission, T , of H_2O - D_2O mixtures with the respective volume fractions of H_2O and D_2O , ϕ_H and ϕ_D measured at the cold neutron imaging beamline ICON at the Paul Scherrer Institute, Villigen, Switzerland.

volume fractions of H_2O and D_2O , ϕ_H and ϕ_D , is plotted. The neutron radiographs are two-dimensional grayscale images with the intensities, $I(x, y)$, and were measured at the ICON beamline. To calculate the transmission, which is the ratio of the transmitted to the incident intensity, $T = I/I_0$, a pixelwise flat-field correction was performed:

$$T(x, y) = \frac{I(x, y) - I_{\text{BG}}(x, y)}{I_0(x, y) - I_{\text{BG}}(x, y)}, \quad (2.2)$$

The incident intensities, $I_0(x, y)$, as well as the background intensities, $I_{\text{BG}}(x, y)$, taken when all shutters in the neutron beamline were closed, were recorded separately. The pixelwise correction accounts for spatial inhomogeneities in the neutron beam and detector efficiency. If necessary, the data can be corrected for potential temporal fluctuations in the neutron beam intensity by monitoring the transmission of a reference area, where no change in transmission is expected during the measurement time. This procedure is explained in detail in Chapter 3.3.

2.2 Experimental Setup

An experimental setup was designed which allows the combination of three complementary imaging techniques: optical imaging (OI), fluorescence imaging (FI), and neutron radio-

graphy (NR). It is described in detail in Chapter 3.1. As neutron radiography experiments can only be performed at large scale facilities, the setup needs to be portable and customized to meet the spatial restrictions of the neutron beamline where the experiments are conducted. All neutron radiography experiments described in this thesis were performed at the cold neutron imaging beamline ICON at the Paul Scherrer Institute located in Villigen in Switzerland [26, 27] and thus the setup described here is optimized for this beamline. Figure 2.7 shows a schematic representation of the imaging setup and two photographs, which illustrate the setup placed in the ICON beamline. The horizontal neutron beam path, in this representation from right to left, can not be changed. Thus, the optical setup is constructed such that a vertical sample orientation is possible and that only the sample and cell and two optical mirrors (M1 and M2) are irradiated by the neutron beam. All other components are placed far enough from the neutron beam and additionally shielded in order to minimize their activation. The two quartz glass mirrors with a chrome-silica coating reflect optical light but have a very low neutron interaction cross-section and thus appear almost transparent to neutrons. Neutrons transmitted from the sample reach the scintillation screen (SC), which re-emits the energy deposited by the incoming neutrons in the form of light which is detected by a CCD camera (NR CAM) and forms the neutron radiograph.

For the optical and fluorescence imaging, the light from an LED lamp (CoolLED pE-2) is guided to an excitation filter (EX) by an optical fiber (OF). The excitation filter usually is

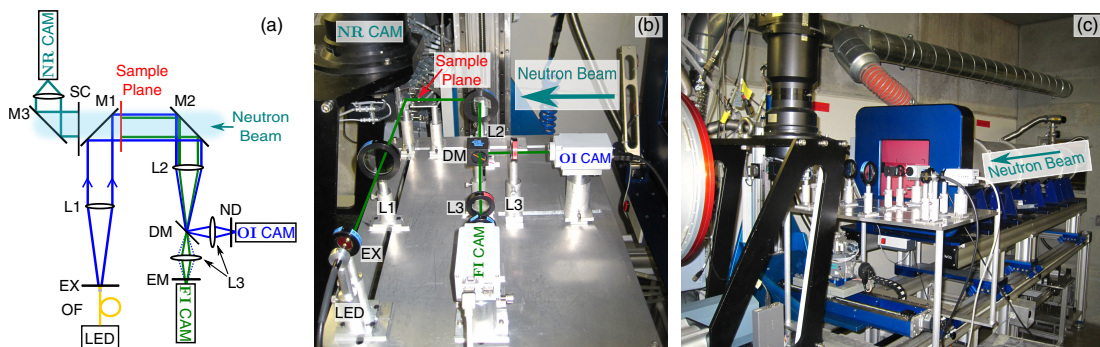


Figure 2.7 (a) Schematic representation and (b) and (c) photographs of the experimental setup in the neutron radiography beamline ICON at the Paul Scherrer Institute. The labels are defined in the main text. In the photographs, there is no sample in the sample plane and shielding to prevent radiation damage of the equipment has been removed. Reprinted from [28] with the permission of AIP Publishing.

2.2 Experimental Setup

a short or band-pass filter and transmits only a certain wavelength range that is suitable to excite fluorophores in the sample. It guarantees that the wavelength of the incident excitation light is well below the emission wavelength of the fluorophores. An achromatic doublet lens (L1) generates a collimated light beam, which is then directed onto the vertically oriented sample using mirror M1. In the sample a fraction of the incident radiation is transmitted while the rest is absorbed by the fluorescent molecules and is subsequently re-emitted with a longer wavelength. Thus, the light beam behind the sample plane consists of two spectral parts, which can be separated using optical filters. A dichroic mirror (DM) in combination with an emission filter (EM) transmit the emitted fluorescence, while the transmitted excitation light is reflected by the DM and subsequently attenuated by a neutral density filter (ND) to avoid overexposure. These two spectral parts contain different information about the sample, which can be visualized by focusing the respective light beams onto two separate CCD cameras (FI CAM and OI CAM) using lenses (L2 and a pair L3). Using a color camera allows the detection of changes in the emission spectrum during an experiment. Instead of the combination of OI and FI with the described setup, one could also introduce additional filters in the OI light path and for instance monitor a second fluorescent species.

As already discussed in Chapter 2.1 and seen in Fig. 2.8 using the example of a polymer hydrogel immersed in a reservoir of fluorescent dye solution, the three imaging methods

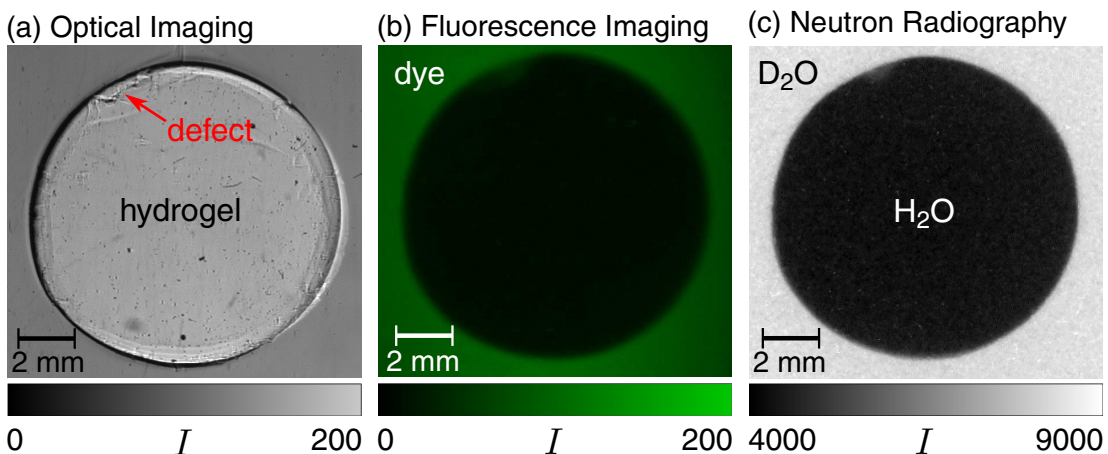


Figure 2.8 Exemplary (a) optical, (b) fluorescence and (c) neutron images of a polymer hydrogel in a reservoir of fluorescein solution. The color and gray scale bars correspond to the original image intensities.

combined in this setup illustrate different properties of the sample. In optical imaging, contrast is generated by differences in the optical density. Size, structure and possibly defects of the sample can be seen (Fig. 2.8 (a)). In fluorescence imaging, only the fluorescent molecules, in this case the sodium salt of fluorescein, are seen (Fig. 2.8 (b)). A higher intensity corresponds to a higher fluorophore concentration and the comparison of images, taken at different times allows the analysis of the diffusion of fluorescein dye from the reservoir into the hydrogel. As opposed to this, contrast in the neutron radiographs is caused by the large difference in attenuation of hydrogen and deuterium (Fig. 2.8 (c)). The hydrogel depicted here is swollen in H_2O , which appears dark in the radiograph, while the fluorescent dye is dissolved in D_2O which appears much brighter. Thus a mixing of the two liquids can be followed by monitoring the spatially and temporally dependent change in image intensities.

In contrast to neutron radiation, which can easily penetrate metallic materials such as aluminum or zirconium, optical transmission imaging is limited to either very thin or optically transparent samples. In the case of opaque samples, the mirror M1 needs to be replaced by a beam splitter in order to realize epi-illumination and thus optical and fluorescence reflection imaging [28].

2.3 Porous Systems and Intruders

2.3.1 Polymer Hydrogels

Hydrogels are three-dimensional networks of crosslinked polymers with intriguing properties. They can for instance absorb large amounts of water due to hydrophilic functional groups and hence swell to many times their original size. The dissolution of the network is prohibited by the crosslinks, which can either be physical or chemical, depending on the polymer and the synthesis conditions. Physical crosslinks arise from ionic or hydrophobic interactions between different polymers, hydrogen bonds or polymer chain entanglements. While these junctions are of transient nature, chemical crosslinks are permanently formed by a chemical reaction [29]. Due to the large variety of suitable polymeric material and crosslinking methods, many different hydrogels have been prepared and studied. Some hydrogels are often referred to as smart materials due to their ability to respond to external stimuli such as a change in pH , temperature, or solvent composition with a drastic volume

2.3 Porous Systems and Intruders

change. Hydrogels are widely used in a broad range of applications from bioadhesives [30], responsive coatings [31, 32] or chemical sensors [33, 34] to controlled drug delivery [35–38] or food products [39, 40].

All experiments described in this thesis were performed with chemically crosslinked polyacrylamide (PAAm) hydrogels, which were synthesized by copolymerization of the monomer acrylamide (AAm) with the tetrafunctional crosslinking agent N,N'-methylenebis(acrylamide) (BIS). Ammonium peroxodisulphate (APDS) and tetramethylethylenediamine (TEMED) were used as redox initiators to start the chemical reaction. One important parameter characterizing the hydrogel is the molar ratio of crosslinker to monomer, usually called the crosslinking ratio, $X = n_{\text{BIS}}/n_{\text{AAm}}$, where n denotes the amount of the respective substance. Hydrogels with two different crosslinking ratios were prepared, $X = 1/60$ and $X = 1/15$. Hydrogels swollen in heavy water (D_2O) were prepared using the same protocol by exchanging H_2O with D_2O in every step. The characteristics of the hydrogel and especially the developed pore sizes are also determined by the degree of swelling, Q , or in other words the amount of solvent comprised by the polymer network:

$$Q = \frac{m_{\text{gel}}}{m_{\text{p}}}, \quad (2.3)$$

with the mass of the hydrogel, m_{gel} , and the polymer mass after complete drying of the hydrogel, m_{p} . The equilibrium degree of swelling evidently depends on the crosslinking ratio and the nature of the polymeric material but also on solvent quality. Instead of the swelling degree, one can also calculate the polymer (or solvent) volume fraction in the hydrogel:

$$\phi_{\text{p}} = \frac{m_{\text{p}}\rho_{\text{s}}}{m_{\text{p}}\rho_{\text{s}} + m_{\text{s}}\rho_{\text{p}}}, \quad (2.4)$$

where ρ denotes the densities of the polymer (subscript p) and the solvent (subscript s). Pore sizes can be calculated based on the Flory-Rehner theory for the swelling of crosslinked polymer networks [41]. These values should only be interpreted as a rough estimate though, as many assumptions are introduced in the calculations. With the known crosslinking ratio, X , and the molecular weight of the repeat unit in the polymer (AAm), $M_{\text{r,AAm}} = 71.1 \text{ g/mol}$, the theoretical average molecular weight of the polymer chain between two crosslinking

points, \bar{M}_c , can be calculated [42, 43]:

$$\bar{M}_c = \frac{M_{r,AAm}}{2X} . \quad (2.5)$$

The mean pore size or network correlation length, ξ , can be interpreted as the end-to-end distance of the polymer chains between two crosslinks [42–44]:

$$\xi = \phi_p^{-1/3} \sqrt{\frac{2C_n \bar{M}_c}{M_{r,AAm}}} l , \quad (2.6)$$

with the carbon–carbon bond length, $l = 0.154$ nm, and the dimensionless characteristic ratio, C_n ($C_n = 2.72$ for PAAm [45]). Table 2.1 shows the characteristics of different polyacrylamide hydrogels in their fully swollen equilibrium state which were used in the experiments based on the Flory-Rehner theory. The calculated pore sizes, ξ , should only be considered as a rough estimate. In a real hydrogel, pore sizes and shapes are neither uniform nor constant in time. The polymer chains are flexible and soft, leading to dynamic fluctuations in the actual pore sizes. For some experiments, the degree of swelling, Q , was altered by partial drying of the hydrogel samples (Chapter 3.3).

solvent	X	Q	ϕ_p	ξ [nm]
H ₂ O	0.0167	20.41	0.038	5.852
H ₂ O	0.0667	15.63	0.050	2.670
D ₂ O	0.0167	16.26	0.053	5.241
D ₂ O	0.0667	13.28	0.065	2.449

Table 2.1 Characteristics of the investigated polyacrylamide hydrogels. They were swollen in either H₂O or D₂O and the crosslinking ratio, X , was varied which resulted in different degrees of swelling, Q , polymer volume fractions, ϕ_p , and pore sizes, ξ .

In a typical experiment, hydrogel discs are constrained between two parallel glass plates and then contacted with fluorescent molecule solutions. As visualized in Figure 2.9, the diffusion of fluorescent molecules and solvent only occurs through the radial edge of the hydrogel discs. Constriction and slight squeezing of the hydrogels is necessary to prevent slipping of the sample which is vertically oriented as required for neutron radiography measurements. It is assumed that this constriction affects the hydrogel structure and possibly introduces an anisotropic pore size distribution. This made a reliable determination of the pore sizes

2.3 Porous Systems and Intruders

experienced by the diffusing molecules in the experiments difficult.

The structure of freeze-dried hydrogels is commonly visualized by scanning electron microscopy experiments. The required freeze-drying prior to the measurements renders the determination of the pore sizes of the hydrogel in its native hydrated state impossible. Dynamic light scattering (DLS) measurements of the polyacrylamide hydrogels were performed in order to estimate the pore size of hydrated samples. Due to the non-ergodicity of gels in general, the measurement procedure and the analysis of light scattering data is complex. From measurements performed, the pore sizes were determined to be in the order of magnitude expected from the Flory-Rehner calculations with rather big deviations between repeat measurements. As these hydrogel samples are not necessarily comparable to those used in the diffusion experiments, these values will not be further dwelled upon. For ease of experimentation, the hydrogels studied with DLS were polymerized directly in the cuvettes and hence were not swollen to equilibrium and then compressed as was the case for the diffusion experiments. Similarly, the interpretation of results from small angle neutron scattering (SANS) experiments was complicated. Those measurements were performed in the exact same sample cells as the diffusion experiments and hence only the sample orientation perpendicular to the diffusion direction (top view in Fig. 2.9) could be probed.

Due to the lack of a reliable technique to determine the hydrogel pore sizes experienced by the diffusants, we used three complementary experimental techniques to study the diffusion of differently sized macromolecules through one particular hydrogel and additionally performed Brownian dynamics simulations to draw conclusions about the pore size distribution (Chapter 3.2).

2.3.2 Mesoporous Silica

For the experiments with the imaging setup in reflection mode, another class of porous materials was used. Mesoporous silica powders with a hierarchic pore structure of well-defined sizes were first developed in 1992 [46]. They exhibit extremely large surface areas of approximately $1000 \text{ m}^2/\text{g}$ and offer many applications in various fields of research such as optical sensing [47, 48], drug delivery [49, 50], and catalysis [51]. The hexagonally ordered silica powder MCM-41 functionalized with the fluorescent dye Nile Red was used in the experiments described in Chapter 3.1. A pathway commonly used to synthesize

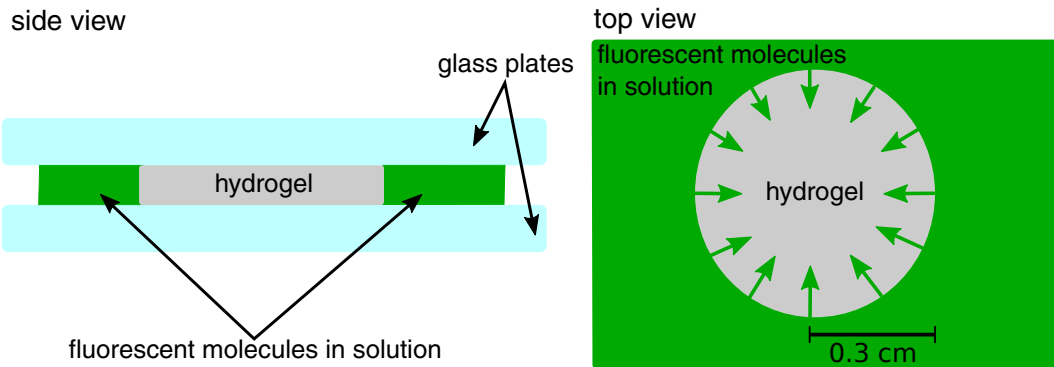


Figure 2.9 Side and top view of a hydrogel disc constrained between two glass plates. Solvent and fluorescent molecules diffuse into the hydrogel through the radial edge.

these materials is schematically shown in Figure 2.10. In a first step, surfactants such as cetyltrimethylammonium bromide form cylindrical micelles in aqueous solutions which subsequently self-assemble into a hexagonal array of micelles. This is then used as a template. A certain silica species is added to the solution and then condensates on the surfactant-rods. Removal of the organic template by thermal treatment (calcination) or solvent extraction yields the mesoporous silica material with a well-defined two-dimensional pore structure. The fluorescent dye Nile red was covalently attached to the mesoporous silica yielding a suitable optical sensor material as Nile red is a solvatochromic dye. Its emitted fluorescence depends strongly on solvent polarity. The MCM-41 materials were characterized by small angle X-ray scattering (SAXS), nitrogen sorption and transmission electron microscopy (TEM) [52]. A bimodal pore size distribution with pore diameters of 1.5 and 2.8 nm was found.

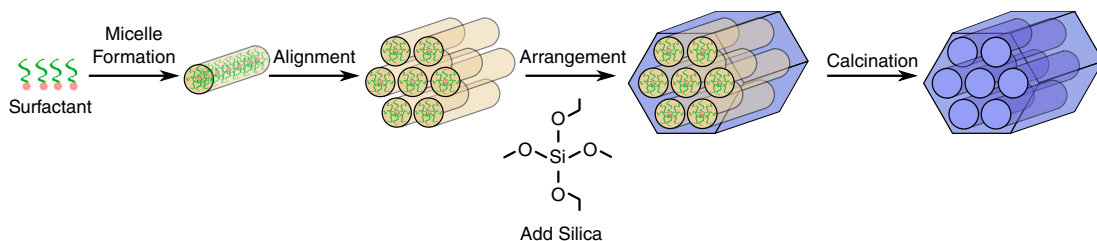


Figure 2.10 Synthesis pathway of MCM-41; adapted from [53].

2.4 Diffusion in Porous Media

2.3.3 Fluorescent Dyes and Macromolecules

The diffusion as a function of the size of the different fluorescent (macro)molecules through porous networks was also studied. An overview of the diffusants used for the experiments in this thesis is given in table 2.2 and their naming convention is introduced. Three different fluorescent dyes (Alexa fluor 488, tetramethylrhodamine and fluorescein) as well as dextran molecules labeled with these dyes were studied. The molecular weights, M_W , were obtained from manufacturer data sheets and range from 0.33 kDa for fluorescein to 2000 kDa for the largest dextran. Hydrodynamic radii of all of the (macro)molecules were calculated from measured diffusion coefficients (see Chapter 3.2) and range between about 0.5 and 40 nm, thus spanning a size regime much smaller to much bigger than the average hydrogel pore sizes (Table 2.1).

	M_W [kDa]	r_h [nm]	Alexa fluor 488	Tetramethylrhodamine	Fluorescein
dyes	0.33	0.56			FLU
	0.39	0.56		TMR	
	0.53	0.54	A488		
dextrans	3	1.7 ± 0.1	A488-D3	TMR-D3	FLU-D3
	10	3.1 ± 0.2	A488-D10	TMR-D10	FLU-D10
	40	6.0 ± 0.3		TMR-D40	FLU-D40
	70	7.9 ± 0.4		TMR-D70	FLU-D70
	500	20 ± 2			FLU-D500
	2000	40 ± 4		TMR-D2000	

Table 2.2 Overview of dyes and dextran molecules of different molecular weights, M_W , hydrodynamic radii, r_h , and their naming convention. The molecular weights were obtained from manufacturer data sheets and the radii were calculated from measured diffusion coefficients (see Chapter 3.2). The dextrans were labeled with one of three different dyes (Alexa fluor 488, tetramethylrhodamine and fluorescein).

2.4 Diffusion in Porous Media

Whenever a porous material is subject of a scientific study, the transport phenomena in and through the material is inevitably addressed. A literature review of porous media does not render many results if the transport properties of the particular material are not discussed. This is due to the fact that it is closely linked to the efficiency for a technical application and

in the case of biological material to its functionality. Technical and industrial applications for porous media and thus also for diffusion in porous media such as fuel cells [54, 55], food production [39, 40], filtration devices [56, 57], and chromatography [58, 59] are widespread. Recently, the biomechanics of natural and engineered porous tissues and in-tissue drug delivery has gained more and more attention [35, 36, 60–62]. In the field of geosciences, concepts and algorithms have been developed to model flow and transport through soils. However, biological and industrial porous media can often be significantly more complex, introducing additional mechanisms, which are not yet completely understood. Fast deformations and fluctuations of the network structure in most biological porous media can affect the diffusion for instance and a large range of pore sizes can be encountered.

Calibration of Optical Imaging Methods

Precise measurements to reveal the underlying transport properties of porous media are evidently required. Chapter 3.2 presents an extensive experimental and theoretical study of the diffusion of differently sized molecules through one specific polymer hydrogel network. The optical and fluorescence imaging methods introduced in Chapters 2.1.1 and 2.1.2 were

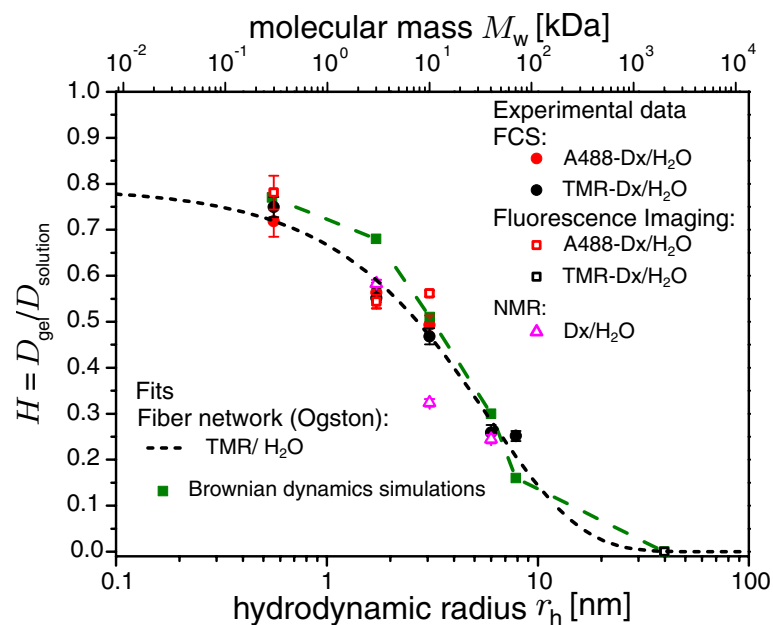


Figure 2.11 Hindrance factors, $H = D_{\text{gel}}/D_{\text{solution}}$ of differently sized dextran molecules obtained from three independent experimental techniques compared to a fit based on a fiber network model and Brownian dynamics simulations. Reproduced from [63] with permission from the PCCP Owner Societies.

2.4 Diffusion in Porous Media

compared with two independent experimental techniques, namely fluorescence correlation spectroscopy (FCS) and nuclear magnetic resonance (NMR) spectroscopy. All techniques were found to yield quantitatively consistent diffusion coefficients even though they probe different length scales of the system. The observed trends were successfully reproduced by coarse grained Brownian dynamics simulations as shown in Figure 2.11. The hindrance factor, H , which is defined as the ratio of the diffusion coefficient measured in the gel, D_{gel} , to the one measured in solution, D_{solution} , decays markedly with increasing size of the diffusing molecules as expected. The agreement of the results obtained with three independent experimental techniques and simulations serves as valuable proof of the accuracy of the individual techniques.

Solvent and Solute Influx into Hydrogels

In a following step, the simultaneous optical and fluorescence imaging experiments were combined with neutron radiography measurements in order to distinguish between solvent and solute motion (Chapter 3.3). The diffusion of fluorescent dyes and macromolecules suspended in either H_2O or D_2O into polyacrylamide hydrogel discs with varying degree of swelling and crosslinking ratio, which were either swollen in H_2O or D_2O , was studied. Time-series of neutron and fluorescence images were recorded and the two-dimensional image intensities, $I(x, y, t)$, were converted into solvent and solute volume fractions, $\phi(x, y, t)$, using appropriate calibrations [28, 64]. Spatial averaging taking into account the distance to the hydrogel disc border yielded solvent and solute volume fraction profiles, $\phi(r, t)$, where r denotes the radial position in the disc. These profiles, showing the time- and position-dependent volume fraction distributions inside the hydrogel discs, were quantitatively analyzed based on solutions to the diffusion equation (Eq. 1.4) considering different boundary conditions.

Figure 2.12 shows an exemplary set of D_2O volume fraction profiles, $\phi_{\text{D}}(r, t)$, which were normalized with the initial and final D_2O volume fractions inside the hydrogel, ϕ_i and ϕ_∞ , respectively. Here, the diffusion of a fluorescein- D_2O solution into a fully swollen H_2O -hydrogel was followed. The data was fitted based on two different solutions to the diffusion equation for cylindrical geometries (Eq. 1.4): firstly, radial diffusion into the cylinder from a stirred, infinite reservoir and secondly, diffusion from a stirred reservoir of limited volume. A stirred reservoir implies a uniform concentration in the entire solution around the cylinder

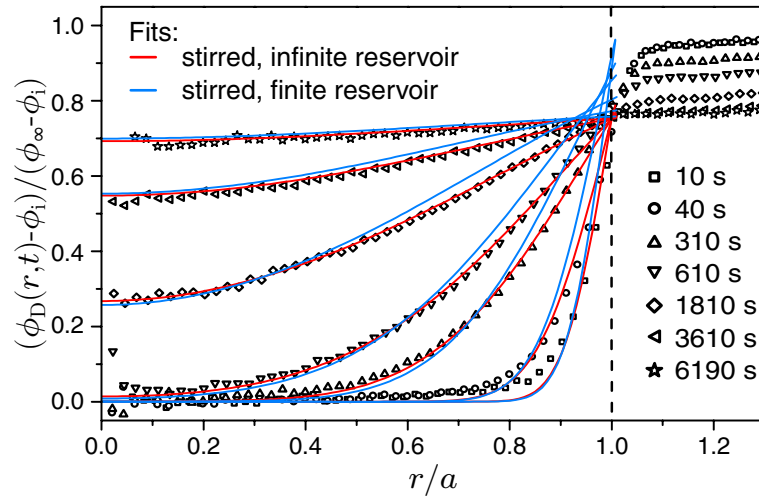


Figure 2.12 Normalized D₂O volume fraction profiles, $\phi_D(r,t)$, for different times (as indicated) after a H₂O-hydrogel with radius, a , and crosslinking ratio, $X = 0.0167$, was contacted with D₂O solution containing fluorescein dye as obtained by neutron radiography. Fits based on two models (red: diffusion from a stirred, infinite reservoir, blue: diffusion from a stirred, finite reservoir) are shown. Reprinted from [64] with the permission of AIP Publishing.

at all times and corresponds to an infinitely large diffusion coefficient in the reservoir. Additionally, the concentrations in the solution and at the reservoir-cylinder interface remain constant in the case of an infinite reservoir size while it decreases in the case of a finite reservoir. Even though the finite reservoir was not stirred in the experiments, a uniform concentration outside the hydrogel discs and a constant concentration at the hydrogel border were found in most measurements (Fig. 2.12). Thus, the first model was found to be suited to fit the experimental volume fraction profiles with one diffusion coefficient, D , while the decreasing concentration in the reservoir solution could be interpreted based on the second model. In Chapter 3.3 a detailed description of the models and an additional comparison to a third model, which describes diffusion in a cylinder from an unstirred, infinite reservoir is given.

With a series of diffusion experiments, it was shown that the mixing of H₂O and D₂O could be followed directly and independently of solute diffusion. This is beneficial compared to techniques where solvent diffusion is monitored implicitly by using tracers. Interestingly, already for small dye molecules, a pronounced difference between solute and solvent diffusivity was seen, which increased with increasing size of the diffusing species. Moreover, the solvent diffusion appears to be very slightly affected by the presence of solutes. This

2.4 Diffusion in Porous Media

can be seen in Figure 2.13, where the normalized H₂O volume fraction, ϕ_H , in the center of the hydrogel disc with radius, a , as a function of time, t , is plotted in the case of D₂O-hydrogels that were contacted with H₂O solutions for different sample compositions. The hydrogel discs were partially dried to approximately 75% of their initial mass prior to the measurements and the crosslinking ratio and fluorescent molecules (fluorescein, 10 kDa dextran, 70 kDa dextran) were varied as indicated.

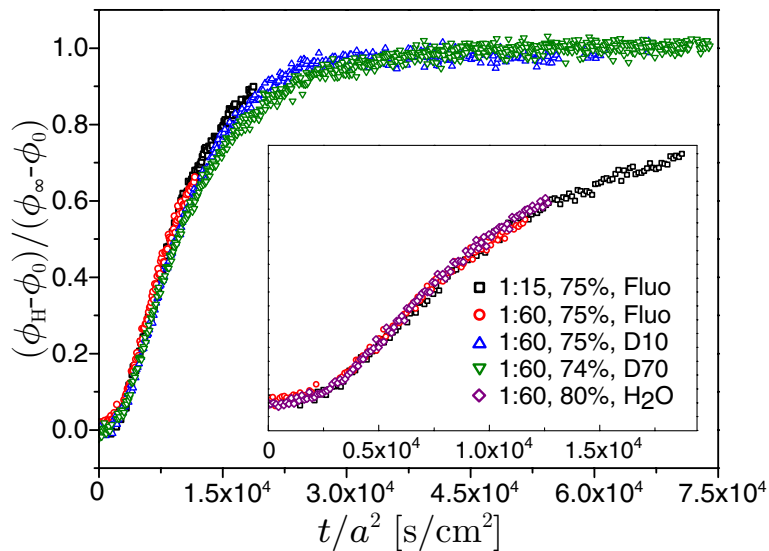


Figure 2.13 Normalized H₂O volume fraction, ϕ_H , in the center of the hydrogel with radius a as a function of time t after the D₂O-hydrogel has been contacted with H₂O solutions containing fluorescent molecules (fluorescein, 10 kDa dextran, 70 kDa dextran) as indicated. The inset shows ϕ_H at short times and includes a hydrogel contacted with pure H₂O. Small differences in the initial disc radii, a , are accounted for by normalizing the time, t , with the squared radius, a^2 . Reprinted from [64] with the permission of AIP Publishing.

Macromolecule Release from Hydrogels

In addition to the investigation of solvent and solute influx into a polymer hydrogel, the reverse process of macromolecule release from the hydrogels was studied (Chapter 3.4). Due to their porous nature, hydrogels are suitable host-materials to incorporate and subsequently release macromolecules such as pharmaceutical drugs into the surrounding [35, 38, 65–67]. Understanding the fundamental concepts and mechanisms influencing the macromolecule diffusion into and out of the hydrogel is essential in order to optimize time- and target-controlled delivery of solutes such as drugs. Thus, an experimental approach to allow a more comprehensive understanding of the mechanisms that influence the diffusion process

was developed. Diffusion of fluorescent (macro)molecules into and out of polyacrylamide hydrogel discs was monitored in-situ using combined fluorescence and optical bright-field transmission imaging. Fluorescence imaging yielded time- and space-resolved information about the (macro)molecule concentration throughout the entire macroscopic observation volume while bright-field transmission imaging served as a control to visualize changes in properties and appearance of the hydrogel as described in the previous chapter.

Figure 2.14 shows the change in normalized (macro)molecule concentration in the center of the hydrogel discs for three differently sized probe molecules (fluorescein, 10 kDa dextran, 70 kDa dextran) as a function of time. Small differences in the initial disc radii, a , are accounted for by normalizing the time, t , with the squared radius. For high (macro)molecule concentration, the behavior during release experiments (open symbols in Fig. 2.14 (b)) corresponds to the behavior observed in influx experiments (Fig. 2.14 (a)). The data could

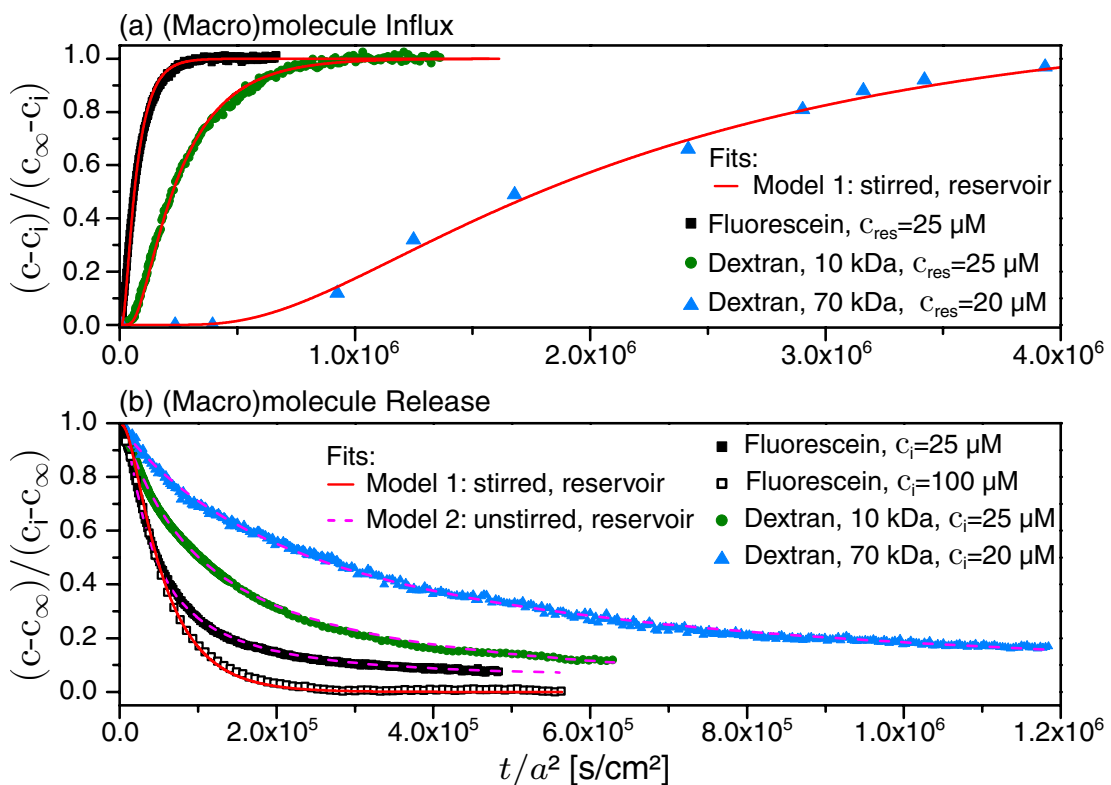


Figure 2.14 Fluorescent (macro)molecule influx into (a) and release from (b) hydrogel discs with radius a were followed. Normalized concentration of (macro)molecules, c , in the center of the discs as a function of normalized time, t/a^2 . Fits based on two models (red lines: diffusion from a stirred, infinite reservoir, magenta dashed lines: diffusion from an unstirred, infinite reservoir) are shown and the initial concentrations in the reservoir, c_{res} , and in the hydrogel, c_i are given.

Bibliography

well be fitted based on the model for radial diffusion into a cylinder from a stirred, infinite reservoir, as described in the previous section. By contrast, a qualitatively different diffusion was observed for release experiments with lower initial (macro)molecule concentrations. The concentration was found to approach the equilibrium value more gradually (Fig. 2.14 (b)), which was successfully fitted based on a second model, describing radial diffusion in a cylinder suspended in an unstirred, infinite reservoir. The apparent difference is caused by the difference in the absolute concentration in the two scenarios and suggests that adsorption might play a role. In the case of release, the diffusing substance is initially located in the hydrogel and thus partially adsorbed, while in influx experiments the fluorescent molecules initially fill the reservoir and only enter the hydrogel and get adsorbed in the course of the experiment.

Bibliography

- [1] Amsden, B. *Macromolecules* **1998**, *31*, 8382–8395.
- [2] Amsden, B. *Polym. Gels Networks* **1998**, *6*, 13–43.
- [3] Liu, D. E.; Kotsmar, C.; Nguyen, F.; Sells, T.; Taylor, N. O.; Prausnitz, J. M.; Radke, C. J. *Ind. Eng. Chem. Res.* **2013**, *52*, 18109–18120.
- [4] Lewus, R. K.; Carta, G. *J. Chromatogr. A* **1999**, *865*, 155–168.
- [5] Lopez-Sanchez, P.; Schuster, E.; Wang, D.; Gidley, M. J.; Strom, A. *Soft Matter* **2015**, *11*, 4002–4010.
- [6] Williams, J. C.; Mark, L. A.; Eichholtz, S. *Biophys. J.* **1998**, *75*, 493–502.
- [7] Tong, J.; Anderson, J. *Biophys. J.* **1996**, *70*, 1505–1513.
- [8] Lehmann, S.; Seiffert, S.; Richtering, W. *J. Am. Chem. Soc.* **2012**, *134*, 15963–15969.
- [9] Haggerty, L.; Sugarman, J.; Prudhomme, R. *Polymer* **1988**, *29*, 1058–1063.
- [10] Ogston, A. G.; Preston, B. N.; Wells, J. D. *R. Soc. Lond. Proc. Ser. A Math. Phys. Eng. Sci.* **1973**, *333*, 297–316.
- [11] Zhou, H.; Chen, S. B. *Phys. Rev. E* **2009**, *79*, 021801.
- [12] McConville, P.; Whittaker, M. K.; Pope, J. M. *Macromolecules* **2002**, *35*, 6961–6969.
- [13] Fornasiero, F.; Tang, D.; Boushehri, A.; Prausnitz, J.; Radke, C. *J. Membr. Sci.* **2008**, *320*, 423–430.
- [14] Nobel Media AB. 2015; <https://www.nobelprize.org/educational/physics/microscopes/powerline/index.html>, Accessed: 2015-12-22.
- [15] Lakowicz, J. R. *Principles of Fluorescence Spectroscopy*; Springer, USA: New York, 2006.
- [16] Guilbault, G. G. *Practical fluorescence*; CRC Press, 1990; Vol. 3.
- [17] Kasha, M. *Discussions of the Faraday society* **1950**, *9*, 14–19.
- [18] Stokes, G. G. *Philosophical Transactions of the Royal Society of London* **1852**, 463–562.

- [19] Chadwick, J. *Nature* **1932**, *129*, 312.
- [20] Chadwick, J. The existence of a neutron. Proceedings of the Royal Society of London A: Mathematical, Physical and Engineering Sciences. 1932; pp 692–708.
- [21] Neutron Imaging at the spallation source SINQ. 2011; <https://www.psi.ch/sinq/neutra/neutron-imaging-brochure>, Accessed: 2016-01-20.
- [22] Anderson, I. S.; McGreevy, R. L.; Bilheux, H. Z. *Neutron imaging and applications*; Springer, 2009.
- [23] Strobl, M.; Manke, I.; Kardjilov, N.; Hilger, A.; Dawson, M.; Banhart, J. *Journal of Physics D: Applied Physics* **2009**, *42*, 243001.
- [24] Sears, V. F. *Neutron News* **1992**, *3*, 29.
- [25] <http://www.ati.ac.at/~neutropt/scattering/ScatteringLengthsAdvTable.pdf>, Accessed: 2016-01-20.
- [26] Kaestner, A.; Hartmann, S.; Kühne, G.; Frei, G.; Grünzweig, C.; Josic, L.; Schmid, F.; Lehmann, E. *Nucl. Instr. Meth. Phys. Res. A* **2011**, *659*, 387–393.
- [27] Lehmann, E.; Kaestner, A.; Josic, L.; Hartmann, S.; Mannes, D. *Nucl. Instr. Meth. Phys. Res. A* **2011**, *651*, 161–165.
- [28] Wagner, D.; Börgardts, M.; Grünzweig, C.; Lehmann, E.; Müller, T. J. J.; Egelhaaf, S. U.; Hermes, H. E. *Rev. Sci. Instrum.* **2015**, *86*, 093706.
- [29] Ebara, M.; Kotsuchibashi, Y.; Uto, K.; Aoyagi, T.; Kim, Y.-J.; Narain, R.; Idota, N.; Hoffman, J. M. *Smart Biomaterials*; Springer, 2014; pp 9–65.
- [30] Peppas, N. A.; Sahlin, J. J. *Biomaterials* **1996**, *17*, 1553–1561.
- [31] Tokarev, I.; Minko, S. *Soft Matter* **2009**, *5*, 511–524.
- [32] Kuckling, D. *Colloid Polym. Sci.* **2009**, *287*, 881–891.
- [33] Guenther, M.; Gerlach, G. *Hydrogel Sensors and Actuators*; Springer, 2010; pp 165–195.
- [34] Richter, A.; Paschew, G.; Klatt, S.; Lienig, J.; Arndt, K.-F.; Adler, H.-J. P. *Sensors* **2008**, *8*, 561–581.
- [35] Hoare, T. R.; Kohane, D. S. *Polymer* **2008**, *49*, 1993–2007.
- [36] Vashist, A.; Vashist, A.; Gupta, Y. K.; Ahmad, S. *J. Mater. Chem. B* **2014**, *2*, 147–166.
- [37] Peppas, N.; Bures, P.; Leobandung, W.; Ichikawa, H. *Eur. J. Pharm. Biopharm.* **2000**, *50*, 27–46.
- [38] Peppas, N. A. *Curr. Opin. Colloid Interface Sci.* **1997**, *2*, 531–537.
- [39] Kemp, M.; Fryer, P. *Innov. Food Sci. Emerg. Technol.* **2007**, *8*, 143–153.
- [40] Samprovalaki, K.; Robbins, P.; Fryer, P. *J. Food Eng.* **2012**, *111*, 537–545.
- [41] Flory, P. J.; Rehner Jr, J. *The Journal of Chemical Physics* **1943**, *11*, 521–526.
- [42] Peppas, N.; Barr-Howell, B. *Hydrogels in medicine and pharmacy* **1986**, *1*, 27–56.
- [43] Gudeman, L. F.; Peppas, N. A. *Journal of applied polymer science* **1995**, *55*, 919–928.
- [44] Carr, D. A.; Peppas, N. A. *Macromolecular bioscience* **2009**, *9*, 497–505.
- [45] Brandrup, J.; Immergut, E. H.; Grulke, E. A.; Abe, A.; Bloch, D. R. *Polymer handbook*; Wiley New York, 1999; Vol. 89.
- [46] Kresge, C. T.; Leonowicz, M. E.; Roth, W. J.; Vartuli, J. C.; Beck, J. S. *nature* **1992**, *359*, 710–712.

Bibliography

- [47] Descalzo, A. B.; Dolores Marcos, M.; Monte, C.; Martínez-Mañez, R.; Rurack, K. *J. Mater. Chem.* **2007**, *17*, 4716.
- [48] Wirnsberger, G.; Scott, B. J.; Stucky, G. D. *Chemical Communications* **2001**, 119–120.
- [49] Mamaeva, V.; Sahlgren, C.; Lindén, M. *Advanced drug delivery reviews* **2013**, *65*, 689–702.
- [50] Rosenholm, J. M.; Sahlgren, C.; Lindén, M. *Nanoscale* **2010**, *2*, 1870–1883.
- [51] Taguchi, A.; Schüth, F. *Microporous and mesoporous materials* **2005**, *77*, 1–45.
- [52] Börgardts, M.; Verlinden, K.; Neidhardt, M.; Wöhrle, T.; Herbst, A.; Laschat, S.; Janiak, C.; Müller, T. J. *RSC Advances* **2016**, *6*, 6209–6222.
- [53] Reichinger, M. Poröse Silicate mit hierarchischer Porenstruktur: Synthese von mikro-/mesoporösen MCM-41 und MCM-48 Materialien aus zeolithischen Baueinheiten des MFI-Gerüststrukturtyps. Ph.D. thesis, 2007.
- [54] Litster, S.; Sinton, D.; Djilali, N. *Journal of Power Sources* **2006**, *154*, 95–105.
- [55] Sinha, P. K.; Wang, C.-Y. *Electrochimica Acta* **2007**, *52*, 7936–7945.
- [56] Barhate, R.; Ramakrishna, S. *Journal of membrane science* **2007**, *296*, 1–8.
- [57] Herzig, J.; Leclerc, D.; Goff, P. L. *Industrial & Engineering Chemistry* **1970**, *62*, 8–35.
- [58] Balke, S.; Hamielec, A.; LeClair, B.; Pearce, S. *Industrial & Engineering Chemistry Product Research and Development* **1969**, *8*, 54–57.
- [59] Dullien, F. A. *Porous media: fluid transport and pore structure*; Academic press, 2012.
- [60] Jen, A. C.; Wake, M. C.; Mikos, A. G. *Biotechnol. Bioeng.* **1996**, *50*, 357–364.
- [61] Drury, J. L.; Mooney, D. J. *Biomaterials* **2003**, *24*, 4337–4351.
- [62] Stuart, M. A. C.; Huck, W. T. S.; Genzer, J.; Müller, M.; Ober, C.; Stamm, M.; Sukhorukov, G. B.; Szleifer, I.; Tsukruk, V. V.; Urban, M. *Nat. Mater.* **2010**, *9*, 101–113.
- [63] Sandrin, D.; Wagner, D.; Sitta, C. E.; Thoma, R.; Felekyan, S.; Hermes, H. E.; Janiak, C.; de Sousa Amadeu, N.; Kühnemuth, R.; Löwen, H.; Egelhaaf, S. U.; Seidel, C. A. M. *Phys. Chem. Chem. Phys.* **2016**,
- [64] Wagner, D.; Burbach, J.; Grünzweig, C.; Hartmann, S.; Lehmann, E.; Egelhaaf, S. U.; Hermes, H. E. *J. Chem. Phys.*, Accepted for publication.
- [65] Hoffman, A. S. *Adv. Drug Deliv. Rev.* **2012**, *64*, 18–23.
- [66] Hamidi, M.; Azadi, A.; Rafiei, P. *Adv. Drug Deliv. Rev.* **2008**, *60*, 1638–1649.
- [67] Bindu Sri, M.; Ashok, V.; Arkendu, C. *Int. J. Pharm. Chem. Sci.* **2012**, *1*, 642–661.

3.1 Neutron, Fluorescence and Optical Imaging: An in-situ Combination of Complementary Techniques

Journal: Review of Scientific Instruments

Reference: *Rev. Sci. Instrum.* **86**, 093706 (2015), DOI: 10.1063/1.4931427

Impact factor: 1.598

Authors: **Dana Wagner**, Markus Börgardts, Christian Grünzweig, Eberhard Lehmann, Thomas J. J. Müller, Stefan U. Egelhaaf, and Helen E. Hermes

1st author

DW and HEH designed the experimental setup and sample cells. DW built and optimized the setup. Sample preparation was done by DW and MB, measurements were performed by DW, HEH and MB. DW and HEH analyzed the data. CG and EL assisted during the beam time at PSI. DW, HEH, TJJM and SUE conceived and discussed the project and HEH and SUE supervised the project. DW, HEH and SUE contributed to the writing of the manuscript.

80% contribution of DW

The article is reprinted with the permission of AIP Publishing.

This page has been left intentionally blank.

Neutron, Fluorescence and Optical Imaging: An in-situ Combination of Complementary Techniques

D. Wagner,¹ M. Börgardts,² C. Grünzweig,³ E. Lehmann,³ T. J. J. Müller,² S. U. Egelhaaf,¹ and H. E. Hermes¹

¹*Condensed Matter Physics Laboratory, Heinrich Heine University, 40225 Düsseldorf, Germany*

²*Institute for Organic and Macromolecular Chemistry, Heinrich Heine University, 40225 Düsseldorf, Germany*

³*Neutron Imaging and Activation Group, Paul Scherrer Institut, 5232 Villigen, Switzerland*

(Dated: 18 July 2016)

An apparatus which enables the simultaneous combination of three complementary imaging techniques, optical imaging, fluorescence imaging and neutron radiography, is presented. While each individual technique can provide information on certain aspects of the sample and their time evolution, a combination of the three techniques in one setup provides a more complete and consistent data set. The setup can be used in transmission and reflection mode and thus with optically transparent as well as opaque samples. Its capabilities are illustrated with two examples. A polymer hydrogel represents a transparent sample and the diffusion of fluorescent particles into and through this polymer matrix is followed. In reflection mode, the absorption of solvent by a Nile red-functionalized mesoporous silica powder and the corresponding change in fluorescent signal is studied.

I. INTRODUCTION

Interest in soft matter and material sciences moves towards increasingly complex samples, e.g. host-guest systems or composite materials.¹⁻⁴ In addition, these are often studied under rather complicated conditions, e.g. external forces, such as shear,⁵⁻⁷ or whilst undergoing structural or phase transitions.⁸⁻¹¹ Furthermore, biologically or industrially relevant samples are typically multi-component systems.¹² Due to their complex nature, completely reproducible samples and kinetic responses are not usually observed such that sequential measurements have only limited value and a better understanding of the samples' behavior can often be obtained by applying different complementary measurement techniques, at the same time.^{13,14} In this article, we describe a setup that has been designed to perform three complementary imaging measurements, namely optical imaging, fluorescence imaging and neutron radiography, simultaneously, i.e. at the same time and on the same sample volume.

A large variety of imaging methods are used in soft matter science, biology and medical diagnostics.^{15,16} Their basic principle is similar: radiation interacts with the sample and the resulting signal is recorded with a two-dimensional detector leading to an image that contains spatially resolved information about certain characteristics of the object. Different features of the sample can be "imaged", depending on the chosen technique and contrast.

In optical imaging (OI), the transmission or reflection of visible light by the sample is recorded as a function of space and time.¹⁷ The recorded light intensity relative to the incident intensity reflects the local optical density of the sample along the light path. By contrast, fluorescence imaging (FI) provides information on the local concentration of fluorophores.¹⁸ The fluorophores are excited by

the incident radiation and emit light with a longer wavelength. The excitation and emission spectra depend on the specific fluorophore and determine the choice of the illumination wavelength(s) and the spectral characteristics of the filters used in the imaging part of the device. The fluorophore is chosen to report on the feature of interest, such as the motion of the fluorophore itself, a local property or the local concentration of some chemical.¹⁹ The fluorophore is thus a specific marker which usually has to be added to the system and hence potentially changes the system. Neutron radiography (NR) provides a transmission image, which depends on the neutron attenuation of the sample and thus probes a different aspect of the sample compared to OI and FI. Neutrons interact with the nuclei and hence the interaction depends on the specific isotope. Therefore, isotope exchange can be exploited to highlight specific parts of the sample, similar to the addition of fluorophores in FI except that isotope exchange tends to affect the sample less. In studies involving biological or soft matter samples, typically the large difference in the attenuation of hydrogen and deuterium is exploited and deuteration is used to highlight or mask specific parts of the sample.²⁰ Due to the much smaller wavelength of neutrons compared to light, the scattering of neutrons by large-scale structures, such as those of interest in biological or soft matter samples, occurs at much smaller scattering angles. Thus, for spatial resolutions and sample thicknesses similar to the ones in these experiments, neutrons scattered by large-scale structures are detected by the same or a neighboring pixel as the transmitted beam. The observed effective transmission is hardly reduced by scattering effects which can hence often be neglected in the data analysis.²¹⁻²³

Neutron radiography and fluorescence imaging have been combined before.^{19,24} In these previous studies, however, the samples had to be moved out of the neu-

3.1 Neutron, Fluorescence and Optical Imaging: An in-situ Combination of Complementary Techniques

2

tron beam to take fluorescence images. Thus, a truly simultaneous observation as well as an imaging of fast kinetic processes was not possible. A further advantage of the setup described here is the significantly better spatial resolution, which is crucial for typical biological or soft matter samples.

II. EXPERIMENTAL SETUP

The setup that combines optical, fluorescence and neutron imaging can be operated in two modes: optical transmission and optical reflection imaging. This allows the investigation of optically transparent and opaque samples. The optical imaging setup is built on an optical breadboard (45 cm × 60 cm) which is placed in the neutron beamline and aligned to the neutron beam. In both setups, neutron radiography is performed in transmission mode.

A. Neutron, Fluorescence and Optical Imaging in Transmission Mode

The imaging setup in transmission mode is schematically shown in figure 1(a) and photographs are presented in figure 2. The setup is designed so that, apart from the sample cell, only two optical mirrors (M1, M2) are located in the neutron beam. The two mirrors are made of quartz glass with a chrome-silica coating and they are sufficiently transparent to neutrons so that the neutron beam is not significantly attenuated or otherwise affected. Nevertheless, the mirrors are accounted for in the data analysis by applying a bright beam correction (Sec. III A). The other components and especially the CCD cameras are placed far enough from the neutron beam and are shielded to minimize their activation. The sample is placed in the neutron beam, as close as possible in front of the scintillator (see below). The transmitted neutrons reach the scintillation screen (SC) which then emits photons. A 10 μm thick gadolinium based scintillator (Gd₂SO₂S:Tb) has been found to be suitable for high-resolution neutron imaging. The emitted photons are reflected from mirror M3 and recorded with a CCD camera (NR cam).²⁵ Thus the gray value in each pixel of the image provides information on the transmitted neutron intensity in the corresponding sample volume.

The divergence of the neutron beam limits the resolution of the image to²⁶

$$u_g = \frac{l}{L/D_{ap}}, \quad (1)$$

where l is the sample-scintillator distance, D_{ap} the diameter of the source aperture and L the distance of this aperture to the detector, i.e. the scintillator. While L and D_{ap} are set by the neutron beamline, the sample-scintillator distance l should be minimized in order to reduce geometrical blurring. In this setup, l is limited

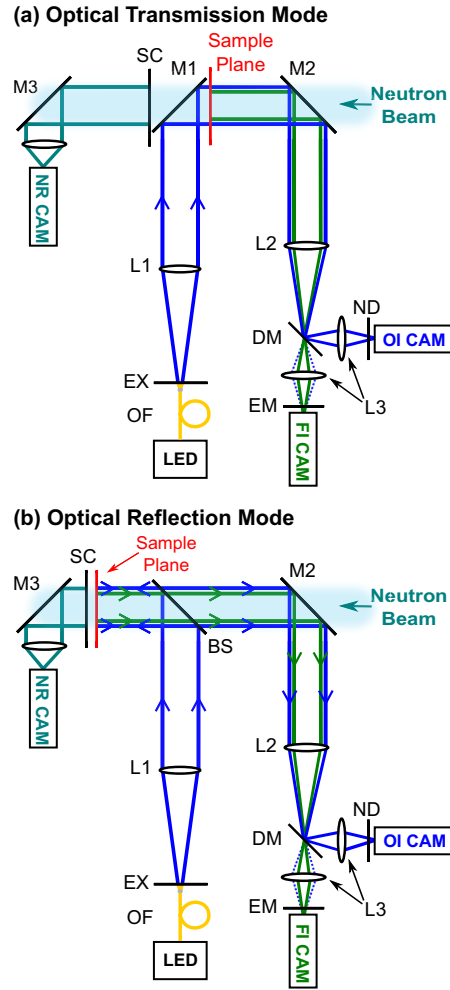


Fig. 1. Schematic representation of the experimental setup in (a) optical transmission and (b) optical reflection mode. See text for details.

by the sizes of the sample cell (Sec. II C) and the mirror M1 which is why this mirror is kept as small as possible while still covering the whole observation volume.

An LED lamp (CoolLED pE-2) is chosen as light source for the optical and fluorescence part of the apparatus. Its intensity was found to be sufficient for our samples and stable for long times. Importantly, its wavelength can be adapted to the excitation spectrum of the fluorescent dye molecules in the sample. This LED lamp can also provide several wavelengths which can be used to excite different fluorophores simultaneously. The light from the LED lamp is guided by an optical fiber (OF) to an excitation filter (EX). This is a short pass or bandpass filter that transmits a narrow range of wavelengths. It ensures that the wavelength of the incident light is well below the emission wavelength of the fluorophore. The light is then collimated using an achromatic doublet lens

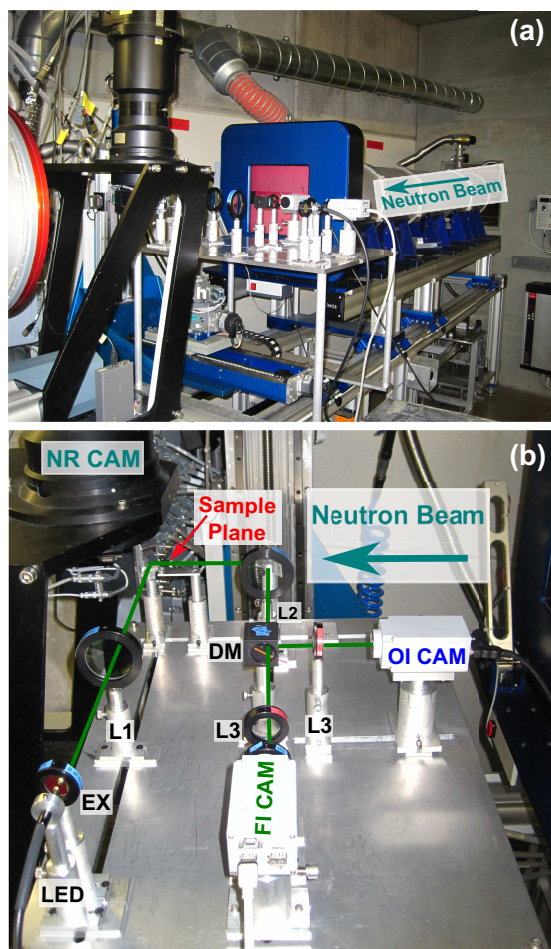


Fig. 2. Optical and fluorescence imaging setup in transmission mode in the neutron radiography beamline ICON at the Paul Scherrer Institute. The labels are as in figure 1 and defined in the main text. Note that there is no sample cell in the sample plane and shielding to protect the equipment, especially the cameras, from radiation damage, has been removed.

with focal length $f_1 = 20$ cm (L1). The lens is placed at its focal length from the exit of the fiber and hence the sample is illuminated by a parallel beam of light. Compared to a focused illumination beam, this exposes the dye molecules to a significantly lower intensity and thus reduces photobleaching. To increase the illumination intensity, a condenser lens could be added behind the optical fiber in order to collect light from a larger solid angle. This was not necessary for our samples. Using a dichroic mirror (DM), the light transmitted by the sample is split into two parts. First, the short-wavelength part, which is the transmitted excitation light that forms the optical transmission image. Second, the long-wavelength part, namely the light emitted by the fluorophores which forms the fluorescence image. These two parts are separately recorded using two cameras (OI

cam, FI cam) for which we use one black and white and one color CCD camera (AVT Stingray), respectively. To reduce the transmitted intensity if necessary, a neutral density filter (ND) can be introduced in front of the OI cam. To ensure that only light emitted by the fluorophores is recorded, an emission filter (EM) is added directly in front of the FI cam. The two images are formed using lenses (L2 and a pair L3). The magnification is determined by the relative focal lengths and positions of the objective lens, an achromatic doublet with focal length $f_2 = 20$ cm (L2), and the focusing lenses, achromatic doublets with $f_3 = 7.5$ cm (L3). In the experiments described here, we typically observe an area of about $2\text{ cm} \times 2\text{ cm}$. This exceeds the sensor size of the cameras ($0.85\text{ cm} \times 0.71\text{ cm}$) and thus a magnification smaller one is necessary; this is realized by choosing focusing lenses (L3) with a focal length smaller than that of the objective lens (L2); $f_3 < f_2$.

The use of a color camera as the FI cam allows changes in the emission spectrum during an experiment to be investigated. Depending on the emitted wavelength, the analysis can be restricted to only one channel of the color camera to enhance the signal-to-noise ratio. The OI camera together with an additional emission filter could also be used to monitor a second fluorophore with a different emission spectrum.

B. Fluorescence and Optical Imaging in Reflection Mode, Neutron Imaging in Transmission Mode

The investigation of samples that are opaque to light but transparent to neutrons is possible after small modifications to the setup. As shown in figure 1(b), epi-illumination is realized by using a beam splitter (BS) instead of the mirror M1. A beam splitter that transmits 70% and reflects 30% of the incident light was found to work well. The beam splitter directs the incident light onto the sample. The reflected as well as the emitted light travel back in the direction of the incident beam and through the beam splitter. As in transmission mode, both parts are separated by the dichroic mirror (DM) and imaged by lenses (L2, L3) onto two separate cameras (OI cam, FI cam). Since mirror M1 is no longer needed, the sample can be moved closer to the scintillator, thus decreasing the geometrical blurring u_g .

C. Sample Cells

In order to be able to analyze the data on a quantitative level, the sample cell has to meet some requirements. Its transmission has to be high for neutrons, and for light at least one transparent window is required. Suitable materials for neutron radiography are, e.g., aluminum or quartz glass. The latter is also transparent to visible light and thus the material of choice for combined imaging experiments. To determine the sample composi-

3.1 Neutron, Fluorescence and Optical Imaging: An in-situ Combination of Complementary Techniques

4

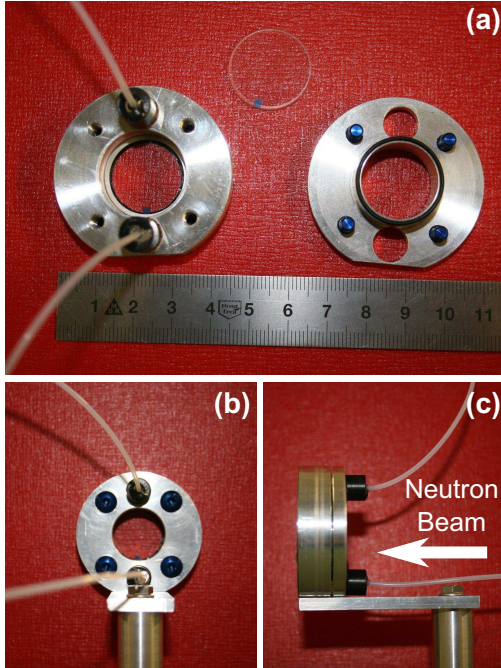


Fig. 3. Demountable watertight sample cell with quartz glass windows and a cell body made of aluminum: demounted cell (a), front (b) and side view (c) of the cell.

tion from its transmission, a uniform and precisely known sample thickness is required. Furthermore, as already mentioned, it is also desirable to minimize the sample-scintillator distance. Thus, the side of the sample cell pointing towards the scintillator should be kept as thin as possible. Due to the horizontal neutron beam, the cell has to be constructed such that a vertical sample orientation is possible. Depending on the sample and experiment to be performed, it can be desirable to construct cells which are demountable and/or watertight. Temperature or pressure control is another feature that might be considered.

For the transmission experiments described below (Sec. IV A), demountable and watertight sample cells were designed (Fig. 3). They consist of a two-piece aluminum alloy body. In contrast to a previous cell consisting only of aluminum,²⁷ the present cell has quartz glass windows. One aluminum part has a spherical window (Hellma, 22 mm diameter, 1.25 mm thickness) glued to it. The sample is placed on this window and then a second quartz glass window is put on top of the sample, whose thickness is determined by a fixed aluminum spacer ring of 0.5 mm thickness and, if required, additional aluminum spacer rings. The cell is sealed using an O-ring and the second aluminum part, which is screwed to the cell body with anodized aluminum screws. The inside of the aluminum body is covered with an inert anti-reflection foil (not shown in Fig. 3) to prevent re-

flections from the inner walls of the sample cell which can be caused by a slight misalignment of the sample cell with respect to the light path and can lead to, e.g., a bright spot in the center of the cell due to its cylindrical geometry. The sample cell has two holes that are connected to PTFE tubes. Through the tubes, the mounted cell can be degassed and filled with liquids. This allows the sample to be monitored in situ before and during contact with a liquid.

Although this cell can also be used in reflection mode, it is not suitable for the second set of experiments presented (Sec. IV B). Thus, a different cell was designed (Fig. 4). It consists of a single aluminum body with one solvent chamber, two rectangular sample chambers and a front window made of a glass slide with a thickness of 1.05 mm. The sample chambers have a height of about 30 mm and a square cross-section of 5.1 mm \times 5.1 mm, i.e. a path length of 5.1 mm while the solvent chamber is taller. All chambers are connected at the top such that saturated solvent vapor is in contact with the samples. The solvent chamber can be filled through PTFE tubes after the cell has been mounted in the neutron beam.

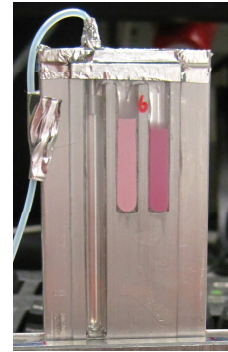


Fig. 4. Sample cell with two sample chambers filled with dye-functionalized mesoporous silica (middle and right) and one solvent chamber (left). The chambers are connected at the top by a groove. The cell is closed with an aluminum lid that is sealed with aluminum adhesive tape which, in the photograph, covers the groove

III. DATA TREATMENT

The raw data obtained from the experiments are stored as series of grayscale or (one channel of) color images depending on the camera used. The time series of two-dimensional images are recorded as intensities of every pixel, $I_{\text{raw}}(x, y, t)$, and are subsequently analyzed.

A. Neutron Radiography

The measured time series of images, i.e. two-dimensional intensities $I_{\text{raw}}(x, y, t)$, are reduced and an-

alyzed as described elsewhere²⁸ and briefly summarized here. (For clarity, in the following the dependence on the position of the pixel, (x, y) , and the time since the experiment has been started, t , is not explicitly given.)

To correct for effects caused by spatial variations in the beam intensity or in the detector efficiency as well as background and electronic noise, a pixelwise correction is applied to I_{raw} to yield the transmission, T :

$$T = \frac{I_{\text{raw}} - I_{\text{D}}}{I_{\text{B}} - I_{\text{D}}}, \quad (2)$$

where I_{D} is the intensity measured with all shutters closed (“dark image”). Furthermore, I_{B} denotes the intensity of a “bright image”, taken without a sample but with the optical setup, in particular mirror M2 and mirror M1 or the beam splitter (BS), in the neutron beam. Even though the NR camera is not directly irradiated by the neutron beam, its CCD chip is exposed to some radiation that results in sporadic high local intensities in the image (“gamma spots”). For I_{D} and I_{B} , a median filter on a stack of ten images is used to avoid effects of gamma spots.²⁹ This approach is not useful for radiographs that capture dynamic processes and is thus not applied to our sample images I_{raw} . For these images, the affected pixels are not included in the data analysis. Figure 5 shows a neutron radiograph of a polymer hydrogel inside the sample cell before and after application of the corrections described by eq. 2, which illustrates that the image becomes more homogeneous by the correction.

The neutron beam might not only be spatially inhomogeneous, but often also fluctuates with time t . Therefore, for time series, the transmission is normalized by the actual incident neutron intensity or a substitute of this quantity that shows the same time dependence. The mean intensity in a reference area where no changes are expected throughout the measurement (for instance a part of the cell body) can be used. Similar to eq. 2, the transmission, averaged over this reference area, relative to the incident beam is

$$\langle T_{\text{ref}} \rangle = \frac{\langle I_{\text{raw,ref}} \rangle - \langle I_{\text{D,ref}} \rangle}{\langle I_{\text{B,ref}} \rangle - \langle I_{\text{D,ref}} \rangle}, \quad (3)$$

where the intensities of the raw, dark and bright images are averaged over the same pixels, representing the reference area. This allows us to calculate the transmission relative to the reference area, and hence correct for time-variations in the incident intensity:

$$T_{\text{rel}} = \frac{T}{\langle T_{\text{ref}} \rangle}. \quad (4)$$

We can now calculate the transmission of the sample, T_{S} , i.e. the transmission of the sample in the cell, $T_{\text{rel,SC}}$, without the contribution of the transmission of the empty cell, $T_{\text{rel,C}}$:

$$T_{\text{S}} = \frac{T_{\text{rel,SC}}}{T_{\text{rel,C}}}. \quad (5)$$

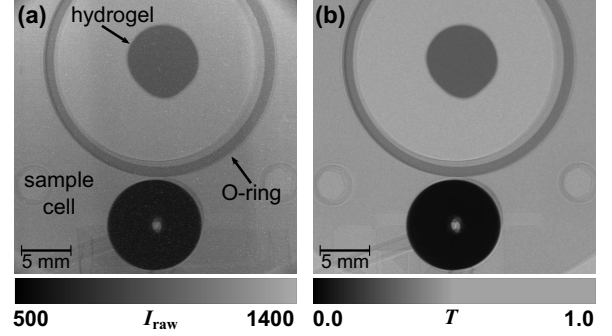


Fig. 5. Neutron radiograph of a polymer hydrogel disc and parts of the sample cell (a) before and (b) after a correction for beam and detector inhomogeneities, background noise and gamma spots, i.e. (a) represents the recorded intensity I_{raw} and (b) the transmission T (eq. 2), respectively.

Note that the values of $\langle T_{\text{ref}} \rangle$ for sample and empty cell are not necessarily the same as they are obtained at different times and thus T_{S} is not necessarily $T_{\text{SC}}/T_{\text{C}}$.

According to the Lambert-Beer law, the transmission of radiation traveling through the sample is linked to the material-specific attenuation coefficient S and the path length d :

$$T_{\text{S}} = e^{-Sd}. \quad (6)$$

For a one-component material i , S_i is related to the number $n_{i,j}$ of each kind of nucleus j in the material (or constituting molecule) i and the total neutron cross section of that nucleus, σ_j ,^{30,31} according to:

$$S_i = \frac{\rho_i}{M_i} N_{\text{A}} \sum_j n_{i,j} \sigma_j, \quad (7)$$

where ρ_i is the density and M_i the molar mass of the molecule and N_{A} Avogadro’s number. The attenuation coefficients S_i can hence be calculated or determined experimentally. For a sample consisting of different components with volume fractions ϕ_i , the total attenuation coefficient is:

$$S = \sum_i \phi_i S_i. \quad (8)$$

For two-component samples, using eqs. 6 and 8, the local volume fractions $\phi_i(x, y, t)$ of the two components can be extracted from the images, provided that the sample thickness d and the attenuation coefficients S_i are known.

B. Optical and Fluorescence Imaging

It was found that the optical illumination and detection are homogeneous and stable in time, the intensity is so high that the background is negligible and the used

3.1 Neutron, Fluorescence and Optical Imaging: An in-situ Combination of Complementary Techniques

6

sample cells are sufficiently transparent to light that corrections as in eqs. 2, 4 and 5 are not necessary for the optical and fluorescence images, i.e. $T_s = I_{\text{raw}}/I_B \propto I_{\text{raw}}$. However, as in any fluorescence experiment, the intensity might be affected by photobleaching. If the fluorescence intensity decreases in a reference area where no change in composition and hence intensity is expected, a photobleaching correction should be applied.^{32,33} If photobleaching is taken into account, we found, for the fluorescent dyes and their concentrations used in the present experiments, a linear relation between corrected intensity and dye concentration, i.e. a linear expansion of eq. 6, can be used. Thus the volume fraction of the fluorescent dye is directly related to the intensity I_{raw} .

IV. EXAMPLES

The capabilities of the setup are illustrated by two examples. The first experiment used the transmission mode to simultaneously investigate the diffusion of dye molecules into a water-swollen polymer hydrogel, the diffusion of solvent molecules into and out of the hydrogel and the swelling of the hydrogel. In the second example, dye-functionalized mesoporous silica was contacted with solvent vapor and, using the reflection mode, the change in fluorescence was compared with the local solvent concentration.

The experiments were performed at the cold neutron imaging facility ICON at the Paul Scherrer Institute (Villigen, Switzerland).^{34,35} The chosen distance of the source aperture, L , and diameter of the aperture, D_{ap} , imply $L/D_{\text{ap}} = 343$. For the samples investigated, this represents the optimum compromise between neutron beam intensity and spatial resolution, which, for the specific sample position, i.e. l , was better than 100 μm in all measurements. Images were collected continuously with an individual measurement time of 20 s to 30 s. Better spatial resolution or much shorter measurement times are possible if appropriate.

Optical transmission and fluorescence images were collected using a camera resolution of 10 μm , a field of view of about 25 mm \times 21 mm and a spatial resolution in the sample plane of about 20 μm . The resolution was chosen to roughly match that of the corresponding neutron radiography measurements. Again, a much better spatial resolution can be obtained if required.

A. Transmission Mode: Dye and Solvent Diffusion into and out of a Polymer Hydrogel

The aim of this experiment was to investigate the diffusion of fluorescent dye into a polymer hydrogel and compare it to that of the solvent while also monitoring the swelling of the hydrogel. Since the sample is transparent to visible light, the setup was used in transmission mode (Fig. 1(a)). This experiment allowed us to separately

but simultaneously follow solvent and solute movement with NR and FI, respectively. At the same time the hydrogel was observed with OI to quantify its swelling or its changing appearance, for example the development or healing of defects.

Polyacrylamide (PAAm) hydrogels with a cross-linker to monomer ratio of 1 : 60 were synthesized in light water (H_2O) following a standard protocol.^{36,37} The initial water content of the hydrogel can be varied by partially drying of the hydrogel; it shrinks upon drying and re-swells after being contacted with solvent. Here, hydrogel discs with a light water (H_2O) volume fraction of $\phi_{\text{H}_2\text{O}} = 0.97$, radius $r \approx 0.45$ cm and height $h \approx 1.5$ mm were cut from the hydrogel and transferred into the sample cell. By using additional spacers in the cell (Sec. II C), the sample was restrained to a thickness of 1 mm to prevent slipping due to the vertical sample orientation. The cell was then placed on its holder in the setup and aligned with respect to the scintillator. During installation of the optical setup, it had been aligned with the neutron beam, namely the scintillator, so that an alignment of the cell with respect to the scintillator assures its proper alignment with the neutron and optical beams.

Fluorescein sodium salt (in the following simply referred to as fluorescein) was chosen as fluorescent dye. This was dissolved in heavy water (D_2O) to obtain a concentration of 26.6 μM . Fluorescein is excited at 496 nm and emits at 525 nm. Thus, an LED with a center wavelength of 490 nm and an excitation filter (EX) that transmits a band of 29 nm width around a center wavelength of 480 nm were used. The emitted fluorescence and the excitation light were separated using a dichroic mirror (DM) that transmits wavelengths above and reflects wavelengths below 502 nm. Additionally, an emission filter (EM) that transmits only wavelengths above 520 nm was added.

At the start of an experiment, several neutron, fluorescence and optical transmission images were collected before the hydrogel was contacted with dye solution. The fluorescein solution was injected using a syringe pump that could be controlled from outside the bunker of the beam line. Thus, images could be taken throughout the filling process. At the end of the filling process, the fluorescein solution filled the whole sample cell, hence completely surrounding the hydrogel. Since the faces of the disc were covered by the glass, diffusion of solvent and fluorescent particles only occurred through the circular edge, hence representing a quasi two-dimensional geometry of an infinite cylinder. Examples of neutron radiographs, fluorescence and optical images taken immediately after contact with the fluorescein solution and 20 min later are shown in Fig. 6. Neutron imaging is sensitive to the isotopic composition of the sample (Sec. I, Sec. III A) and reveals the diffusion of heavy water (initially outside the hydrogel) and light water (initially in the hydrogel) into and out of the hydrogel, respectively. Initially, a strong contrast between the hydrogel and the surrounding solution is observed (Fig. 6(a), left). In the

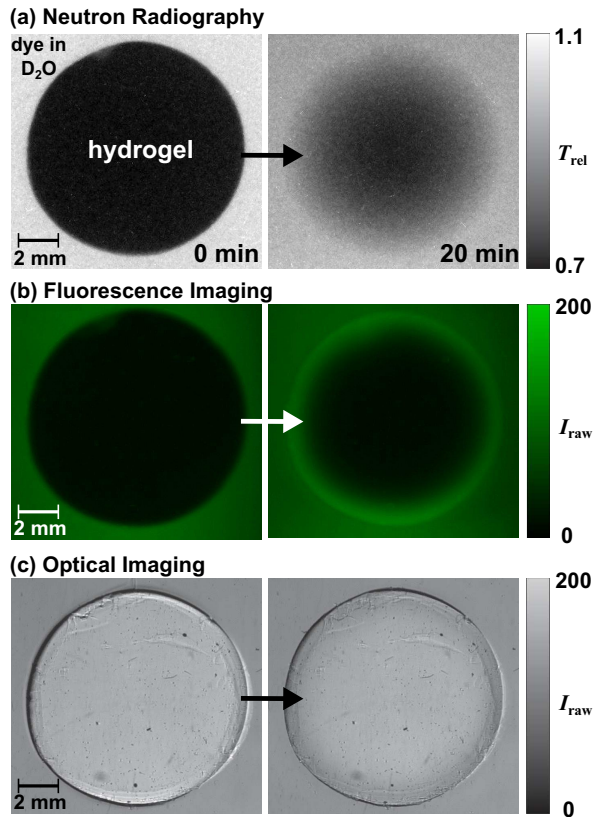


Fig. 6. Fully swollen polymer hydrogel in light water (H_2O), (left) immediately and (right) 20 min after contact with fluorescein in heavy water (D_2O) as observed simultaneously by (a) neutron radiography, (b) fluorescence imaging and (c) optical transmission imaging.

course of the experiment, the contrast between the hydrogel and the solvent becomes less pronounced (Fig. 6(a), right) and eventually vanishes. This indicates the interdiffusion of heavy and light water.

Fluorescence imaging shows an increasing fluorescence intensity and hence fluorescein concentration inside the hydrogel with time (Fig. 6(b)). This reflects the diffusion of fluorescein molecules into the hydrogel. The fluorescein molecules clearly enter the hydrogel at a slower rate than the heavy water. This is consistent with the larger size, and thus a lower diffusion coefficient, of a fluorescein molecule compared to a water molecule. It also shows that the setup is able to discriminate between solvent and solute movement. Note that the bright rim at the hydrogel-solution interface arises from scattering at the (rough) hydrogel edge and precludes an analysis of the fluorescence data close to the interface. This effect is particularly pronounced, for example compared to optical transmission imaging, as the fluorescence intensity is relatively low. It illustrates the advantage of neutrons with their smaller wavelength and thus smaller scatter-

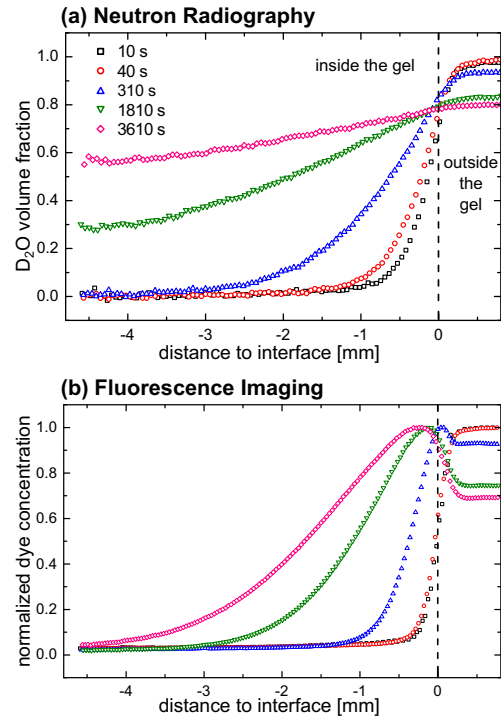


Fig. 7. (a) D_2O volume fraction and (b) fluorescein concentration (normalized to the maximum) profiles inside and outside the polymer hydrogel at different times after contact with fluorescein solution as determined by neutron radiography and fluorescence imaging, respectively. Symbols correspond to the same times in both figures (as indicated).

ing angles such that neutrons scattered by mesoscopic structures are recorded by (almost) the same pixel as the transmitted neutrons. Furthermore, the refractive index differences experienced by neutrons are typically much smaller.

Optical transmission imaging shows a slight decrease in hydrogel size of about 0.03 mm. The optical images also provide useful information on, e.g., defects, as can be seen in the upper left region of the hydrogel shown in Fig. 6(c). The evolution of the defects, for example their healing, can be followed. Furthermore, since such defects lead to a faster ingress of the fluorescein solution, this region can be excluded from the quantitative analysis of the fluorescence and neutron images.

To access quantitative information from the images, the intensity, I_{raw} , was analyzed pixelwise (Sec. III) and then averaged to obtain the time-evolution of the concentration profiles, i.e. the concentration as a function of the distance to the hydrogel-solution interface (Fig. 7). The temporal evolutions of these profiles provide detailed and quantitative information on the diffusion processes with very good statistics, which can be quantitatively analyzed to yield, e.g., the diffusion coefficients of the solvent(s) and fluorescein molecules in the solution and

3.1 Neutron, Fluorescence and Optical Imaging: An in-situ Combination of Complementary Techniques

8

hydrogel. A quantitative analysis of the concentration profiles is ongoing³⁷ and beyond the scope of the present manuscript.

B. Optical Reflection Imaging: Mesoporous Silica Contacted with Solvent Vapor

This second example investigates the solvent uptake of a Nile red-functionalized mesoporous silica (MCM-41) powder which is not transparent to light so that the apparatus had to be used in reflection mode. Functionalized mesoporous silica powders have been proposed as chemical sensors.³⁸ Due to their porous structure, these powders exhibit a very large surface area (approximately $1000 \text{ m}^2/\text{g}$).³⁹ While the pores in the powder particles are mainly responsible for this large surface area, there are also relatively large cavities between the individual particles. Thus, the powder contains intra- as well as interparticle cavities.

In this experiment MCM-41 powder (Sigma Aldrich) loaded with approximately $9 \mu\text{mol/g}$ of Nile red⁴⁰ was contacted with diethyl ether vapor. The aim of this experiment was to compare the uptake of solvent, using NR, and the corresponding change in fluorescence, using FI, after contact with solvent vapor. Generally, the fluorescence of such powders changes when they are contacted with a solvent. The solvent polarity has a strong effect on both the excitation and in particular the emission wavelengths, i.e. these materials exhibit solvatochromism. By using a color camera it is possible to identify changes in the fluorescence wavelengths, which are very pronounced in the present system,⁴⁰ and thus differentiate between different solvents absorbed. However, in this exploratory example, the intensity of the green component of the fluorescence was rather weak. Thus, we do not consider this possibility further here.

Nile red is excited at 552 nm , a different wavelength compared to fluorescein. Hence, the following components of the apparatus were substituted for the ones previously used: an LED with a center wavelength of 525 nm , an excitation filter (EX) that transmits a band of 20 nm around a center wavelength of 542 nm , a dichroic mirror (DM) that reflects wavelengths below and transmits wavelengths above 568 nm , and an emission filter (EM) that transmits a band of 52 nm around 620 nm . Approximately 100 mg powder was held in one chamber of the sample cell shown in figure 4. The glass window enabled visual verification of the homogeneity of the powder packing. The experiments were performed at room temperature and atmospheric pressure. To ensure that the time of initial contact with the vapor was known, solvent was injected remotely into the solvent chamber after several images of the dry powder had been collected.

During the experiment, the solvent migrated from top to bottom into the sample. Visual observation of the fluorescence images suggests only small changes in the fluorescence of the sample with time (Fig. 8(c) and (d)).

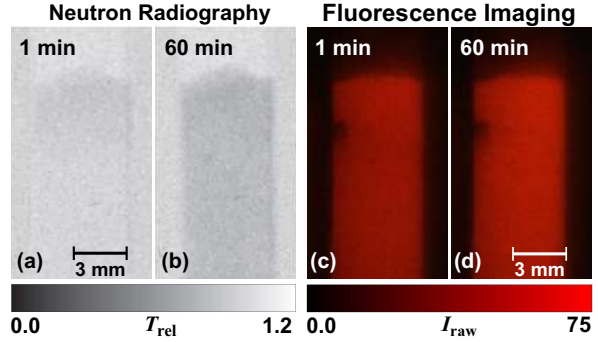


Fig. 8. Neutron radiographs ((a), (b)) and fluorescence images ((c), (d)) of MCM-41 powder loaded with $9 \mu\text{mol/g}$ Nile red right after contact with diethyl ether and one hour later.

Clearer changes can be seen in the neutron transmission images (Fig. 8(a) and (b)): Silica powder does not absorb neutrons strongly and appears light gray whereas the wet powder appears darker corresponding to a lower neutron transmission due to the presence of liquid solvent containing hydrogen (H) (Fig. 8(b)). Due to its very low density, solvent vapor is practically transparent to neutrons and hence cannot account for the decrease in transmission.

The neutron transmission images can be quantitatively analyzed in a similar manner to that described in the previous example. In addition, solvent migration is homogeneous, i.e. the solvent concentration is independent of the position in the plane perpendicular to the ingress of solvent (Fig. 8). Hence, the data can be averaged horizontally across the sample to improve statistics. Furthermore, homogeneity in a horizontal plane ensures that the results of reflection imaging are independent of penetration depth and can be compared directly with the neutron imaging results obtained as a projection through the entire sample thickness.

To improve the statistics further, in the analysis, the sample was divided into seven volumes at different heights h in the sample. Edge and surface effects were avoided by binning over an image area 4.05 mm wide (sample width 5.1 mm) by 1.35 mm height and excluding about 2.4 mm at the top and several millimeters at the bottom of the sample. The same areas were used in NR and FI.

The neutron transmission $T_S(h, t)$ and the fluorescence intensity $I(h, t)$ were converted to solvent filling factor, f_{NR} , and fractional fluorescence intensity, f_{FI} , respectively as follows:

$$f_{\text{NR}} = \frac{T_S(h, t=0) - T_S(h, t)}{T_S(h, t=0) - T_S(h, t \rightarrow \infty)}, \quad (9)$$

$$f_{\text{FI}} = \frac{I(h, t) - I(h, t=0)}{I(h, t \rightarrow \infty) - I(h, t=0)}, \quad (10)$$

and plotted as a function of time (Fig. 9). This assumes

linear relationships between solvent content and the NR and FI signals, which is reasonable for the solvent contents considered, and a fully saturated sample at long times, which also appears reasonable given that both, f_{NR} and f_{FI} , saturate at long times (Fig. 9). Since the neutron absorption of vapor is very small, f_{NR} is a measure of the volume filled with liquid which might be inside or between the powder particles. By contrast, f_{FI} is sensitive to the amount of the Nile red wetted by the solvent. As the Nile red is attached to the surfaces, both of the pores and the particles, this quantity reports on the fraction of surface that is wetted.

Both, f_{NR} and f_{FI} , increase with time with the increase occurring earlier closer to the top of the powder sample (Fig. 9). The increase in f_{NR} happens in two steps; a fast increase to a value of about 0.3 and a subsequent slower increase to full saturation. While in the first step mainly f_{NR} increases, in the second step, f_{FI} follows f_{NR} closely (Fig. 10). The delay between the increases in f_{NR} and f_{FI} becomes longer as volumes deeper in the sample are considered. This observation suggests that migration of solvent molecules into the free volume occurs in two stages. First, they quickly move into the large cavities between the particles, which, due to their relatively large size, have a large volume-to-surface ratio and thus lead to the significant increase in f_{NR} but only a modest increase

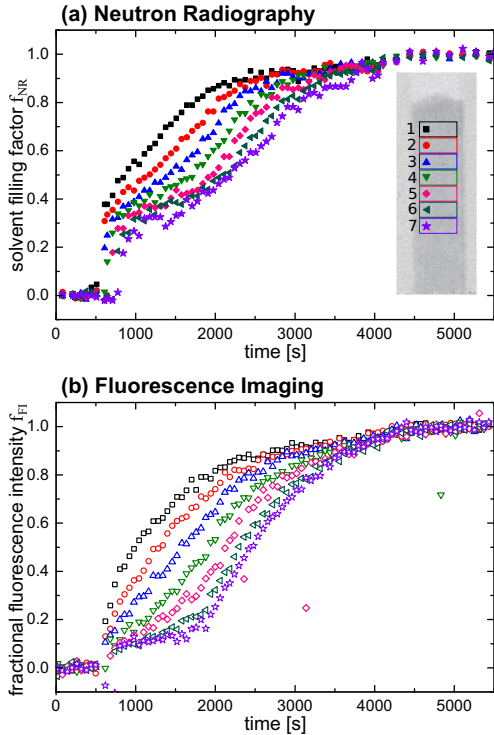


Fig. 9. (a) Solvent filling factor f_{NR} and (b) fractional fluorescence intensity f_{FI} in volumes at different positions in the MCM-41 sample (as indicated in (a)).

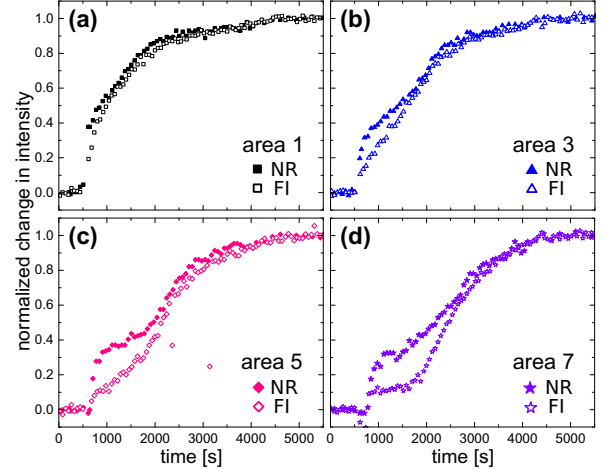


Fig. 10. Direct comparison of the temporal change in f_{NR} (closed symbols) and f_{FI} (open symbols) for four selected volumes in the sample. Shape and color of the symbols correspond to the respective sample volumes depicted in Fig. 9

in f_{FI} . Subsequently, in a much slower process solvent moves from these cavities into the smaller pores inside the particles. The pores have a large surface-to-volume ratio and hence both, f_{NR} and f_{FI} , increase. This is consistent with theoretical considerations, which predict larger cavities to fill more rapidly than small pores.^{41,42} Furthermore, it is conceivable that the total volume of the large cavities represents about one third of the free volume.⁴³ The neutron and fluorescence data allow for a more quantitative analysis of the transport process,^{41,42,44,45} which, however, is beyond the scope of this report. Nevertheless, these experiments illustrate that valuable quantitative and complementary information on the migration of solvent into porous systems can be obtained by simultaneously performing neutron and fluorescence imaging, here on the filled volume and wetted surface, respectively. This can then be exploited for the rational design of hierarchically porous systems.^{46–48}

V. SUMMARY AND CONCLUSION

We have designed and constructed an apparatus which enables neutron radiography to be simultaneously combined with optical and fluorescence imaging. Imaging can be performed in transmission or reflection mode to investigate optically transparent or opaque samples, respectively. The combination with neutron radiography is rendered possible because the optical setup is compact and hence can be incorporated into neutron radiography beamlines. Additionally, the optical components that need to be in the neutron beam do not significantly affect the neutron beam. Therefore, the three techniques can be used simultaneously to obtain complementary and

3.1 Neutron, Fluorescence and Optical Imaging: An in-situ Combination of Complementary Techniques

10

quantitative information on different aspects of the sample and their time dependencies.

To illustrate the operation of the apparatus, two examples were presented. First, the transmission mode was used to investigate diffusion processes following the contact of a polymer hydrogel with dye solution. The three imaging techniques allowed us to follow the diffusion of both solvent and solute (dye), as well as changes in the hydrogel. In the second example, the reflection mode was used to study dye-functionalized mesoporous silica after it was brought in contact with solvent vapor. Differences in solvent content and wetted surface area were revealed which allowed us to disentangle and distinguish the filling of pores in the particles and cavities between the particles. Extensions of the apparatus, for example to follow simultaneously two fluorophores or to study solvatochromism, were also indicated.

ACKNOWLEDGEMENT

We thank the Paul Scherrer Institute (Villigen, Switzerland) for beamtime and the coated mirrors as well as the workshop of the Research Centre Jülich for the manufacturing of the sample cells. We furthermore acknowledge support by the Strategic Research Fund of the Heinrich Heine University, the International Helmholtz Research School of Biophysics and Soft Matter (IHRS BioSoft) and we thank Jennifer Burbach and Annette Schmidt for assistance with sample preparation and sample advice, respectively.

- ¹P. Huber, *J. Phys.: Condens. Matter* **27**, 103102 (2015).
- ²D. W. Schaefer and R. S. Justice, *Macromol.* **40**, 8501 (2007).
- ³M. Moniruzzaman and K. I. Winey, *Macromol.* **39**, 5194 (2006).
- ⁴J. Oberdisse, *Soft Matter* **2**, 29 (2006).
- ⁵C. A. Dreiss, *Soft Matter* **3**, 956 (2007).
- ⁶J. Vermant and M. J. Solomon, *J. Phys.: Condens. Matter* **17**, R187 (2005).
- ⁷P. T. Callaghan, *Rep. Prog. Phys.* **62**, 599 (1999).
- ⁸S. U. Egelhaaf, U. Olsson, and P. Schurtenberger, *Physica B* **326**, 276 (2000).
- ⁹S. U. Egelhaaf, U. Olsson, P. Schurtenberger, J. Morris, and H. Wennerström, *Phys. Rev. E* **60**, 5681 (1999).
- ¹⁰S. U. Egelhaaf and P. Schurtenberger, *Phys. Rev. Lett.* **82**, 2804 (1999).
- ¹¹A. Onuki, *J. Phys.: Condens. Matter* **9**, 6119 (1997).
- ¹²R. Mezzenga, P. Schurtenberger, A. Burbidge, and M. Michel, *Nat. Mater.* **4**, 729 (2005).
- ¹³B. Kainz, E. A. Oprzeska-Zingrebe, and J. L. Herrera, *Biotechnol. J.* **9**, 51 (2013).
- ¹⁴G. Sirinakis, Y. Ren, Y. Gao, Z. Xi, and Y. Zhang, *Rev. Sci. Instrum.* **83**, 093708 (2012).
- ¹⁵A. R. Kherlopian, T. Song, Q. Duan, M. A. Neimark, M. J. Po, J. K. Gohagan, and A. F. Laine, *BMC Syst. Biol.* **2**, 74 (2008).
- ¹⁶D. Ganguly, S. Chakraborty, M. Balitanas, and T.-h. Kim, in *Security-Enriched Urban Computing and Smart Grid*, Vol. 78, edited by T.-h. Kim, A. Stoica, and R.-S. Chang (Springer Berlin Heidelberg, 2010) pp. 504–516.
- ¹⁷D. B. Murphy and M. W. Davidson, *Fundamentals of Light Microscopy and Electronic Imaging*, 2nd ed. (John Wiley & Sons, Inc., New York, 2012).
- ¹⁸J. R. Lakowicz, *Principles of Fluorescence Spectroscopy* (Springer, USA, New York, 2006).
- ¹⁹N. Rudolph, H. G. Esser, A. Carminati, A. B. Moradi, A. Hilger, N. Kardjilov, S. Nagl, and S. E. Oswald, *J. Soils Sediment* **12**, 63 (2011).
- ²⁰P. Schurtenberger, in *Neutrons, X-Rays and Light: Scattering Methods Applied to Soft Condensed Matter*, edited by P. Lindner and T. Zemb (North-Holland, Elsevier Science B. V., Amsterdam, 2002) pp. 145–170.
- ²¹R. Hassanein, E. Lehmann, and P. Vontobel, *Nucl. Instr. Meth. Phys. Res. A* **542**, 353 (2005).
- ²²R. Hassanein, F. de Beer, N. Kardjilov, and E. Lehmann, *Physica B* **385-386**, 1194 (2006).
- ²³A. S. Tremsin, E. H. Lehmann, N. Kardjilov, M. Strobl, I. Manke, J. B. McPhate, J. V. Vallerga, O. H. W. Siegmund, and W. B. Feller, *J. Instrum.* **7**, C02047 (2012).
- ²⁴U. Matsushima, N. Kardjilov, A. Hilger, I. Manke, H. Shono, and W. Herppich, *Nucl. Instr. Meth. Phys. Res. A* **605**, 185 (2009).
- ²⁵L. Crow, in *Neutron Imaging and Applications - A Reference for the Imaging Community*, edited by I. S. Anderson, R. L. McGreevy, and H. Z. Bilheux (Springer, New York, 2009) pp. 47–63.
- ²⁶E. Lehmann, G. Frei, G. Kühne, and P. Boillat, *Nucl. Instr. Meth. Phys. Res. A* **576**, 389 (2007).
- ²⁷H. E. Hermes, C. E. Sitta, B. Schillinger, H. Löwen, and S. U. Egelhaaf, *Phys. Chem. Chem. Phys.* **17**, 15781 (2015).
- ²⁸H. E. Hermes, R. L. Hanes, D. Wagner, S. Hartmann, A. Kaestner, M. Schulz, B. Schillinger, E. H. Lehmann, and S. U. Egelhaaf, In preparation.
- ²⁹H. Li, B. Schillinger, E. Calzada, L. Yinong, and M. Muehlbauer, *Nucl. Instr. Meth. Phys. Res. A* **564**, 405 (2006).
- ³⁰V. F. Sears, *Neutron News* **3**, 29 (1992).
- ³¹<http://www.ati.ac.at/~neutropt/scattering/ScatteringLengths-AdvTable.pdf>, accessed 21-Jun-2015.
- ³²N. B. Vicente, J. E. D. Zamboni, J. F. Adur, E. V. Paravani, and V. H. Casco, *J. Phys.: Conf. Ser.* **90**, 012068 (2007).
- ³³L. Hodgson, P. Nalbant, F. Shen, and K. Hahn, *Meth. Enzym.* **406**, 140 (2006).
- ³⁴A. Kaestner, S. Hartmann, G. Kühne, G. Frei, C. Grünzweig, L. Josic, F. Schmid, and E. Lehmann, *Nucl. Instr. Meth. Phys. Res. A* **659**, 387 (2011).
- ³⁵E. Lehmann, A. Kaestner, L. Josic, S. Hartmann, and D. Mannes, *Nucl. Instr. Meth. Phys. Res. A* **651**, 161 (2011).
- ³⁶R. Messing, N. Frickel, L. Belkoura, R. Strey, H. Rahn, S. Odenbach, and A. M. Schmidt, *Macromol.* **44**, 2990 (2011).
- ³⁷D. Wagner, J. Burbach, S. U. Egelhaaf, and H. E. Hermes, (2015), in preparation.
- ³⁸B. G. Trewyn, S. Giri, I. I. Slowing, and V. S.-Y. Lin, *Chem. Commun.*, 3236 (2007).
- ³⁹J. S. Beck, J. C. Vartuli, W. J. Roth, M. E. Leonowicz, C. T. Kresge, K. D. Schmitt, C. T. W. Chu, D. H. Olson, and E. W. Sheppard, *J. Am. Chem. Soc.* **114**, 10834 (1992).
- ⁴⁰M. Börgardt, (2015), in preparation.
- ⁴¹M. Alava, M. Dube, and M. Rost, *Adv. Phys.* **53**, 83 (2004).
- ⁴²S. T. Oyama, M. Yamada, T. Sugawara, A. Takagaki, and R. Kikuchi, *J. Jpn. Petrol. Inst.* **54**, 298 (2011).
- ⁴³I. Biazzo, F. Caltagirone, G. Parisi, and F. Zamponi, *Phys. Rev. Lett.* **102**, 195701 (2009).
- ⁴⁴S. Gruener, Z. Sadjadi, H. E. Hermes, A. V. Kityk, K. Knorr, S. U. Egelhaaf, H. Rieger, and P. Huber, *Proc. Natl. Acad. Sci.* **109**, 10245 (2012).
- ⁴⁵S. Gruener and P. Huber, *Phys. Rev. Lett.* **100**, 064502 (2008).
- ⁴⁶P. Innocenzi, L. Malfatti, and G. J. A. A. Soler-Ilia, *Chem. Mater.* **23**, 2501 (2011).
- ⁴⁷C. M. A. Parlett, K. Wilson, and A. F. Lee, *Chem. Soc. Rev.* **42**, 3876 (2013).
- ⁴⁸N. D. Petkovich and A. Stein, *Chem. Soc. Rev.* **42**, 3721 (2013).

3.2 Diffusion of macromolecules in a polymer hydrogel: from macroscopic to microscopic scales

Journal: Physical Chemistry Chemical Physics

Reference: *Phys. Chem. Chem. Phys.* **18**, 12860 (2016), DOI: 10.1039/c5cp07781h

Impact factor: 4.493

Authors: Deborah Sandrin, **Dana Wagner**, Christoph E. Sitta, Roland Thoma, Suren Felekyan, Helen E. Hermes, Christoph Janiak, Nader de Sousa Amadeu, Ralf Kühnemuth, Hartmut Löwen, Stefan U. Egelhaaf, and Claus A. M. Seidel

joint 1st author

DS, DW and RT prepared the samples. DS and RK performed confocal fluorescence image spectroscopy (MFIS), DW macroscopic transmission imaging and RT NMR spectroscopy. DS, DW, RT, SF, NdSA and RK analyzed the data. CES performed the Brownian dynamics simulations. SF developed the software for MFIS analysis. HEH, CJ, NdSA, RK, HL, SUE and CAMS designed the research and supervised the project. All authors interpreted data and wrote the manuscript.

20% contribution of DW

The article is reproduced with permission from the PCCP Owner Societies.

This page has been left intentionally blank.



PCCP

PAPER

View Article Online
View Journal

Cite this: DOI: 10.1039/c5cp07781h

Diffusion of macromolecules in a polymer hydrogel: from microscopic to macroscopic scales†

D. Sandrin,^{‡a} D. Wagner,^{‡b} C. E. Sitta,^{‡c} R. Thoma,^d S. Felekyan,^a H. E. Hermes,^b C. Janiak,^d N. de Sousa Amadeu,^d R. Kühnemuth,^{*a} H. Löwen,^{*c} S. U. Egelhaaf^{*b} and C. A. M. Seidel^{*a}

To gain insight into the fundamental processes determining the motion of macromolecules in polymeric matrices, the dynamical hindrance of polymeric dextran molecules diffusing as probe through a polyacrylamide hydrogel is systematically explored. Three complementary experimental methods combined with Brownian dynamics simulations are used to study a broad range of dextran molecular weights and salt concentrations. While multi-parameter fluorescence image spectroscopy (MFIS) is applied to investigate the local diffusion of single molecules on a microscopic length scale inside the hydrogel, a macroscopic transmission imaging (MTI) fluorescence technique and nuclear magnetic resonance (NMR) are used to study the collective motion of dextrans on the macroscopic scale. These fundamentally different experimental methods, probing different length scales of the system, yield long-time diffusion coefficients for the dextran molecules which agree quantitatively. The measured diffusion coefficients decay markedly with increasing molecular weight of the dextran and fall onto a master curve. The observed trends of the hindrance factors are consistent with Brownian dynamics simulations. The simulations also allow us to estimate the mean pore size for the herein investigated experimental conditions. In addition to the diffusing molecules, MFIS detects temporarily trapped molecules inside the matrix with diffusion times above 10 ms, which is also confirmed by anisotropy analysis. The fraction of bound molecules depends on the ionic strength of the solution and the charge of the dye. Using fluorescence intensity analysis, also MTI confirms the observation of the interaction of dextrans with the hydrogel. Moreover, pixelwise analysis permits to show significant heterogeneity of the gel on the microscopic scale.

Received 16th December 2015,
Accepted 17th March 2016

DOI: 10.1039/c5cp07781h

www.rsc.org/pccp

1. Introduction

The motion of macromolecules through disordered matrices is of great importance in analytical and preparatory techniques (chromatography,¹ expansion microscopy,² genomics,³ biofilms⁴) as well as in biomedical (imbibition,⁵ controlled drug delivery,^{6–9} flow control,¹⁰ implantable devices,⁹ contact lenses,¹¹ cellular and

tissue engineering^{12,13}) and technical applications (enhanced oil recovery^{14,15}). From a fundamental point of view, precise measurements for model systems are needed to reveal the underlying transport principles.^{16–19} It is known that the presence of obstacles slows down the transport and that this is more pronounced for larger molecules. However, the basic underlying mechanisms and their effects are not yet completely understood. In particular, the motion of particles through a gel matrix represents an intricate problem as the gel matrix can respond to the particle motion. A nontrivial dependence of the diffusion behavior on both the host and the guest, *i.e.* the gel and the diffusing particles, is expected. The behavior of the host is mainly characterized by a typical pore size. However, topological constraints resulting from the nontrivial and dynamically changing connectivity of the pores²⁰ also have an impact on the diffusion of the guest molecules. This connectivity is expected to result in a wide spread in the translocation rate of the individual particles. The translational rate is also influenced by the structural properties of the guest molecules

^a Institut für Physikalische Chemie II, Molekulare Physikalische Chemie, Heinrich-Heine-Universität, Universitätsstr. 1, 40225 Düsseldorf, Germany. E-mail: raf.kuehnemuth@hhu.de, cseidel@hhu.de

^b Institut für Experimentelle Physik der Kondensierten Materie, Heinrich-Heine-Universität, Universitätsstr. 1, 40225 Düsseldorf, Germany. E-mail: stefan.egelhaaf@hhu.de

^c Institut für Theoretische Physik II: Weiche Materie, Heinrich-Heine-Universität, Universitätsstr. 1, 40225 Düsseldorf, Germany. E-mail: hlowen@hhu.de

^d Institut für Anorganische Chemie und Strukturchemie, Heinrich-Heine-Universität, Universitätsstr. 1, 40225 Düsseldorf, Germany

† Electronic supplementary information (ESI) available. See DOI: 10.1039/c5cp07781h

‡ These authors have contributed equally to this work.

3.2 Diffusion of macromolecules in a polymer hydrogel: from macroscopic to microscopic scales

View Article Online

Paper

PCCP

such as hydrodynamic radius, shape, molecular weight or charge distribution. The significance of sieving, entanglements, (chemical) interactions, partitioning, oscillation of pores *etc.* is still controversially discussed.^{21–27} In addition, the average size of the pores is also under debate.^{23,28–34}

It is accepted that the mesh sizes in polymer hydrogels depend on the specific gel preparation such as (I) the mass concentration of polymeric material in the reaction solution, $[T]$, and (II) the weight fraction of cross-linker, C_R , but the absolute average size of the pores is subject to debate.^{23,28–34} Considering hydrogels ($0.035 \text{ g ml}^{-1} \leq [T] \leq 0.065 \text{ g ml}^{-1}$, $0.02 \leq C_R \leq 0.05$) with similar compositions to the one studied here ($[T] = 0.04 \text{ g ml}^{-1}$, $C_R = 0.035$), different methods give very different results for the pore sizes (please note that the numbers given for $[T]$ and C_R , multiplied by 100, correspond to the parameters %T and %C, respectively, which were used in the above publications). The reported pore sizes range from 2.00–2.25 nm (chromatography²⁸) through 5–9 nm (electrophoresis studies in the 1960s and 1980s^{29,30}) and 60–156 nm (electrophoresis studies in 1991^{23,31}) up to values of 2–20 μm (for the largest pores found by scanning electron microscopy^{32–34}). This also complicates any systematic study of particle diffusion in a well-characterized model system, which however is important to understand the principles of translocation and to test theoretical approaches.

Here we study polymeric dextran molecules diffusing through a polyacrylamide hydrogel without interfering with the sample during the measurements. We use dextrans as tracer particles, because they have a good water solubility, low toxicity, relative inertness and are flexible polymers. Moreover, they are commercially available over a broad range of molecular weights and hence sizes. Most dextrans can be also obtained as derivatives labelled with fluorescent dyes (fluorescein sodium salt (FLU), Alexa Fluor 488 (A488), tetramethylrhodamine (TMR)). The molecular weight of the dextrans is varied between $M_w = 3 \text{ kDa}$ to 2000 kDa. For comparison the diffusion of free dyes, FLU, A488 and TMR is studied in our hydrogel, too. To investigate the interactions of the particles with the hydrogel in more detail, we study the influence of solution conditions like pH-value, salt and tracer particle concentrations. Using three complementary methods, multiparameter fluorescence image spectroscopy (MFIS), macroscopic transmission imaging (MTI) with fluorescence detection and nuclear magnetic resonance (NMR), we measure the long-time diffusion coefficient of the fluorescently labelled and unlabelled probe particles, respectively. MFIS also allows us to detect the heterogeneity of the gel. The data are compared to a model by Ogston³⁵ which predicts the dynamical hindrance in a network of randomly distributed fibers due to geometric confinement. The Ogston model provides a simple analytical formula for the particle dynamics *via* an effective excluded volume. Another theoretical approach is to perform computer simulations. As modeling a hydrogel on an atomic basis over huge length- and timescales is computational unaffordable, various different model assumptions including different degrees of molecular details have been used in the past.^{36–48} The most detailed model for the gel matrix was used by Linse and

coworkers^{36–39} and Holm and coworkers^{40–42} who resolved the monomers of the polymer chains connecting the nodes explicitly within a bead-spring model. Within their approach the swelling behavior of the gels was explored but the diffusion of tracer particles within the gel network was not addressed. In a more coarse-grained approach, the matrix was described by either a static network of points,⁴³ rods,^{43,44} or chains⁴⁵ or as fluctuating network of spheres^{46,47} which indeed allows for the computation of tracer diffusion. Following the latter coarse grained approach of Zhou and Chen,⁴⁷ we perform Brownian dynamics (BD) simulations representing three different levels of complexity to resolve the different physical effects that are operating in the hydrogel. Our simulation study provides a simple and systematic framework, taking into account the flexibility of the matrix particles, the effective dextran–matrix excluded volume and finding strong indications for effective attractive interactions. Our combined results provide a consistent picture of polymers diffusing through a hydrogel matrix and may serve to test more quantitative theories and other experimental approaches.

2. Materials and methods

2.1. Samples

2.1.1. Hydrogel: a polymer matrix in an aqueous environment. The polyacrylamide (PAAm) hydrogels were formed by copolymerization of acrylamide (AAm, monomer) with the tetrafunctional cross-linking agent *N,N'*-methylenebis(acrylamide) (BIS), using ammonium peroxodisulphate (APDS) and tetramethylethylenediamine (TEMED) as redox initiators. The monomer and cross-linker were both purchased from Sigma-Aldrich, APDS from Roth and TEMED from Merck. All components were used without further purification. AAm, BIS and APDS were separately dissolved in deionized and filtered water and cooled to 4 °C. The individual solutions were then mixed at a low temperature. The reaction mixture contained 75 mg of AAm, 2.71 mg of BIS, 6 mg of APDS and 10 μl of TEMED in a total volume of 2 ml which corresponds to a molar ratio of cross-linker to monomer of 1:60. The total monomer concentration, defined as the mass concentration of AAm and BIS in the total reaction volume, is $[T] = 0.04 \text{ g ml}^{-1}$ and the weight fraction of cross-linker with respect to the total mass of the polymeric material (AAm and BIS) is $C_R = 0.035$.

After mixing, the solution was transferred to Teflon molds and allowed to warm up and react at room temperature. After one to two hours, polymerization was complete and the hydrogel was transferred into a larger container filled with deionized water. The gel was left for five days to ensure that the hydrogel swells to equilibrium. The excess water was exchanged daily to wash out residual chemicals that had not reacted in the gelation process.⁴⁹

Discs with a radius $R_d \approx 0.3 \text{ cm}$ were cut from the hydrogels using a simple stamp. In corresponding MTI and MFIS experiments, samples cut from one gel block were used. For the NMR measurements, the gelation process was carried out in cylindrical

Teflon molds ($R_d \approx 0.5$ cm, height 5 cm). The hydrogels were then transferred into a container filled with deuterium oxide.

The hydrogel was characterized by determining the polymer volume fraction in the fully swollen state, ϕ , the average molecular weight between cross-linking points, M_c , and the mesh size, ξ . The polymer volume fraction of the hydrogel in the swollen state ϕ was calculated directly from eqn (1):^{50,51}

$$\phi = \frac{V_p}{V_{\text{gel}}} = \frac{m_p \rho_{\text{H}_2\text{O}}}{m_p \rho_{\text{H}_2\text{O}} + m_{\text{H}_2\text{O}} \rho_p} \quad (1)$$

where V_p is the volume of the dry polymer (PAAm), V_{gel} is the volume of the hydrogel after equilibrium swelling, m_p is the mass of the polymer, $m_{\text{H}_2\text{O}}$ is the mass of water in the swollen gel and ρ_p and $\rho_{\text{H}_2\text{O}}$ are the densities of polymer and water, respectively.

The mass of the fully swollen hydrogel was measured after removing the liquid on the surface of the hydrogel with a pipette. It was then dried at 40 °C under vacuum for at least 6 h until constant weight was reached to determine m_p . The experiment was repeated for different pieces of hydrogel, and the mass fraction was converted into volume fraction using the known polymer density ($\rho_p = 1.3$ g cm⁻³).⁵²

The theoretical molecular weight of the polymer between cross-links M_c is related to the degree of cross-linking in the hydrogel, X (*i.e.*, the molar ratio of cross-linker to monomer) and the molecular weight of the repeating units ($M_{r,\text{AAm}} = 71.1$ g mol⁻¹).^{51,53}

$$M_c = \frac{M_r}{2X} \quad (2)$$

The mesh size, ξ , which characterizes the space between macromolecular chains can be calculated using:^{50,54,55}

$$\xi = \phi^{-1/3} \zeta \left(\frac{C_n 2M_c}{M_r} \right)^{1/2} \quad (3)$$

where C_n is Flory's characteristic ratio ($C_{n,\text{AAm}} = 2.72$) and ζ is the carbon-carbon bond length ($\zeta = 0.154$ nm).⁵⁶ This calculation assumes ideal solvent quality, homogeneous cross-linking densities and Gaussian distribution of chain lengths.

We characterized the polyacrylamide hydrogels as used in these experiments, *i.e.* in water and in a 20 mM potassium carbonate buffer at pH 10. The results are shown in Table 1.

2.1.2. Diffusing polymeric guest molecules. The dextrans (Table 2) and free dyes were purchased from Invitrogen. For the NMR experiments, unlabelled dextrans were dissolved in deuterium oxide with a purity of 99.9% from Deutero GmbH. For the remaining experiments, dextrans conjugated with Alexa

Table 2 Overview of dyes and dextrans of different molecular weights, M_w , as obtained from manufacturer (for labelled dextrans already including the dye) and their naming convention. The dextrans were either unlabelled or conjugated with one of three different dyes: Alexa Fluor 488, tetramethylrhodamine and fluorescein. For more detailed information see S1.1 and S1.2 (ESI)

M_w [kDa]	Unlabelled	Alexa fluor 488	Tetramethylrhodamine	Fluorescein
0.33				FLU
0.39			TMR	
0.53		A488		
3	D3	A488-D3	TMR-D3	FLU-D3
10	D10	A488-D10	TMR-D10	FLU-D10
40	D40		TMR-D40	FLU-D40
70			TMR-D70	
500				FLU-D500
2000			TMR-D2000	

Fluor 488 (A488) or tetramethylrhodamine (TMR) were dissolved in deionized water. To exclude fluorescence blinking due to protonation-deprotonation dynamics, dextrans labelled with fluorescein (FLU) were prepared in potassium carbonate buffer at pH = 10, (20 mM) and the fluorescence measurements were conducted after addition of 100 μ M Trolox (Sigma-Aldrich) to avoid photobleaching of the dye.

To investigate the local environment and possible probe-polymer interactions inside the gel matrix, we measured the most polar dye attached to one of the smaller dextrans, A488-D10 under five different conditions: (i) H₂O, (ii) aqueous KClO₄ solution (10 mM, 20 mM, 40 mM, and 60 mM), (iii) aqueous KCl solution (20 mM), (iv) aqueous potassium carbonate buffer (20 mM) at pH = 7, and (v) at pH = 10.

2.1.3. Addition of polymeric guest molecules to the hydrogel. For MFIS experiments, each hydrogel disc was placed in a chambered cover glass (Lab-Tek™, Thermo Fisher Scientific, USA), incubated with guest molecule solution (400 μ l in total) and allowed to reach equilibrium before the measurement was started (2 to 7 days depending on dextran size). When electrolyte solutions were used, the solution was exchanged approximately every 12 h during the incubation period to ensure defined concentrations.

In the MTI experiments, the initial particle concentration in the hydrogel was 0 and the concentration in the surrounding solution was varied between 0.1 and 10 μ M. The hydrogel matrix was contacted with the particle (dye or dextran) solution at the beginning of the experiments and the diffusion of guest molecules from the solution into the hydrogel was studied.

For NMR measurements, the hydrogel cylinders were incubated with concentrated amino dextran solution in deuterium oxide for at least 48 h. The samples were then carefully transferred into NMR tubes ensuring that the gel texture was not destroyed. Concentrations below 1 mM were used in order to avoid aggregation. Bubbles were successfully avoided.

2.2. Measurement methods

2.2.1. Multiparameter fluorescence image spectroscopy (MFIS). All measurements were conducted on a confocal fluorescence microscope (FV1000 Olympus, Hamburg, Germany),

Table 1 Polymer volume fraction in the swollen state (ϕ), molecular weight of the polymer between cross-links (M_c) and mesh size (ξ) for the PAAm hydrogel in water and in potassium carbonate buffer 20 mM at pH 10. The errors are the standard errors of repeated measurements of the polymer volume fraction

	PAAm in water	PAAm pH 10
ϕ	0.0390 \pm 0.0004	0.0150 \pm 0.0001
M_c [g mol ⁻¹]	2141	2141
ξ [nm]	5.7 \pm 0.1	7.8 \pm 0.1

3.2 Diffusion of macromolecules in a polymer hydrogel: from macroscopic to microscopic scales

View Article Online

Paper

PCCP

which had been modified to allow time-resolved experiments.^{57,58} A488 and FLU were excited using a polarized pulsed diode-laser (LDH-D-C-485, PicoQuant, Berlin, Germany) at 485 nm, while for TMR a supercontinuum laser (SuperK Extreme, NKT Photonics, Birkerød, Denmark) at 555 nm was employed. Laser light was directed into a 60× water immersion objective (NA = 1.2) by a dichroic beam splitter and focused into the sample close to the diffraction limit. The light emitted was collected by the same objective and separated into two polarizations (parallel and perpendicular) relative to the excitation beam. The fluorescence signal was further divided into two spectral ranges (BS 560, AHF, Tübingen, Germany). Bandpass filters for A488/FLU and TMR fluorescence (HC 520/35 and HC 607/70, AHF), were placed in front of the detectors. The signal from single photon sensitive detectors (PDM50-CTC, Micro Photon Devices, Bolzano, Italy and HPMC-100-40, Becker&Hickl, Berlin, Germany, respectively) was recorded photon-by-photon with picosecond accuracy (HydraHarp400, PicoQuant) and analyzed using custom software (LabVIEW based). The temperature during all measurements was 22.5 ± 0.5 °C and the concentration of the dextrans was adjusted between 0.05 and 3 nM, depending on their different degree of labelling.

The sample was mounted on a piezo-controlled x-y scanner (P-733.2CL, Physik Instrumente, Karlsruhe, Germany) and moved perpendicular to the optical axis. It was moved in a stepwise manner to permit multiparameter fluorescence detection at defined locations. The pixel size is defined by the step size of the scan (in our experiments 10.00 μm) while photons are collected from the confocal detection volume only ($V_{\text{det}} = 0.55$ fl). The integration time per pixel was 30 min and the complete image contains 18 pixels (probed spots).

2.2.2. Macroscopic transmission imaging (MTI). The macroscopic transmission imaging experiments were performed using a custom-built imaging apparatus similar to that described previously.⁵⁹ The sample was illuminated by a parallel beam of light from an LED lamp (CoolLED, center wavelength of 490 nm) whose wavelength was chosen to excite the fluorescent particles in the sample. Using a dichroic mirror that transmits wavelengths above and reflects wavelengths below 502 nm, the transmitted light was split into excitation light (bright-field transmission image) and emitted light from the fluorophores (fluorescence image). The images were then focused onto separate CCD cameras. Additional fluorescence filters (excitation filter: 480/25, emission filter: longpass LP 520) were applied. The hydrogel discs were placed between two horizontally held glass plates with a fixed distance between the plates of 1.5 mm using aluminum spacers. This distance was chosen to ensure that the gels were compressed as little as possible but still in contact with both glass plates. The particle solution was added around the gel discs and allowed to diffuse into the gel matrix. The image collection time was varied between 5 s at the beginning and up to 300 s at the end of a measurement. Images were collected for 3 to 72 h. The sample cells were sealed to ensure that the solvent did not evaporate and measurements were performed at room temperature (23 °C).

2.2.3. Nuclear magnetic resonance (NMR). A Bruker AVANCE DRX-500 NMR spectrometer operating at 500 MHz for ¹H was used. The spectrometer was equipped with a Bruker Great 1/10 gradient amplifier and a Bruker selective inverse (SEI) probe with z-gradient coils. The gradient amplitudes were calibrated using dodecane, 1-pentanol and water as standard samples.⁶⁰ The temperature sensor was calibrated using methanol as described by van Geet.⁶¹ All diffusion measurements were acquired by using stimulated echo with bipolar gradient pulses (pulse program name STEBPGP).^{62,63} This sequence was also followed by a WATERGATE sequence to suppress the water signal.^{64,65}

In each experiment, the magnetic field gradient strength of the bipolar pulses was linearly arrayed along 16 values from 10 to 60 G cm⁻¹ while all other parameters were kept constant. The gradient pulse length, δ and the diffusion delay, Δ_N , were chosen such that the echo signal was suppressed considerably.

The diffusion coefficients of unlabelled aminodextrans in hydrogels and in deuterium oxide were measured at 23 °C in NMR sample tubes of 5 mm diameter. Dextran concentrations depended on the dextran's molecular weight and varied from 3.0 M for the 3 kDa dextran to 0.3 M for the 40 kDa dextran to avoid agglomeration in solution. We performed several diffusion measurements with each sample, varying the key parameters δ and Δ_N . Our experience showed that this is a good practice which helps identifying artifacts affecting the experiments or errors in the processing routines. The diffusion delays, Δ_N were chosen between 0.1 and 2.0 s and the gradient pulse widths, δ were between 600 and 1400 μs. Several combinations of Δ_N and δ were applied within those ranges. Later examination revealed high agreement among all those measurements, indicating good reproducibility.

2.3. Analysis methods

2.3.1. Multiparameter fluorescence image spectroscopy (MFIS). The recorded MFIS data can be correlated to yield correlation curves (fluorescence correlation spectroscopy, FCS, is part of the MFIS). Those fluorescence correlation curves that were measured inside the hydrogel usually exhibited multiple overlapping bunching terms in the time regime of the diffusion process. To establish the number of independent species, M , needed in the model function to reproduce the data, we fitted a distribution of diffusion coefficients applying the maximum entropy method (MEMFCS).⁶⁶ Having determined M we then fitted a model function containing M diffusion terms (eqn (4)):

$$G(t_c) = 1 + \frac{1}{N} \sum_{i=1}^M x_i \left(\left(1 + \frac{t_c}{t_{d,i}} \right) \sqrt{1 + \frac{t_c}{(z_0/\omega_0)^2 \cdot t_{d,i}}} \right)^{-1} \times \left(1 - A_T + A_T \cdot e^{-\frac{t_c}{T_T}} \right) \quad \text{with} \quad \sum_{i=1}^M x_i = 1 \quad (4)$$

For species with identical brightness, x_i represents their true molecular fractions. In this case, N is the number of molecules in the singlet state in the detection volume element and t_c is the correlation time. The model assumes a three-dimensional Gaussian-shaped volume element with spatial distribution of

the detection probabilities $w(x,y,z) = \exp(-2(x^2 + y^2)/\omega_0^2) \exp(-2z^2/z_0^2)$. The $1/e^2$ radii in x and y or in z direction are denoted by ω_0 or z_0 , respectively. The characteristic diffusion time is $t_d = \omega_0^2/4D$, with the translational diffusion coefficient D . The confocal detection volume, V_{det} is calculated as follows: $V_{\text{det}} = \pi^{3/2}z_0\omega_0^2$.

Basic photophysical processes such as triplet transitions which result in temporary dark states are accounted for by an additional bunching term. Here A_T and t_T represent the triplet population and the triplet relaxation time.

The correlation curves for A488- and TMR-dextran in water and most FLU-dextran in carbonate buffer were fitted pixel by pixel, the remaining samples image-integrated. At mean irradiances in the focus of 1.2 kW cm^{-2} , A488- and TMR-samples did not exhibit noticeable triplet populations ($A_T < 0.01$), only fluorescein showed fluorescence bunching in the μs regime at even lower irradiances of 0.4 kW cm^{-2} . For pixelwise analysis, error bars for t_d (and equivalently for D) were calculated as standard error of the mean while for single point (*i.e.* solution) or image integrated measurements a bootstrapping procedure was applied.

Diffusion coefficients can be derived from the extracted diffusion times (t_d) provided that the size and shape of the confocal detection volume element are characterized. In practice, a photostable reference dye with known diffusion properties is used to calibrate the system. In the present case, we chose rhodamine 110 (Rh110). Thus all presented diffusion coefficients derived from FCS are based on the reported value of $D_{\text{Rh110}} = (4.3 \pm 0.3) \times 10^{-6} \text{ cm}^2 \text{ s}^{-1}$ at 295.65 K in dilute aqueous solutions.⁶⁷ The characteristic diffusion time of Rh110 in deionized water was $t_d = 30 \mu\text{s}$ with day-to-day variations of less than 5%. Due to increased aberrations with changes in the refractive index upon addition of salt, a systematic increase of t_d was observed (*e.g.* $t_d = 33 \mu\text{s}$ for Rh110 in 20 mM potassium carbonate buffer at $\text{pH } 7$ and $\text{pH } 10$, respectively). The longer wavelength required for the TMR experiments caused an increase in focus area $\pi\omega_0^2 = t_d 4\pi D$ and thus of t_d of about 30%, as expected from the changed diffraction limit.

A variety of possible artifacts have been reported that could cause uncertainties in translational diffusion measurements by FCS.⁶⁸ In particular optical saturation effects are known to distort the detection volume element and thus alter the observed average dwell times of the fluorophores. These effects have been minimized by keeping the excitation power low and by performing reference measurements under identical conditions. Low excitation power also diminishes the probability of photobleaching. Successful minimization of this effect is confirmed by the observation of extremely slow diffusing molecules with dwell times of up to 1 s.

A further possible artifact, focal distortions due to a refractive index mismatch (below 0.01, see S1.6, ESI†) is estimated to result in a small corresponding error in D (below 1%⁶⁹). This is supported by the good agreement of the FCS data with the independent MTI and NMR results (see below). Additionally, the possible refractive index mismatch between solution and hydrogel was checked using FCS and found to be negligible.

No readjustment of the correction collar setting on the objective was required after switching the sample from pure water to hydrogel (see S1.6, ESI†).

The steady state anisotropy, r , which is another parameter detected by MFIS is defined *via* the intensities of the fluorescence signal polarized parallel (F_{\parallel}) and perpendicular (F_{\perp}) with respect to the excitation polarization. As described by Koshioka *et al.*,⁷⁰ the fluorescence signal recorded with a confocal microscope is slightly depolarized by the objective due to its high numerical aperture. To account for this experimental artifact, correction factors l_1 and l_2 have been introduced:⁷⁰

$$r = \frac{GF_{\parallel} - F_{\perp}}{(1 - 3l_2)GF_{\parallel} + (2 - 3l_1)2F_{\perp}} \quad (5)$$

The correction factors l_1 and l_2 as well as the factor G , that compensates for the slightly different detection efficiencies of the two detection channels, were determined experimentally using the reference dyes enhanced green fluorescent protein (EGFP)⁵⁸ or rhodamine 110 and TMR, respectively, ($l_1 = 0.0308$, $l_2 = 0.0368$, $G = 0.99$). In detail, the G -factor is defined as the ratio of the detection efficiencies between perpendicular and parallel polarized fluorescence light. The fluorescence signal F is obtained from the detected signal by subtracting the appropriate background (scattering) measured in clean water or an unloaded gel.

2.3.2. Macroscopic transmission imaging (MTI). We found a linear relation between fluorescence intensity and concentration in the concentration range of 0.1 to $10 \mu\text{M}$ for all samples. Thus, we can directly determine the relative change in concentration from the image intensity. Especially for the larger dextran molecules, equilibration between the hydrogel and the surrounding solution takes several days. However, for most samples, it was found that measurement times of about 24 h were sufficient to allow diffusion coefficients to be extracted from the data. Some additional longer measurements were performed to capture the long time behavior. Even though the dyes used were relatively photostable and the incident intensity was reduced as much as possible, some photobleaching could be seen for these long measurement times. Thus, a photobleaching correction as described in ref. 71 and 72 was applied: the change in the normalized intensity F of an area in the solvent far outside the hydrogel, where no significant change in the concentration is expected, could be fitted with a double exponential function:

$$\frac{F(t)}{F(t=0)} = Pe^{-pt} + Qe^{-qt} \quad (6)$$

The intensity of the region of interest in the gel of every image was then corrected by dividing the original value by the one extracted from the bleach curve.

The hydrogel discs had a quasi-two-dimensional geometry and homogeneous radial diffusion was observed. Thus, by azimuthally averaging all pixels that are a certain distance away from the gel-reservoir interface, a concentration profile for every time step could be determined. Comparison of the concentration profiles with diffusion equations, including appropriate boundary conditions, yields diffusion coefficients (see Section 3.2.1).

3.2 Diffusion of macromolecules in a polymer hydrogel: from macroscopic to microscopic scales

View Article Online

Paper

PCCP

The hydrogels were fully swollen and in equilibrium before the measurements and no change in the hydrogel size was expected. However, for some samples we observed a decreasing gel radius of up to 6% within the first hours of the experiments in the bright-field transmission images and the change in radius was taken into account in the analysis. The reason for this is not clear. A change in temperature or an expansion of the sample cell and with that a slight increase in sample thickness might play a role.⁷³

2.3.3. Nuclear magnetic resonance (NMR). As is usual practice, the diffusion coefficients D were obtained by fitting the echo amplitudes (integral of the signals between 2.8 and 4.4 ppm) to the following equation:^{74,75}

$$\frac{E_i}{E_0} = \exp \left[-D(\gamma g_i \delta)^2 \left(\Delta_N - \frac{\delta}{3} - \frac{\tau_N}{2} \right) \right] \quad (7)$$

where E_i and E_0 are the echo intensities at increment i and with zero gradient applied, γ is the gyromagnetic ratio, g_i is the gradient amplitude at increment i , δ is the gradient pulse width, Δ_N is the diffusion delay and τ_N is the delay between the two magnetic field gradient pulses laying at one side of the echo pulse sequence. For the purpose of comparison, the diffusion coefficients measured in D_2O were recalculated for H_2O using the known viscosities of both solvents.⁷⁶

2.4. Models for Brownian dynamics simulations

Brownian dynamics simulations were used to calculate the diffusion coefficients of dextran particles within the polymer network. Inspired by previous investigations,^{46,47} we considered simple models of effective spheres for the matrix particles and the dextrans. For this, we used a microscopic model resolving the matrix explicitly and coarse-graining the diffusing polymer coil as an effective soft sphere. There are further underlying model assumptions: (i) the polymer matrix is not resolved on the monomer level, (ii) the matrix structure is derived from a periodic structure, and (iii) explicit hydrodynamic interactions caused by the solvent are ignored.

In order to obtain a systematic insight, the flexibility of the polymer matrix and the softness of the dextran–matrix interaction were modeled on three different levels. A schematic illustration of the models is shown in the Results section (see Section 3.2.2 and Fig. 9). On the first level (also referred to as model 1 in the following), the matrix particles were fixed on a periodic simple-cubic lattice with lattice constant a providing static steric obstacles for the diffusing dextran molecules. For simplicity, the latter were modeled as effective spheres. On this crude level any fluctuations in the pore sizes were neglected. The repulsive steric interaction between an obstacle i at position \vec{s}_i and another particle j (either tracer or obstacle) at position \vec{s}_j , separated by the distance s_{ij} , was modeled as in ref. 47 with a truncated and shifted repulsive Lennard Jones potential (also known as WCA-potential):

$$U_s(s_{ij}) = 4\epsilon_s \left[\left(\frac{\sigma_{ij}}{s_{ij}} \right)^{12} - \left(\frac{\sigma_{ij}}{s_{ij}} \right)^6 + \frac{1}{4} \right] \quad (8)$$

where $\epsilon_s = 1k_B T$ ($\sim 4.05 \times 10^{-21}$ J at 20 °C) and the additive diameter $\sigma_{ij} = 2R_{\text{obst}}$ for the obstacle–obstacle-interaction and $\sigma_{ij} = R_{\text{obst}} + R_h$ for the interaction between a matrix obstacle and a tracer of radius R_h . The cutoff was set at the potential's minimum at $l_{ij} = 2^{1/6}\sigma_{ij}$.

For the second level (model 2), we introduced fluctuating matrix particles. The network connectivity was ensured by coupling neighboring matrix particles by harmonic springs. For the harmonic spring potentials, we used Hooke's law:

$$U_{\text{sp}}(s_{ij}) = 0.5k(s_{ij} - s_{0,ij})^2 \quad (9)$$

for two matrix particles i and j with their distance at rest $s_{0,ij}$. Setting $k = 2k_B T / (2R_{h,D3})^2$ (~ 0.6 mJ m⁻²) allowed the dextran D3 to push a gap of its own diameter $2R_{h,D3}$ through two neighboring matrix particles in rest positions when overcoming an energy of $1k_B T$. This parameter is kept fixed in all simulations. Moreover the matrix particles were exposed to thermal fluctuations and repelled each other and the dextran particles *via* steric interactions as in model 1 (eqn (8)). To broaden the pore size distribution, the matrix particles were randomly shifted up to half the lattice constant a in each direction with respect to their initial positions before attaching undistorted springs between neighboring matrix particles.

At a third level of modeling, two different extensions were tested by changing the dextran–matrix interactions. In model 3a, we replaced the WCA potential for the steric interactions with a softer effective Gaussian potential which is a good model for penetrating polymer coils of different architecture:^{77–79}

$$U_G(s_{ij}) = \epsilon_G \exp \left(-\frac{s_{ij}^2}{2b^2} \right) \quad (10)$$

with $b^2 = (R_i + R_j)^2 / (2 \ln(\epsilon_G / (k_B T)))$. This relation keeps the potential at $s_{ij} = R_i + R_j$ for $1k_B T$. We used $\epsilon_G = 12k_B T$ (for more details see S11, ESI†).

In model 3b, an attractive shell with the size of a typical fluorescent dye's radius ($R_{D0} = 0.55$ nm) was added to the steric repulsion to account for a possible weak sticking of the dextrans to the matrix using a cosine function for a smooth transition:

$$U_{\text{sp}}(s_{ij}) = \begin{cases} 4\epsilon_s \left[\left(\frac{\sigma_{ij}}{s_{ij}} \right)^{12} - \left(\frac{\sigma_{ij}}{s_{ij}} \right)^6 + \frac{1}{4} \right] - \epsilon_a & s_{ij} \leq l_{ij} \\ -\frac{\epsilon_a}{2} \left[\cos \left(\frac{\pi(s_{ij} - l_{ij})}{R_{D0}} \right) + 1 \right] & l_{ij} < s_{ij} \leq l_{ij} + R_{D0} \\ 0 & l_{ij} + R_{D0} \leq s_{ij} \end{cases} \quad (11)$$

We obtained $\epsilon_a = 3.0 \pm 0.3 k_B T$ as fitted value in both investigated systems. This value seems reasonable as it should cause a significant slowdown of the dextrans' motion while still allowing a thermal escape out of the shells.

By tracking the tracer's trajectories, the mean square displacements can be calculated as:

$$\Delta s^2(t) = \langle (\vec{s}(t_0 + t) - \vec{s}(t_0))^2 \rangle \quad (12)$$

For a given sufficiently large elapsed time t , the long-time diffusion coefficients could then be extracted as:^{80,81}

$$D = \lim_{t \rightarrow \infty} \frac{1}{6} \frac{d}{dt} \Delta s^2(t) \quad (13)$$

such that the hindrance factors are D/D_0 .

For a given value of a , which sets the mean pore size, the hindrance factors for all tracer particles were calculated and this set of simulation data was compared to the experimental data. An optimal value for a was found by the best fit, using a as the single fitting parameter. Only in model 3b, ε_a was used as a second fitting parameter. For more technical details, see S11 (ESI†).

3. Results and discussion

The different experimental techniques used here allowed us to estimate the precision of the measurements in different ways. In MTI and NMR, the experiments are conducted by averaging over one gel, calculating therefore the dispersion of the data between different gels.

In MFIS we are able to detect two kinds of dispersion of the data: (i) we measured different spots within the same gel (pixelwise analysis) and (ii) we executed measurements between different gels (different data points in Fig. 12b).

It is known that the hydrogels in practice always exhibit an inhomogeneous cross-link density distribution, causing spatial heterogeneity.^{82,83} The scattering of experimental data from various independent measurements, beyond the shot noise limits of the single measurements, indicates the heterogeneity in the gel structure. Spatial heterogeneity on the macroscopic scale is detected by pixelwise analysis. Different locations within the same gel display slightly different results. These feature were visible in all MFIS studies reported below.

3.1. Several populations of guest molecules detected by MFIS

FCS. In contrast to the single diffusion times observed in solution, for most of the gel samples we have observed that up to three independent diffusion times are needed to fit the

FCS curves. Differently diffusing species, extending from free molecules just hindered by the limiting pore size ($t_d \sim 410 \mu\text{s}$) up to temporarily trapped particles ($t_d > 10 \text{ ms}$) were found (SI2–4, ESI†). Fig. 1a displays a set of image-integrated correlation curves for A488-D10 at different electrolyte conditions which reveal the decreasing fraction of slowly diffusing temporarily trapped particles for increasing salt concentration. Temporary sticking and accumulation of the probe molecules in the hydrogel are indicated by time trace analysis (Fig. 4a). Such tracer–hydrogel interactions already have been studied in the past, showing different effects depending on the chemical structure of the gel, the solvent and the nature of the tracer.^{21,25,27}

Interestingly, Vagias and coworkers²¹ also found interactions between the hydrogel and different tracers when employing FCS. Although they used another hydrogel than in our study, the different fluorescence intensity between gel and solution is clearly shown by them.

A simple binding model was applied to describe the observed equilibrium fractions of mobile and trapped probe molecules (x_{bound}), where f_{free} is the activity coefficient for free molecules and K_d' the effective binding constant (see S1.7, ESI†):

$$x_{\text{bound}} = \frac{f_{\text{free}} K_d'}{1 + f_{\text{free}} K_d'} \quad (14a)$$

It was assumed that the activity of the freely diffusing (mobile) species is most affected by the ionic strength of the solvent. The Debye–Hückel equation⁸⁴ describes the dependency of the activity coefficient, f_{free} , on the charge, Z_i , the effective radius of the ion, R_i , and the ionic strength, I , in the limit of low salt concentrations:

$$f_{\text{free}} = 10^{-\frac{AZ_i^2 \sqrt{I}}{1 + BR_i \sqrt{I}}} \quad (14b)$$

with tabulated values⁸⁴ for the constants $A = 0.507 \text{ mol}^{-1/2} \text{ dm}^{3/2}$ and $B = 3.28 \text{ nm}^{-1} \text{ mol}^{-1/2} \text{ dm}^{3/2}$ for aqueous solution at 22.5 °C. A combination of eqn (14a) and (14b) can be fit to the equilibrium fraction of trapped molecules as a function of the ionic strength. The fit shown in Fig. 1b yields $Z_i \approx 3$, which is in good agreement with the estimated mean number of

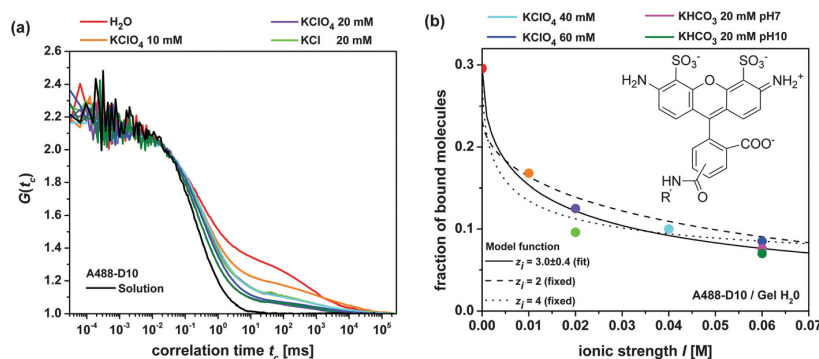


Fig. 1 (a) Image-integrated normalized correlation curves for A488-D10 in hydrogels at different salt conditions, (b) decreasing fraction of slow, temporarily bound molecules for A488-D10 in the hydrogel with increasing ionic strength I . A fit of eqn (14) yields $Z_i = 3.0 \pm 0.4$; $K_d' = 0.42 \pm 0.03$; $R_i = (0.7 \pm 0.5) \text{ nm}$. The inset shows one possible mesomeric structure and charge distribution of Alexa488.

3.2 Diffusion of macromolecules in a polymer hydrogel: from macroscopic to microscopic scales

View Article Online

PCCP

Paper

charges per labelled dextran, estimated as follows. D10 samples have ~ 5 labelling sites per molecule. The specified mean degree of labelling (DoL_{av}) of the investigated A488-D10 samples is 1, if the unlabelled dextran molecules are also considered. However, considering only labelled dextrans in a first approximation of random labelling, we can expect around 1.5 dyes per labelled and thus detected dextran (for more details of this calculation, see S1.3, ESI[†]), which corresponds to a mean charge $Z_i(\text{A488-D10}) \approx 3$. For the higher salt concentrations, the Debye length κ^{-1} is of the order of the macromolecule's dimension ($\kappa^{-1} \approx 1.4$ nm for $I = 0.05$ M), producing conditions beyond some of the approximations made to derive eqn (14b). Nevertheless, the fit shown in Fig. 1b describes the experimental data sufficiently well.

The analysis reveals that mainly the presence or screening of charges determine the sticking behavior of the probe molecules and not the kind of anion as suggested by the Hofmeister series.^{85,86} In particular, perchlorate, chloride or hydrogen carbonate ions at the same ionic strength had a comparable influence on the diffusion properties of the studied samples (see Fig. 1b).

Fluorescence anisotropy. To compare the restricted motion of A488-D10, TMR-D10 and FLU-D10 in the hydrogel to its behavior in solution, we performed measurements of steady state anisotropy r and time resolved anisotropy $r(t)$ for each pixel. For this, a possible distribution of r due to the heterogeneous environment needed to be separated from shot-noise broadening. Thus, a plot of r vs. number of detected photons, N_F , was analyzed (Fig. 2a), and the mean anisotropy, $\langle r \rangle$ was calculated:⁸⁷

$$r = \langle r \rangle \pm \frac{1}{3} \frac{(2 + \langle r \rangle) \sqrt{(1 - \langle r \rangle)(1 + 2\langle r \rangle)}}{\sqrt{N_F}} \quad (15)$$

It is clear that, on average, A488-D10 exhibits a higher anisotropy in the gel than in aqueous solution. This can be attributed to a temporary trapping of the solute in the matrix network. The plotted values for r in the gel are pixel-averages where

about 30% of molecules were trapped for this sample (Fig. 1b). During the measurement time of 1800 s, many probe transits are averaged, so that the anisotropy reports on the average trapping probability. In our samples different pixels display different anisotropies, so that the width of the distribution significantly exceeds the shot-noise broadening as found in the solution measurement. This can only be explained by the spatial heterogeneity of the hydrogel.

To study probe-polymer interactions inside the gel matrix, r measurements were performed for A488-D10 under different conditions (KClO_4 10 mM, 20 mM, 40 mM, 60 mM; KCl 20 mM; potassium carbonate buffer pH 7, 20 mM and pH 10, 20 mM, for TMR-D10 and FLU-D10 in H_2O , in potassium carbonate buffer 20 mM pH 10 and in Tris buffer 50 mM pH 7.5). The 2D r - N_F plots for all conditions are shown in S7 (ESI[†]). Fig. 3 shows the relation of the ratio of r in the hydrogel to r in different aqueous electrolyte solution and the fraction of trapped particles, x , which is directly calculated from FCS curves by applying eqn (4) (for values see Table S8, ESI[†]).

In a two-component system the additive behavior of anisotropies predicts a linear dependence of r_{gel} on the fraction of the trapped species x : $r_{\text{gel}} = x r_{\text{trapped}} + (1 - x) r_{\text{sol}}$. To take into account different initial solution anisotropies of the differently labeled probe molecules relative anisotropies $r_{\text{gel}}/r_{\text{sol}}$ are plotted in Fig. 3. By fitting a line to the data and using $r_{\text{sol}} = 0.037$ (Fig. 2) we estimate mean $r_{\text{trapped}} = 0.10 \pm 0.01$ for A488-D10. This is much less than the fundamental anisotropy of A488 ($r_0 = 0.37$) which would be expected for the completely immobilized dye. The low density of labels renders energy transfer between identical chromophores an unlikely cause for the reduced anisotropy, leaving partial mobility of the dye even in the trapped environment as most probable explanation.

Fluorescence time traces. Time-traces of A488-D10 at low concentration in the hydrogel were investigated to further analyze the sticking behavior (Fig. 4a). Temporary sticking and accumulation of the probe molecules in the hydrogel are indicated by relatively long dwell times (up to seconds) and count rates which are significantly above average, both of

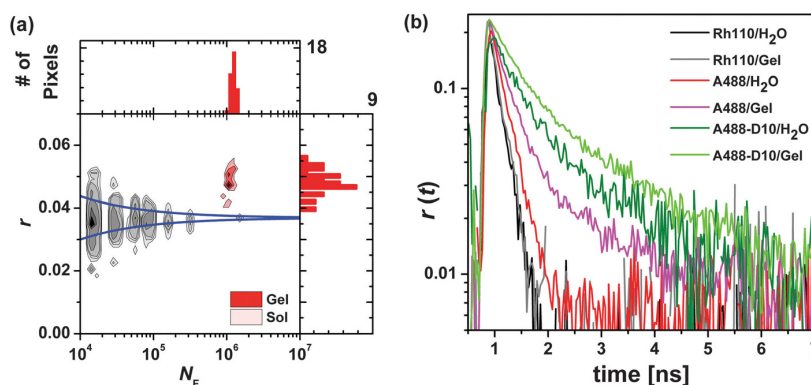


Fig. 2 (a) Anisotropy r vs. photon number N_F in different time windows for A488-D10 in water (gray contour lines) and in hydrogel (red contour lines) with one-dimensional projections for the gel data. The time window for the gel data was 1800 s. The theoretical shot-noise limits of r are calculated with eqn (15) with $\langle r \rangle = 0.037$ (blue lines). (b) Anisotropy decays, $r(t)$ for Rh110, A488 and A488-D10 in H_2O and gel/ H_2O .

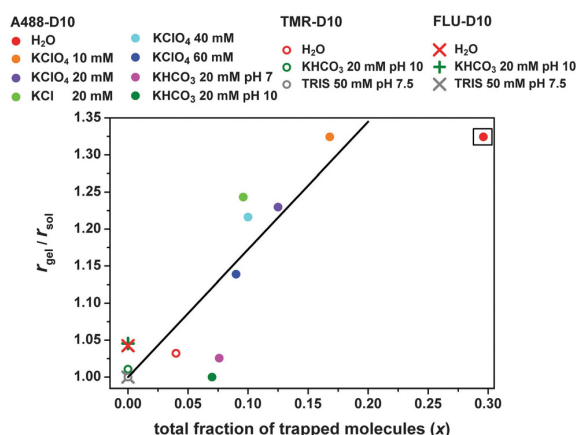


Fig. 3 Average anisotropy ratio, $r_{\text{gel}}/r_{\text{sol}}$ as a function of the fraction of trapped particles derived from FCS measurements for A488-D10 (see Fig. 1), TMR-D10 and FLU-D10. Linear extrapolation (without H₂O value) yields $r_{\text{gel}}/r_{\text{sol}} = 2.7 \pm 0.3$ for $x = 1$.

which are not observed for molecules freely diffusing in solution (Fig. 4a). A strong correlation between the fraction of the trapped molecules is revealed by the slow decay between 10 ms and several seconds and the mean count rate for this time range in the corresponding fluorescence correlation curves (Fig. 4b).

The interaction of A488-D10 with the matrix is revealed by several different observations: first, a reduction of the fluorescence lifetime ($\tau_{\text{gel}}/\tau_{\text{sol}} \approx 0.95$), mainly attributed to quenching since a change in radiative lifetime due to refractive index differences between gel and solvent is expected to only account for 1/3 of the effect ($\tau_{\text{r(gel)}}/\tau_{\text{r(sol)}} \approx 0.987$, see S1.6, ESI[†]),^{88,89} and, second, an increased anisotropy ($r_{\text{sol}} = 0.037$, $r_{\text{gel}} = 0.049$) with broadened distribution inside the gel (see Fig. 2 and 3). Third, the apparent brightness B_{app} of A488-D10 in the hydrogel, obtained as the ratio of detected count rate to the apparent number of particles N (taken from the FCS amplitude, eqn (4)), is significantly lower than B measured in solution ($B_{\text{app}}/B \approx 0.37$) which is not consistent with the weak dynamic quenching indicated by the small change in fluorescence lifetime. One possible explanation could be that a fraction of the molecules are

trapped on a longer time scale (> 1 min) which results in a virtually uncorrelated background reducing the correlation amplitude. Taking long term trapping into account for the highly interacting A488-D10, an effective concentration of trapping sites in the range from 10 to 50 nM can be deduced for low salt conditions (detailed discussion in the S1.4 and S1.5, ESI[†]). The observation of systematically higher fluorescence intensities inside the loaded gel than in the surrounding solution supports the idea of the enrichment of probe molecules in the gel (for details see S1.1 and S6, ESI[†]).

3.2. Mobile guest molecules

3.2.1. Experimental results

MFIS. As already discussed, the analysis of FCS correlation curves as displayed in Fig. 1a revealed different populations of guest molecules with differing diffusion times. In this section, we only consider the freely diffusing species with the smallest diffusion time. With MFIS, the hydrogel was studied in deionized water as well as in 20 mM potassium carbonate buffer at pH 10. Significantly different results were found for the two experimental conditions. These differences can be explained by a solvent dependent degree of swelling of the hydrogel (see sample details, Section 2.1.1). The diffusion coefficients from FCS experiments are shown in Table 3.

MTI. Fig. 5a shows an example set of fluorescence images at the beginning and the end of an MTI experiment of A488-D10 diffusing into a hydrogel disc. Due to the influx of fluorescent particles into the polymer hydrogel, the fluorescence intensity inside the hydrogel increases with time. A higher intensity inside the hydrogel is clearly visible at the end of the measurement. This indicates enhanced fluorescence of the dyes inside the gel and/or an attraction of the dye to the hydrogel. As expected, a variation of the particle concentration between 0.1 μM and 10 μM did not change the diffusion coefficient.

In these experiments the two faces of the hydrogel discs were not accessible to the solvent. Thus, the samples can be described as infinitely long cylinders in a reservoir of dye or dextran in solution, *i.e.* a quasi two-dimensional geometry with radial diffusion. Assuming azimuthally homogeneous diffusion, for every fluorescence image, the azimuthally averaged

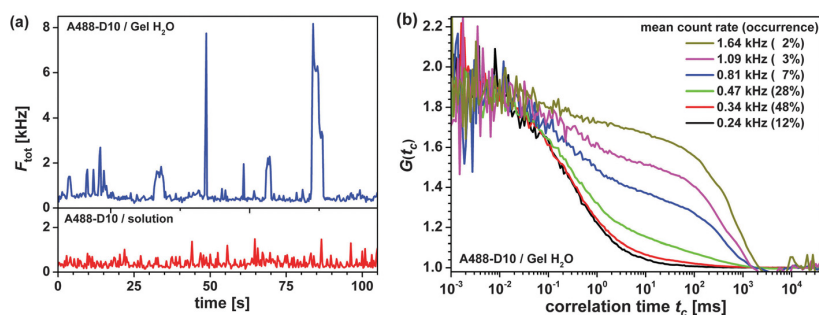


Fig. 4 (a) Fluorescence time traces (sum of perpendicular and parallel channel) for a single pixel in the image of A488-D10 in solution and in the gel in water conditions, (b) correlation curves of count rate selected subsets of the trace (for details see S5, ESI[†]).

3.2 Diffusion of macromolecules in a polymer hydrogel: from macroscopic to microscopic scales

View Article Online

PCCP

Paper

Table 3 Diffusion coefficients of free dye and dextran conjugates in solution, D_{sol} , and in the hydrogel, D_{gel} , at 22.5 °C

Sample	Dye ^a	M_w^b [kDa]	R_h^c [nm]	D_{sol} [10^{-6} cm ² s ⁻¹]	D_{gel} [10^{-6} cm ² s ⁻¹]
Free dye	A488	0.53	0.56	3.69 ± 0.05	2.7 ± 0.1
	TMR	0.39	0.56	3.45 ± 0.07	2.6 ± 0.1
	FLU	0.33	0.54	4.33 ± 0.09	3.9 ± 0.1
D3	A488	3	1.7 ± 0.1	1.05 ± 0.02	0.59 ± 0.02
	TMR			1.13 ± 0.02	0.62 ± 0.02
	FLU			1.45 ± 0.03	1.24 ± 0.04
D10	A488	10	3.1 ± 0.2	0.64 ± 0.01	0.32 ± 0.02
	TMR			0.99 ± 0.02	0.47 ± 0.02
	FLU			0.60 ± 0.02	0.54 ± 0.02
D40	TMR	40	6.0 ± 0.3	0.38 ± 0.01	0.10 ± 0.01
	FLU			0.32 ± 0.01	0.18 ± 0.03
D70	TMR	70	7.9 ± 0.4	0.33 ± 0.01	0.083 ± 0.004
D500	FLU	500	20 ± 2	0.107 ± 0.002	0.04 ± 0.02
D2000	TMR	2000	40 ± 4	0.068 ± 0.002	—
	FLU			0.060 ± 0.001	—

^a A488 and TMR samples measured in deionized water, FLU in 20 mM potassium carbonate buffer at pH10. ^b Molecular mass M_w as obtained from manufacturer. ^c Hydrodynamic radii R_h for free dyes are calculated from reported diffusion coefficients *via* Stokes–Einstein equation.^{90–93} R_h of dextran conjugates are obtained from a fitted Flory scaling law to our MFIS and NMR data (see Fig. 8). Errors for D_{sol} and D_{gel} are standard errors of the averages from multiple measurements, errors for R_h are 68% confidence intervals ($\pm 1\sigma$) from the fit.

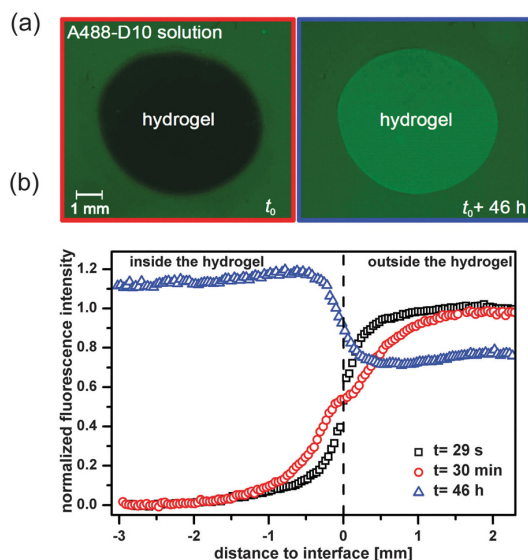


Fig. 5 (a) Example fluorescence images at the beginning (t_0) and the end of an experiment, (b) intensity–distance profiles for 29 s, 30 min and 46 h after contacting a cylindrical polymer hydrogel with A488-D10 solution.

intensity profiles were determined. Typical intensity–distance profiles for three times are displayed in Fig. 5b. The 46 h data illustrate that the fluorescence intensity in the gel is higher than in solution.

Diffusion equations for radial diffusion in an infinite cylinder with radius R_d suspended in an infinite reservoir with a diffusion coefficient D_{gel} yield a radial concentration profile $c(s,t)$ of the diffusing substance with the radial position s inside the infinite cylinder:⁹⁴

$$c(s,t) = c_\infty + \left(\frac{c_i - c_\infty}{2D_{\text{gel}}t} \right) e^{-\frac{s^2}{4D_{\text{gel}}t}} \int_0^{R_d} e^{-\frac{s'^2}{4D_{\text{gel}}t}} I_0 \left(\frac{ss'}{2D_{\text{gel}}t} \right) s' ds' \quad (16)$$

with the modified Bessel function of the first kind of order zero, I_0 , and the initial and final concentrations c_i and c_∞ , respectively.

Analysis of the complete concentration profiles is nontrivial because if the hydrogel edge is not perfectly perpendicular, this can lead to scattering and edge effects which will influence the shape of the measured concentration profiles. We thus first considered a more robust approach and analyzed the temporal increase in concentration in the center of the hydrogel. To enhance statistics, we averaged over an area of 0.2 mm by 0.2 mm in the center of the hydrogel. This area is small compared to the overall size of the gel ($R_d \approx 3.5$ mm). One typical dataset for the increase of A488-D10 in the center of a cylindrical hydrogel is shown in Fig. 6.

From eqn (16) an expression for $s = 0$ was derived:⁹⁴

$$c(t) = c_i + (c_\infty - c_i) e^{-\frac{R_d^2}{4D_{\text{gel}}(t+t_0)}} \quad (17)$$

An imperfectly perpendicular hydrogel edge and potential scattering from the gel edge will lead to a broadened start profile (Fig. 5). This was accounted for by adding a time-offset t_0 in eqn (17). This equation was fitted to the time evolution of the intensity in the center of the hydrogel. This resulted in very good agreement with the data (see Fig. 6). As the gel radius plays an important role in the determination of D_{gel} , we fitted all datasets with both the initial and the final radius (given in Section 2.3.2) and estimated D_{gel} to be between the values we get from these fits (Table 4).

Since the reservoir in the experiments was finite, the above model does not perfectly describe the experimental conditions. In the experiments, the volume of the solution surrounding the

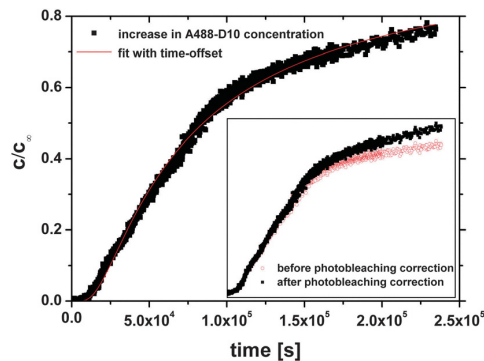


Fig. 6 Increase in A488-D10 concentration in the center of a hydrogel disc with time. The inset shows the original data (open circles) and the data after a photobleaching correction has been applied (closed squares).

Table 4 Diffusion coefficients of A488 free dye and dextran conjugates in the hydrogel at 23 °C measured by MTI. Errors for D_{gel} are standard errors of the averages from multiple measurements

Sample	Dye	D_{gel} [10^{-6} cm 2 s $^{-1}$]
Free dye	A488	3.2 ± 0.1
D3	A488	0.73 ± 0.02
D10	A488	0.42 ± 0.01

gel was about 11 times the cylinder volume. This should result in a homogeneous final dye concentration $c_{\infty} \approx 0.92c_i$ in both the gel and reservoir. This has not been observed (Fig. 5). Thus we considered a second model; diffusion into a cylinder from a stirred solution of limited volume.⁹⁴ The fitting results from this model were compared to those from the above model (eqn (16)). The second model was found to describe the data for short and intermediate measurement times, but failed to describe the long time behavior. The model suggests that saturation between cylinder and reservoir should be achieved much faster than seen in the experiments. This discrepancy could be due to an attractive interaction between the hydrogel and the diffusing molecules as indicated by the MFIS experiments. In line with this idea is the observation that for all measurements with Alexa-labelled particles, the fluorescence intensity of the hydrogel was higher than that of the surrounding solution at the end of the measurement (Fig. 5). If the particles are attracted to the hydrogel, they will preferentially diffuse into the gel even after the concentration difference between gel and reservoir is balanced. This corresponds to a larger effective reservoir as described by eqn (16), which is based on an infinite reservoir.

NMR. Diffusion coefficients of unlabelled dextrans in D₂O and inside the hydrogel were extracted from the NMR measurements using eqn (7) to fit the echo amplitudes. For D40 in the hydrogel, one typical decay curve and the corresponding fit using eqn (7) is shown in Fig. 7 (for more details see S10, ESI†).

Very good agreement between experimental data and the fit can be observed. The resulting diffusion coefficients (average of three measurements with varying gradient length) are shown in Table 5.

Summary. Although all applied techniques probe different length scales of the sample, for the same conditions they yield

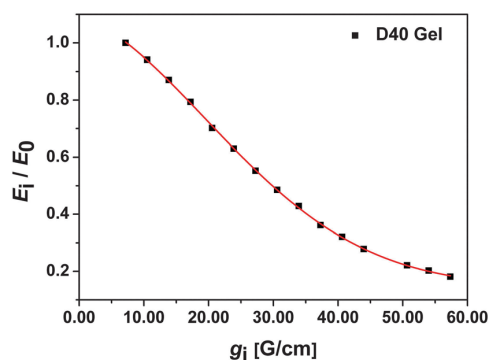


Fig. 7 NMR data and fit using eqn (7) for unlabelled dextrans (40 kDa) in the hydrogel. The data was normalized.

Table 5 Diffusion coefficients of unlabelled dextran in solution, D_{solution} , and in the hydrogel, D_{gel} , at 23 °C measured by NMR

Sample	Dye	R_h^a [nm]	D_{solution} [10^{-6} cm 2 s $^{-1}$]	D_{gel} [10^{-6} cm 2 s $^{-1}$]
D3	unl.	1.7 ± 0.1	1.37 ± 0.01	0.80 ± 0.01
D10	unl.	3.1 ± 0.2	1.158 ± 0.003	0.38 ± 0.01
D40	unl.	6.0 ± 0.3	0.451 ± 0.003	0.110 ± 0.003

^a Hydrodynamic radii R_h from D_{solution} (free dye) or fitted power law (dextran conjugates, from experimental data, see Table 3). Errors for D_{solution} and D_{gel} are standard errors of the averages from multiple measurements, errors for R_h are 68% confidence intervals ($\pm 1\sigma$) from the fit.

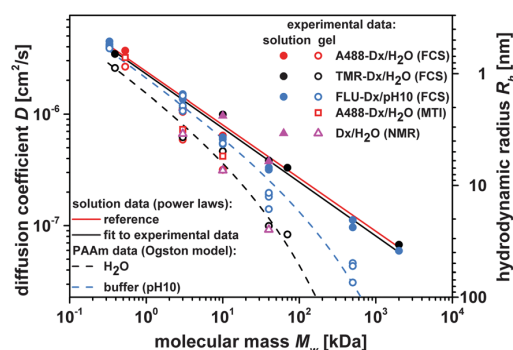


Fig. 8 Experimental diffusion coefficients D at 22.5 °C and (for solution data) hydrodynamic radii R_h for equivalent spheres as estimated by the Stokes–Einstein equation. Solution data (filled symbols) were approximated by the Flory scaling law (red line, R_h [nm] = $(1.01 \pm 0.07) \times (M_w$ [kDa]) $^{0.48 \pm 0.02}$), and compared to reference data (black line, R_h [nm] = $(0.96 \pm 0.13) \times (M_w$ [kDa]) $^{0.48 \pm 0.04}$, see S9, ESI†)^{90,95,96} Dashed lines represent fits of the Ogston model (black: H₂O, blue: buffered solution at pH 10; for parameters see Table 6) to the gel data (open symbols).

remarkably consistent diffusion coefficients, which are displayed in Fig. 8. Fits to the Flory scaling law were used to determine the hydrodynamic radii R_h (also see S9, ESI†) of the dextrans in solution. As expected, the diffusion coefficients of all our guest molecules decay markedly with increasing molecular weight and the results for all methods agree quantitatively. The heterogeneity in the gel structure is indicated by the scatter of the gel data around the fit curve from various independent measurements beyond the shot noise limit.

3.2.2. Comparison with Ogston theory. Besides adsorption or temporary binding phenomena, the hindrance of diffusion, *i.e.* a reduction of the macroscopic diffusion coefficient inside the matrix with respect to the bulk diffusion coefficient is a fundamental property characterizing the transport behavior of particles within the matrix. Diffusion of solutes inside the pores has been approximated by many models.^{97–99} Here we applied a simple fiber network theory. This model goes back to Ogston *et al.*³⁵ and describes a hydrogel as a network of randomly distributed fibers. Based on this model, the hindrance factor is

$$H = \exp\left(-\sqrt{\phi\left(1 + \frac{R_h}{R_f}\right)^2}\right) \quad (18)$$

3.2 Diffusion of macromolecules in a polymer hydrogel: from macroscopic to microscopic scales

View Article Online

PCCP

Paper

where R_f is the radius and φ the volume fraction of the fibers in the gel and R_h the hydrodynamic radius of the diffusing species.

The important assumptions behind this model are known: (i) the solute/fiber interaction is purely hard-sphere in nature, (ii) the fibers are infinitely long and were placed randomly in the matrix, and (iii) the solute concentration is very low, so that solute–solute interactions are negligible in both phases. It is clear that such approach can only be a crude approximation of the real physical effects that are governing the translocation in the matrix in our system. Nevertheless, Ogston's model yields a convenient and simple analytic expression to analyze fundamental trends. Moreover, such approach implies the use of effective parameters, permitting in terms of the volume fraction (φ), to obtain reasonable results in comparison to the experimental values as estimated from analysis of the swelling behavior (see Section 2.1.1).

As expected and shown in Fig. 8, the diffusion coefficient D decreases with dextran size, with the decrease being more pronounced in the gel. Thus, the hindrance factor, $H = D_{\text{gel}}/D_{\text{sol}}$, will also decrease with increasing hydrodynamic radius R_h of the dextrans (see Fig. 12).

Dashed lines in Fig. 8 represent the curves calculated with the Ogston model (eqn (18)) using the fit parameters listed in Table 6.

Table 6 Results from fitted model function with standard errors and the experimentally determined polymer volume fraction (φ in the swollen hydrogel)

		TMR-Dx/H ₂ O	FLU-Dx/pH 10
Fiber network model (eqn (18))	φ (exp.)	0.0390 ± 0.0004	0.0150 ± 0.0001
	φ	0.06 ± 0.03	0.005 ± 0.007
	R_f [nm]	1.4 ± 0.5	1.3 ± 1.1

The agreement with our data is already very good. Using newer, comparable models (such as the Amsden-model⁹⁷) did not noticeably improve agreement with our data (thus not shown in Fig. 8).

3.2.3. Comparison with Brownian dynamics simulations.

While the Ogston model provides a simple analytical formula to describe the trends for the dextran dynamics with an effective excluded volume, we now apply our Brownian dynamics simulations (see Section 2.4) for a more detailed modeling approach. Different approaches to model a hydrogel have been used in previous works. When investigating the swelling behavior of a gel, Linse and coworkers^{36–39} and Holm and coworkers^{40–42} resolved the individual monomers of the gel network. However the dynamics of tracer particles through the network was not performed within this level of modelling. Addressing tracer motion within monomer-resolved modelling requires much more computational resources in particular for long-time diffusion. Also the fitting procedure would require several sets of runs. Therefore we leave monomer-resolved studies to future work. Instead we decided to follow the more coarse-grained approach by Zhou and Chen.⁴⁷ This type of modeling provides a simple and systematic framework in which to include different physical effects, namely the mobility of the matrix particles (*i.e.* fluctuations in the matrix structure), the effective dextran–matrix excluded volume, and sticky attractions. The matrix-dextran interactions are expected to play a key role in spreading the delay times of the diffusive process of the dextran molecules through the matrix. Fig. 9 shows schematic two-dimensional representations of the three-dimensional simulations on the three different levels that were used to explain the experimental data.

In qualitative terms, one would expect increasing agreement between the simulation and experimental data as we increase

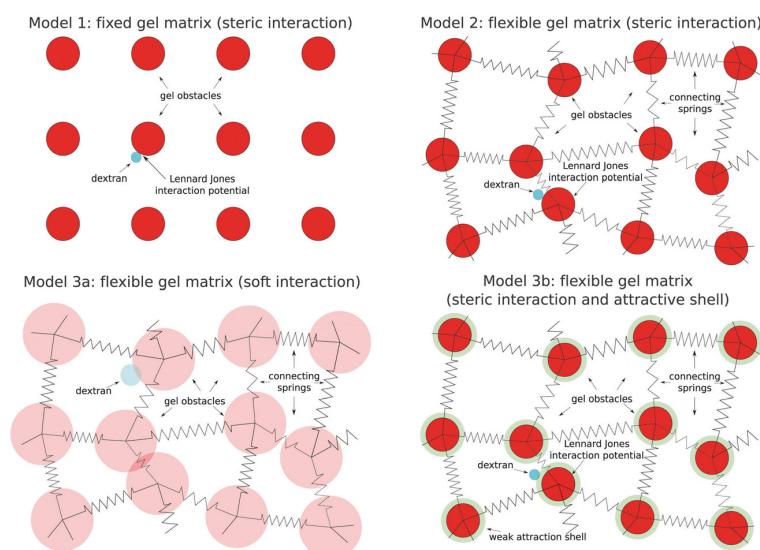


Fig. 9 Four models for the dextran–matrix system. Model 1: fixed gel matrix (steric interaction, eqn (8)), model 2: flexible gel matrix (steric interaction, eqn (8)), model 3a: flexible gel matrix (soft interaction, eqn (10)) and model 3b: flexible gel matrix (steric interaction and attractive shell, eqn (11)). The sketches illustrate two-dimensional representations of the three-dimensional models used for the simulations.

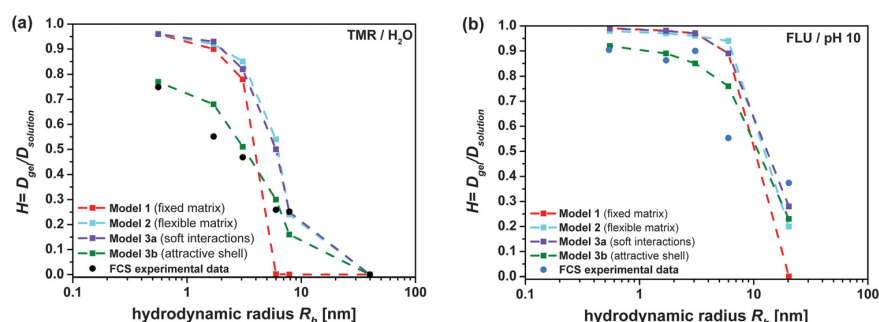


Fig. 10 Comparison between FCS experimental data and Brownian dynamic simulations with 4 different models for TMR-dextran in water conditions (a) and FLU-dextran in 20 mM potassium carbonate buffer at pH 10 (b).

the level of complexity. This is indeed what is observed and displayed in Fig. 10, where the different simulation results are compared to FCS data. In model 1, hard matrix particles are fixed on simple cubic lattice sites, providing a uniform matrix with just one pore size. This results in a very sharp drop in the hindrance factor when the dextran's size is increased to this pore size. Introducing elastically connected matrix particles (model 2) broadens the pore size distribution and leads to a slower decrease of the hindrance factors with dextran size, as expected. However, this decrease is still too sharp compared to the experimental data. Softening the interactions by changing the interaction potentials from WCA to a Gaussian potential (model 3a) shows an even lower, yet still too distinct decrease, of the hindrance factor with increasing dextran size. The agreement is still unsatisfactory. Especially the hindrance of the smaller dextrans is too weak in the previous approaches. When these small dextrans collide with matrix particles, they can easily find another way to pass due to their small size.

The introduction of an attractive contribution in the matrix-guest interaction (model 3b) is found to be crucial to describe the observed slow decay with increasing dextran sizes. If the smaller dextrans collide with matrix particles in this model, they can still find another path to pass. However, they are more likely to first become stuck resulting in a slowdown even for small dextrans.

Model 3b is the only one which includes a repulsive interaction and an attractive shell and it is the best representation of our experimental data. Additional simulations performed within model 3b using a Gaussian softened core showed a similar fit quality as that with a WCA-core. The results show that, within the framework of the model classes considered here, an effective attraction is needed to describe the spreading of the dynamics correctly given the statistical uncertainties of the experimental data. The origin of this attraction still needs to be resolved. For specific simulation parameters see the Table S11 (ESI[†]).

3.3. Estimation of the average pore size

The theoretical study permits an estimation of the average pore size of the investigated hydrogel in the two experimental environments. We optimized for the *a priori* unknown average pore size by fitting the simulated hindrance factors to the experimental data. Since the positions of all matrix particles in the BD-simulation

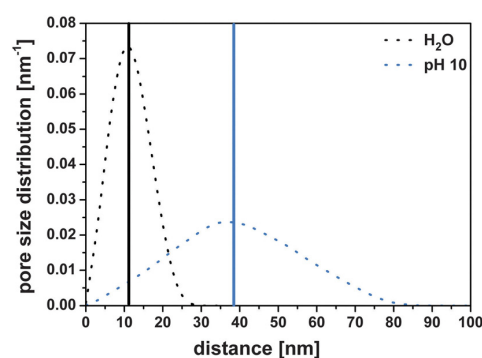


Fig. 11 The distribution of the free space between connected matrix particles (dots) in the BD simulation and the average pore size (bars) of the polymer matrix in both experimental conditions. It is based on the final set of parameters after the fit within the applied model 3b. Black dots correspond to H₂O, blue dots to 20 mM potassium carbonate buffer at pH 10 (for details see text).

are known, one can estimate the size of a specific pore in the gel as the center-to-center distance of two neighboring matrix-particles minus the matrix-particle-diameter. The decision which matrix particle pairs have to be counted as 'neighbors', is subject to a certain degree of arbitrariness. We chose to consider all particle pairs that are connected with springs, therefore possibly overestimating the correct value by neglecting close, but unconnected, matrix particle-pairs. Fig. 11 shows this distribution for both investigated conditions calculated using model 3b.

We obtained an average value of 11 ± 1 nm for gels in water and 38 ± 3 nm for gels in buffer at pH 10 for the final set of parameters after the fit. While this average pore size is an output from fitting the simulated hindrance factors to the experimental data, the shape of the distribution is rather an input as the width of this distribution (standard deviation $\sigma = 5$ nm for water, $\sigma = 16$ nm for pH 10 in Fig. 11) scales with the average value as defined in the models. The average values are in the same order of magnitude as calculated from swelling experiments, where we estimated 5.7 nm and 7.8 nm, respectively, assuming ideal solvent quality, homogeneous cross-linking densities and Gaussian distribution of chain lengths (see Section 2.1.1). In H₂O both results differ by less than a factor of 2.

3.2 Diffusion of macromolecules in a polymer hydrogel: from macroscopic to microscopic scales

View Article Online

PCCP

Paper

We now compare the results of our gel ($[T] = 0.04 \text{ g ml}^{-1}$, $C_R = 0.035$), obtained in water conditions, with literature values for gels with similar composition. Significant discrepancy between pore size values resulting from scanning electron microscopy SEM (10–20 μm)^{32–34} and swelling analysis (2.0 nm) was reported.³³ When using SEM, the structure of the gel may become damaged during the freeze-drying processes, resulting in systematically too large pore sizes. In our study, we measured under native conditions without disturbing the gel matrix structure thus circumventing this problem.

In gel electrophoresis with DNA as a cylindrical tracer molecule,^{23,30,31} pore sizes between 5.9 and 133 nm are reported for gels with similar composition to ours. The hydrodynamic radius of the DNA was not measured directly but calculated using different models which is known to be an intrinsic problem. Approximating DNA by a sphere becomes more reasonable for shorter DNA molecules. Therefore it is notable, that the electrophoresis study using the shortest DNA³⁰ matches our result the best.

Very early work of polyacrylamide gels, using electrophoresis of proteins²⁹ in phosphate buffer, pH 7 ($[T] = 0.06 \text{ g ml}^{-1}$, $C_R = 0.05$) and chromatography of proteins²⁸ in water ($[T] = 0.065 \text{ g ml}^{-1}$, $C_R = 0.02$) agree well with our results, yielding 8.5 nm and 2.25 nm, respectively. In addition, recent studies⁹⁶ based on dynamic light scattering revealed mesh sizes of the same order of magnitude for polyacrylamide hydrogels of about 15 nm and for poly(*N*-isopropylacrylamide) of about 19 nm.

4. Combined results and conclusions

All data for the hindrance factor H obtained from the three different and independent methods we have applied are displayed and compared to Brownian dynamics simulations performed with model 3b in Fig. 12. For the MTI measurements, the average values of D_{sol} from NMR and MFIS were used to scale the data, as they could not be measured with this technique.

We have shown that the long time diffusion coefficients of dextran molecules moving in solution and in a polyacrylamide gel

matrix determined on different length scales by using multiparameter fluorescence image spectroscopy (MFIS), macroscopic transmission imaging (MTI) and nuclear magnetic resonance (NMR) are consistent. The measured diffusion coefficients decrease with increasing molecular weight and fall on a master curve. This supports the reliability of our data set, which might thus serve as possible calibration data for future experiments and theories.

In addition, although our results could be described by the Ogston model (Fig. 12), a more realistic model of a flexible gel matrix was applied to describe the experimental data and to estimate the average pore size in the gel. The simulated average pore sizes of 11 nm (water) and 38 nm (pH 10) agree reasonably well with estimations from swelling theory of 5.7 nm and 7.8 nm, respectively. Within the experimental error bars and the limitations of the applied models, our results for the gel equilibrated in water are in good agreement with published studies employing comparable globular macromolecular probes (2.25 nm²⁸ or 8.5 nm²⁹) as well as with light scattering investigations (15 nm)⁹⁶ in native gels with similar composition.

Combining experiments and simulations enabled us to achieve a better understanding of the effects determining the diffusion of molecules in the gel network. Moreover, using the MFIS method, a significant interaction between hydrogel and macromolecules was observed, in particular for A488 samples. The MTI results support the idea of the attractive interaction of Alexa-labelled particles and the gel, showing that the fluorescence intensity in the hydrogel was higher than that of the surrounding solution at the end of the measurements. This suggests to use uncharged dyes or, in case of charged dyes, to add a sufficiently high salt concentration for future investigations.

The heterogeneity inside a single hydrogel sample was probed on a length scale of 10 μm in anisotropy experiments by comparing different pixels and hence different positions in the hydrogel (Fig. 2). Furthermore, for the experiments at pH 10, the scattering of data from various independent samples in Fig. 12b was significantly beyond shot noise limits (or other experimental uncertainties), revealing a heterogeneity, which persisted over the complete measurement times.^{82,83}

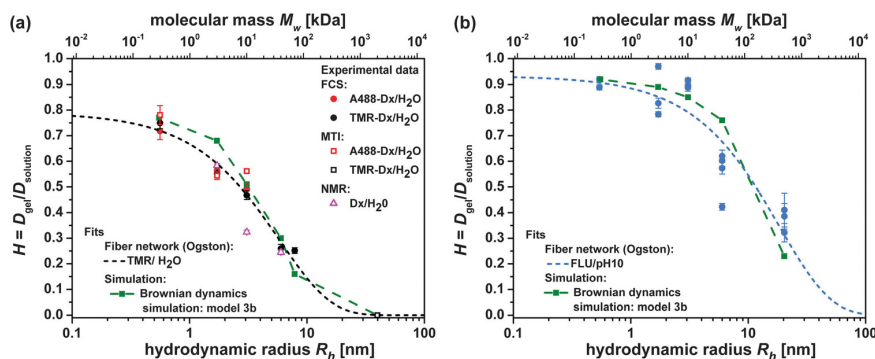


Fig. 12 Hindrance factors $H = D_{\text{gel}}/D_{\text{sol}}$ of dextrans in hydrogel. A488 (red), TMR (black) and unlabelled samples (magenta) measured in deionized water (a), FLU labelled samples (blue) measured in 20 mM potassium carbonate buffer at pH 10 (b). Experimental data: FCS (filled circles); MTI (open squares); NMR (open triangles); fitted model function: fiber network (eqn (18), dashed black and blue lines, parameters Table 6) and Brownian dynamics simulation (green points). The errors are the standard errors of repeat measurements.

Despite our application of a wide range of methods and the general consistency of the results we have obtained, open questions remain. For example, while the hindrance factor in the limit of small tracer particle sizes tends to 1 in our FLU/pH 10 system, it seems to approach ~ 0.8 in our TMR/H₂O system (Fig. 12). A value close to 1 might still be approached for smaller tracer particles in our H₂O system, but we could not investigate these in our study due to experimental limitations. If one assumes that there really is a difference for smaller tracer molecules, the question whether this is due to different swelling in different environments or caused by different interactions of the matrix with different dyes cannot be answered with certainty yet.

For future studies, the diffusion of the same dextran molecules with the same dyes in differently crosslinked matrices should be explored systematically in order to distinguish between different modes governing the translocation.

Abbreviations

Mass concentration of polymeric material in total volume	[T]
Weight fraction of cross-linker with respect to the total mass of the polymeric material	C_R
Diffusion time	t_d
Gel disk radius	R_d
Volume dry polymer	V_p
Volume gel after swelling	V_{gel}
Mass	m
Water density	$\rho_{\text{H}_2\text{O}}$
Polymer density	ρ_p
Polymer volume fraction in the swollen state	φ
Molecular weight of the polymer between cross-links points	M_c
Molecular weight of the repeating units	M_r
Polymer mesh size	ξ
Cross-linking degree in the hydrogel	X
Carbon-carbon bond length	ζ
Flory characteristic ratio	C_n
Numerical aperture	NA
Detection volume in MFIS	V_{det}
Temperature	T
Diffusion coefficient	D
Gradient pulse width	δ
Diffusion delay	Δ_N
FCS fit model function	$G(t_c)$
Triplet time	t_T
Triplet amplitude	A_T
Correlation time	t_c
Confocal volume radius in x and y	ω_0
Confocal volume radius in z	z_0
Detection probability	$w(x,y,z)$
Number of molecules	N
Molecular fraction	x_i
Position coordinates	x, y, z
Fluorescence intensity	$F, F_{\parallel}, F_{\perp}$

Polarization correction factors	l_1, l_2
Fluorescence anisotropy of species i	r_i
G -Factor	G
Intensity fit parameters in MTI	P, p, Q, q
Echo intensities	E_i, E_0
Gyromagnetic ratio	γ
Gradient amplitude at increment i	g_i
Delay between pulses	τ_N
Boltzmann constant	k_B
Lattice constant	a
Distance in simulations models	s_{ij}
Radius	R
Hydrodynamic radius	R_h
Matrix particle radius	R_{obst}
Position of particles in simulations models	\vec{s}
Mean square displacement	Δs^2
Time, reference time	t, t_0
Potential between i and j particles	U_{ij}
Energy steric constant	e_s
Energy Gaussian constant	e_G
Energy attractive constant	e_a
Constant in simulations models	b
Additive diameter	σ_{ij}
Position of minimum in simulations models	l_{ij}
Hindrance factor	H
Charge	Z_i
Effective binding constant	K_d'
Ionic strength	I
Effective ion radius	R_i
Activity	a_i
Concentration	c_i
Activity coefficient	f_i
Debye-Hückel constants	A, B
Debye length	κ^{-1}
Photon number	N_F
Fluorescence lifetime of species i	τ_i
Radiative lifetime of species i	$\tau_{r,i}$
Bessel function	I_0
Radial position inside an infinity cylinder for MTI fit	s, s'
Fiber radius	R_f

Acknowledgements

C. J., H. L., S. U. E., and C. A. M. S. gratefully acknowledge partial financial support from the Strategic Research Fund of the HHU. Additional funding was given to D. W. by BioSoft and to C. E. S. and H. L. by the ERC Advanced Grant INTERCOCOS (grant agreement 267499).

References

- 1 S. T. Balke, A. E. Hamielec, B. P. LeClair and S. L. Pearce, *Ind. Eng. Chem. Prod. Res. Dev.*, 1969, **8**, 54–57.
- 2 F. Chen, P. Tillberg and E. Boyden, *Science*, 2015, **347**, 543–548.

3.2 Diffusion of macromolecules in a polymer hydrogel: from macroscopic to microscopic scales

View Article Online

PCCP

Paper

- 3 V. E. Barsky, A. M. Kolchinsky, Y. P. Lysov and A. D. Mirzabekov, *Mol. Biol.*, 2002, **36**, 437–455.
- 4 T.-O. Peulen and K. J. Wilkinson, *Environ. Sci. Technol.*, 2011, **45**, 3367–3373.
- 5 S. Brahim, D. Narinesingh and A. Guiseppi-Elie, *Biomacromolecules*, 2003, **4**, 1224–1231.
- 6 N. Murthy, Y. X. Thng, S. Schuck, M. C. Xu and J. M. J. Fréchet, *J. Am. Chem. Soc.*, 2002, **124**, 12398–12399.
- 7 P. Gupta, K. Vermani and S. Garg, *Drug Discovery Today*, 2002, **7**, 569–579.
- 8 R. Morita, R. Honda and Y. Takahashi, *J. Controlled Release*, 2000, **68**, 115–120.
- 9 S. Sershen and J. West, *Adv. Drug Delivery Rev.*, 2002, **54**, 1225–1235.
- 10 D. T. Eddington and D. J. Beebe, *Adv. Drug Delivery Rev.*, 2004, **56**, 199–210.
- 11 O. Wichterle and D. Lim, *Nature*, 1960, **185**, 117–118.
- 12 H.-W. Kang, Y. Tabata and Y. Ikada, *Biomaterials*, 1999, **20**, 1339–1344.
- 13 A. S. Hoffman, *Adv. Drug Delivery Rev.*, 2002, **54**, 3–12.
- 14 A. Z. Abidin, T. Puspasari and W. A. Nugroho, *Procedia Chem.*, 2012, **4**, 11–16.
- 15 R. Zolfaghari, A. A. Katbab, J. Nabavizadeh, R. Y. Tabasi and M. H. Nejad, *J. Appl. Polym. Sci.*, 2006, **100**, 2096–2103.
- 16 A. Meller, *J. Phys.: Condens. Matter*, 2003, **15**, R581.
- 17 A. Milchev, *J. Phys.: Condens. Matter*, 2011, **23**, 103101.
- 18 R. Metzler and J. Klafter, *Phys. Rep.*, 2000, **339**, 1–77.
- 19 F. Höfling and T. Franosch, *Rep. Prog. Phys.*, 2013, **76**, 046602.
- 20 K. Mecke, *Acta Phys. Pol., B*, 1997, **28**, 1747–1782.
- 21 A. Vagias, R. Raccis, K. Koynov, U. Jonas, H.-J. Butt, G. Fytas, P. Košován, O. Lenz and C. Holm, *Phys. Rev. Lett.*, 2013, **111**, 088301.
- 22 L. Haggerty, J. H. Sugarman and R. K. Prud'homme, *Polymer*, 1988, **29**, 1058–1063.
- 23 D. L. Holmes and N. C. Stellwagen, *Electrophoresis*, 1991, **12**, 253–263.
- 24 M. Kremer, E. Pothmann, T. Rössler, J. Baker, A. Yee, H. Blanch and J. M. Prausnitz, *Macromolecules*, 1994, **27**, 2965–2973.
- 25 J. Tong and J. L. Anderson, *Biophys. J.*, 1996, **70**, 1505–1513.
- 26 S. M. Russell and G. Carta, *Ind. Eng. Chem. Res.*, 2005, **44**, 8213–8217.
- 27 A. Stellwagen and N. C. Stellwagen, *Biopolymers*, 1990, **30**, 309–324.
- 28 J. S. Fawcett and C. J. O. R. Morris, *Sep. Sci.*, 1966, **1**, 9–26.
- 29 M. P. Tombs, *Anal. Biochem.*, 1965, **13**, 121–132.
- 30 N. C. Stellwagen, *Biochemistry*, 1983, **22**, 6186–6193.
- 31 D. L. Holmes and N. C. Stellwagen, *Electrophoresis*, 1991, **12**, 612–619.
- 32 R. Rüchel and M. D. Brager, *Anal. Biochem.*, 1975, **68**, 415–428.
- 33 L. M. Lira, K. A. Martins and S. I. C. D. Torresi, *Eur. Polym. J.*, 2009, **45**, 1232–1238.
- 34 Z. Blank and A. C. Reimschuessel, *J. Mater. Sci.*, 1974, **9**, 1815–1822.
- 35 A. G. Ogston, B. N. Preston and J. D. Wells, *Proc. R. Soc. London, Ser. A*, 1973, **333**, 297–316.
- 36 S. Schneider and P. Linse, *Macromolecules*, 2004, **37**, 3850–3856.
- 37 S. Edgecombe, S. Schneider and P. Linse, *Macromolecules*, 2004, **37**, 10089–10100.
- 38 S. Schneider and P. Linse, *J. Phys. Chem. B*, 2003, **107**, 8030–8040.
- 39 S. Schneider and P. Linse, *Eur. Phys. J. E: Soft Matter Biol. Phys.*, 2002, **8**, 457–460.
- 40 B. A. F. Mann, K. Kremer, O. Lenz and C. Holm, *Macromol. Theory Simul.*, 2011, **20**, 721–734.
- 41 B. A. Mann, C. Holm and K. Kremer, *J. Chem. Phys.*, 2005, **122**, 154903.
- 42 B. A. Mann, R. Everaers, C. Holm and K. Kremer, *EPL*, 2004, **67**, 786.
- 43 P. A. Netz and T. Dorfmueller, *J. Chem. Phys.*, 1997, **107**, 9221–9233.
- 44 H. Pei, S. Allison, B. M. H. Haynes and D. Augustin, *J. Phys. Chem. B*, 2009, **113**, 2564–2571.
- 45 L. Johansson and J. E. Löfroth, *J. Chem. Phys.*, 1993, **98**, 7471–7479.
- 46 P. Licinio and A. V. Teixeira, *Phys. Rev. E: Stat. Phys., Plasmas, Fluids, Relat. Interdiscip. Top.*, 1997, **56**, 631–634.
- 47 H. Zhou and S. B. Chen, *Phys. Rev. E: Stat., Nonlinear, Soft Matter Phys.*, 2009, **79**, 021801.
- 48 K. Kremer, *Comput. Mater. Sci.*, 1998, **10**, 168–174.
- 49 R. Messing, N. Frickel, L. Belkoura, R. Strey, H. Rahn, S. Odenbach and A. M. Schmidt, *Macromolecules*, 2011, **44**, 2990–2999.
- 50 D. A. Carr and N. A. Peppas, *Macromol. Biosci.*, 2009, **9**, 497–505.
- 51 F. Ganji, S. Vasheghani-Farahani and E. Vasheghani-Farahani, *Iran. Polym. J.*, 2010, **19**, 375–398.
- 52 H. Durchschlag and P. Zipper, in *Ultracentrifugation*, ed. M. D. Lechner, Steinkopff, 1994, ch. 3, vol. 94, pp. 20–39.
- 53 J. Jovanovic and B. Adnadjevic, *Polym. Bull.*, 2007, **58**, 243–252.
- 54 M. K. Krušić, M. Ilić and J. Filipović, *Polym. Bull.*, 2009, **63**, 197–211.
- 55 A. M. Lowman and N. A. Peppas, *Macromolecules*, 1997, **30**, 4959–4965.
- 56 A. Thakur, *Chem. Biochem. Eng. Q.*, 2011, **25**, 181.
- 57 S. Weidtkamp-Peters, S. Felekyan, A. Bleckmann, R. Simon, W. Becker, R. Kühnemuth and C. A. M. Seidel, *Photochem. Photobiol. Sci.*, 2009, **8**, 470–480.
- 58 Y. Stahl, S. Grabowski, A. Bleckmann, R. Kühnemuth, S. Weidtkamp-Peters, K. G. Pinto, G. K. Kirschner, J. B. Schmid, R. H. Wink, A. Hülsewede, S. Felekyan, C. A. M. Seidel and R. Simon, *Curr. Biol.*, 2013, **23**, 362–371.
- 59 D. Wagner, M. Börgardt, C. Grünzweig, E. Lehmann, T. J. J. Müller, S. U. Egelhaaf and H. E. Hermes, *Rev. Sci. Instrum.*, 2015, **86**, 093706.
- 60 M. Holz, S. R. Heil and A. Sacco, *Phys. Chem. Chem. Phys.*, 2000, **2**, 4740–4742.
- 61 A. L. van Geet, *Anal. Chem.*, 1970, **42**, 679–680.

- 62 D. H. Wu, A. D. Chen and C. S. Johnson, *J. Magn. Reson., Ser. A*, 1995, **115**, 260–264.
- 63 G. Wider, V. Dötsch and K. Wüthrich, *J. Magn. Reson., Ser. A*, 1994, **108**, 255–258.
- 64 V. Sklenar, M. Piotto, R. Leppik and V. Saudek, *J. Magn. Reson., Ser. A*, 1993, **102**, 241–245.
- 65 M. Piotto, V. Saudek and V. Sklenář, *J. Biomol. NMR*, 1992, **2**, 661–665.
- 66 P. Sengupta, K. Garai, J. Balaji, N. Periasamy and S. Maiti, *Biophys. J.*, 2003, **84**, 1977–1984.
- 67 P. O. Gendron, F. Avaltroni and K. J. Wilkinson, *J. Fluoresc.*, 2008, **18**, 1093–1101.
- 68 J. Enderlein, I. Gregor, D. Patra, T. Dertinger and U. B. Kaupp, *ChemPhysChem*, 2005, **6**, 2324–2336.
- 69 J. Enderlein, I. Gregor, D. Patra and J. Fitter, *Curr. Pharm. Biotechnol.*, 2004, **5**, 155–161.
- 70 M. Koshioka, K. Sasaki and H. Masuhara, *Appl. Spectrosc.*, 1995, **49**, 224–228.
- 71 N. B. Vicente, J. E. Diaz Zamboni, J. F. Adur, E. V. Paravani and V. H. Casco, *J. Phys.: Conf. Ser.*, 2007, **90**, 012068.
- 72 L. Hodgson, P. Nalbant, F. Shen and K. Hahn, *Methods Enzymol.*, 2006, **406**, 140–156.
- 73 D. Wagner, J. Burbach, C. Grünzweig, E. Lehmann, S. U. Egelhaaf and H. E. Hermes, unpublished work.
- 74 W. S. Price, *Concepts Magn. Reson.*, 1997, **9**, 299–336.
- 75 C. S. Johnson Jr., *Prog. Nucl. Magn. Reson. Spectrosc.*, 1999, **34**, 203–256.
- 76 F. J. Millero, R. Dexter and E. Hoff, *J. Chem. Eng. Data*, 1971, **16**, 85–87.
- 77 P. G. Bolhuis, A. A. Louis, J. P. Hansen and E. J. Meijer, *J. Chem. Phys.*, 2001, **114**, 4296–4311.
- 78 A. A. Louis, P. G. Bolhuis, E. J. Meijer and J. P. Hansen, *J. Chem. Phys.*, 2002, **117**, 1893–1907.
- 79 J. Dzubiella, A. Jusufi, C. N. Likos, C. von Ferber, H. Löwen, J. Stellbrink, J. Allgaier, D. Richter, A. B. Schofield, P. A. Smith, W. C. K. Poon and P. N. Pusey, *Phys. Rev. E: Stat., Nonlinear, Soft Matter Phys.*, 2001, **64**, 010401.
- 80 M. P. Allen and D. J. Tildesley, *Computer Simulation of Liquids*, Oxford Science Publications, Oxford University Press, 1989.
- 81 B. J. Alder, D. M. Gass and T. E. Wainwright, *J. Chem. Phys.*, 1970, **53**, 3813–3826.
- 82 M. Y. Kizilay and O. Okay, *Macromolecules*, 2003, **36**, 6856–6862.
- 83 A. M. Hecht, R. Duplessix and E. Geissler, *Macromolecules*, 1985, **18**, 2167–2173.
- 84 P. Debye and E. Hückel, *Phys. Z.*, 1923, **24**, 185–206.
- 85 F. Hofmeister, *Arch. Exp. Pathol. Pharmacol.*, 1888, **24**, 247–260.
- 86 K. D. Collins and M. W. Washabaugh, *Q. Rev. Biophys.*, 1985, **18**, 323–422.
- 87 C. Eggeling, PhD dissertation, Georg-August-Universität zu Göttingen, 1999.
- 88 J. Stejskal and J. Horská, *Makromol. Chem.*, 1982, **183**, 2527–2535.
- 89 D. Topygin, *J. Fluoresc.*, 2003, **13**, 201–219.
- 90 Z. Zhang, E. Nadezhina and K. J. Wilkinson, *Antimicrob. Agents Chemother.*, 2011, **55**, 1075–1081.
- 91 A. W. Moore Jr. and J. W. Jorgenson, *Anal. Chem.*, 1993, **65**, 3550–3560.
- 92 Z. Petrášek and P. Schwille, *Biophys. J.*, 2008, **94**, 1437–1448.
- 93 E. P. Petrov, T. Ohrt, R. G. Winkler and P. Schwille, *Phys. Rev. Lett.*, 2006, **97**, 258101.
- 94 J. Crank, *The Mathematics of Diffusion*, Clarendon Press, Oxford, 2nd edn, 1975.
- 95 T. Kihara, J. Ito and J. Miyake, *PLoS One*, 2013, **8**, e82382.
- 96 S. Lehmann, S. Seiffert and W. Richtering, *J. Am. Chem. Soc.*, 2012, **134**, 15963–15969.
- 97 B. Amsden, *Macromolecules*, 1998, **31**, 8382–8395.
- 98 L. Masaro and X. X. Zhu, *Prog. Polym. Sci.*, 1999, **24**, 731–775.
- 99 B. A. Westrin, A. Axelsson and G. Zacchi, *J. Controlled Release*, 1994, **30**, 189–199.

This page has been left intentionally blank.

Electronic Supplementary Material (ESI) for Physical Chemistry Chemical Physics.
This journal is © the Owner Societies 2016

SUPPORTING INFORMATION

Diffusion of macromolecules in a polymer hydrogel: from microscopic to macroscopic scales

D. Sandrin,^{1,*} D. Wagner,^{2,*} C. E. Sitta,^{3,*} R. Thoma,⁴ S. Felekyan,¹ H. E. Hermes,²
C. Janiak,⁴ N. de Sousa Amadeu,⁴ R. Kühnemuth,^{1,†} H. Löwen,^{3,‡} S. U. Egelhaaf,
^{2,§} C. A. M. Seidel^{1,¶}

¹ *Institut für Physikalische Chemie II, Molekulare Physikalische Chemie,*

Heinrich-Heine-Universität, Universitätsstr. 1, 40225 Düsseldorf, Germany

² *Institut für Experimentelle Physik der kondensierten Materie,*

Heinrich-Heine-Universität, Universitätsstr. 1, 40225 Düsseldorf, Germany

³ *Institut für Theoretische Physik II: Weiche Materie,*

Heinrich-Heine-Universität, Universitätsstr. 1, 40225 Düsseldorf, Germany

⁴ *Institut für Anorganische Chemie und Strukturchemie,*

Heinrich-Heine-Universität, Universitätsstr. 1, 40225 Düsseldorf, Germany

(Dated: February 26, 2016)

*these authors have contributed equally to this work

† ralf.kuehnemuth@hhu.de; corresponding author

‡ hlowen@hhu.de; corresponding author

§ stefan.egelhaaf@hhu.de; corresponding author

¶ cseidel@hhu.de; corresponding author

3.2 Diffusion of macromolecules in a polymer hydrogel: from macroscopic to microscopic scales

Materials and Methods

S1. Dextran samples & hydrogel – fluorescence properties and quantitative FCS

S1.1. Manufacturers details of fluorescent samples

Samples	Degree of labelling	Number of lysines	Number of amines ^(a)	Charge ^(b)	Absorption Max [nm]	Emission Max [nm]	Quantum yield ^(c)
A488-D3	1	0	≥ 1	a	495	517	0.6
A488-D10	1	10	≥ 2.5	a	494	516	0.6
FLU-D3	1	0	≥ 1	a	497	523	0.5
FLU-D10	2	0	≥ 2.5	a	496	521	0.5
FLU-D40	5	0	≥ 5	a	496	521	0.5
FLU-D500	86	58	≥ 50	a	496	521	0.2
TMR-D3	1	0	≥ 1	a	560	584	0.7
TMR-D10	3	0	≥ 2.5	n	559	586	0.5
TMR-D40	8	0	≥ 5	n	560	586	0.6
TMR-D70	10	0	≥ 10	n	560	585	1
TMR-D2000	138	456	not specified	not specified	560	583	0.8

Table S1. The table shows the manufacturers specification of dye-labelled dextran conjugates (data sheets of used sample batches, Invitrogen). ^(a) Specified for unlabelled aminodextrans. ^(b) a: anionic, n: neutral. ^(c) Fluorescence quantum yield Φ_F determined relative to fluorescein at pH 8.0 (FLU and A488; $\Phi_F^{\text{FLU}} = 0.925 \pm 0.015$) or relative to 5-(and-6)-carboxytetramethylrhodamine (TMR).

S1.2. Investigation of partial quenching (quantum yield and fluorescence lifetime):

For the sample A488-D10 the partial quenching of the labels as indicated in table S1 was investigated applying time-correlated single photon counting (TCSPC, table S2).

fl. lifetime (species fraction)	τ_1 [ns] (x_1)	τ_2 [ns] (x_2)	τ_3 [ns] (x_3)	τ_4 [ns] (x_4)	τ_5 [ns] (x_5)	χ^2	τ_x [ns]
A488 / H ₂ O	4.125 (0.978)	0.459 (0.022)	/	/	/	1.13	4.045
A488-D10 / H ₂ O	4.125 (0.742)	2.459 (0.104)	0.932 (0.066)	0.260 (0.089)	/	1.30	3.400
A488-D10 / H ₂ O (corr.)	4.125 (0.548)	2.459 (0.077)	0.932 (0.049)	0.260 (0.065)	0 (0.262)	1.30	2.511

Table S2. Lifetime components of A488 and A488-D10 in H₂O (FT300, PicoQuant, Berlin; excitation: 485 nm, emission: 517-523 nm, magic angle, photons recorded: total 5×10^8 , peak channel 10^6 photons, T=20 °C). τ_x : species averaged fluorescence lifetime.

While free A488 decays almost mono-exponentially its D10-conjugate exhibits at least four lifetime components, indicating dynamic quenching of a subset of the labels. Albeit, the obtained species averaged lifetimes, $\tau_x = \sum x_i \tau_i$, of conjugated and free dye are not consistent with the determined corresponding fluorescence quantum yields, Φ_F . According to the ratio of the quantum yields of the labelled dextran ($\Phi_F^{A488-D10(\text{exp})} = 0.57$, measured versus Rhodamine 110, $\Phi_F^{\text{Rh110}} = 0.85$,² consistent with manufacturers information $\Phi_F^{A488-D10(\text{man})} = 0.6 \times 0.925 = 0.56$) and the A488 dye free in aqueous solution ($\Phi_F^{A488} = 0.92$, Invitrogen online) a ratio of the species averaged fluorescence lifetimes of $\tau_x^{A488-D10} / \tau_x^{A488} \equiv \Phi_F^{A488-D10} / \Phi_F^{A488} = 0.57 / 0.92 = 0.62$ is expected. Thus a fraction of completely (statically) quenched labels of $x_5 = 0.262$ can be deduced (last row in table S2; $\tau_x^{A488-D10, \text{corr}} / \tau_x^{A488} = 2.511 / 4.045 = 0.62$). The resulting unquenched fraction then is $x_1^{A488-D10} / x_1^{A488} = 0.560$ and the remaining fraction of $1 - 0.560 - 0.262 = 0.179$ represents the partially (=dynamically) quenched dyes. For sake of simplicity, in the following the partially quenched fraction will be ignored and instead an effective totally quenched portion of $x_q = 0.38$ and a corresponding fluorescent portion of $x_f = 1 - x_q = 0.62$ will be assumed.

3.2 Diffusion of macromolecules in a polymer hydrogel: from macroscopic to microscopic scales

S1.3. The effective degree of labelling (DoL_{eff}):

The fluorescently labelled dextrans (as provided by Invitrogen, their specifications being summarized in table S1) are produced by exposing aminodextrans with an average number n_a of free amino groups to amine-reactive dye conjugates. Except for the A488 conjugates, once the dye has been added, the unreacted amines on the dextran are capped to yield a neutral or anionic dextran. Some of the samples carry additional lysines. Due to the applied labelling procedure, for any average degree of labelling, DoL_{av} , a distribution, $P(n_d)$, of the number of dyes per dextran molecule, n_d , is anticipated, i.e. even samples with a $DoL_{av} = 1$ will contain unlabelled as well as higher ($n_a \geq n_d > 1$) labelled molecules. In case of random labelling, the distribution of n_d can be approximated by the binomial distribution:

$$P(n_d, n_a, DoL_{av}) = \frac{n_a!}{n_d!(n_a - n_d)!} \left(\frac{DoL_{av}}{n_a} \right)^{n_d} \left(1 - \frac{DoL_{av}}{n_a} \right)^{n_a - n_d} \quad (S1)$$

For many labelled dextrans the fluorescence quantum yield is significantly reduced as compared to the free dye. Assuming only static quenching of the dyes (on the time scale of the experiment) three different distributions can be defined: (1) the distribution of dextrans $P(n_t)$ containing any number n_t of dyes (fluorescent or quenched) in the range of $n_a \geq n_t \geq 0$, (2) the distribution of dextrans $P(n_f)$ carrying n_f fluorescent (non-quenched) dyes, and (3) the distribution of dextrans containing any dye (fluorescent or quenched) under the condition that at least one fluorescent dye is present, $P(n_{t(f)})$. While $P(n_t) = P(n_d)$, $P(n_f)$ can easily be obtained from eq. S1 by replacing DoL_{av} with $DoL_{av} \times x_f$. The fluorescent fraction of the dyes x_f is approximated by the relative quantum yield of the labelled dextran as compared to the corresponding free dye, $x_f = \Phi_F^{dextran} / \Phi_F^{free\ dye}$ (see S1.2). The third distribution, $P(n_{t(f)})$, is obtained for $n_a \geq n_{t(f)} > 0$ from $P(n_t)$ by randomly distributing quenched dyes among the labelled dextrans, i.e. multiplying a second binomial distribution with $P(n_t)$ and adding the probabilities for all species with the same n_t that contain at least one fluorescent label. The unlabelled fraction is $P(n_{t(f)} = 0) = P(n_f = 0)$.

By omitting the corresponding unlabelled fractions ($n_t = 0$, $n_f = 0$ or $n_{t(f)} = 0$, respectively), three different effective degrees of labelling, DoL_{eff}^x , can be calculated from the obtained distributions using eq. S2:

$$DoL_{eff}^x = \frac{\sum_{n_x=1}^{n_a} n_x P(n_x)}{\sum_{n_x=1}^{n_a} P(n_x)} \quad (S2)$$

with $x = t, f$ or $t(f)$, as defined above.

For A488-D10, the sample investigated in greatest detail in the current study, this will be shown in the following (table S3). For this sample $DoL_{av} = 1$ as determined by the manufacturer and $x_f = 0.62$ for the fluorescent fraction of the labels (see lifetime analysis S1.2) was assumed. Since the number of initial amino groups (n_a) per dextran could not be obtained from the manufacturer an average number of $n_a=5$ was estimated (being the mean $\langle n_a \rangle$ for the currently available 18 batches of unlabelled aminodextrans D10 as specified on the manufacturers homepage). Choosing $n_a=4$ or $n_a=6$ does not significantly change the following considerations.

n_x	0	1	2	3	4	5	DoL_{eff}^x	x_f
$P(n_t)$	0.328	0.410	0.205	0.051	0.006	3×10^{-4}	1.49	1
$P(n_f)$	0.515	0.365	0.104	0.015	0.001	3×10^{-5}	1.28	0.62
$P(n_{t(f)})$	0.515	0.254	0.175	0.048	0.006	0.003	1.60	0.62

Table S3. Expected distribution of probabilities of labelled dextrans D10 ($P(n_t)$) assuming random labelling and a binomial distribution of the labels number, n_t , as well as corresponding distributions taking the fluorophores partial static quenching into account ($P(n_f)$ and $P(n_{t(f)})$). $DoL_{av}=1$, available labelling sites $n_a=5$. x_f is the fluorescent (non-quenched) fraction of the dyes. DoL_{eff}^x with $x = t, f, t(f)$ are the effective degrees of labelling considering all labels and labelled dextrans, only fluorescent labels and fluorescently labelled dextrans and all labels but only fluorescent dextrans, respectively.

The estimation of $DoL_{eff}^{t(f)}$ assumed only static quenching for the partially quenched sample and thus presents a border case, but can be justified by the fact that, according to fluorescence lifetime analysis, the fraction of completely quenched dyes significantly exceeds the dynamically quenched portion (26% vs. 18%). The distribution of the total number of labels ($P(n_t)$ or $P(n_{t(f)})$) is relevant for the estimation of average ionic charges carried by the label. Here $P(n_{t(f)})$ yields the higher number of the two but might be an overestimation, since partial quenching of the individual fluorophores was excluded. Thus the true value of $DoL_{eff}^{t(f)}$ as required to estimate the molecular charge due to labelling is expected to be in between the lower and upper limits as calculated via $P(n_t)$ and $P(n_{t(f)})$, respectively.

The distribution of fluorescent labels, $P(n_f)$, has implications on the molecular brightness as observed by FCS as will be shown in S1.4.

3.2 Diffusion of macromolecules in a polymer hydrogel: from macroscopic to microscopic scales

S1.4. Implications of the distribution of molecular brightnesses for quantitative FCS:

In FCS the molecular brightness B is estimated by dividing the detected fluorescence count rate F by the observed number of fluorescent molecules, N_{tot} , simultaneously present in the confocal detection volume element, $B = F/N_{\text{tot}}$. In case of identical brightness of all particles N_{tot} can directly be obtained from the amplitude of the correlation function (eq. 4 main document, $N_{\text{tot}}=N$ for negligible triplet population). A distribution of brightnesses as discussed above would increase the observed amplitude, i.e. yielding an apparent (or effective) number of molecules N_{eff} (eq. S3).³

$$N_{\text{eff}} = N_{\text{tot}} \left(\sum_{n_f} n_f P(n_f) \right)^2 / \sum_{n_f} n_f^2 P(n_f) \quad (\text{S3})$$

Applying eq. S3 to the numbers in the table S3 yields $N_{\text{eff}}=0.856 N_{\text{tot}}$. With $DoL_{\text{eff}, f}=1.28$ an effective molecular brightness $B^{\text{A488-D10}}/B^{\text{A488}}=1.28/0.856=1.5$ is predicted and fully confirmed by experiment ($B^{\text{A488-D10}} \approx 6.8$ kHz/molecule, $B^{\text{A488}} \approx 4.5$ kHz/molecule; $\rightarrow B^{\text{A488-D10}}/B^{\text{A488}} = 1.5$). Ignoring the distribution of labels would falsify the determined molecular concentrations by almost 15 % and the corresponding brightnesses by 50 %. To derive the total number of dextran molecules, N_{dex} , in the confocal volume in addition the non-fluorescent labels portion needs to be considered ($P(n_f=0) = 0.515$, table SI 3): $N_{\text{dex}}=N_{\text{eff}} \cdot (0.856)^{-1} \times (1-0.515)^{-1} = 2.41 \cdot N_{\text{eff}}$. Comparing the concentrations of a series of A488-D10/H₂O solutions (not shown) as determined by FCS (confocal detection volume element $V_{\text{det}}=0.55$ fl) and its extinction (71,000 cm⁻¹M⁻¹ at 496 nm, Invitrogen) we find $N_{\text{dex}}(\text{exp})=2.9 N_{\text{eff}}$, consistent with the estimated number within the anticipated uncertainties of the confocal volume determination (± 15 %), the measured quantum yield (± 10 %), the average degree of labelling (manufacturers specification) and the approximations made by calculating the dye distributions.

The experimental confirmation of the estimated effective brightness justifies the assumption made above of a random distribution of the quenched labels. An alternative scenario, e.g. quenching due to dye-dye interaction, might be indicated by the similarity of the estimated portion of the singly labelled dextrans ($P(n_f=1)=0.41$, corresponding to 61 % of the labelled molecules) and the fraction of unquenched dye as determined by TCSPC (56 %). This would lead to an expected effective molecular brightness of the dextran A488-D10 close to the free dye brightness and is not consistent with our FCS results.

S1.5. *Effect of immobile fluorophores on molecular brightness in FCS:*

In a stationary confocal measurement, i.e. keeping the location of the confocal volume fixed, the number of fluorophores that are immobile on the time scale of the experiment, N_{immob} , will not contribute to fluctuations of the fluorescence, provided temporary dark state population is negligible. In that case their fluorescence, F_{immob} , can be considered like uncorrelated background. This would reduce the correlation amplitude, $1/N_{\text{mob}}$ (the inverse number of diffusing fluorescent particles) corresponding to the fluorescence, F_{mob} , of mobile fluorophores and yield an apparent amplitude, $1/N_{\text{app}}^3$.

$$N_{\text{mob}} = N_{\text{app}} \left(\frac{F_{\text{mob}}}{F_{\text{mob}} + F_{\text{immob}}} \right)^2 = N_{\text{app}} \left(\frac{F_{\text{mob}}}{F_{\text{tot}}} \right)^2 \quad (\text{S4})$$

$F_{\text{tot}}=F_{\text{mob}}+F_{\text{immob}}$ is the total fluorescence, $N_{\text{tot}}=N_{\text{mob}}+N_{\text{immob}}$ the total number of fluorescent particles. For brightness $B_{\text{mob}}=B$ of mobile and $B_{\text{immob}}=n_i B$ of immobile particles follows (with $n_i>0$):

$$N_{\text{mob}} = N_{\text{app}} \left(\frac{N_{\text{mob}}}{N_{\text{F}}} \right)^2 = N_{\text{app}} \left(\frac{N_{\text{mob}}}{N_{\text{mob}} + n_i N_{\text{immob}}} \right)^2 = N_{\text{app}} \left(\frac{N_{\text{mob}}}{n_i N_{\text{tot}} - (n_i - 1) N_{\text{mob}}} \right)^2.$$

Here N_{F} is the equivalent total number of fluorophores with brightness B . With the apparent brightness $B_{\text{app}} = \frac{F_{\text{tot}}}{N_{\text{app}}}$ we get

$$B = \frac{F_{\text{mob}}}{N_{\text{mob}}} = \frac{F_{\text{tot}}}{n_i N_{\text{tot}} - (n_i - 1) N_{\text{mob}}} = B_{\text{app}} \frac{N_{\text{app}}}{n_i N_{\text{tot}} - (n_i - 1) N_{\text{mob}}} \quad \text{and}$$

$$\begin{aligned} N_{\text{mob}} &= N_{\text{app}} \left(\frac{B_{\text{app}}}{B} \right)^2 \\ n_i N_{\text{tot}} - (n_i - 1) N_{\text{mob}} &= N_{\text{app}} \frac{B_{\text{app}}}{B} = \frac{F_{\text{tot}}}{B} \\ \Rightarrow \frac{n_i N_{\text{tot}} - (n_i - 1) N_{\text{mob}}}{N_{\text{mob}}} &= \frac{B}{B_{\text{app}}} = \frac{n_i N_{\text{tot}}}{N_{\text{mob}}} - (n_i - 1) \\ \Rightarrow x_{\text{mob}} = \frac{N_{\text{mob}}}{N_{\text{tot}}} &= n_i \left(\frac{B}{B_{\text{app}}} + n_i - 1 \right)^{-1} = 1 - x_{\text{immob}} \end{aligned} \quad (\text{S5})$$

Provided translational diffusion is the only process leading to fluorescence fluctuations, e.g. for $n_i=1$ (identical brightness), the mobile fraction can easily be obtained from $x_{\text{mob}}=N_{\text{mob}}/N_{\text{tot}}=B_{\text{app}}/B$. Thus the apparent change in molecular brightness as determined by stationary FCS can give information about the portion of mobile species otherwise invisible to this method.

3.2 Diffusion of macromolecules in a polymer hydrogel: from macroscopic to microscopic scales

For the samples studied, in particular the A488-D10, only a minor change in fluorescence lifetime due to quenching upon entering the hydrogel was observed ($\tau_{\text{gel}}/\tau_{\text{sol}}\approx 0.97$, approximately half of the effect being caused by refractive index changes. See main document and S1.6), suggesting that the average molecular brightness in a first approximation can be considered as unaffected by the hydrogel. From FCS investigations of different concentrations of A488-D10/H₂O in the hydrogel between 30 and 100 nM we obtained an apparent molecular brightness of $B_{\text{app}}\approx 2.5$ kHz/molecule. With $B\approx 6.8$ kHz/molecule as measured free in solution a completely immobile fraction of $x_{\text{immob}}\approx 0.63$ would have to be concluded from eq. S5. Since higher labelled molecules are preferentially trapped (see main document) this must be considered as an upper limit. In case all immobile particles were doubly labelled and the mobile ones would carry one fluorophore ($B_{\text{mob}}=B^{A488}=4.5$ kHz/molecule= $0.5B_{\text{immob}}$) an estimation according to the above analysis would yield $x_{\text{mob}}=2/((B/B_{\text{app}})+1)$ and $x_{\text{immob}}\approx 0.29$. This is higher than the estimated fraction of A488-D10 with $n_f > 1$ (12 %, table S3) and could indicate an enrichment of higher labelled dextrans inside the hydrogel, consistent with the observation of a higher binding constant for those probe molecules (main document).

S1.6. Refractive index mismatch – effect on fluorescence lifetime and diffusion measurements:

Inside the PAAm hydrogel the refractive index, n , is reported to be slightly higher than in dilute aqueous solutions.⁴ For the densities of hydrogels and the wavelength used in our study a linear dependence of $dn/dc'=0.188$ ml/g can be extracted, with c' being the mass of PAAm per ml hydrogel. With $n_0=1.3361$ for water ($\lambda=525$ nm and $T=22$ °C)⁵ and the measured densities of the gels (see main document, converted using a density of $\rho_{(\text{PAA})}=1.3$ g/cm³) we estimate the refractive indices in table S4.

Based on the refractive index, changes in radiative lifetimes, τ_r , can be calculated according to Toptygin by a modified Strickler-Berg approach.⁶ The empty spherical cavity model (ESC, Toptygin, eq. 59) was found to successfully describe radiative lifetimes of small fluorophores in solution (eq. S1.5):

$$\frac{\tau_{r,2}}{\tau_{r,1}} = \left(\frac{n_1}{n_2} \right)^5 \left(\frac{2n_2^2 + 1}{2n_1^2 + 1} \right)^2 \quad (\text{S6})$$

$\tau_{r,1}$ and n_1 are radiative lifetime and index of refraction in water, $\tau_{r,2}$ and n_2 the corresponding quantities in the gel (table S.4).

hydrogel	c [ml/ml]	c' [g/ml]	n	$\tau_{r(\text{gel})}/\tau_{r(\text{sol})}$
pH7	0.038	0.049	1.3454	0.987
ph10	0.015	0.020	1.3398	0.995

Table S4. Index of refraction at $\lambda=525$ nm and $T=22$ °C for PAAm hydrogels and its estimated effect on radiative lifetimes.

For A488 and A488-D10 the observed changes in fluorescence lifetimes are bigger than the predicted changes in radiative lifetime, suggesting additional fluorescence quenching due to matrix effects (see main document).

The relative small deviation of n from n_0 (H_2O) is well within the range of the correction collar of current water immersion objectives. This was shown for a Zeiss CApo40x/1.2 W objective,⁷ comparable to our Olympus UPlanSApo 60x/1.2 W, and verified by experiment. Furthermore, in a calibration measurement we confirmed that for our conditions (wavelength, depth of the focal point in the sample) no readjustment of the correction collar setting was required after switching the sample from pure water to hydrogel.

SI.7. Binding model

A simple binding model was applied to describe the observed equilibrium fractions of mobile and trapped probe molecules:

$$\begin{aligned}
 K_d &= \frac{a_{\text{bound}}}{a_{\text{free}} \cdot a_{\text{sites}}} \\
 K_d' &\approx K_d \cdot a_{\text{sites}} = \frac{a_{\text{bound}}}{a_{\text{free}}} \approx \frac{c_{\text{bound}}}{f_{\text{free}} c_{\text{free}}} \\
 \Rightarrow \frac{c_{\text{bound}}}{c_{\text{free}}} &= f_{\text{free}} K_d' \\
 \Rightarrow \frac{c_{\text{bound}}}{c_{\text{free}} + c_{\text{bound}}} &= x_{\text{bound}} = \frac{f_{\text{free}} K_d'}{1 + f_{\text{free}} K_d'}
 \end{aligned} \tag{S7}$$

Here, K_d is the binding constant, a the activity for free (a_{free}) and bound (a_{bound}) molecules with the respective concentration (c_{bound} and c_{free}). The number of binding sites in the matrix a_{sites} defines the effective binding constant K_d' .

3.2 Diffusion of macromolecules in a polymer hydrogel: from macroscopic to microscopic scales

Results

S2. Image integrated normalized correlations curves measured in hydrogel for A488-Dx and TMR-Dx in water and for FLU-Dx in carbonate buffer 20 mM pH 10

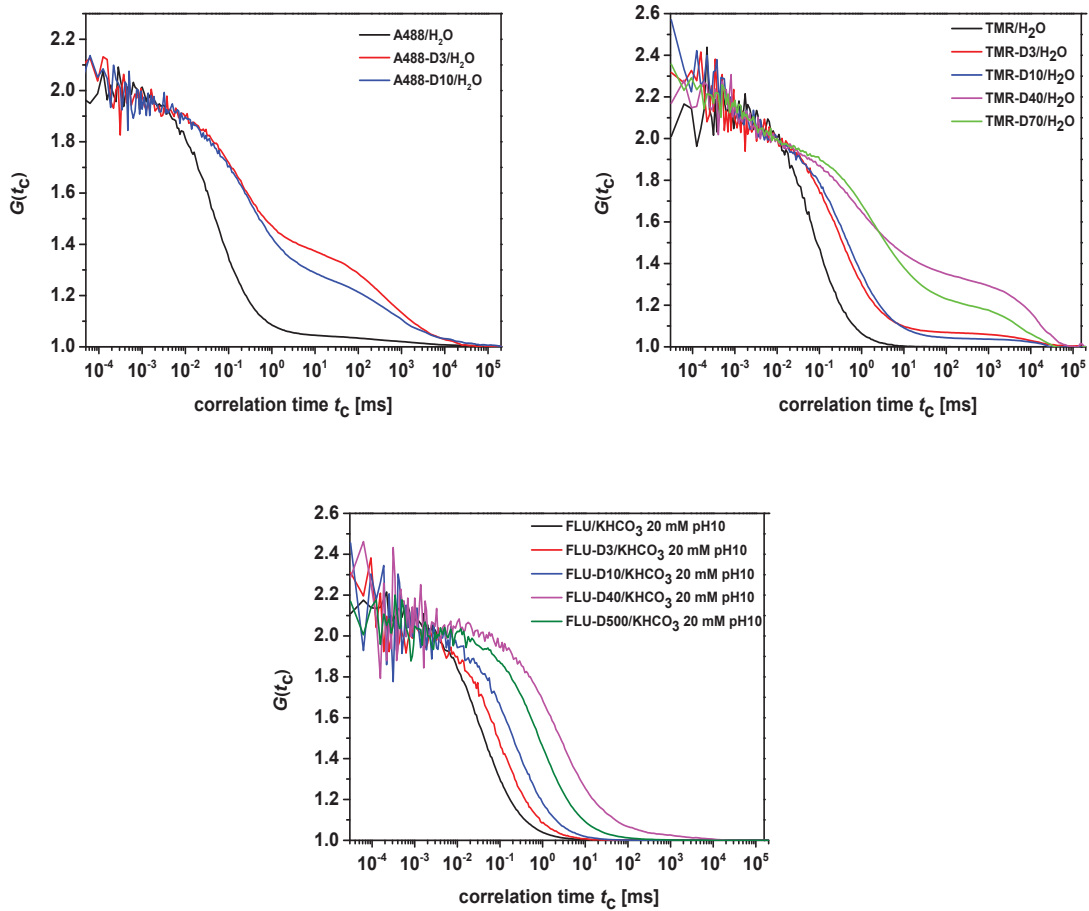


Figure S1. Image integrated normalized correlations curves for A488 and TMR free dye and with dextran in hydrogel in water conditions. In this case, more than one diffusion time is clearly visible, indicating the presence of temporarily trapped molecules in the hydrogel. FLU samples were measured in carbonate buffer 20 mM, pH 10, in this case the bound molecules are much less, only for samples D40 and D500 trapping is visible and amounts to about 1%.

S3. Diffusion times from FCS experiments in the hydrogel at standard conditions

Table S5 shows the diffusion times for A488, TMR and FLU for free dye and with dextran at standard conditions: water for A488 and TMR, carbonate buffer pH 10 for FLU in the hydrogel.

Dye	Sample	Solvent	fast component		slow component	
			t_d [ms]	fraction x	t_d [ms]	fraction x
A488	Free dye	H ₂ O	0.049 ± 0.002	0.991	200-500	0.009
A488	D3	H ₂ O	0.220 ± 0.007	0.626	10-2000	0.374
A488	D10	H ₂ O	0.410 ± 0.017	0.704	10-6000	0.296
TMR	Free dye	H ₂ O	0.065 ± 0.001	1	-	0
TMR	D3	H ₂ O	0.272 ± 0.010	0.873	10-8000	0.127
TMR	D10	H ₂ O	0.363 ± 0.011	0.962	1000-10000	0.038
TMR	D40	H ₂ O	1.699 ± 0.105	0.688	20-10000	0.312
TMR	D70	H ₂ O	2.026 ± 0.079	0.719	40-12000	0.281
FLU	Free dye	KHCO ₃ 20 mM pH 10	0.036 ± 0.001	1	-	0
FLU	D3	KHCO ₃ 20 mM pH 10	0.116 ± 0.001	1	-	0
FLU	D10	KHCO ₃ 20 mM pH 10	0.263 ± 0.004	1	-	0
FLU	D40	KHCO ₃ 20 mM pH 10	0.823 ± 0.032	0.992	10-140	0.008
FLU	D500	KHCO ₃ 20 mM pH 10	3.664 ± 0.470	0.988	20-3000	0.012

Table S5. Results of FCS fits for A488, TMR and FLU (free dye and labelled dextran) in hydrogel. For some samples fitting the model function to the data required two or more diffusion times. In the latter case the fraction of the slow component (last column) is the sum of two terms that in total represent the fraction of trapped molecules. The diffusion times of fast components are the averages from different pixels. For the slow component, t_d is given as range because it significantly differs from pixel to pixel.

3.2 Diffusion of macromolecules in a polymer hydrogel: from macroscopic to microscopic scales

S4. Diffusion times from FCS experiments for Rh110, A488, TMR and FLU free dye and labelled D10 at different salt conditions in the hydrogel.

Sample	Solvent	fast component		slow component	
		t_d [ms]	fraction x	t_d [ms]	fraction x
Rh110	H ₂ O	0.036	1	-	0
A488	H ₂ O	0.049	0.991	200-500	0.009
A488-D10	H ₂ O	0.410	0.704	10-6000	0.296
A488-D10	KClO ₄ 10 mM	0.384	0.832	10-6000	0.168
A488-D10	KClO ₄ 20 mM	0.383	0.875	10-6000	0.125
A488-D10	KCl 20 mM	0.352	0.904	400-6000	0.096
A488-D10	KClO ₄ 40 mM	0.401	0.900	10-6000	0.100
A488-D10	KClO ₄ 60 mM	0.352	0.910	10-6000	0.090
A488-D10	KHCO ₃ 20 mM pH 7	0.345	0.924	400-6000	0.076
A488-D10	KHCO ₃ 20 mM pH 10	0.354	0.930	400-6000	0.070
TMR-D10	H ₂ O	0.363	0.960	500-7000	0.040
TMR-D10	KHCO ₃ 20 mM pH 10	0.303	1	-	0
TMR-D10	TRIS 50 mM pH 7.5	0.212	1	-	0
FLU-D10	KHCO ₃ 20 mM pH 10	0.265	1	-	0
FLU-D10	H ₂ O	0.260	1	-	0
FLU-D10	TRIS 50 mM pH 7.5	0.262	1	-	0

Table S6. Results of FCS fits for the reference Rh110, A488, A488-D10, TMR-D10 and FLU-D10 in solution and in the hydrogel at different salt conditions. For some samples fitting the model function to the data required two or more diffusion times. In the latter case the fraction of the slow component (last column) is the sum of two terms that in total represent the fraction of trapped molecules. The diffusion times of the fast components are the averages obtained from different pixels. For the slow component, t_d is given as range because it significantly differs from pixel to pixel.

S5. Trace analysis

The fluorescence time trace was split into small segments and sorted according to their approximated mean count rate employing a special feature of the binary single photon data format *.ht3 (PicoQuant, Berlin, Germany). Depending on the inter-photon time (i.e. the inverse count rate) in addition to the photon information extra entries are generated to store each overflow of the macroscopic time counter. Thus, sections containing the same total number of entries (as were generated upon splitting the recorded file) can be sorted by their content of photons and extra entries and thereby by their mean count rate. The produced subsets of split files were subsequently correlated and analyzed.

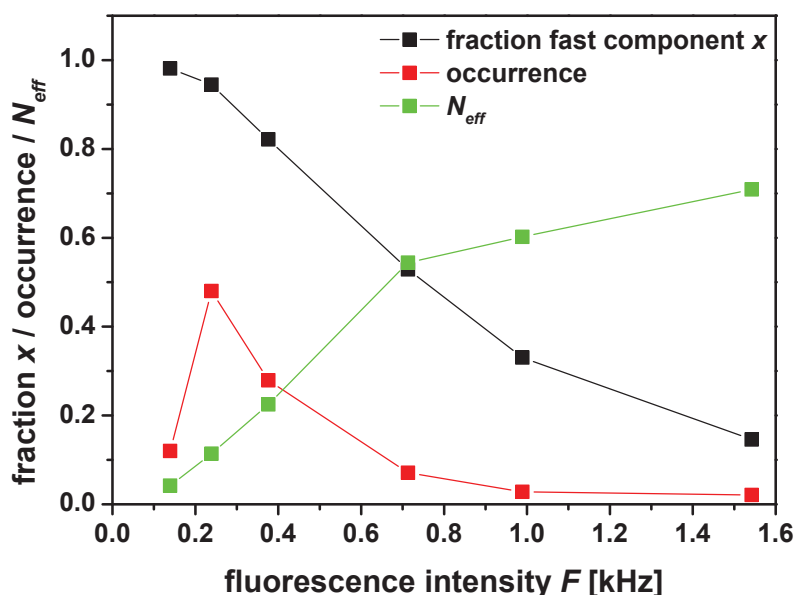


Figure S2. Fraction of fast component x , effective mean fluorophore number N_{eff} and occurrence of different count-rate based sections in time trace (Main document Figure 4). N_{eff} is the inverse correlation amplitude at $\tau_c=0$ and corresponds to the total number of diffusing molecules in case of equal brightness for all components. Temporary accumulation of particles due to trapping is clearly visible.

3.2 Diffusion of macromolecules in a polymer hydrogel: from macroscopic to microscopic scales

S6. Fluorescence intensity ratio between gel and the solution surrounding the gel plotted against experimental concentration for A488-D10 in H₂O from FCS measurements

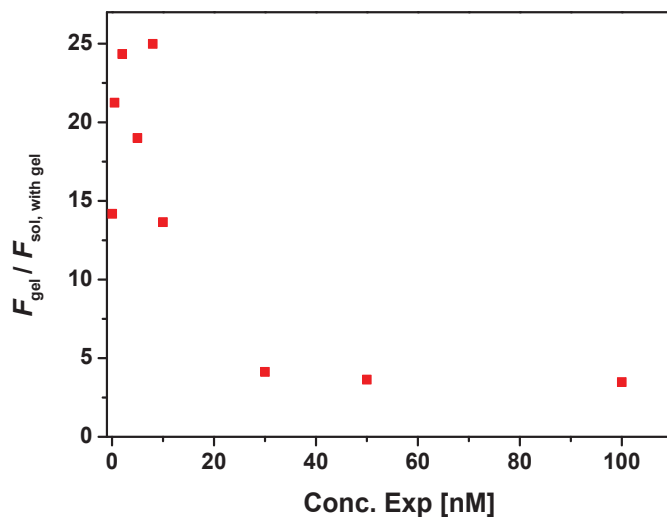
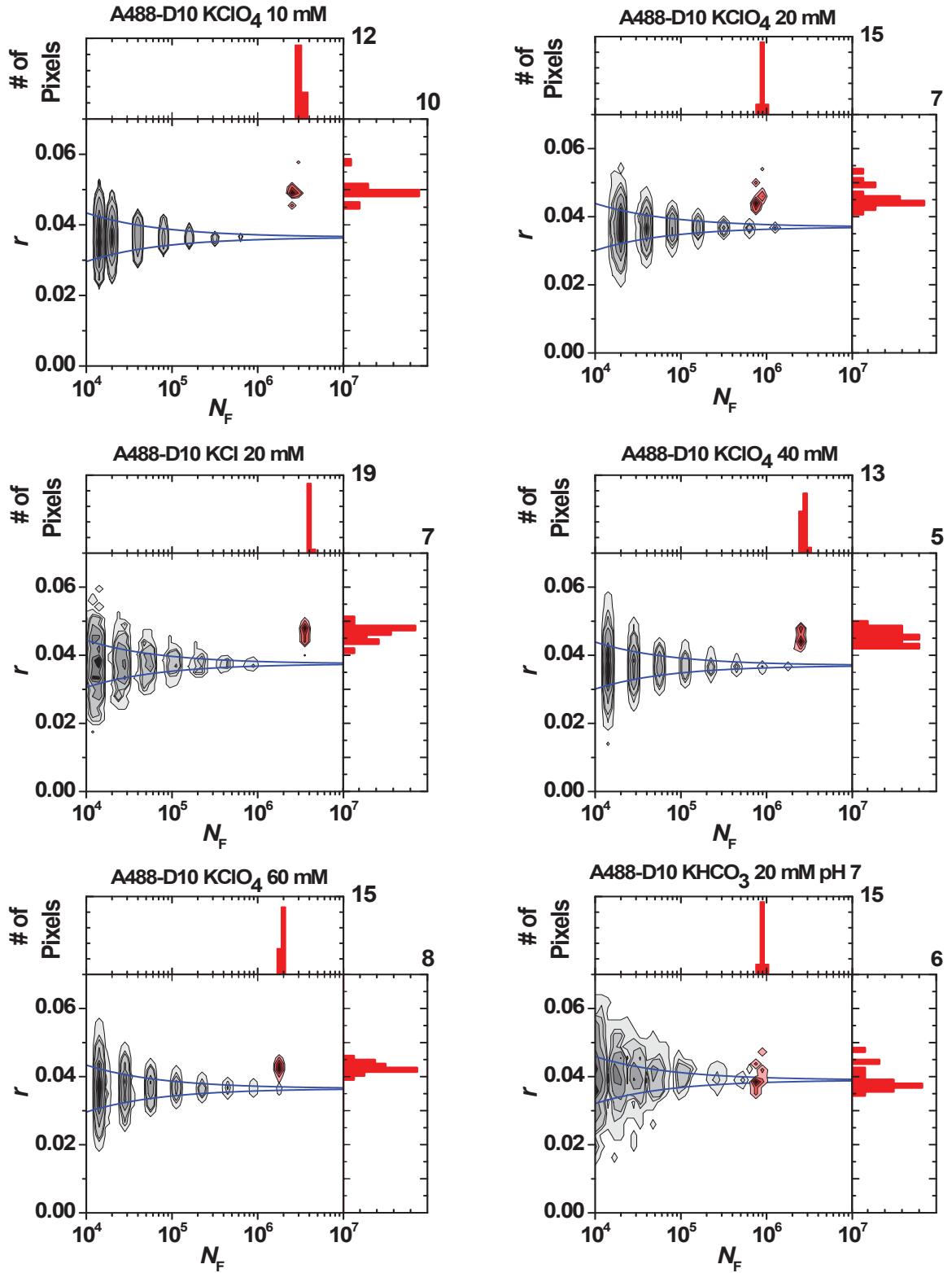
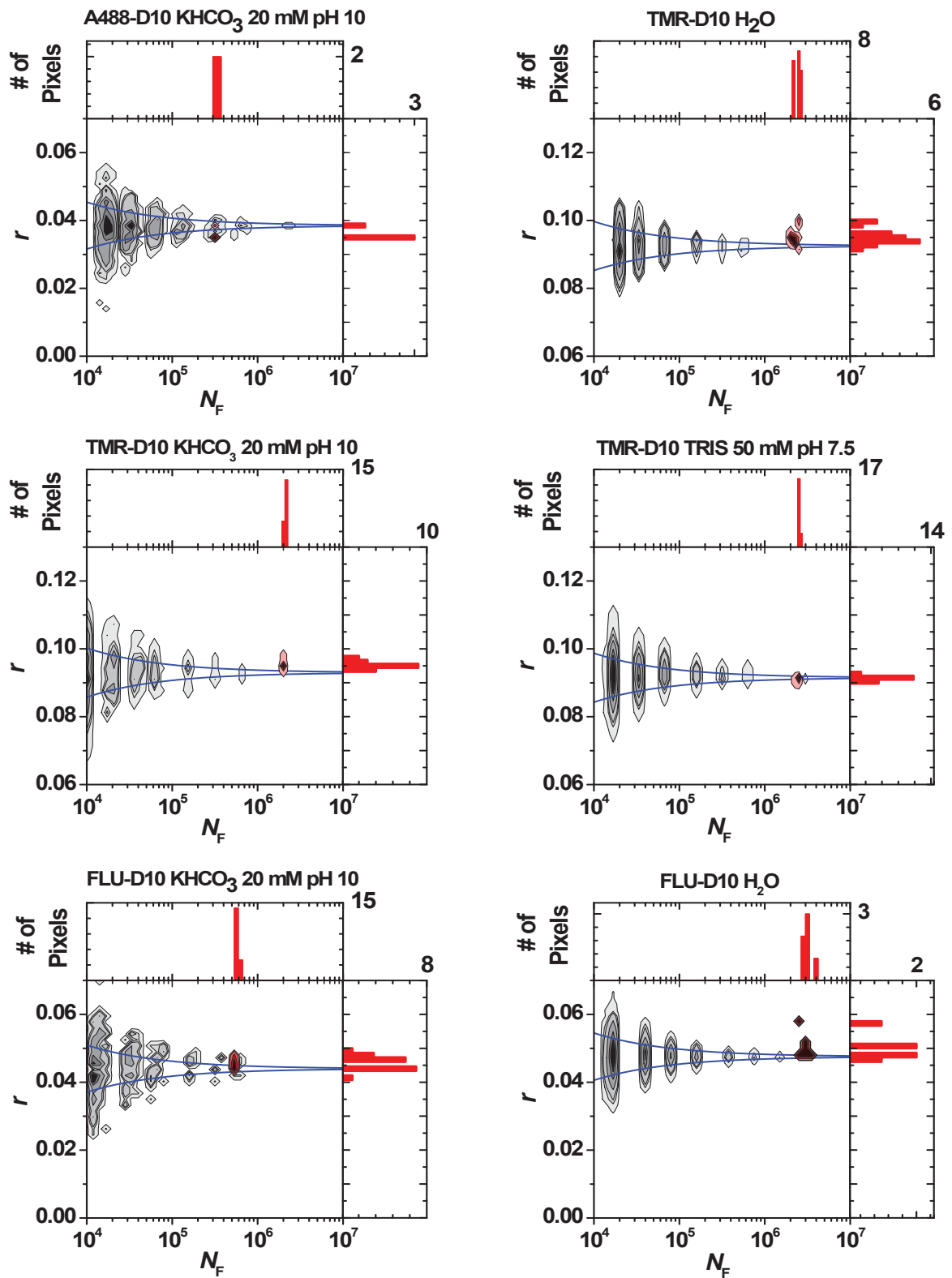


Figure S3. The plot shows that the fluorescence intensity ratio between gel and the solution surrounding the gel, $F_{\text{gel}} / F_{\text{sol, with gel}}$, is decreasing with increasing experimental concentration. The enrichment of the fluorophores inside the gel, as indicated by the fluorescence intensity ratio is concentration dependent and strongest for small concentrations until high-affinity trap sites are saturated.

S7. Fluorescence anisotropies of A488-D10, TMR-D10 and FLU-D10 in solution and hydrogel



3.2 Diffusion of macromolecules in a polymer hydrogel: from macroscopic to microscopic scales



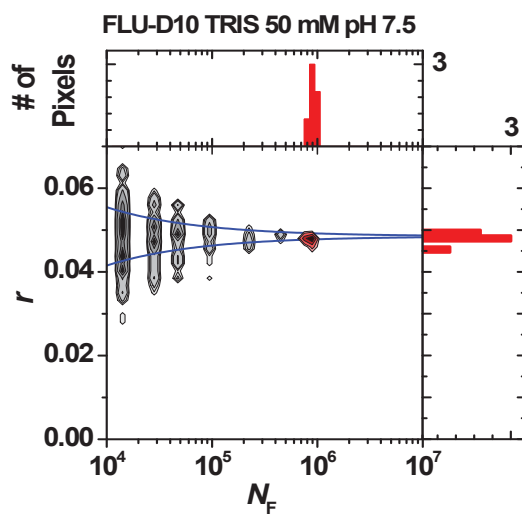


Figure S4. 2D plots of anisotropy r vs. photon number N_F for A488-D10, TMR-D10 and FLU-D10 in solution (gray contour lines) and in hydrogel (red contour lines) with 1D projections for the gel data.

For A488-D10 the plots show markedly different anisotropies inside the hydrogel for different solvent conditions. In case of KClO_4 10 mM, 20 mM, 40 mM and KCl 20 mM the anisotropy in the gel is higher as compared to the solution value, in these cases the trapped fraction is $\geq 10\%$. The decrease in anisotropy starts with higher ionic strength: 60 mM KClO_4 and 20 mM in carbonate buffer pH 7 and 10, clearly correlated with the trapped fraction of the molecules as determined by FCS. For TMR-D10 and FLU-D10 the anisotropy is slightly higher or equal in comparison to solution measurements in different conditions (trapped fraction $\leq 4\%$).

3.2 Diffusion of macromolecules in a polymer hydrogel: from macroscopic to microscopic scales

S8. Fluorescence anisotropy A488-D10, TMR-D10 and FLU-D10

Sample	Solvent	<i>r</i>		Trapped fraction x
		Solution	Hydrogel	
Rh110	H ₂ O	0.010	0.010	0
A488	H ₂ O	0.014	0.018	0.011
A488-D10	H ₂ O	0.037	0.049	0.296
A488-D10	KClO ₄ 10 mM	0.037	0.049	0.168
A488-D10	KClO ₄ 20 mM	0.037	0.046	0.125
A488-D10	KCl 20 mM	0.037	0.046	0.096
A488-D10	KClO ₄ 40 mM	0.037	0.045	0.100
A488-D10	KClO ₄ 60 mM	0.036	0.041	0.090
A488-D10	KHCO ₃ 20 mM pH 7	0.039	0.040	0.076
A488-D10	KHCO ₃ 20 mM pH 10	0.037	0.037	0.070
TMR-D10	H ₂ O	0.093	0.096	0.040
TMR-D10	KHCO ₃ 20 mM pH 10	0.093	0.094	0
TMR-D10	TRIS 50 mM pH 7.5	0.092	0.092	0
FLU-D10	KHCO ₃ 20 mM pH 10	0.044	0.046	0
FLU-D10	H ₂ O	0.047	0.049	0
FLU-D10	TRIS 50 mM pH 7.5	0.047	0.047	0

Table S7. Average anisotropy (*r*) for Rh110, A488, A488-D10, TMR-D10 and FLU-D10 in solution and in the hydrogel for different salt conditions.

S9. Reference data

Published experimental hydrodynamic radii for dextrans labelled with A488, TMR or fluorescein are compiled in Figure SI 5.

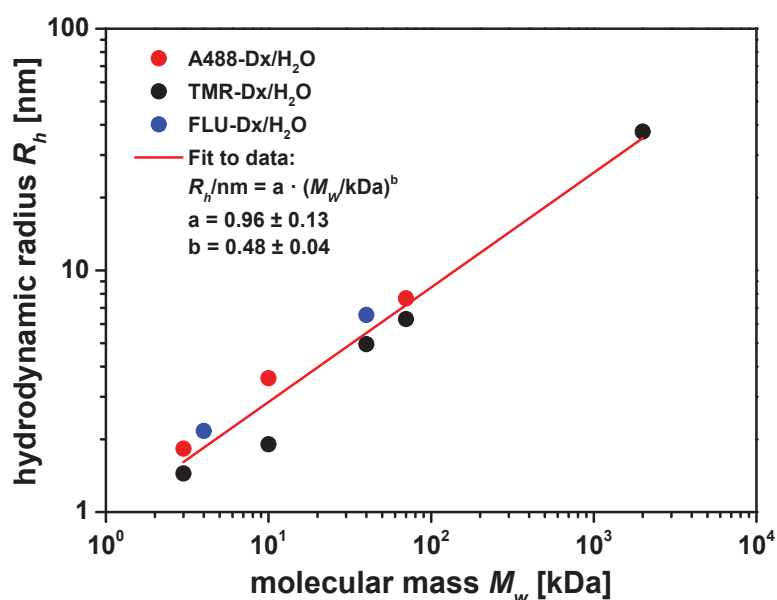


Figure S5. Fit of Flory scaling law to reference data for A488-D3 & A488-D10⁸, A488-D70⁹, TMR-Dx¹⁰ and FLU-Dx⁸. R_h was taken as published or calculated via Stokes-Einstein equation. The systematic difference between TMR-Dx data (measured at 23 °C) and A488-Dx and Flu-Dx data (measured at 32 °C, except A488-D70 measured at 25 °C) is mainly attributed to calibration uncertainties. Reported temperature effects on R_h of dextrans in the relevant temperature and size range are about one order of magnitude smaller than the deviation of the two data sets and in the opposite direction: $-\Delta R_h / (R_h \Delta T) < 0.003 \text{ K}^{-1}$ (extracted from Figure 1 in ref.¹¹).

3.2 Diffusion of macromolecules in a polymer hydrogel: from macroscopic to microscopic scales

S10. NMR Measurements

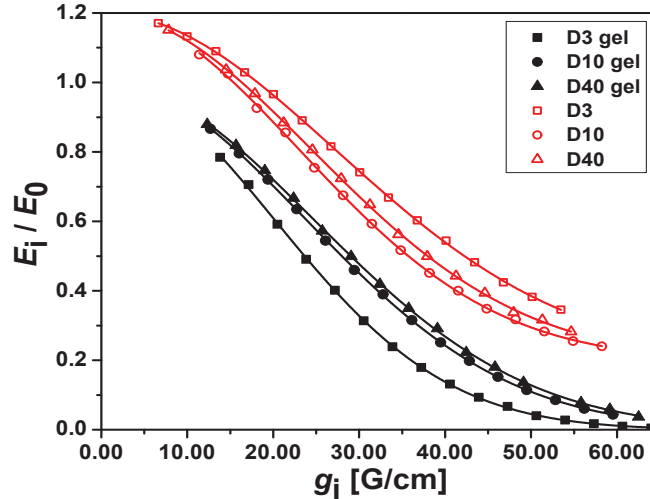


Figure S6. NMR data and fits for unlabelled dextrans (3 kDa, 10 kDa and 40 kDa) in hydrogels and in D_2O . Data was normalized and xy offset-corrected. For clarity reasons, the solution data (red) was vertically offset by 0.2.

The diffusion coefficients D were obtained by fitting the echo amplitudes (integral of the signals between 2.8 and 4.4 ppm) using Eq.7 (See main text). We performed several diffusion measurements with each sample, varying the key parameters δ and Δ_N and keeping constant the values of $\tau_N = 0.001$ s and $\gamma = 26752.22005$ rad/s Gauss. Several combinations of Δ_N and δ were applied and the specific parameters are listed in the table S8.

	Solution			Hydrogel		
	δ [μ s]	Δ_N [s]	D_{sol} [$10^{-10}m^2/s$]	δ [μ s]	Δ_N [s]	D_{gel} [$10^{-10}m^2/s$]
D3	600	0.60	1.12	600	1.80	0.67
	800	0.30	1.15	700	1.40	0.65
	1000	0.10	1.16	800	1.00	0.68
D10	1000	0.30	0.97	750	1.70	0.30
	1200	0.25	0.96	1000	1.30	0.33
	1600	0.10	0.97	1500	0.50	0.31
D40	800	1.00	0.38	1200	1.60	0.096
	1000	0.80	0.38	1300	2.00	0.085
	1200	0.60	0.37	1400	1.80	0.096

Table S8. Parameters used for NMR measurements for unlabelled dextrans D3, D10 and D40. The fit provides the diffusion coefficient for each sample for the different experimental settings. The rows marked in yellow represent the curves shown in figure S6.

S11. *Technical details of the Brownian dynamics simulation***General**

In our Brownian dynamics simulation¹², we use a cubic simulation box with periodic boundary conditions containing 512 matrix particles and 1 tracer particle. About 200 independent simulation runs have been performed to generate typical trajectories for the statistical averages of the tracer's mean square displacements. The Brownian equations of motion were integrated with an Euler-algorithm. The time step Δt for the integration was chosen as $\Delta t < 2 \cdot 10^{-5} \tau_B$ (for model 1, 2 and 3a, TMR) and $\Delta t < 1.5 \cdot 10^{-6} \tau_B$ (for model 3b, TMR). $\tau_B = a^2 / D_0$ denotes the Brownian time. Here, a is the lattice constant of the matrix and D_0 the diffusion constant of the tracer particle in a pure solvent as obtained from the experiments. For FLU, Δt had to be chosen 10 times smaller. We carefully checked that the results for the statistical averages did not change upon further decreasing the time step such that the magnitude of Δt was small enough.

Simulation protocol

In our simulations we used the following protocol:

- Generation of the underlying gel structure:
 - The gel obstacles were placed on a simple cubic lattice of lattice constant a .
 - The matrix particles were randomly shifted up to half the lattice constant in each direction in model 2, 3a and 3b.
 - Springs were attached between the centers of neighboring matrix particles which were all undistorted, i.e. the rest lengths equaled exactly the corresponding particle separations.
- The tracer particle was placed in a void.
- The BD simulation was started and the system was equilibrated for a typical time of $t_{\text{eq}} \gg 1 \tau_B$.
- Statistics for the dynamical correlations was gathered by storing at least 100000 snapshots of the tracer trajectory $\dot{s}(t)$ at equidistant times within a sufficiently large time window of $t_{\text{max}} \gg 40 \tau_B$. In this time window, the tracer moved on average a distance of several lattice constants a .

3.2 Diffusion of macromolecules in a polymer hydrogel: from macroscopic to microscopic scales

Calculation of the hindrance factors

It was carefully checked that the long-time limit of the tracer's mean square displacement $\Delta s^2(t) = \left\langle \left(\vec{s}(t_0 + t) - \vec{s}(t_0) \right)^2 \right\rangle$ was reached. Here, $\langle \dots \rangle$ denotes the average over all $t_0 \in [0, t_{\max} - t]$

and all independent simulation runs. The diffusion coefficient was obtained as $D = \lim_{t \rightarrow \infty} \frac{1}{6} \frac{d}{dt} \Delta s^2(t)$.^{12,}

¹³ As for an example, see Figure S7. We then performed a fitting procedure to describe the experimental hindrance factors $H=D/D_0$ as a function of R_h .

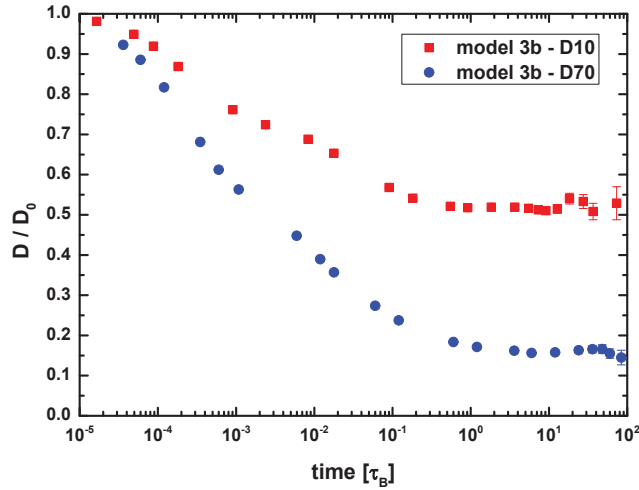


Figure S7. Hindrance factor D/D_0 versus time for two different tracers (D10 and D70) within model 3b. For very short times, the Diffusion coefficient approaches the Diffusion coefficient in solution D_0 , as no collisions occur during these times. The long-time-limes is reached before $1 \tau_B$, as the diffusion coefficient does not decrease any further

Parameters

All model parameters were fixed according to Table S9 except the lattice constant a , which sets the pore size, and the obstacle radius R_{obst} , which was scaled with a factor such that the constraint of the experimentally prescribed volume fraction, φ , (measured by swelling analysis, see main text

Sec.2.1.1) was fulfilled: $R_{\text{obst}} = \sqrt[3]{\frac{3\varphi}{4\pi}} a$. This leads to a coarse-grained obstacle radius comparable to

the tracer size at least of the same order of magnitude. The additive diameters σ_{ij} used in Eq. (8), (10), (11) were therefore also fixed by $\sigma_{ij}=2 R_{\text{obst}}$ for the obstacle-obstacle-interaction and $\sigma_{ij}=R_{\text{obst}} + R_h$ for the interaction between a matrix obstacle and a tracer of radius R_h . For the guest particle radii

R_h , we used our experimental values (see R_h in Table 3 in the results, 3.2.1). The short-time diffusivity of the obstacles was calculated via the Stokes-Einstein relation $D_{obst} = \frac{k_B T}{6\pi\eta R_{obst}}$. Here, $\eta = 0.00095$ Pa s is the viscosity of the solvent at $T = 295$ K ($= 22$ °C). We used $\varepsilon_s = 1 k_B T$ for the WCA-potential used in model 1, 2 and 3b. In model 3a, we used $\varepsilon_G = 12 k_B T$ since this value is above the value of $2 k_B T$, which is found for self-avoiding polymers¹⁴ but we expect our system to be stiffer. We have changed ε_G within the range of $4 k_B T$ and $20 k_B T$ and did not obtain an improved fit to the experimental data.

In conclusion, out of the 12 parameters shown in Table S9, 9 are fixed by physical constraints, namely the obstacle radius R_{obst} , and consequently also the obstacle self-diffusion constant D_{obst} and the additive diameters $\sigma_{obst, obst}$, $\sigma_{obst, D0}$, $\sigma_{obst, D3}$, $\sigma_{obst, D10}$, $\sigma_{obst, D40}$, $\sigma_{obst, D70}$, $\sigma_{obst, D500}$. Hence only 3 parameters are left: The lattice constant a , the spring constant k and the interaction parameters ε_s , resp. ε_G , (plus possibly the parameter ε_a in model 3b). ε_a and a are real fit parameters. We have checked that a change of k and the interaction parameters ε_s , resp. ε_G give indifferent fit quality.

Fitting and conclusion

For the fixed choice of a , the whole hindrance factors H were simulated as a function of R_h , i.e. for all tracer radii used in the experiments. These sets of simulation data were compared to the experimental data and an optimal value of a was obtained by the best fit. For model 3b, two fit parameters were used, namely the lattice constant a and the attraction strength ε_a . This results in better fitting in particular for small R_h . We remark here that the attraction was essential. In a purely repulsive dextran-matrix interaction model, a second fit parameter would not give a significant improvement of the fit. Additional simulations performed within model 3b using a Gaussian softened core showed a similar fit quality as that with a WCA-core such that we conclude that the attraction itself rather than the details of the repulsion is crucial to describe the experimental data properly.

3.2 Diffusion of macromolecules in a polymer hydrogel: from macroscopic to microscopic scales

Dye	Model	initial gel simple cubic lattice constant	obstacle radius	obstacle self diffusion constant	spring constant	Matrix-dextran-interaction parameters (at T=20 °C)	$\sigma_{\text{obst,obst}}$	$\sigma_{\text{obst,D0}}$	$\sigma_{\text{obst,D3}}$	$\sigma_{\text{obst,D10}}$	$\sigma_{\text{obst,D40}}$	$\sigma_{\text{obst,D70}}$	$\sigma_{\text{obst,D500}}$
		[10 ⁻⁹ m]	[10 ⁻⁹ m]	[10 ⁻¹¹ m ² /s]	[10 ⁻⁴ N/m]	[10 ⁻²⁰ J]	[10 ⁻⁹ m]	[10 ⁻⁹ m]	[10 ⁻⁹ m]	[10 ⁻⁹ m]	[10 ⁻⁹ m]	[10 ⁻⁹ m]	[10 ⁻⁹ m]
TMR	1	11.75	2.48	0	inf	$\epsilon_s = 1k_B T \approx 0.405$	4.95	3.03	4.19	5.55	8.48	10.34	
	2	11.75	2.48	9.18	6.17	$\epsilon_s = 1k_B T \approx 0.405$	4.95	3.03	4.19	5.55	8.48	10.34	
	3a	10.03	2.11	10.77	6.17	$\epsilon_G = 12k_B T \approx 4.86$	4.23	2.66	3.82	5.18	8.11	9.97	
	3b	14.35	3.02	7.52	6.17	$\epsilon_s = 1k_B T \approx 0.405$ $\epsilon_a = 3k_B T \approx 1.21$	6.05	3.57	4.73	6.09	9.02	10.88	
FLU	1	31.73	4.86	0	inf	$\epsilon_s = 1k_B T \approx 0.405$	9.73	5.41	6.57	7.93	10.86		25.16
	2	31.73	4.86	4.68	6.17	$\epsilon_s = 1k_B T \approx 0.405$	9.73	5.41	6.57	7.93	10.86		25.16
	3a	30.29	4.64	4.90	6.17	$\epsilon_G = 12k_B T \approx 4.86$	9.29	5.19	6.35	7.71	10.64		24.94
	3b	44.71	6.85	3.32	6.17	$\epsilon_s = 1k_B T \approx 0.405$ $\epsilon_a = 3k_B T \approx 1.21$	13.71	7.40	8.56	9.92	12.85		27.15

	D0	D3	D10	D40	D70	D500
radius [10 ⁻⁹ m]	0.55	1.7	3.1	6.0	7.9	20

Table S9. Parameters used for Brownian dynamics simulations for model 1 (fixed gel matrix, steric interaction), model 2 (flexible gel matrix, steric interaction), model 3a (flexible gel matrix, soft interaction), model 3b (flexible gel matrix, steric interaction and attractive shell).

References

1. D. Magde, R. Wong and P. G. Seybold, *Photochem. Photobiol.*, 2002, **75**, 327-334.
2. X.-F. Zhang, Y. Zhang and L. Liu, *J. Lumin.*, 2014, **145**, 448-453.
3. N. L. Thompson, in *Topics in Fluorescence Spectroscopy*, ed. J. R. Lakowicz, Plenum Press, New York, 1991, vol. 1, pp. 337-378.
4. J. Stejskal and J. Horská, *Makromol. Chem.*, 1982, **183**, 2527-2535.
5. *Release on the Refractive Index of Ordinary Water Substance as a Function of Wavelength, Temperature and Pressure*, The International Association for the Properties of Water and Steam, Erlangen, Germany, 1997.
6. D. Topygin, *J. Fluoresc.*, 2003, **13**, 201-219.
7. E. Banachowicz, A. Patkowski, G. Meier, K. Klamecka and J. Gapinski, *Langmuir*, 2014, **30**, 8945-8955.
8. T. Kihara, J. Ito and J. Miyake, *PLoS One*, 2013, **8**, e82382.
9. S. Lehmann, S. Seiffert and W. Richtering, *J. Am. Chem. Soc.*, 2012, **134**, 15963-15969.
10. Z. Zhang, E. Nadezhina and K. J. Wilkinson, *Antimicrob. Agents Chemother.*, 2011, **55**, 1075-1081.
11. M. A. Masuelli, *J. Polym. Biopolym. Phys. Chem.*, 2013, **1**, 13-21.
12. M. P. Allen and D. J. Tildesley, *Computer Simulation of Liquids (Oxford Science Publications)*, Oxford University Press, 1989.
13. B. J. Alder, D. M. Gass and T. E. Wainwright, *J. Chem. Phys*, 1970, **53**, 3813-3826.
14. A. A. Louis, P. G. Bolhuis, E. J. Meijer and J. P. Hansen, *J. Chem. Phys*, 2002, **117**, 1893-1907.

This page has been left intentionally blank.

3.3 Solvent and solute ingress into a polymer hydrogel resolved by a combination of imaging techniques

Journal: The Journal of Chemical Physics

Reference: *J. Chem. Phys.* **144**, 204903 (2016), DOI: 10.1063/1.4950954

Article was selected as Editor's pick

Impact factor: 2.952

Authors: **Dana Wagner**, Jennifer Burbach, Christian Grünzweig, Stefan Hartmann, Eberhard Lehmann, Stefan U. Egelhaaf, and Helen E. Hermes

1st author

DW designed and built the experimental setup. Sample preparation was done by DW and JB, measurements were performed by DW, HEH and JB. DW analyzed the data. CG, SH and EL assisted during the beam time at PSI. DW, HEH and SUE conceived and discussed the project and HEH and SUE supervised the project. DW wrote the manuscript and HEH and SUE contributed to the writing.

85% contribution of DW

The article is reprinted with the permission of AIP Publishing.

This page has been left intentionally blank.

Solvent and solute ingress into hydrogels resolved by a combination of imaging techniques

D. Wagner,¹ J. Burbach,¹ C. Grünzweig,² S. Hartmann,² E. Lehmann,² S. U. Egelhaaf,¹ and H. E. Hermes¹

¹*Condensed Matter Physics Laboratory, Heinrich Heine University, 40225 Düsseldorf, Germany*

²*Neutron Imaging and Activation Group, Paul Scherrer Institute, 5232 Villigen, Switzerland*

(Dated: 18 July 2016)

Using simultaneous neutron, fluorescence, and optical brightfield transmission imaging, the diffusion of solvent, fluorescent dyes and macromolecules into a crosslinked polyacrylamide hydrogel was investigated. This novel combination of different imaging techniques enables us to distinguish the movements of the solvent and fluorescent molecules. Additionally, the swelling or deswelling of the hydrogels can be monitored. From the sequence of images, dye and solvent concentrations were extracted spatially and temporally resolved. Diffusion equations and different boundary conditions, represented by different models, were used to quantitatively analyze the temporal evolution of these concentration profiles and to determine the diffusion coefficients of solvent and solutes. Solute size and network properties were varied and their effect investigated. Increasing the crosslinking ratio or partially drying the hydrogel were found to hinder solute diffusion due to the reduced pore size. By contrast, solvent diffusion seemed to be slightly faster if the hydrogel was only partially swollen and hence solvent uptake enhanced.

I. INTRODUCTION

Hydrogels are used in a broad range of applications from chemical sensors,^{1,2} responsive coatings,^{3,4} bioadhesives⁵ or soft contact lenses^{6,7} to food products,^{8,9} drug delivery applications,^{10–13} and potential scaffolds for artificial tissue and organs.^{14–17} In many of these applications the diffusion of molecules or particles in and through hydrogels is crucial and the focus of numerous experimental and theoretical studies.^{18–29} However, only few studies explicitly monitor the solvent diffusion and its interplay with the solute motion.^{7,30}

We simultaneously followed solvent and solute to investigate their diffusion and their effects on each other as well as on the hydrogel. This was done using a novel setup, which combines neutron radiography (NR), fluorescence imaging (FI) and optical brightfield imaging (OI).³¹ These three imaging techniques monitor different properties of the samples. In the optical images, contrast is generated by differences in the local optical density of the sample. The hydrogel can be distinguished from the solvent and a potential change in hydrogel size due to solvent uptake or loss can be monitored and also defects in the sample can be observed. FI provides information about the local fluorophore concentration and thus enables us to study, e.g., the diffusion of fluorescent molecules independently of solvent diffusion. The fluorophores can be used to label specific molecules, particles or structures and can additionally report on properties such as *pH*, temperature or chemical environment. By contrast, the interaction of neutrons occurs with the nuclei and thus depends strongly on the specific isotope. Hence, isotope exchange can be exploited to change the contrast between different parts of the sample and thus highlight them. In the present experiments, the contrast

between light (H_2O) and heavy (D_2O) water was used to distinguish water initially inside or outside the hydrogel, respectively. The number of transmitted neutrons, i.e. intensity, provides spatially and temporally resolved information about the composition of the sample.^{31–33} This has already successfully been applied to investigate the flux of liquids.^{34–39} Exploiting this effect, this allowed us to monitor solvent diffusion into and out of the hydrogel. The simultaneous application of these techniques thus provides information on the diffusion of fluorescent molecules or macromolecules as well as solvent into and out of the hydrogel, while the hydrogel size is monitored. The diffusion of the different species was studied for different characteristics of the hydrogel. Its pore size was changed by varying the crosslinking ratio and the degree of swelling. Furthermore, different fluorescent molecules and initial solvent compositions were investigated.

II. MATERIALS AND METHODS

A. Samples

Polyacrylamide (PAAm) networks were synthesized by copolymerization of the monomer acrylamide (AAm) with the tetrafunctional crosslinking agent *N,N'*-methylenebis(acrylamide) (BIS), using ammonium peroxodisulphate (APDS) and tetramethylethylenediamine (TEMED) as redox initiators. Monomer and crosslinker were both purchased from Sigma-Aldrich, APDS from Roth and TEMED from Merck. All components were used without further purification. AAm, BIS and APDS were first separately dissolved in deionized, filtered water and cooled down to 4 °C. To slow down the reaction, the individual solutions were then mixed at this low tempera-

3.3 Solvent and solute ingress into a polymer hydrogel resolved by a combination of imaging techniques

2

ture. The crosslinking ratio (molar ratio of crosslinker to monomer) determines the pore size and the characteristics of the hydrogel; ratios of 1:15 and 1:60 were studied. A 2 ml reaction mixture of the 1:15 hydrogel contained 75 mg of AAm, 10.83 mg of BIS, 6 mg of APDS and 10 μ l of TEMED. The same applied to the 1:60 hydrogel, but the reaction mixture only contained 2.71 mg of BIS. Once mixed with the desired ratio, the reaction mixture was transferred to Teflon molds (3.5 cm \times 3.5 cm \times 0.15 cm) using a glass pipette and allowed to warm up and react at room temperature. After one to two hours, polymerization was complete and the hydrogel was transferred into a larger container filled with deionized water. At this point, the hydrogels could still take up water and swell. With gravimetric measurements, it was found that all hydrogels used here swelled for three to five days. The hydrogels hence were left in deionized water for one week to ensure swelling was complete. During this time, the excess water was exchanged every day in order to wash out residual chemicals that had not reacted.^{40,41} Afterwards, discs with a radius $a \approx 0.3$ cm to 0.5 cm were cut from the hydrogels using a stamp. The same preparation protocol was applied for D₂O-hydrogels but in every step, D₂O (Deutero GmbH, Kastellaun, Germany, minimum content of 99.9% D₂O was used instead of H₂O. All vials with solutions containing D₂O were flushed with nitrogen after mixing in order to reduce H₂O uptake from moisture in the air.

Some hydrogel discs were partially dried before the measurement, leading to a change in hydrogel pore structure. During drying, solvent evaporates from the surface of the hydrogel discs, leading to an inhomogeneous solvent distribution inside the hydrogel. Thus, the dried gels were kept in small, tightly sealed containers for at least three days before the measurement to achieve homogeneity. The degree of swelling, m_{ds} , of every sample was determined directly before the measurements. It is defined via the mass fraction of the hydrogel sample, m_{gel} , with respect to the mass of the fully swollen gel, $m_{gel,fs}$:

$$m_{ds} = \frac{m_{gel}}{m_{gel,fs}}. \quad (1)$$

Five separately prepared pieces of every type of hydrogel were weighed to determine $m_{gel,fs}$, then dried until all solvent had been removed and then again weighed to get the polymer mass, m_p . This allowed us to calculate the polymer volume fraction in the fully swollen state:

$$\phi_{p,fs} = \frac{m_p \rho_s}{m_p \rho_s + m_s \rho_p}, \quad (2)$$

where $\rho_p = 1.30$ g/cm³ is the polymer density, $\rho_s = 1.00$ g/cm³ and $\rho_s = 1.107$ g/cm³ are the solvent densities for H₂O and D₂O, respectively. The polymer volume fraction, ϕ_p , of partially dried hydrogels was calculated from the experimentally observed sample volume (disc radii determined with OI, Sec. IIC (ii) 3) and the known mass of polymer in the sample, m_p . It is

assumed that ϕ_p is independent of the position within the hydrogel.

The fluorescent dye fluorescein sodium salt (in the following referred to as fluorescein (Fluo) and fluorescein-labeled dextrans with different molar masses; D10, 10 kDa (from Sigma-Aldrich for combined FI and NR and from Invitrogen for separate FI) and D70, 70 kDa (from Sigma-Aldrich) were used. They were dissolved in deionized light (H₂O) or heavy (D₂O) water at concentrations of about 25 μ M, which was found to yield a good fluorescent signal while still being dilute enough to not affect the diffusion coefficients of the fluorescent molecules. The samples that were studied with simultaneous NR, OI and FI experiments are listed in table I.

B. Combined Imaging Experiments

A detailed description of the home-built imaging-apparatus to perform optical transmission imaging (OI) and fluorescence imaging (FI) experiments concurrently with neutron radiography (NR) can be found elsewhere.³¹ The sample was irradiated with a parallel beam of light and a collimated neutron beam at the cold neutron imaging facility ICON at the Paul Scherrer Institute (Villigen, Switzerland) and time series of images were recorded with separate CCD cameras for each imaging technique. The chosen distance of the neutron source aperture, L , and diameter of the aperture, D_{ap} , yielded $L/D_{ap} = 343$. This value, together with the distance between sample and scintillator, l , limit the best possible resolution, u_g , of the neutron radiograph:

$$u_g = \frac{l}{L/D_{ap}}. \quad (3)$$

In these measurements, a 10 μ m thick gadolinium based scintillator (Gd₂SO₂S:Tb) and a cooled charge-coupled device (CCD; Andor Neo sCMOS, 2560 \times 2160 pixels, pixel size: 6.5 μ m) were used to convert transmitted neutrons and record the neutron radiographs, respectively. The effective spatial resolution was found to be better than 100 μ m. Images were collected continuously with an individual measurement time of 20 to 30 s, which was found to be the best compromise between image quality and time-resolution.

Optical transmission and fluorescence imaging were performed with a camera resolution of 10 μ m, a field of view of about 25 mm \times 21 mm and a spatial resolution of about 20 μ m. It was chosen to roughly match the one of the corresponding neutron radiography measurements although a significantly better spatial resolution could be obtained. The wavelength of the optical beam was optimized to excite the fluorophores in the sample (LED lamp with a center wavelength of 490 nm). Optical filters were used in the light path to split the light leaving the sample into attenuated excitation light and emitted fluorescence which

Gel	m_{ds}	1:15, D ₂ O, $\phi_{p,fs} = 0.065$				1:60, D ₂ O, $\phi_{p,fs} = 0.053$						1:60, H ₂ O, $\phi_{p,fs} = 0.038$	
		0.73	0.75	0.8	1.00	0.74	0.75	0.78	0.80	0.81	1.00	0.64	1.00
Solute	H ₂ O								x				
	Fluo D ₂ O					x						sample B	sample A
	Fluo H ₂ O		x		x		x		x	x	x		
	D10 H ₂ O				x		x	x					
	D70 H ₂ O	x				x							

Tab. I. Compositions of the hydrogel samples and solutions investigated are indicated by an x. The crosslinking ratio cr , solvent in the hydrogel, polymer volume fraction in the fully swollen state, $\phi_{p,fs}$, and the degree of swelling m_{ds} of the hydrogel are indicated as well as the different solutes. Samples A and B are discussed in detail in Sec. IV B 1.

are then focused onto the OI and FI cameras, respectively. In NR and OI monochrome cameras were used whereas the FI camera was a color camera.

In a typical experiment, the sample was constrained between two glass plates in a specifically designed sample cell that consisted of an aluminum body and quartz glass windows.³¹ The cell was aligned with respect to the neutron and light beams. As neutron radiography experiments can only be performed at large scale facilities where beam time is severely limited, time series of images were recorded for a maximum of 3 to 8 hours. It was found that for the FI experiments, and especially when the larger dextran molecules were used as diffusers, much longer measurement times would be favorable. Thus, additional longer FI and OI experiments extending over several days were performed with all sample systems indicated in table I. Several neutron and optical images of the hydrogel were collected before the solution was injected into the sample cell. By using a syringe pump that was controlled from outside the bunker of the neutron imaging instrument, the injection process could be followed and the time, t_0 , when the hydrogel was contacted with the solution determined. After injection of the solution, the solvent and the fluorescent molecules diffused into the hydrogel. Diffusion only occurred through the radial edges while the hydrogel faces were covered by the glass windows. FI measurements were continued beyond the end of the NR measurements, until the slightly activated sample cell could be handled and exchanged.

C. Data Reduction

The data were obtained as series of two-dimensional grayscale (OI, NR) or color (FI) images with intensities, $I_{raw}(x, y, t)$. (Note that the dependence on position, (x, y) , and time since the start of the experiment, t , is not explicitly given in the following equations.) As described elsewhere in more detail,^{31,32} based on I_{raw} , the absolute transmission of the sample, T_S , and then the concentration or composition was determined.

(i) Absolute Transmission

In the first step of the analysis of the neutron data, complementary dark images (I_D), taken when all shutters in the neutron beamline were closed, and bright images (I_B), taken with the sample removed from the sample position, were used to apply a pixelwise correction to the images to account for spatial inhomogeneities in the neutron beam and detector efficiency as well as neutron and electronic background, yielding the transmission T :

$$T = \frac{I_{raw} - I_D}{I_B - I_D}. \quad (4)$$

On the series of dark and bright images taken before contact with solution, a median filter was applied to remove randomly distributed and fluctuating bright spots that can be caused by high intensity γ -particles directly hitting the CCD chip. Bright spots in the images of the time series were omitted during the averaging process described later.

Additionally, the mean transmission in a reference area, $\langle T_{ref} \rangle$, where no temporal changes in the image intensity were expected (e.g. a part of the cell body) was calculated for every image:

$$\langle T_{ref} \rangle = \frac{\langle I_{raw,ref} \rangle - \langle I_{D,ref} \rangle}{\langle I_{B,ref} \rangle - \langle I_{D,ref} \rangle}. \quad (5)$$

This was used to calculate the transmission of the sample relative to the reference area, T_{rel} , which is thus not only corrected for spatial but also for temporal fluctuations in the neutron beam intensity:

$$T_{rel} = \frac{T}{\langle T_{ref} \rangle}. \quad (6)$$

The absolute transmission of the sample, T_S , was obtained by

$$T_S = \frac{T_{rel}}{T_{rel,EC}}, \quad (7)$$

3.3 Solvent and solute ingress into a polymer hydrogel resolved by a combination of imaging techniques

4

where $T_{\text{rel,EC}}$ is the relative transmission of the empty sample cell.

Tests showed that the raw optical and fluorescence images did not need to be corrected for inhomogeneities in illumination, detector efficiency or background. As fluorescein emits light with a center wavelength of 525 nm, only the green channel, which contained the fluorescence signal, was used for further analysis.

(ii) Sample Composition

1. Solvent Concentrations from Neutron Radiography

The experimentally determined neutron transmission of the sample, T_S , was used to determine the spatially and temporally resolved sample composition by

$$T_S = e^{-Sd}, \quad (8)$$

where d is the sample thickness and S the specific attenuation coefficient. The investigated samples consisted of up to four components: the polymer, H_2O , D_2O and the fluorescent molecules with the volume fractions ϕ_p , ϕ_H , ϕ_D and ϕ_f , respectively. Due to the low volume fraction of the fluorescent molecules ($\phi_f \approx 10^{-6}$), their contribution to the neutron signal can be neglected and thus:

$$S = \phi_D S_D + \phi_H S_H + \phi_p S_p, \quad (9)$$

with

$$\phi_D + \phi_H + \phi_p = 1. \quad (10)$$

Using equations 8, 9 and 10, ϕ_D , could be determined from T_S :

$$\phi_D = \frac{\ln T_S + (1 - \phi_p) S_H d + \phi_p S_p d}{(S_H - S_D) d}, \quad (11)$$

and ϕ_H , could be obtained similarly, since ϕ_p was known (Sec. II A).

For every component, i , the attenuation coefficient S_i was calculated using the total neutron cross-sections, σ_j , of each kind of nucleus, j , in the material:^{42,43}

$$S_i = \frac{\rho_i}{M_i} N_A \sum_j n_{i,j} \sigma_j, \quad (12)$$

where $n_{i,j}$ is the number of each nucleus j , ρ_i the material density, M_i the molar mass, and N_A Avogadro's constant. Polyacrylamide consists of repeat units $\text{C}_3\text{H}_5\text{NO}$ of molar mass $M_p = 71.08 \text{ g/mol}$ and has a density $\rho_p = 1.30 \text{ g/cm}^3$. Total neutron cross-sections, σ_j , can be found in data libraries:^{42,43} $\sigma_H = 82.36 \text{ b}$, $\sigma_C = 5.5555 \text{ b}$, $\sigma_N = 13.41 \text{ b}$, and $\sigma_O = 4.23219 \text{ b}$ for a neutron wavelength of $\lambda = 0.1798 \text{ nm}$. This yields an attenuation coefficient $S_{p,H} = 4.913 \text{ cm}^{-1}$. If the hydrogels are swollen in D_2O instead of H_2O , hydrogen might be replaced by deu-

terium ($\sigma_D = 7.64052 \text{ b}$), resulting in $S_{p,D} = 0.799 \text{ cm}^{-1}$ (if all H are replaced by D). For light and heavy water, $S_H = 5.648 \text{ cm}^{-1}$ and $S_D = 0.651 \text{ cm}^{-1}$, respectively, were calculated similarly.

The attenuation coefficient of the polymer, S_p , could not be measured easily. Because the value of S_p has a negligible effect on the values of the determined diffusion coefficients of solvent and solute the calculated values were used (see Supplementary Material). However, S_D and S_H were also determined experimentally because they strongly depend on the setting of the instrument (e.g. filters and apertures), the wavelength distribution of the neutrons and also on the sample properties, such as density and possible impurities. Neutron radiographs of a series of H_2O - D_2O mixtures were investigated. Their absolute transmission is (Eqs. 8, 9):

$$-\ln T_S = (\phi_D S_D + \phi_H S_H) d = (S_D - S_H) d \phi_D + S_H d, \quad (13)$$

with $\phi_H = 1 - \phi_D$. Thus, $-\ln T_S(\phi_D)$ decays linearly with slope $(S_D - S_H) d$ and intercept $S_H d$ (Fig. 1). It was found that $S_H = 4.067 \text{ cm}^{-1}$ and $S_D = 0.604 \text{ cm}^{-1}$ best describe the experimental data. Although these values significantly deviate from the values calculated for $\lambda = 0.1798 \text{ nm}$, they agree with values previously measured at ICON.⁴⁴ Interestingly, the value of the neutron attenuation coefficients S_D , S_H and S_p were found to not affect the value of the diffusion coefficient determined by a fit to the transmission in the center of the hydrogel (Sec. IV B).

The neutron radiographs of the H_2O - D_2O mixtures were recorded in the same sample cell as used in the diffusion experiments, with the optical imaging setup in place and with an expected sample thickness of $d = 0.101 \text{ cm}$. The

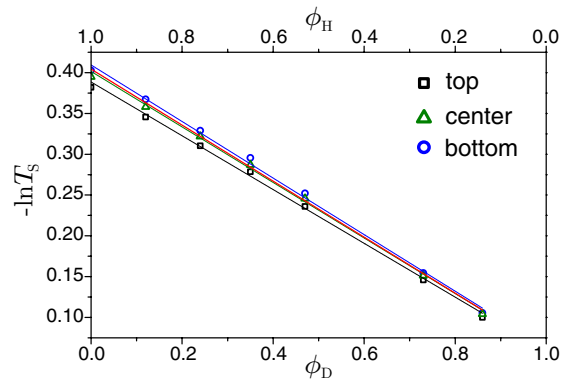


Fig. 1. Absolute neutron transmission, T_S , of mixtures of D_2O and H_2O with their volume fractions, ϕ_D and ϕ_H , respectively. The mixtures were contained in the same sample cell as used for the other experiments. The transmission, T_S , was averaged over an area of 40×40 pixels in the top, center and the bottom of the cell (as indicated). A linear fit (Eq. 13) was applied to the individual data sets (lines of corresponding colors) and their average (red line).

sample cell was not moved between the measurements but rinsed with an appropriate amount of the mixture to be measured next to match the experimental conditions to those of the actual experiments. This was important because for H₂O the measured absolute transmission decreases with increasing distance of the sample from the scintillator due to incoherent scattering.^{45,46} Furthermore, the sample thickness, d , might slightly vary with sample position although care was taken when the sample cells were manually screwed together. The variation in d was estimated by determining the transmissions at the top, center, and bottom of the cell separately (Fig. 1). Indeed, the transmission T_S slightly depends on the location as does the slope of $-\ln T_S$ versus the H₂O-D₂O composition. We found that the thickness at the top and bottom differed by about -3% and $+2\%$ from that at the center, respectively; thus $d = 0.101 \pm 0.003$ cm. Hence, in the data analysis the sample thickness d has to be considered carefully. This is particularly important for large H₂O content, where T_S shows a stronger variation due to the larger total neutron cross-section of hydrogen. In general, hydrogen in H₂O mainly attenuates the neutron beam by incoherent scattering, which influences the measured transmission. This can lead to blurry radiographs and an underestimated H₂O content. It was previously shown that incoherent scattering from H₂O samples plays a dominant role for sample thicknesses greater than 0.2 cm.^{47,48} As our samples are thinner and we observe a very sharp interface between the reservoir edge and the sample cell in the neutron radiographs³¹ (not shown), these effects are neglected in the present experiments.

2. Fluorophore Concentrations from Fluorescence Imaging

For all fluorescent molecules studied here, a linear relation between fluorescence intensity and concentration was found in the concentration range of 0 to 50 μM . Thus, the intensity can directly be related to the concentration, ϕ_f . However, the absolute concentration could not be deduced from the intensity as it is affected by the illumination and the alignment of the sample cell as well as photobleaching, which might also have occurred before the measurement. The absolute detected intensities between repeat measurements performed under the same experimental conditions varied by less than 15%. A normalization of the raw intensities with the initial and final values of the intensity inside the hydrogel, I_i and I_∞ , respectively, was performed to obtain a normalized volume fraction of fluorescent molecules:

$$\phi_f = (I - I_i)/(I_\infty - I_i) \quad (14)$$

This resulted in a very good agreement of ϕ_f between different measurements and hence indicates good reproducibility.

3. Hydrogel Radius from Optical Imaging

For every time step, the hydrogel radius was determined from the optical transmission images. The area, $A(t)$, taken up by the hydrogel was determined by applying a reasonable threshold and using the image processing software ImageJ. Then the radius of a circle with the equivalent area, $a(t) = \sqrt{A(t)/\pi}$, was calculated.⁴⁹

(iii) Spatial Averaging

The time dependences of the detected signals, i.e. of the absolute neutron transmission, $T_S(x, y, t)$, and the fluorescence intensity, $I(x, y, t)$, were analyzed in two ways. First, the signal measured in a limited region of the sample, here the center of the hydrogel, was considered as a function of time. To improve statistics, the average over an area of 20×20 pixels, which is small compared to the hydrogel disc radius ($a \approx 350$ pixels), was determined for each image.

In a second approach, intensity profiles were calculated for each time step. An image recorded shortly before (NR) or immediately after (FI) the hydrogel was contacted with solution was used to define the initial hydrogel-solution interface. This was used to calculate for each pixel its shortest distance, r^* , to the initial interface using a Danielsson algorithm.⁵⁰ By averaging all signals at positions with the same r^* , profiles were calculated. An upper threshold was applied in the averaging process to remove bright spots in the neutron radiographs that are caused by, e.g. high intensity γ -particles. Due to the macroscopic sample size, this approach yielded very good statistics except in the center of the hydrogel disc. In the following, we use the normalized distance to the center of the hydrogel, $r/a = 1 - r^*/a$.

(iv) Photobleaching Correction

Even though the excitation light was not focused into the sample and its intensity was minimized, photobleaching of the fluorescent dyes was observed especially for long measurements of several hours. This made a photobleaching correction necessary.^{51,52}

We considered a region in the reservoir around the hydrogel, where for long times the decrease of the fluorescence intensity is mainly governed by bleaching rather than dilution. The time-dependence of the fluorescence intensity of this region was fitted by an exponential decay, which yielded the time-dependent bleach parameter, $\xi(t)$. Then the intensities, $I(x, y, t)$, or equivalently, the intensity profiles, $I(r, t)$, were corrected by dividing through $\xi(t)$.

It was found that the bleaching behavior in the reservoir and inside the hydrogel were not necessarily identical. Thus, a long measurement was performed. The intensity in the center of a fully swollen 1:60 hydrogel

3.3 Solvent and solute ingress into a polymer hydrogel resolved by a combination of imaging techniques

6

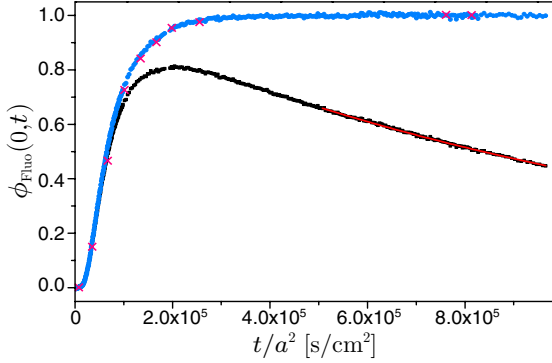


Fig. 2. Normalized fluorescein concentration, $\phi_{Fluo}(0, t)$, in the center ($r = 0$) of a hydrogel (sample A) with radius a (Tab. II) as a function of time, t , without (black squares) and with (blue circles) correction for photobleaching. Photo-bleaching is assumed to lead to an exponential decay of the intensity (red line). The magenta crosses indicate $\phi_{Fluo}(0, t)$ obtained at very few times, t , thus avoiding photobleaching.

is expected to initially increase and then saturate when the equilibrium concentration is reached. However, for long times the intensity decreases due to photobleaching (Fig. 2). The long-time behavior again was fitted by an exponential decay, yielding $\xi(t)$, which was then used for the photobleaching correction inside the hydrogel. The procedure was tested by performing measurements during which photobleaching was avoided by illuminating the sample only occasionally, yielding very similar results (Fig. 2).

III. DIFFUSION – THEORETICAL MODELS

The cylindrical hydrogels were sandwiched between two parallel glass plates, which prevent flux through the faces of the hydrogels. Thus, the hydrogels can be described as infinitely long cylinders with radial diffusion only. These cylinders are immersed in a finite unstirred reservoir. To our knowledge, there is no model that considers such a boundary condition and different diffusion coefficients in the cylinder and reservoir. Thus, different solutions for the cylindrical geometry with similar, although not identical boundary conditions were compared and used to interpret the data.

A. Models 1a and 1b: Cylinder in a stirred, infinite or finite reservoir

The first model describes radial diffusion into a cylinder of radius a and volume V_{cyl} immersed in a stirred reservoir of volume $V_{res} = \beta V_{cyl}$. This situation is identical to an unstirred reservoir with an (infinitely) large diffusion coefficient in the reservoir. Due to stirring, the concentration in the reservoir, $\phi_{res}(t)$, is uniform and only

depends on time and the initial concentration $\phi_{res,i}$. The initial and final concentrations inside the cylinder are denoted as ϕ_i and ϕ_∞ , respectively. Mass conservation implies $\phi_\infty = V_{res} \phi_{res,i} / (V_{res} + V_{cyl})$ in the cylinder and reservoir at equilibrium. Thus, $\phi_{res}(t)$ decreases with time. These boundary conditions lead to the following expression for the time and position dependent concentration in the cylinder:⁵³

$$\frac{\phi(r, t) - \phi_i}{\phi_\infty - \phi_i} = 1 + \sum_{n=1}^{\infty} \frac{(4 + 4\beta) \exp(-Dq_n^2 t/a^2) J_0(q_n r/a)}{(4 + 4\beta + \beta^2 q_n^2) J_0(q_n)}, \quad (15)$$

where D is the diffusion coefficient, q_n are the positive roots of $\beta q_n J_0(q_n) + 2J_1(q_n) = 0$, J_0 is the Bessel function of the first kind of order zero, and J_1 is the Bessel function of the first order. In the following, this will be called model 1b.

In the case of an infinite reservoir ($\beta \rightarrow \infty$, model 1a), $\phi_{res}(t)$ remains constant and the concentration in the cylinder, $\phi(r, t)$, becomes:⁵³

$$\frac{\phi(r, t) - \phi_i}{\phi_\infty - \phi_i} = 1 - \frac{2}{a} \sum_{n=1}^{\infty} \frac{\exp(-D\alpha_n^2 t) J_0(r\alpha_n)}{\alpha_n J_1(a\alpha_n)}, \quad (16)$$

where α_n are the positive roots of $J_0(a\alpha_n) = 0$.

Although this model assumes a stirred reservoir, for an unstirred reservoir it becomes a good approximation if diffusion outside the cylinder is very fast compared to diffusion inside the cylinder, which results in an approximately uniform concentration in the reservoir. However, if the experimentally observed concentration profile outside the cylinder is not constant, it cannot be described by this model.

B. Model 2: Cylinder in an unstirred, infinite reservoir

Since in this model the reservoir is not stirred, a concentration profile develops inside and outside the cylinder. Inside the cylinder, the concentration increases from the initial uniform concentration ϕ_i to the uniform equilibrium concentration ϕ_∞ . By contrast, in the reservoir, the concentration is initially uniform, $\phi_{res,i}$, then decreases toward the cylinder to eventually rise again towards the initial, uniform reservoir concentration, $\phi_{res,i}$, due to the infinite reservoir volume. The concentration profiles can be calculated inside and outside the cylinder.⁵³

$$\phi(r, t) = \phi_\infty + \frac{\phi_i - \phi_\infty}{2Dt} e^{-r^2/4Dt} \int_0^a e^{-r'^2/4Dt} I_0\left(\frac{rr'}{2Dt}\right) r' dr', \quad (17)$$

with I_0 , the modified Bessel function of the first kind of order zero. In the center of the cylinder ($r = 0$) a much simpler expression is found:

$$\phi(0, t) = \phi_i + (\phi_\infty - \phi_i) e^{-a^2/4Dt}. \quad (18)$$

In both models, the diffusion coefficient is assumed to be independent of concentrations of the diffusing molecules. Although in our experiments the local concentrations change over the course of a measurement their effect on the diffusion coefficient is considered small enough to be neglected. Furthermore, the concentration profile covers the entire hydrogel and large part of the reservoir, but only the profile in the hydrogel is considered. Thus, the reservoir only enters through the concentration at the interface of the cylinder which was fitted. Thus emphasis is given to the diffusion in the hydrogel and the diffusion coefficient in the reservoir is assumed to be identical to the one in the hydrogel to reduce the number of free parameters. The above models are compared for typical values of our experiments in the Supplementary Material.

IV. RESULTS AND DISCUSSION

A. Images and Profiles

Applying OI, FI, and NR simultaneously, the evolution of the systems was followed in order to study the diffusion of solvent and solute into polymer hydrogels. The obtained data is illustrated for the case of a 1:60 hydrogel swollen in D₂O with a degree of swelling $m_{ds} = 0.75$ that was contacted with fluorescein in H₂O (Fig. 3). OI indicates that the size of the hydrogel remained about constant, i.e. the hydrogel did not swell or shrink significantly (Fig. 3 (a)). A slight change in contrast due to solvent and solute ingress can be observed in the OI images. Additionally, small defects, such as an air bubble in the hydrogel, can be identified in the brightfield images and these areas were omitted in the averaging process of the other imaging techniques. As observed by FI, the fluorescence intensity and thus the dye concentration inside the hydrogel increased with time and the front broadened (Fig. 3 (b)). The same small air bubble is observed with FI as in OI. NR shows that the neutron transmission inside the hydrogel decreased with time starting at the hydrogel-solution interface, which also becomes blurred. (Fig. 3 (c)). Due to the significantly higher neutron attenuation coefficient of H₂O compared to D₂O, this implies that H₂O diffused into the hydrogel. Thus, mixing of the solvents inside and outside the hydrogel can be captured by NR. In NR the air bubble is better visible at later times as the contrast between air and D₂O is much smaller than between air and H₂O.

The images were quantitatively analyzed to yield the time-evolutions of the concentration profiles and of the concentration in the center of the hydrogel (Sec. II C (iii)). Fig. 4 shows profiles of the fluorescence intensity, $I(r, t)$, and hence volume fraction of the fluorescent molecules, $\phi_f(r, t)$, as well as neutron transmission, $T_S(r, t)$, and hence H₂O volume fraction, $\phi_H(r, t)$, for different times. The data were obtained from four simultaneous FI (top row) and NR (middle and bottom row) experiments, with different hydrogels and diffusants. The

effect of the crosslinking ratio (Fig. 4 (a) and (b)) as well as the molar mass and hence the size of the diffusant, namely fluorescein, 10 kDa, and 70 kDa dextrans (Fig. 4 (b)-(d)) is illustrated. The profiles depicted in Fig. 4 (b) correspond to the images shown in Fig. 3.

The fluorescence intensity profiles, $I(r, t)$, were normalized to 0 inside the initial hydrogel and 1 in the reservoir close to the hydrogel (Eq. 14). They can directly be related to the concentration of fluorescent molecules, $\phi_f(r, t)$ (Sec. II C (ii) 2). With time, $I(r, t)$ increases inside the hydrogel and reaches further into the hydrogel while it decreases outside the hydrogel. The profiles hence reflect the ingress of fluorophores. The changes in the concentration profiles occur at a slower rate as the size of the diffusing molecules increases. By contrast, a decreasing crosslinking ratio within the range studied does not seem to influence the dye diffusion very strongly. For some samples, a particularly high fluorescence intensity was observed close to the hydrogel-solution interface. This can be seen as a peak in $I(r, t)$ that becomes more pronounced with time (Fig. 4 (a)). It is attributed to scattering at the interface which may neither be smooth nor perpendicular to the illumination, or different fluorescence intensities inside, in the vicinity or outside the hydrogel. This is supported by the finding that no systematic behavior was observed. In the present system a higher intensity inside the hydrogel compared to the reservoir is not caused by an increased fluorophore concentration due to attractive interactions between the hydrogel and the diffusing molecules.²⁹ In many measurements, the intensities inside and outside the hydrogel were identical after equilibration. A similar fluorescence intensity peak just inside the hydrogel was previously seen when concentration profiles of fluorescent macromolecules were observed diffusing into HEMA/MAA hydrogel slabs by confocal microscopy.²⁰ In those experiments, the hydrogel slabs were immersed in fluorescent macromolecule solution and removed for taking the confocal images at predefined times. Thus the concentration profiles could not be measured in-situ. The observed intensity peaks were attributed to a locally dried hydrogel surface due to the measurement procedure and neglected in their analysis. Interestingly, the authors found that the measured concentration profiles did not change whether the reservoir was stirred between taking the confocal images or not.²⁰

The neutron transmission was converted to H₂O volume fraction profiles, $\phi_H(r, t)$, using Eq. 11. They reflect the solvent ingress into the hydrogel and the increasing amount of H₂O in the hydrogel. At the same time, the H₂O content in the reservoir slightly decreases. Solvent ingress occurs much faster than solute ingress due to the smaller size of the solvent molecules compared to the size of fluorescein.

In contrast to the FI results, the neutron transmission, $T_S(r, t)$, does not show an increased intensity at the interface. The observed neutron transmission is less affected by scattering since the same structures, here the

3.3 Solvent and solute ingress into a polymer hydrogel resolved by a combination of imaging techniques

8

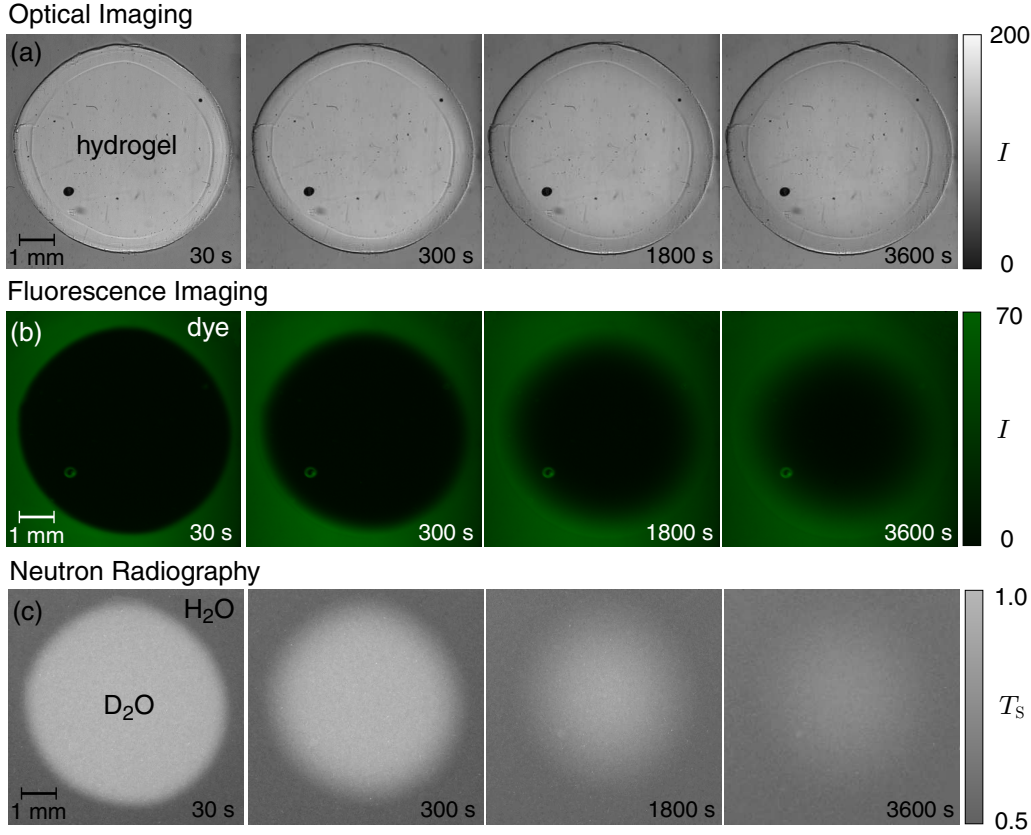


Fig. 3. Series of simultaneously recorded (a) optical brightfield images, (b) fluorescence images, and (c) normalized neutron radiographs of a 1:60 hydrogel swollen in D₂O with a degree of swelling $m_{ds} \approx 0.75$, contacted with fluorescein in H₂O at times since contact as indicated.

hydrogel-solution interface, scatter at smaller scattering angles due to the smaller wavelength of neutrons compared to light. Neutrons scattered by relatively large structures are scattered in forward direction and thus arrive in (about) the same pixel as the transmitted neutrons. Thus, scattering remains largely unnoticed.

The increase in H₂O volume fraction, $\phi_H(0, t)$, in the center of the hydrogels (Fig. 5) provides the time scale and thus the diffusion coefficient of the influx and also facilitates the comparison of different measurements more directly. The addition of small fluorescent molecules or larger macromolecules as well as the crosslinking ratio of the hydrogel do not influence the diffusion behavior of the solvent very strongly. This is consistent with the similarity of the solvent profiles of the four measurements shown in Fig. 4 (bottom). Nevertheless, with increasing solute size, $\phi_H(0, t)$ appears to be very slightly shifted to longer times, indicating slightly slower diffusion of the solvent in the presence of larger molecules. This is supported by the additional observation that the presence of fluorescein appears to slow down solvent diffusion compared to its absence, i.e. pure water (Fig. 5, inset). This might be due to the hydration of the solutes, which slows

down a small part of the solvent molecules.

B. Quantitative Analysis and Interpretation

The sequence of images (e.g. Fig. 3), profiles (e.g. Fig. 4) and data at the center (e.g. Fig. 5) are quantitatively interpreted using the models presented above (Sec. III). Due to their specific features, all four combinations of hydrogel solvent (H₂O or D₂O) and contacting solvent (H₂O or D₂O) can provide information on different aspects of the diffusion of solvent and solute. Thus, they are presented and discussed in turn.

1. H₂O-Hydrogels Contacted with D₂O Solutions

Two different hydrogels with a crosslinking ratio of 1:60, fully (sample A) and partially (sample B) swollen in light water (H₂O), respectively, were contacted with D₂O containing fluorescein (Tab. II).

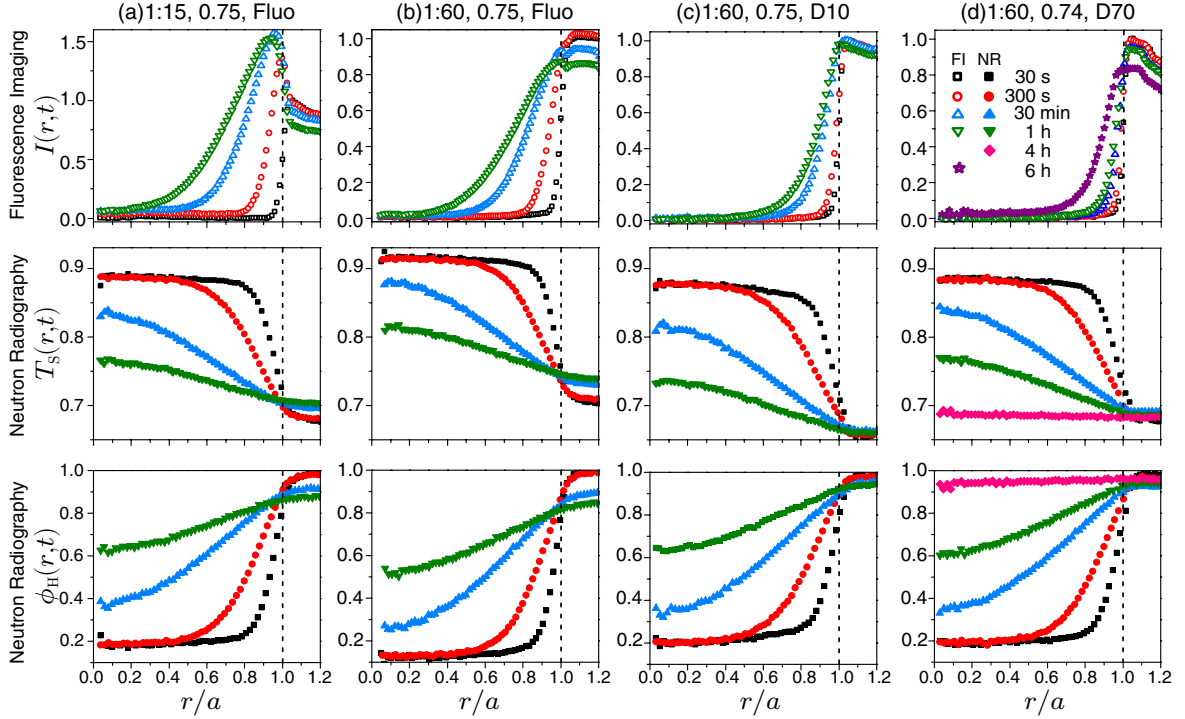


Fig. 4. (top) Intensity profiles, $I(r, t)$, determined by FI and (middle) transmission profiles, $T_S(r, t)$, and (bottom) H_2O volume fraction profiles, $\phi_H(r, t)$, both based on NR as a function of the normalized distance to the hydrogel cylinder, r/a , at different times, t , after contact with solution (as indicated). The samples consisted of D_2O -hydrogels with different crosslinking ratios and a degree of swelling, $m_{ds} \approx 0.75$ (as indicated), that were contacted with H_2O solutions containing different fluorescent molecules (fluorescein, 10 kDa dextran, 70 kDa dextran as indicated).

(i) Hydrogel size from optical imaging

Optical brightfield transmission imaging allows us to follow the changes in the hydrogel. Slight decreases in the hydrogel radii of 4% and 0.4% were observed for samples A and B, respectively (Tab. II). Initially the polymer network was swollen in H_2O , while the D_2O -content increased during the experiments. Polyacrylamide hydrogels are known to exhibit a different degree of swelling depending on the solvent.^{54,55} This is confirmed by the dependence of the polymer volume fraction in the fully swollen hydrogels, $\phi_{p,fs}$, on the solvent: $\phi_{p,fs} = 0.053$ and $\phi_{p,fs} = 0.038$ for D_2O and H_2O , respectively (Tab. I). Fully swollen H_2O -hydrogels were found to shrink when contacted with D_2O , and D_2O -hydrogels to swell when contacted with H_2O . However, some H_2O -hydrogels were also observed to shrink after contact with H_2O , indicating that factors other than solvent quality can also induce size changes. Due to the very small fluorophore concentration, osmotic deswelling of the hydrogels is not expected. This is confirmed by the observation that equilibrated, fully swollen hydrogels did not change their size within two weeks after contact with solutions with even higher dye concentrations. Moreover, deswelling was oc-

asionally seen after hydrogels were contacted with pure water. An apparent shrinking of the hydrogel might also be caused by a slight expansion of the sample cell.

(ii) Diffusion of solvent into the hydrogel

Neutron radiography allows us to follow the diffusion of solvent. In a first step, only the center of the hydrogel disc is considered. Figure 6 (a) shows the time dependence of the D_2O volume fraction in the center of the hydrogels, $\phi_D(0, t)$, for both samples. Since $\phi_D(0, t)$ depends on the radius, a , of the hydrogel, the time axis is scaled as t/a^2 (Fig. 6 (b)). This almost leads to an overlap of the two NR curves, indicating that the diffusion of D_2O hardly depends on the initial degree of swelling. All three models have been fitted to the data (Tab. II and Fig. 6 (a)). Models 1a and b both describe the data very well. By contrast, model 2 fails to fit the long time behavior. If the final volume fraction, $\phi_{D,\infty}$, is fixed to an unrealistically high value, at least the initial rise in $\phi_D(0, t)$ can be fitted. In the fully swollen hydrogel A, the diffusion coefficient, D_D , is very close to the bulk diffusion coefficient of D_2O ($1.7 \times 10^{-5} \text{ cm}^2/\text{s}$).⁵⁶⁻⁵⁸ For the partially swollen hydrogel B, D_D , as determined us-

3.3 Solvent and solute ingress into a polymer hydrogel resolved by a combination of imaging techniques

10

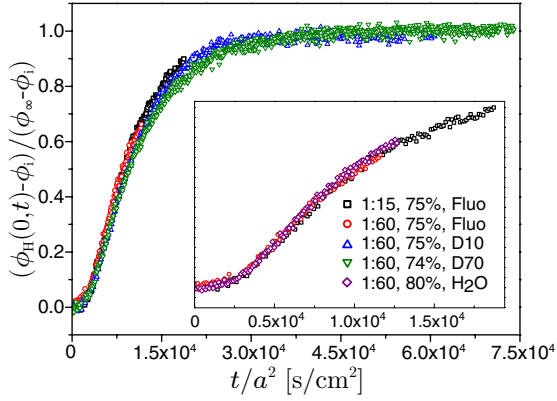


Fig. 5. Normalized H_2O volume fraction, $\phi_{\text{H}}(0,t)$, in the center of the hydrogel with radius a as a function of time t after the D_2O -hydrogel has been contacted with H_2O solutions for different sample compositions, i.e. crosslinking ratios, degree of swelling $m_{\text{ds}} \approx 0.75$, and fluorescent molecules (fluorescein, 10 kDa dextran, 70 kDa dextran as indicated). The inset shows $\phi_{\text{H}}(0,t)$ at short times and includes a hydrogel contacted with pure H_2O . Small differences in the initial disc radii, a , are accounted for by normalizing the time t with the squared radius, a^2 .

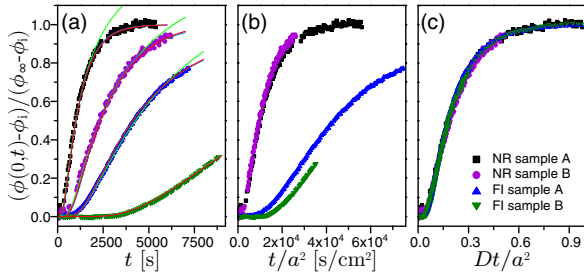


Fig. 6. Normalized volume fractions of D_2O , $\phi_{\text{D}}(0,t)$, and fluorescein, $\phi_{\text{Fluo}}(0,t)$, in the center of the H_2O -hydrogels with radius a (samples A and B, Tab. II) as a function of (a) time, t , after contact with D_2O solution (b) normalized time, t/a^2 , and (c) $\tau = Dt/a^2$ with D the diffusion coefficient as determined based on model 1a (Tab. II) by simultaneous FI and NR measurements. The FI data in (c) were complemented by long repeat measurements of both samples. Lines in (a) represent fits based on models 1a (red), 1b (blue), and 2 (green).

ing model 1 is about 12% larger (Sec. IV B 1 (iv)). The corresponding fitted $\phi_{\text{D},\infty}$ are only slightly higher than expected (Tab. II).

Figure 7 shows the experimentally determined D_2O volume fraction profiles, $\phi_{\text{D}}(r,t)$, for sample B. To take hydrogel swelling into account, for each time step, the actual radius, $a(t)$, was determined from the corresponding brightfield image and used in the model calculations. The D_2O volume fraction decreases outside the hydrogel, but at the interface ($r = a$) the concentration is essentially constant. Thus, model 1b, which predicts a decreasing

	Sample A	Sample B	Sample C
cr	1:60	1:60	1:60
m_{ds}	1.00	0.64	1.00
$\phi_{\text{p},i}$	0.038	0.060	0.038
$\phi_{\text{H},i}$	0.962	0.940	0.962
a_i [cm]	0.310	0.489	0.341
a_∞ [cm]	0.298	0.487	0.325
d_i [cm]	0.146 (0.150)	0.098 (0.100)	– (0.100)
final D_2O volume fraction $\phi_{\text{D},\infty}$			
expected	0.875	0.745	–
Models 1a & b	0.880	0.753	–
Model 2	1.250	1.100	–
D_2O diffusion coefficient D_{D} [10^{-6} cm²/s]			
1a, profile	17.5 ± 0.2	19.8 ± 0.2	–
1a, center	17.5 ± 0.1	19.8 ± 0.2	–
1b, center	17.1 ± 0.1	19.1 ± 0.2	–
2, center	19.2 ± 0.6	22.9 ± 0.5	–
Fluorescein diffusion coefficient D_{Fluo} [10^{-6} cm²/s]			
1a, profile	4.09 ± 0.02 (4.01 ± 0.02)	3.71 ± 0.03 (3.68 ± 0.02)	– (3.89 ± 0.02)
1a, center	4.07 ± 0.03 (4.02 ± 0.01)	3.60 ± 0.03 (3.62 ± 0.02)	– (3.85 ± 0.01)

Tab. II. Sample composition and size for measurements of H_2O -hydrogels contacted with D_2O solution containing fluorescein; crosslinking ratio cr , degree of swelling m_{ds} , initial polymer and H_2O volume fractions, $\phi_{\text{p},i}$ and $\phi_{\text{H},i}$, respectively, initial and final hydrogel radii, a_i and a_∞ , respectively and initial sample thickness, d_i . The final D_2O volume fraction, $\phi_{\text{D},\infty}$, was calculated based on the composition and fitted using models 1a, 1b, and 2. The diffusion coefficient of D_2O was obtained by fitting models 1a, 1b, and 2 to the data in the center. The whole profile and the FI data was analyzed based on model 1a only. Values in brackets correspond to the average values of three to five additional long FI measurements during which equilibration of the hydrogel and reservoir was achieved.

concentration at the interface, is not appropriate and especially fails close to the hydrogel border. By contrast, model 1a describes the profiles inside the hydrogel very well although it assumes a homogeneous reservoir concentration. In the following, model 1a will be used to interpret the data. The fitted values of the diffusion coefficients (Tab. II) are identical to the values obtained by considering the center only. On the other hand, the decrease of $\phi_{\text{D}}(r,t)$ in the reservoir can be fitted by model 1b, yielding a diffusion coefficient about 6% larger than derived from the data in the center.

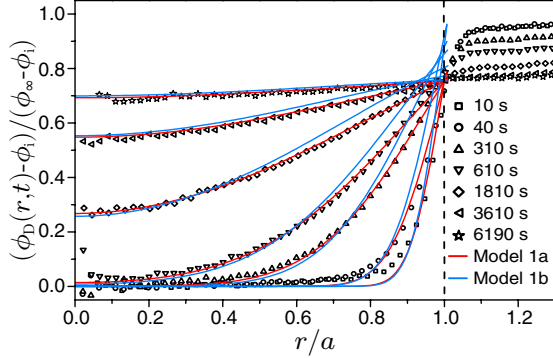


Fig. 7. Normalized D₂O volume fraction profiles, $\phi_D(r, t)$, for different times (as indicated) after the H₂O-hydrogel (sample B) has been contacted with D₂O solution containing fluorescein as obtained by NR. Fits based on models 1a (red lines) and 1b (blue lines) as well as the data are corrected for the time dependence of the hydrogel radius, $a(t)$.

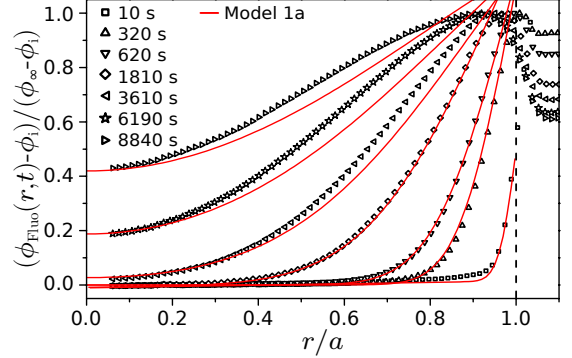


Fig. 8. Normalized fluorescein concentration profiles, $\phi_{\text{Fluo}}(r, t)$, for different times (as indicated) after the H₂O-hydrogel (sample B) has been contacted with D₂O solution containing fluorescein as obtained by FI. Fits based on model 1a (red lines) as well as the data are corrected for the time dependence of the hydrogel radius, $a(t)$.

(iii) Diffusion of fluorescent dye into the hydrogel

The increase of the fluorophore concentration in the center of the hydrogel was followed (Fig 6 (a)). The restriction to the center of the hydrogel avoids effects of the hydrogel-solution interface like scattering (Sec. IV A). However, in the center equilibrium was not reached during the measurement time due to the slower diffusion compared to that of the solvent (and the limited neutron beam time). Thus the equilibrium values of the fluorescein concentration, $\phi_{\text{Fluo},\infty}$, which are required to normalize the data, were extracted from a region closer to the hydrogel border, where saturation was reached earlier. In contrast to the time dependence of the D₂O volume fraction, $\phi_D(0, t)$, scaling of the time t with a^2 does not lead to an overlap of the FI data (Fig. 6 (b)). This indicates a smaller diffusion coefficient of fluorescein in the partially swollen sample B than in the fully swollen sample A. Analysis with model 1a yields diffusion coefficients $D_{\text{Fluo},A} = 0.407 \times 10^{-5} \text{ cm}^2/\text{s}$ and $D_{\text{Fluo},B} = 0.360 \times 10^{-5} \text{ cm}^2/\text{s}$. If the normalized concentration curves are plotted as a function of the dimensionless time $\tau = Dt/a^2$ all four curves of sample A and B agree (Fig. 6 (c)). They also agree with longer FI measurements, which were performed outside the neutron beamline.

In the experimental data the initial plateau in the concentration trace, which represents the time needed for the first fluorescent molecules to reach the hydrogel center, is not always as pronounced as expected. The reason for this is a not perfectly perpendicular and smooth hydrogel border leading to an already initially broadened concentration profile.

The normalized fluorescein concentration profiles, $\phi_{\text{Fluo}}(r, t)$, were also fitted by model 1a. The fit parameter $\phi_{\text{Fluo},\infty}$ was adjusted for each profile individually such

that it matched the experimental value at the hydrogel-solvent interface. This accounts for the effect of photo-bleaching and for potential changes in sample thickness. As already discussed in section IV A, in some samples a particularly high fluorescence intensity close to the hydrogel-solvent interface was found, which was interpreted as an artifact caused by scattering from the interface. The corresponding peak in the concentration profiles propagates further into the hydrogel with increasing time (as seen in Fig. 8) and leads to an inflection point in the profiles that can not be fitted using model 1a. For short and intermediate times, the fit works nicely, if the region close to the hydrogel-solution interface is ignored. The validity of this fitting procedure was proven by many additional measurements (outside the neutron beamline), where this artifact was not seen and which yielded comparable diffusion coefficients. This approach was also used previously by another group.²⁰ For all FI measurements, three to five additional long measurements, during which equilibration of the hydrogel and reservoir was achieved, were performed and the results averaged (values in brackets in Tab. II). The results of the individual measurements and analysis of the center intensities and complete concentration profiles show good agreement (Tab. II). Thus, rather short measurement times appear sufficient, which is favorable for the combined imaging experiments requiring central facilities.

(iv) Dependence of diffusion coefficients on hydrogel properties

The diffusion of solvent and fluorophore was found to depend on the hydrogel studied (sample A and B). These differed in thickness and their degree of swelling, which affects the pore size and influx of solvent. To disentangle

3.3 Solvent and solute ingress into a polymer hydrogel resolved by a combination of imaging techniques

12

gle the effects of these two parameters, we performed FI measurements with a third sample, which had the degree of swelling of sample A and the thickness of sample B (sample C, Tab. II).

The diffusion coefficient of fluorescein, D_{Fluo} , increases from sample B to C to A. The reduction of the mean pore size by partial drying of sample B thus leads to a slower fluorescein diffusion. As compression to $d = 0.1$ cm (sample C) also influences the solute diffusion, it appears to affect the pore structure within the hydrogels. With $d = 0.15$ cm, the fully swollen hydrogel discs (sample A) are compressed as little as possible to still guarantee contact with both glass plates. This is hence expected to result in the largest mean pore size and indeed yields the largest diffusion coefficient. Thus the diffusion coefficients reflect the obstruction by pores of different sizes. This is consistent with previous observations on various hydrogels and solutes^{24,26,59–61} as well as theoretical predictions.^{18,27,62}

The diffusion coefficient of D₂O decreases from sample B to A. The diffusion of the much smaller D₂O molecules is expected to be less affected by the pore size, which points to another mechanism increasing its mobility. Even though H₂O is a better solvent than D₂O, the partially swollen H₂O-hydrogel with $\phi_{p,i} = 0.06$ (Tab. II) contains more polymer than a fully swollen D₂O-hydrogel ($\phi_{p,fs} = 0.053$, Tab. I) and is thus expected to take up solvent. This seems to speed up the D₂O influx in order to reach equilibrium.^{63–66} Since this follows similar time-dependencies as diffusion, it cannot be disentangled. This effect is expected to be even more pronounced for D₂O-gels contacted with H₂O, which will be discussed in section IV B 3.

2. D₂O-Hydrogels Contacted with D₂O Solutions

During the handling of D₂O-hydrogel samples the uptake of moisture (H₂O) has to be avoided. To validate the sample preparation and storage procedure, one short combined OI, FI, and NR measurement was performed. A hydrogel partially swollen in D₂O with $m_{ds} = 0.75$ and a crosslinking ratio of 1:60 was contacted with D₂O solution containing fluorescein. Although no change in the neutron transmission was expected, a slight increase in transmission inside the hydrogel was monitored (data not shown). This suggests that some H₂O was contained in the initial D₂O-hydrogel. To determine the fraction of H₂O in the initial hydrogel, the sample thickness, d , is required. Its determination from the neutron transmission of the initial hydrogel is not possible due to the uncertainty in the sample composition. Instead, the transmissions of four regions in the reservoir around the hydrogel right after injection of the D₂O solution were used to determine the sample thickness, $d = 0.098$ cm, which is close to the expected value (0.101 cm). With this value, the initial composition of the sample was calculated (Eq. 11): $\phi_{p,i} = 0.072$, $\phi_{D,i} = 0.768$ and $\phi_{H,i} = 0.160$.

The initial D₂O-hydrogels hence may contain a significant amount of H₂O that originates from moisture during sample preparation and storage. Therefore, the possible contamination with H₂O has been taken into account in the analysis of all measurements with D₂O-hydrogels (Sec. IV B 3).

Having determined the initial fraction of H₂O, not only the diffusion coefficient of fluorescein but also of D₂O was determined. The D₂O volume fraction inside the hydrogel increased from $\phi_{D,i} = 0.768$ to $\phi_{D,\infty} = 0.890$ in equilibrium. This relatively small increase and the short measurement time rendered an analysis based on the data in the center of the hydrogel unreliable. Additionally, the measurement time was not long enough for the fluorescein concentration to approach saturation. Thus, an analysis of the data in the center was not performed. However, the volume fraction profiles were analyzed using model 1a, which resulted in $D_D = 1.89 \times 10^{-5}$ cm²/s and $D_{\text{Fluo}} = 0.369 \times 10^{-5}$ cm²/s, consistent with the above results (Tab. II). The other models also adequately described the NR data and yield the same D_D . This is due to the small absolute change in D₂O volume fraction, which renders the different boundary conditions less crucial (see Supplementary Material). This finding also supports the notion that, for short times, the models are essentially indistinguishable.

3. D₂O-Hydrogels Contacted with H₂O Solutions

Imaging experiments on different D₂O-hydrogels contacted with a selection of fluorescent molecules solved in H₂O (Tab. I) were performed. The measurements and data analysis are illustrated for one D₂O-hydrogel with a crosslinking ratio of 1:60. This hydrogel was partially swollen, $m_{ds} = 0.78$, corresponding to an initial polymer volume fraction, $\phi_{p,i} = 0.068$, and was contacted with H₂O solution containing fluorescent 10 kDa dextran (Figs. 9, 10 and 11). The same analysis procedure was applied to the data from the other D₂O-hydrogels contacted with H₂O solutions and the results are summarized in table III.

(i) Initial and equilibrium composition

From the initial neutron transmission of the solution around the hydrogel, $T_{S,i}^{\text{sol}} = 0.679$, the sample thickness was determined to be $d_i = 0.095$ cm. Using this value, $\phi_{p,i} = 0.068$, and the neutron transmission of the hydrogel before contact, $T_{S,i}^{\text{gel}} = 0.901$ (Fig. 9), $\phi_{D,i} = 0.793$ and $\phi_{H,i} = 0.139$, were determined. They are close to the initial D₂O-H₂O composition found for D₂O-hydrogels contacted with D₂O solutions (Sec. IV B 2). Having determined the initial composition, we turn to the final, equilibrium composition after contact with the H₂O solution. During the measurement, the hydrogel radius increased from $a_i = 0.558$ cm to $a_\infty = 0.582$ cm

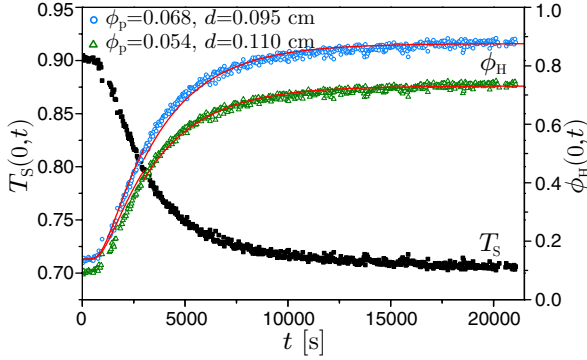


Fig. 9. Transmission, $T_S(0,t)$, and corresponding normalized H_2O volume fraction, $\phi_H(0,t)$, in the center of a partially swollen D_2O -hydrogel with crosslinking ratio of 1:60 as a function of time, t , after contact with H_2O solution containing fluorescent 10 kDa dextran calculated assuming different polymer volume fractions, ϕ_p , and sample thicknesses, d (as indicated). Lines are fits based on model 1a (see text for details).

as determined by OI. Based on a constant sample thickness, d , the final polymer volume fraction $\phi_{p,\infty} = 0.063$ was calculated. Moreover, $T_{S,\infty}^{\text{gel}} = 0.707$ (Fig. 9), implies a final H_2O volume fraction $\phi_{H,\infty} = 0.876$ (Eq. 11). This value is significantly larger than expected based on the sample and reservoir volumes: $\phi_{H,\text{EQ}} = 0.723$. This is in contrast to findings with H_2O -hydrogels contacted with D_2O solutions (Sec. IV B 1), where expected and fitted equilibrium values were very similar. This could be due to the relatively large amount of H_2O in the sample, which might result in more scattering and hence might change the measured transmission. Furthermore, a possibly small deviation in d leads to a larger uncertainty in measured transmission (Fig. 1).

Thus, we do not assume a constant sample thickness, d , but calculate the apparent final sample thickness, d_∞ , based on the expected final H_2O - D_2O sample composition, $\phi_{H,\text{EQ}}/\phi_{D,\text{EQ}} = 3.83$, the transmission, $T_{S,\infty} = 0.707$ as well as the sample geometry, i.e. d_i , a_i and a_∞ as given above. With equations 10, 11 and $\phi_{p,\infty} = (a_i^2 d_i / a_\infty^2 d_\infty) \phi_{p,i}$ this yields $\phi_{H,\text{EQ}} = 0.730$, $\phi_{D,\text{EQ}} = 0.216$, $\phi_{p,\infty} = 0.0539$ and $d_\infty = 0.110$ cm. These values appear more consistent and will thus be used in the following. The same analysis was performed for the other measurements where equilibration between H_2O and D_2O was reached. This resulted in very similar values for d_i , d_∞ and $\phi_{p,\infty}$.

Thus, D_2O -hydrogels contacted with H_2O appear to swell towards the equilibrium state. The swelling appears to slightly change the sample thickness, d , which has to be considered carefully in the data analysis. In fact, the small mismatch between expected and fitted equilibrium sample compositions for H_2O -hydrogels contacted with D_2O solutions, which deswelled during the experiments (Sec. IV B 1) could be explained by a slight decrease in

sample thickness: from $d_i = 0.146$ cm to $d_\infty = 0.143$ cm for sample A and from $d_i = 0.098$ cm to $d_\infty = 0.096$ cm for sample B. This possible small change in d does not, however, affect the fitted values of the diffusion coefficients but only the absolute values of the volume fractions (see Supplementary Material). Similarly, a small variation of the polymer volume fraction, ϕ_p , is found to be negligible (see Supplementary Material).

(ii) Diffusion of solvent into the hydrogel

Based on the limiting sets of parameters, the initial values $\phi_{p,i} = 0.068$ and $d_i = 0.095$ cm and the equilibrium values $\phi_{p,\infty} = 0.054$ and $d_\infty = 0.110$ cm, respectively, two limiting cases for the increase in H_2O volume fraction, $\phi_H(0,t)$, were calculated (Fig. 9). The two data sets represent the initial ($t < 3000$ s) and later behavior with the corresponding radii of the hydrogel. Fits based on model 1a and using $\phi_{H,i} = 0.139$ and the corresponding $\phi_{H,\infty} = 0.876$ (blue) and $\phi_{H,\infty} = 0.730$ (green) both yielded $D_H = 2.11 \times 10^{-5}$ cm^2/s . The diffusion coefficient of H_2O , D_H , is slightly larger than that of D_2O , $D_D = 1.98 \times 10^{-5}$ cm^2/s (Tab. II). This is consistent with previous findings in bulk.⁵⁷ Moreover, in the present situation the difference might be enhanced since H_2O is the better solvent and hence preferentially enters the hydrogel.

With both parameter sets, concentration profiles for distinct time steps were calculated (Fig. 10). For short times ($t \lesssim 3000$ s) using the parameters describing the initial hydrogel and for long times ($t \gtrsim 3000$ s) using the parameters describing the final hydrogel, a fit yielded the same diffusion coefficient as the analysis based on the hydrogel center only. This supports the findings above and the interpretation that the sample thickness increased during

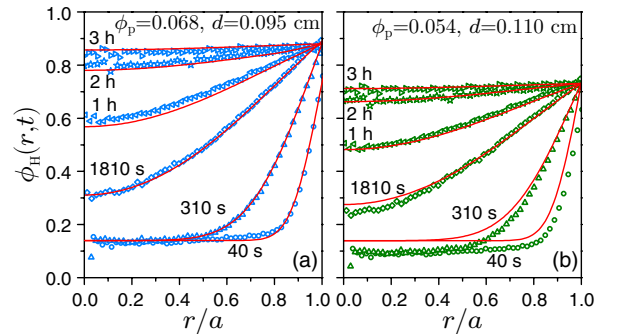


Fig. 10. H_2O volume fraction profiles, $\phi_H(r,t)$, for different times (as indicated) after the D_2O -hydrogel has been contacted with H_2O solution containing fluorescent 10 kDa dextran. The two limiting parameter sets were used for the calculations: (a) $\phi_{p,i} = 0.068$ and $d_i = 0.095$ cm and (b) $\phi_{p,\infty} = 0.054$ and $d_\infty = 0.110$ cm. Fits based on model 1a (red lines) and the data are corrected for the time dependence of the hydrogel radius, $a(t)$.

3.3 Solvent and solute ingress into a polymer hydrogel resolved by a combination of imaging techniques

the measurement.

(iii) Diffusion of fluorescent molecules into the hydrogel

For the same experiment, FI yielded concentration profiles of the fluorescent molecules, $\phi_f(r, t)$ (Fig. 11). FI is not sensitive to the isotope and hence, the initial H₂O contamination of the D₂O-hydrogels did not have to be considered and the data could be analyzed as described in section IV B 1. The normalized D10 volume fraction profiles, $\phi_f(r, t)$, were fitted by model 1a (Fig. 11), yielding the diffusion coefficient of fluorescent 10 kDa dextran, $D_{D10} = 0.085 \times 10^{-5} \text{ cm}^2/\text{s}$. As this value is slightly higher than a published bulk value ($0.083 \pm 0.008 \times 10^{-5} \text{ cm}^2/\text{s}$),²² longer separate FI experiments were performed with D10 from another supplier (Invitrogen as in²²). These measurements yielded qualitatively consistent results, but slightly different (about 15% lower) diffusion coefficients (Tab. III). This is attributed to the different statistics and duration of the experiments as well as possibly e.g. different average molar mass and polydispersity of the dextrans. In all measurements where a D₂O-hydrogel was contacted with H₂O solution containing fluorescent 10 kDa dextran, the fluorescence intensity inside and outside the hydrogel were identical after equilibration was reached. In addition, no enhanced intensity close to the hydrogel-solution interface was observed (Fig. 11).

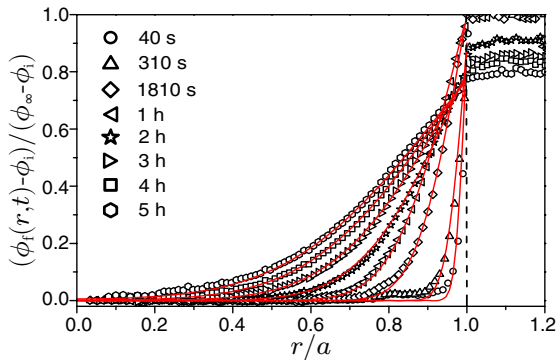


Fig. 11. Normalized fluorescent molecule volume fraction profiles, $\phi_f(r, t)$, for different times (as indicated) after the D₂O-hydrogel has been contacted with H₂O solution containing fluorescent 10 kDa dextran. Fits based on model 1a (red lines) as well as the data are corrected for the time dependence of the hydrogel radius, $a(t)$.

(iv) Dependence of diffusion coefficients on hydrogel properties

The diffusion of different molecules into various hydrogels with different properties was studied. For all samples, the same analysis procedure as described above was

performed. The initial sample thickness, d_i , and H₂O volume fraction, $\phi_{H,i}$, were determined. Then, the H₂O increase in the sample center, $\phi_H(0, t)$, and concentration profiles, $\phi_H(r, t)$, were calculated with the two limiting parameter sets and the diffusion coefficients, D_H , were deduced by fitting model 1a to the data. Due to the need to use central facilities, D_H was obtained from a single measurement only and thus is associated with a relatively large uncertainty. Nevertheless, we found good agreement between the values obtained by considering the center concentrations and profiles, respectively. With FI and OI, three to five additional longer measurements were performed and the concentration profiles of the fluorescent molecules, $\phi_f(r, t)$, were analyzed based on model 1a. For the largest and hence slowest dextran (D70), equilibrium was only reached after about 14 days (data not shown). Due to the very long measurement time, a very stable setup was required and at later times images were recorded only once per day to reduce photobleaching. The obtained diffusion coefficient $D_{D70} = 0.027 \times 10^{-5} \text{ cm}^2/\text{s}$ is consistent with the ones obtained in shorter measurements (Tab. III). Hence, again, short measurements seem to provide reliable results, as in the case of H₂O-hydrogels and D₂O solutions (Sec. IV B 1). The results for all samples are summarized in table III.

The solvent diffusion coefficient is comparable to previous findings^{56–58} and slightly increases upon partial drying of the hydrogel. This is in line with the results presented in section IV B 1 and might be related to the solvent uptake during swelling. By contrast, the fluorescent molecule diffusivity decreases with the reduced swelling of the initial hydrogel and hence with the decreasing pore size. In the case of D10, the decrease from the bulk value ($0.083 \pm 0.008 \times 10^{-5} \text{ cm}^2/\text{s}$)²² is less pronounced than for the larger D70 ($0.030 \pm 0.002 \times 10^{-5} \text{ cm}^2/\text{s}$)²² which drops very significantly (Tab. III). The decrease of the diffusion coefficient of Fluo is more pronounced than D10 and less than D70. A decrease of diffusion coefficients with decreasing pore size is due to the increasing obstruction by the hydrogel and consistent with previous findings in similar systems^{23,24,26,59,67} and from theoretical considerations.^{18,27,62} By contrast, the larger drop in the case of Fluo compared to D10 might be due to specific interactions.²⁹

Furthermore, the H₂O diffusion coefficient, D_H , tends to very slightly drop with increasing size of the solute, consistent with the observations described above (Fig. 5).

4. H₂O-Hydrogels Contacted with H₂O Solutions

For H₂O-Hydrogels contacted with H₂O solutions, neutron radiography can not provide information on solvent diffusion due to the missing contrast and hence was not performed. However, FI and OI experiments are able to yield information and were conducted. Figure 12 shows typical FI intensity profiles of fluorescein in H₂O diffus-

m_{ds}	$\phi_{p,i}$	cr	d_i [cm]	$\phi_{H,i}$	fluorescent molecule	D_H [10^{-5} cm ² /s]	D_f [10^{-5} cm ² /s]
0.80	0.0664	1:60	0.095	0.139	–	2.13 ± 0.01	–
1.00	0.0530	1:60	0.099	0.005	Fluo	2.03 ± 0.02	0.382 ± 0.002
1.00	0.0650	1:15	0.096	0.010	Fluo	2.05 ± 0.02	0.360 ± 0.003
0.81	0.0656	1:60	0.097	0.089	Fluo	2.07 ± 0.02	0.359 ± 0.002
0.80	0.0664	1:60	0.099	0.120	Fluo	2.10 ± 0.02	0.352 ± 0.002
0.75	0.0709	1:60	0.102	0.159	Fluo	2.11 ± 0.02	0.341 ± 0.003
0.75	0.0870	1:15	0.096	0.173	Fluo	2.13 ± 0.02	0.295 ± 0.003
0.78	0.0681	1:60	0.095	0.139	D10	2.11 ± 0.01	0.076 ± 0.003
0.75	0.0709	1:60	0.101	0.164	D10	2.11 ± 0.02	0.071 ± 0.002
0.80	0.0815	1:15	0.090	0.138	D10	2.13 ± 0.01	0.070 ± 0.003
1.00	0.0530	1:60	0.100	–	D70	–	0.017 ± 0.003
0.74	0.0718	1:60	0.095	0.187	D70	2.05 ± 0.02	0.015 ± 0.004
0.73	0.0894	1:15	0.098	0.194	D70	2.08 ± 0.02	0.011 ± 0.004

Tab. III. Diffusion coefficients for H₂O, D_H , and fluorescent molecules, D_f , obtained by combined NR and FI for hydrogels with a different degree of swelling, m_{ds} , polymer volume fraction, $\phi_{p,i}$, crosslinking ratio, cr , initial sample thickness, d_i , and initial H₂O volume fraction, $\phi_{H,i}$. Additional longer FI measurements were performed and the listed diffusion coefficients, D_f , are the mean values of three to five measurements.

ing into a H₂O swollen hydrogel.

Compared to the previously discussed results, a qualitatively different behavior is observed. The concentration profiles of the fluorescent molecules presented in the previous sections (Figs. 4, 8, 11), show an essentially constant concentration in the reservoir except close to the hydrogel. Here, however, for short and intermediate times, a pronounced intensity profile developed outside the hydrogel. Furthermore, in the equilibrated state, the intensity of the fluorescent molecules in the hydrogel was higher than in the solvent reservoir. The reasons for these effects are not clear. Optical effects might play a role, e.g. scattering from the hydrogel-reservoir interface or an enhanced fluorescence of molecules in a H₂O-swollen hydrogel compared to the same molecule in solution. Again, for measurements with fluorescent 10 kDa dextran, the same fluorescence intensity in the hydrogel and in the reservoir was observed after equilibration. While the concentration profiles well inside a H₂O-swollen hydrogel in H₂O solution and in other porous materials have been reported,^{20,21,68} we are not aware of any experimental study, where concentration profiles inside as well as outside a hydrogel have been measured and reported. Thus, we restricted our analysis to the concentration profiles inside the hydrogel. We again applied model 1a to quantitatively analyze the data. If the region around the hydrogel-solution interface is ignored, this provided reasonable fits (Fig. 12) and a fluorescein diffusion coefficient $D_{Fluo} = 0.355 \times 10^{-5}$ cm²/s.

The complete profiles, except the region around the hydrogel edge, qualitatively resemble profiles predicted by

model 2. In a previous study, we used the dye alexa488 instead of fluorescein (at a slightly smaller concentration of up to 10 μ M), while the hydrogels studied and measurement procedure were the same.²⁹ Interestingly, for those samples, the long time behavior could not be explained with model 1a, but with model 2. With FCS measurements, we found evidence for adsorption of alexa488 to the polymer, which leads to its continued diffusion to-

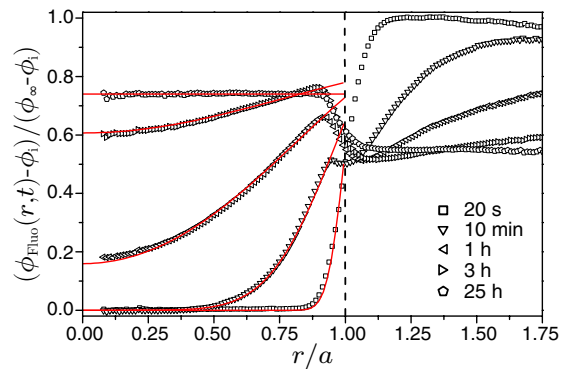


Fig. 12. Normalized fluorescein concentration profiles, $\phi_{Fluo}(r, t)$, for different times (as indicated) after a H₂O-hydrogel with crosslinking ratio 1:60, a degree of swelling $m_{ds} = 0.80$ and sample thickness $d_i = 0.100$ cm has been contacted with H₂O solution containing fluorescein as obtained by FI. Fits based on model 1a (red lines) as well as the data are corrected for the time dependence of the hydrogel radius, $a(t)$.

3.3 Solvent and solute ingress into a polymer hydrogel resolved by a combination of imaging techniques

16

wards and enrichment inside the hydrogel. Hence, in the case of an adsorbing solute, the assumption of an infinite reservoir becomes more realistic, while for the present system model 1a seems appropriate.

V. CONCLUSIONS

Using simultaneous neutron, fluorescence and optical transmission imaging, we were able to distinguish solvent and solute diffusion into a polymer hydrogel and, at the same time, monitor macroscopic hydrogel swelling or shrinking. Polyacrylamide hydrogel discs, swollen in either H₂O or D₂O, were contacted with different sized fluorescent molecules, fluorescein and fluorescein-labeled dextrans, dissolved in H₂O or D₂O. Based on the neutron and fluorescence images, solvent and solute concentration profiles, respectively, were determined. They were quantitatively interpreted using different models describing diffusion. The data were best described when the hydrogel was modeled as a cylinder in a stirred infinite reservoir or, equivalently, with a much larger diffusion coefficient outside than inside the hydrogel. Diffusion markedly slows down with increasing molecule size and also depends on the hydrogel properties as expected based on previous studies on similar systems.^{23,24,26,59,67} Increasing the crosslinking ratio or partially drying the hydrogel both reduce the pore size and were found to slow down solute diffusion, in particular of the large solutes. The determination of quantitative results required the careful and precise consideration of several experimental parameters. The sample thickness might change over the course of the experiment, the initial D₂O-H₂O composition in the hydrogels might be affected by moisture, and scattering from the hydrogel-reservoir interface can affect the results. If these effects are taken into account, the methods and procedures presented provide detailed quantitative information on the motion of the different species simultaneously. With additional filters, it would furthermore be possible to distinguish different fluorophore species and simultaneously study the diffusion of different macromolecules and their effect on each other.

SUPPLEMENTARY MATERIAL

A more detailed comparison of the applied theoretical models can be found in the Supplementary Material. Additionally, the effects of uncertainties in sample thickness and polymer volume fraction on the determination of the diffusion coefficients is evaluated.

ACKNOWLEDGEMENT

We thank Annette Schmidt (University of Cologne) for advice on the samples. Moreover, we thank the Paul

Scherrer Institute (Villigen, Switzerland) for beamtime and the coated mirrors that were used in the optical setup. We furthermore acknowledge support from the International Helmholtz Research School of Biophysics and Soft Matter (IHRS BioSoft) and the Heinrich Heine University through the Strategic Research Fund.

- ¹M. Guenther and G. Gerlach, in *Hydrogel Sensors and Actuators* (Springer, 2010) pp. 165–195.
- ²A. Richter, G. Paschew, S. Klatt, J. Lienig, K.-F. Arndt, and H.-J. P. Adler, *Sensors* **8**, 561 (2008).
- ³I. Tokarev and S. Minko, *Soft Matter* **5**, 511 (2009).
- ⁴D. Kuckling, *Colloid Polym. Sci.* **287**, 881 (2009).
- ⁵N. A. Peppas and J. J. Sahlin, *Biomaterials* **17**, 1553 (1996).
- ⁶L. Guan, M. E. González-Jiménez, C. Walowski, A. Boushehri, J. M. Prausnitz, and C. J. Radke, *J. Appl. Polym. Sci.* **122**, 1457 (2011).
- ⁷F. Fornasiero, D. Tang, A. Boushehri, J. Prausnitz, and C. Radke, *J. Membr. Sci.* **320**, 423 (2008).
- ⁸M. Kemp and P. Fryer, *Innov. Food Sci. Emerg. Technol.* **8**, 143 (2007).
- ⁹K. Samprovalaki, P. Robbins, and P. Fryer, *J. Food Eng.* **111**, 537 (2012).
- ¹⁰T. R. Hoare and D. S. Kohane, *Polymer* **49**, 1993 (2008).
- ¹¹A. Vashist, A. Vashist, Y. K. Gupta, and S. Ahmad, *J. Mater. Chem. B* **2**, 147 (2014).
- ¹²N. Peppas, P. Bures, W. Leobandung, and H. Ichikawa, *Eur. J. Pharm. Biopharm.* **50**, 27 (2000).
- ¹³N. A. Peppas, *Curr. Opin. Colloid Interface Sci.* **2**, 531 (1997).
- ¹⁴K. Y. Lee and D. J. Mooney, *Chem. Rev.* **101**, 1869 (2001).
- ¹⁵J. L. Drury and D. J. Mooney, *Biomaterials* **24**, 4337 (2003).
- ¹⁶A. S. Hoffman, *Adv. Drug Deliv. Rev.* **64**, 18 (2012).
- ¹⁷B. J. Walthall, Y. E. McHugh, and H. F. Voss, “Transplantable artificial tissue,” (1990), US Patent 4,902,295.
- ¹⁸B. Amsden, *Macromolecules* **31**, 8382 (1998).
- ¹⁹B. Amsden, *Polym. Gels Networks* **6**, 13 (1998).
- ²⁰D. E. Liu, C. Kotsmar, F. Nguyen, T. Sells, N. O. Taylor, J. M. Prausnitz, and C. J. Radke, *Ind. Eng. Chem. Res.* **52**, 18109 (2013).
- ²¹R. K. Lewus and G. Carta, *J. Chromatogr. A* **865**, 155 (1999).
- ²²P. Lopez-Sanchez, E. Schuster, D. Wang, M. J. Gidley, and A. Strom, *Soft Matter* **11**, 4002 (2015).
- ²³J. C. Williams, L. A. Mark, and S. Eichholtz, *Biophys. J.* **75**, 493 (1998).
- ²⁴J. Tong and J. Anderson, *Biophys. J.* **70**, 1505 (1996).
- ²⁵S. Lehmann, S. Seiffert, and W. Richtering, *J. Am. Chem. Soc.* **134**, 15963 (2012).
- ²⁶L. Haggerty, J. Sugarman, and R. Prudhomme, *Polymer* **29**, 1058 (1988).
- ²⁷A. G. Ogston, B. N. Preston, and J. D. Wells, *R. Soc. Lond. Proc. Ser. A Math. Phys. Eng. Sci.* **333**, 297 (1973).
- ²⁸H. Zhou and S. B. Chen, *Phys. Rev. E* **79** (2009).
- ²⁹D. Sandrin, D. Wagner, C. E. Sitta, R. Thoma, S. Felekyan, H. E. Hermes, C. Janiak, N. de Sousa Amadeu, R. Kühnemuth, H. Löwen, S. U. Egelhaaf, and C. A. M. Seidel, *Phys. Chem. Chem. Phys.* (2016), 10.1039/C5CP07781H.
- ³⁰P. McConville, M. K. Whittaker, and J. M. Pope, *Macromolecules* **35**, 6961 (2002).
- ³¹D. Wagner, M. Börgardt, C. Grünzweig, E. Lehmann, T. J. J. Müller, S. U. Egelhaaf, and H. E. Hermes, *Rev. Sci. Instrum.* **86**, 093706 (2015).
- ³²H. E. Hermes, R. L. Hanes, D. Wagner, S. Hartmann, A. Kaestner, M. Schulz, B. Schillinger, E. H. Lehmann, and S. U. Egelhaaf, (2016), in preparation.
- ³³I. S. Anderson, R. L. McGreevy, and H. Z. Bilheux, *Neutron imaging and applications* (Springer, 2009).
- ³⁴H. E. Hermes, C. E. Sitta, B. Schillinger, H. Löwen, and S. U. Egelhaaf, *Phys. Chem. Chem. Phys.* **17**, 15781 (2015).

- ³⁵S. Gruener, Z. Sadjadi, H. E. Hermes, A. V. Kityk, K. Knorr, S. U. Egelhaaf, H. Rieger, and P. Huber, *Proc. Natl. Acad. Sci.* **109**, 10245 (2012).
- ³⁶N. Rudolph, H. G. Esser, A. Carminati, A. B. Moradi, A. Hilger, N. Kardjilov, S. Nagl, and S. E. Oswald, *J. Soils Sediment* **12**, 63 (2011).
- ³⁷S. E. Oswald, M. Menon, A. Carminati, P. Vontobel, E. Lehmann, and R. Schulin, *Vadose Zone Journal* **7**, 1035 (2008).
- ³⁸R. Hassanein, H. Meyer, A. Carminati, M. Estermann, E. Lehmann, and P. Vontobel, *J. Phys. D: Appl. Phys.* **39**, 4284 (2006).
- ³⁹J. J. Milczarek, A. Czachor, A. E.-G. El Abd, and Z. Wiśniewski, *Nucl. Instr. Meth. Phys. Res. A* **542**, 232 (2005).
- ⁴⁰R. Messing, N. Frickel, L. Belkoura, R. Strey, H. Rahn, S. Odenbach, and A. M. Schmidt, *Macromolecules* **44**, 2990 (2011).
- ⁴¹A. M. Mathur, S. K. Moorjani, and A. B. Scranton, *J. Macromol. Sci., Rev. Macromol. Chem. Phys.* **36**, 405 (1996).
- ⁴²V. F. Sears, *Neutron News* **3**, 29 (1992).
- ⁴³<http://www.ati.ac.at/~neutropt/scattering/ScatteringLengths-AdvTable.pdf>, accessed 20-Jan-2016.
- ⁴⁴E. Lehmann, P. Boillat, G. Scherrer, and G. Frei, *Nucl. Instr. Meth. Phys. Res. A* **605**, 123 (2009).
- ⁴⁵I. Grillo, in *Soft Matter Characterization* (Springer, 2008) pp. 723–782.
- ⁴⁶J. S. Higgins and H. Benoit, *Polymers and Neutron Scattering* (Clarendon Press Oxford, 1994).
- ⁴⁷M. Kang, H. Z. Bilheux, S. Voisin, C. Cheng, E. Perfect, J. Horita, and J. Warren, *Nucl. Instr. Meth. Phys. Res. A* **708**, 24 (2013).
- ⁴⁸E. H. Lehmann, P. Vontobel, and N. Kardjilov, *Appl. Rad. Isotop.* **61**, 503 (2004).
- ⁴⁹H. E. Hermes, T. Sentjabrskaja, R. Messing, A. Kaestner, A. M. Schmidt, and S. U. Egelhaaf, “Solvent ingress into a cross-linked polymer hydrogel: in-situ neutron imaging of swelling under confinement,” (2016), in preparation.
- ⁵⁰P.-E. Danielsson, *Comput. Vision Graph* **14**, 227 (1980).
- ⁵¹N. B. Vicente, J. E. D. Zamboni, J. F. Adur, E. V. Paravani, and V. H. Casco, *J. Phys.: Conf. Ser.* **90**, 012068 (2007).
- ⁵²L. Hodgson, P. Nalbant, F. Shen, and K. Hahn, *Meth. Enzym.* **406**, 140 (2006).
- ⁵³J. Crank, *The Mathematics of Diffusion* (Oxford University Press, New York, 1979).
- ⁵⁴H. Shirota and K. Horie, *Chem. Phys.* **242**, 115 (1999).
- ⁵⁵H. Shirota and K. Horie, in *Macromol. Symp.*, Vol. 207 (2004).
- ⁵⁶D. Wilbur, T. DeFries, and J. Jonas, *J. Chem. Phys.* **65**, 1783 (1976).
- ⁵⁷R. Mills, *J. Phys. Chem.* **77**, 685 (1973).
- ⁵⁸V. Klepko, *Polym. Eng. Sci.* **39**, 437 (1999).
- ⁵⁹A. H. Muhr and J. M. Blanshard, *Polymer* **23**, 1012 (1982).
- ⁶⁰S. Liang, J. Xu, L. Weng, H. Dai, X. Zhang, and L. Zhang, *J. Control. Release* **115**, 189 (2006).
- ⁶¹V. Hagel, T. Haraszti, and H. Boehm, *Biointerphases* **8**, 36 (2013).
- ⁶²H. Brinkman, *Appl. Sci. Res.* **1**, 27 (1949).
- ⁶³M. Alava, M. Dube, and M. Rost, *Adv. Phys.* **53**, 83 (2004).
- ⁶⁴D. C. Standnes, *J. Petr. Sci. Eng.* **50**, 151 (2006).
- ⁶⁵E. Achilleos, K. Christodoulou, and I. Kevrekidis, *Comput. Theor. Polym. Sci.* **11**, 63 (2001).
- ⁶⁶S. Boral, A. N. Gupta, and H. Bohidar, *Int. J. Biol. Macromol.* **39**, 240 (2006).
- ⁶⁷A. Pluen, P. A. Netti, R. K. Jain, and D. A. Berk, *Biophys. J.* **77**, 542 (1999).
- ⁶⁸L. Heinke and J. Kärger, *New J. Phys.* **10**, 023035 (2008).

This page has been left intentionally blank.

Supplementary Material for "Solvent and solute ingress into hydrogels resolved by a combination of imaging techniques"

D. Wagner,¹ J. Burbach,¹ C. Grünzweig,² S. Hartmann,² E. Lehmann,² S. U. Egelhaaf,¹ and H. E. Hermes¹

¹Condensed Matter Physics Laboratory, Heinrich Heine University, 40225 Düsseldorf, Germany

²Neutron Imaging and Activation Group, Paul Scherrer Institute, 5232 Villigen, Switzerland

(Dated: 18 July 2016)

I. COMPARISON OF MODELS

Cylinders in stirred infinite and finite reservoirs, i.e. models 1a (main text, Eq. 16) and 1b (main text, Eq. 15), respectively, yield qualitatively similar concentration profiles (Fig. SM – 1). The effect of the finite reservoir volume depends on the reservoir to cylinder volume ratio, β ; in our experiments $3 \leq \beta \leq 11$. For $\beta = 11$, no significant effect of the finite reservoir can be seen (Fig. SM – 1 (a)). The difference between model 1a and 1b increases with decreasing β especially for intermediate times and close to the cylinder border (Fig. SM – 1 (b)). For a finite reservoir (model 1b), normalized concentrations at the border, $(\phi(a, t) - \phi_i) / (\phi_\infty - \phi_i)$, can become larger than one. This is due to the normalization by the difference between the initial, ϕ_i , and equilibrium, ϕ_∞ , concentrations inside the cylinder. The concentration in the reservoir, and hence at the hydrogel border, decreases from the initial reservoir concentration, $\phi_{res,i}$, to the equilibrium concentration, ϕ_∞ , due to the limited reservoir volume.

Figure SM – 2 shows a comparison of cylinders in stirred

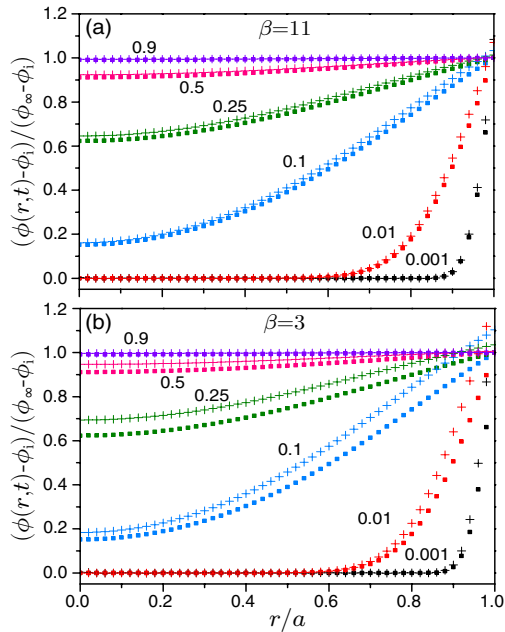


Fig. SM – 1. Normalized radial concentration profiles, $\phi(r, t)$, calculated with model 1a (main text, Eq. 16, closed squares) and model 1b (main text, Eq. 15, crosses) for the two limiting reservoir to cylinder volume ratios, β , explored: (a) $\beta = 11$ and (b) $\beta = 3$. The profiles are shown for different times, t , with the normalized time $\tau = Dt/a^2$ indicated.

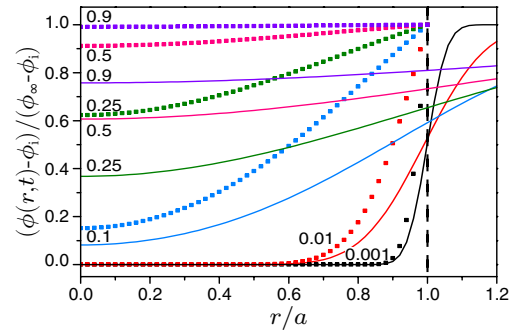


Fig. SM – 2. Normalized radial concentration profiles, $\phi(r, t)$, calculated with model 1a (main text, Eq. 16, closed squares) and model 2 (main text, Eq. 17, solid lines). The profiles are shown for different times, t , with the normalized time $\tau = Dt/a^2$ indicated.

(model 1a, closed squares) and unstirred (model 2, solid lines) infinite reservoirs. In model 1a, a concentration profile develops inside the cylinder, whereas the concentration is uniform and constant outside the cylinder. By contrast, in model 2 the concentration changes inside and outside the cylinder. Outside the cylinder, the concentration initially decreases toward the cylinder as diffusants enter the cylinder, but rises again later due to the infinite reservoir. This occurs on a rather long timescale as the concentration gradient in the reservoir is very small. Thus, model 2 predicts that the concentration at the interface ($r = a$) first drops and then increases again with time whereas it is constant in model 1a and continuously decreases in model 1b. This difference leads to significant differences in the shape and location of the concentration profiles.

The comparison of the different models shows that the time evolution of the concentration at the cylinder-reservoir-interface, $\phi(a, t)$, is important for the evolution of the concentration profiles inside the cylinder. To investigate this effect further, the concentration profiles were scaled to $\phi(a, t)$. This was done for $\beta = 3$, where the largest differences between the models are expected, by adjusting the final concentration in the cylinder, ϕ_∞ , in models 1a and 2 for each τ such that $\phi(a, t)$ coincides with the one of model 1b. This yields very small deviations between the results of the models for short and intermediate times, $\tau \lesssim 0.14$ (Fig. SM – 3) and implies that, for these times, the different models yield very similar concentration profiles except for the different concentrations at the interface.

The time-dependence of the concentration in the center of the cylinder, $\phi(0, t)$, was also predicted using the different models (Fig. SM – 4). Model 1a and 1b yield very similar $\phi(0, t)$. Due to the finite reservoir in model 1b, saturation

3.3 Solvent and solute ingress into a polymer hydrogel resolved by a combination of imaging techniques

2

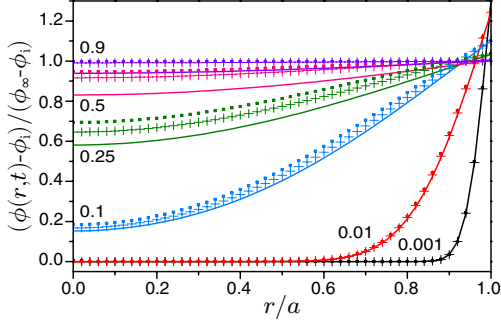


Fig. SM – 3. Normalized radial concentration profiles, $\phi(r, t)$, calculated with all three models (model 1a: squares; model 1b with $\beta = 3$: crosses; model 2: lines). The profiles are shown for different times, t , with the normalized time $\tau = Dt/a^2$ indicated. For every value of τ , the final concentrations in models 1a and 2 were adapted such that the surface concentrations, $\phi(a, t)$, match those calculated with model 1b.

is reached earlier so that normalization to $\phi_\infty = 1$ leads to a slightly steeper initial increase. In both models 1a and 1b the concentration saturates much faster than in model 2, which predicts a more gradual change in concentration and the equilibrium value is approached much more slowly.

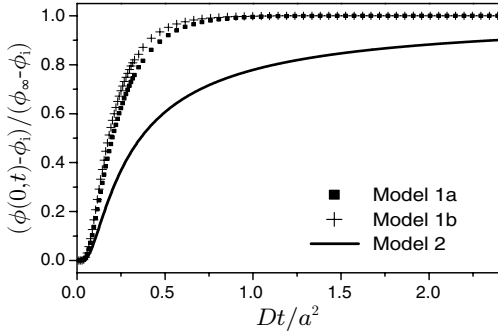


Fig. SM – 4. Normalized concentration in the center of the cylinder, $\phi(0, t)$, as a function of dimensionless time $\tau = Dt/a^2$, calculated using model 1a (squares), model 1b ($\beta = 3$, crosses), and model 2 (line).

II. EFFECT OF SAMPLE THICKNESS AND POLYMER VOLUME FRACTION ON THE DETERMINATION OF THE DIFFUSION COEFFICIENT

The determined D_2O volume fraction, ϕ_D depends on the chosen value of the sample thickness, d (main text, Eq. 11). To investigate the effect of d , it was varied from 0.13 cm to 0.16 cm in the model calculations. This is a larger range than covered in the experiments. A variation of d in the calculation of $\phi_D(0, t)$ from the neutron transmission, T_S , leads to a change in the slope of $\phi_D(0, t)$, the initial, $\phi_{D,i}$, and equilibrium volume fraction, $\phi_{D,\infty}$ (Fig. SM – 5 (a)). However, by choosing appropriate $\phi_{D,i}$ and $\phi_{D,\infty}$, all curves can be fitted with the same diffusion coefficient, D_D , which is even obtained for a continuously increasing (or decreasing) d (red line in Fig. SM – 5 (a)).

Thus the value of d affects $\phi_D(0, t)$ at all times but our fitting procedure provides the same value of D_D irrespective of d .

If the hydrogels swell or deswell, the polymer volume fraction, ϕ_p , changes. This may be in addition to a change in d . Using the example of hydrogel A (main text, Sec. IV B1), the effects of these changes on a typical data set were estimated. During this measurement, the hydrogel radius was found to decrease from $a_i = 0.310$ cm to $a_\infty = 0.298$ cm. This change might be due to the exchange of solvent, leading to an increase in polymer volume fraction from $\phi_{p,i} = 0.038$ to $\phi_{p,i} = 0.040$ or an increase in sample thickness from $d_i = 0.146$ cm to $d_\infty = 0.158$ cm. The effects of both changes are illustrated in Fig. SM – 5 (b). The influence of a variation in ϕ_p is found to be very small and can thus be neglected, which renders a change in sample thickness likely.

Even if the hydrogel radius remains constant, the hydrogel might swell and at the same time the sample thickness increase. A comparison of the expected volume fractions inside and outside the hydrogel after equilibration with the values determined from the neutron radiographs can then be used in order to estimate how much d changed during the measurement. Nevertheless, as already mentioned, the diffusion coefficient D is not affected by using a possibly slightly differing value for the sample thickness.

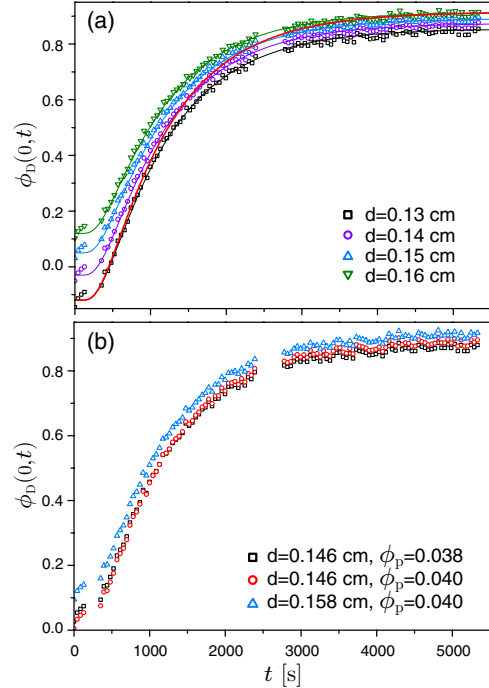


Fig. SM – 5. (a) D_2O volume fraction, $\phi_D(0, t)$, in the center of the hydrogel (sample A), as a function of time, t , calculated with $\phi_p = 0.038$ and different values for the sample thickness d (as indicated). Lines of corresponding colors are calculated using model 1a with $D = 1.75 \text{ cm}^2/\text{s}$. The initial, $\phi_{D,i}$, and final, $\phi_{D,\infty}$, volume fractions are fitted to the data. The red line represents a continuously increasing d and is also calculated with the same diffusion coefficient. (b) $\phi_D(0, t)$ calculated for different combinations of ϕ_p and d (as indicated), which include the maximal range expected for this sample.

3.4 Release of macromolecules from polyacrylamide hydrogels

Journal: Macromolecules

Status: In Preparation

Impact factor: 5.800

Authors: **Dana Wagner**, Helen E. Hermes, and Stefan U. Egelhaaf

1st author

DW designed and built the experimental setup, carried out measurements and analyzed the data. DW, HEH and SUE conceived and discussed the project and HEH and SUE supervised the project. DW wrote the manuscript and all authors contributed to the writing.

90% contribution of DW

This page has been left intentionally blank.

Release of macromolecules from polyacrylamide hydrogels

D. Wagner,¹ H. E. Hermes,¹ and S. U. Egelhaaf¹

Condensed Matter Physics Laboratory, Heinrich Heine University, 40225 Düsseldorf, Germany

(Dated: 18 July 2016)

Macromolecules can be incorporated in and later released from polymer hydrogels due to their porous network structure. The diffusion of differently sized fluorescent macromolecules into, in, and especially out of a polyacrylamide hydrogel was investigated with simultaneous fluorescent and optical bright-field imaging. The data were quantitatively analyzed using models describing diffusion with different boundary conditions. A qualitatively different behavior for influx and release is observed and discussed.

I. INTRODUCTION

Hydrogels are polymeric networks swollen in water. They have been studied widely as, e.g. tunable drug delivery system.^{1–6} Their network structure allows for the incorporation of (macro)molecules in the hydrogel matrix and subsequent controlled release.⁷ The release rate depends on both, the diffusion coefficient of the molecules and the boundary conditions, like the initial concentration gradient as well as the properties and especially the volume of the surroundings.^{6,8–10} This will affect the release and hence the performance of hydrogel-based materials and devices. A better understanding of the mechanisms that influence diffusion can be exploited to optimize the time dependence and extent of the uptake and delivery of solutes into and from hydrogels.

We followed the diffusion of fluorescently labeled (macro)molecules, namely fluorescent dye (Fluo) and polymers (dextrans) with different sizes, into and out of polyacrylamide hydrogels in-situ using combined fluorescent and optical bright-field transmission imaging.¹¹ Fluorescence imaging yielded time- and space-resolved information about the particle concentration throughout the entire macroscopic observation volume while bright-field transmission imaging was used to monitor changes in the properties and appearance of the hydrogel. The data were quantitatively analyzed using diffusion models describing diffusion into and out of a cylinder. Although both processes can be described by the same equations, we observed a qualitatively different behavior, indicating that the different boundary conditions affect the diffusion very noticeably.

II. MATERIALS AND METHODS

A. Samples

Polyacrylamide (PAAm) hydrogels with a crosslinking-density, i.e. molar ratio of crosslinker to monomer, of 1 : 60 were synthesized using a standard polymerisation protocol.^{12,13} The monomer acrylamide (AAm) and the tetrafunctional crosslinking agent *N,N'*-methylenebis(acrylamide) (BIS) were purchased from Sigma-Aldrich. Ammonium peroxodisulphate (APDS) from

Roth and tetramethylethylenediamine (TEMED) from Merck were used as redox initiators. All components were used without further purification. AAm, BIS and APDS were first dissolved in deionized, filtered water and cooled down to 4 °C. The solutions were then mixed at this temperature to minimize the gelation process. 2 ml reaction mixture contained 75 mg of AAm, 2.71 mg of BIS, 6 mg of APDS and 10 μ l of TEMED. The reaction mixture was transferred to Teflon molds using a glass pipette and allowed to warm up and react at room temperature for one to two hours. The hydrogel was then transferred into a larger container filled with deionized water and left for one week to swell to equilibrium. In order to wash out residual chemicals, the excess water was exchanged every day. Discs with a radius $a \approx 0.3$ cm to $a \approx 0.5$ cm were cut from the fully swollen hydrogels using a simple stamp and used like this for influx measurements. For release measurements, hydrogel discs were placed in a vial containing a fluorescent (macro)molecule solution for several days until a uniform distribution inside the gel discs was reached. The time needed for this sorption process depended on the size of the fluorescent molecules.

Three differently sized fluorescent (macro)molecules were used. A fluorescent dye, fluorescein sodium salt (Fluo: hydrodynamic radius as quoted by the supplier $r_h \approx 0.54$ nm), and two differently sized dextrans (D10: 10 kDa, $r_h \approx 2.3$ nm, and D70: 70 kDa, $r_h \approx 6.0$ nm; hydrodynamic radii as quoted by the supplier) labeled with the same dye were purchased from Sigma-Aldrich and dissolved in deionized, filtered water at concentrations of about 25 μ M or 100 μ M.

B. Experimental Setup

The home-built imaging-apparatus which was used to perform the simultaneous fluorescence and optical bright-field transmission imaging experiments was previously described.¹⁴ Briefly, hydrogel discs were constrained to a thickness of 1.5 mm between two horizontal glass plates. The samples were illuminated with a parallel beam of light from a LED lamp (CoolLED pE-2) with a nominal wavelength of 490 nm. This illumination was suitable to excite the fluorescein dye in the sample, which then emits light of a longer wavelength. A dichroic mir-

ror was used to separate the transmitted excitation light from the emitted fluorescence. The two light beams were then focused onto separate CCD cameras, forming the bright-field and fluorescence images.

C. Measurements and Data Analysis

Calibration measurements revealed a linear relation between fluorescence intensity and (macro)molecule concentration inside the hydrogel and also in the reservoir for all investigated (macro)molecules in a concentration range of 0 to 100 μM . Thus, the fluorescence intensity was taken to represent the (macro)molecule concentration. Before each measurement, the hydrogels and (macro)molecule distributions were checked for homogeneity. A uniform initial intensity indicates a homogeneous distribution throughout the hydrogel or reservoir in the case of release or influx measurements, respectively. Only gel discs without significant concentration gradients were used for the release experiments. In all influx experiments, a homogeneous concentration in the reservoir was found. Pure water or (macro)molecule solution were added to the sample cell such that they completely surrounded the hydrogel discs. The reservoir volume was approximately 11 times the hydrogel volume. During the course of the experiment, fluorescent molecules diffused from the hydrogel into the reservoir or vice versa until equilibrium was reached. The ingress or release was monitored by recording time series of images and subsequently analyzing the time evolution in the fluorescence intensity inside the hydrogel. This yielded transient concentration profiles, i.e. the concentration, $c(r, t)$, as a function of radial position, r , in the hydrogel cylinder and time, t , since contact. To facilitate direct comparison of different measurements, the change in normalized concentration in the center of the hydrogel discs, $c(r = 0, t)$, for the three differently sized probe particles was also considered.

All data were corrected for photobleaching. For the influx experiments, we followed a previously developed bleach correction procedure.¹¹ The intensity in the center of a hydrogel was found to initially increase and at long times to decrease solely due to photobleaching. Fitting an exponential decay function to this part of the intensity trace yielded a bleach curve based on which the raw intensities were corrected. This approach could not be applied to the release experiments, because the intensity inside the hydrogel decreased due to the (macro)molecules leaving the hydrogel as well as due to photobleaching. Instead, the concentration in the reservoir is expected to reach a constant level at long times. Hence, the decrease of the intensity can be attributed to photobleaching only and was fitted by an exponential decay. Based on this, a photobleaching correction was performed.

III. RESULTS AND DISCUSSION

A. Theoretical Models

As the hydrogel discs were held between two glass plates, diffusion only occurred in radial direction through the gel-solvent interface. Additionally, the height of the cylindrical discs was much larger than the size of the diffusants. Thus, the samples can be described as infinite cylinders with radius a . Here, we consider two models. In the first model, the infinite reservoir is stirred which corresponds to an infinitely large diffusion coefficient in the reservoir. It implies a constant concentration in the reservoir and at the cylinder-reservoir interface. The second model is based on an infinite, unstirred reservoir. Both models were previously considered to describe the diffusion of solutes and solvents into hydrogel discs.^{11,15} The initial and final concentrations inside the cylinder are denoted as c_i and c_∞ , respectively. In the case of an infinite, stirred reservoir (Model 1), the concentration in the cylinder, $c(r, t)$, can be calculated as a function of the radial position, r , and time, t :¹⁶

$$\frac{c(r, t) - c_i}{c_\infty - c_i} = 1 - \frac{2}{a} \sum_{n=1}^{\infty} \frac{\exp(-D\alpha_n^2(t + t_0)) J_0(r\alpha_n)}{\alpha_n J_1(a\alpha_n)}, \quad (1)$$

where D is the diffusion coefficient, J_0 the Bessel function of the first kind of order zero, J_1 the Bessel function of the first order, and α_n the positive roots of $J_0(a\alpha_n) = 0$. If the infinite reservoir is not stirred (Model 2), a concentration profile develops also in the reservoir. The concentration in the cylinder and the reservoir is:¹⁶

$$c(r, t) = c_\infty + \frac{c_i - c_\infty}{2D(t + t_0)} e^{-r^2/4D(t+t_0)} \times \int_0^a e^{-r'^2/4D(t+t_0)} I_0\left(\frac{rr'}{2D(t+t_0)}\right) r' dr', \quad (2)$$

with I_0 the modified Bessel function of the first kind of order zero. In the center of the cylinder ($r = 0$) a much simpler relation is found:

$$c(r = 0, t) = c_i + (c_\infty - c_i) e^{-a^2/4D(t+t_0)}. \quad (3)$$

A time-offset, t_0 , was used to account for a not perfectly perpendicular hydrogel edge and potential scattering from this edge, which both lead to deviations of the observed initial concentration profile from a step function. Depending on the values of c_i and c_∞ , these equations describe both, diffusion into and out of the cylinder.

B. Influx of (Macro)molecules into Polymer Hydrogels

The diffusion of fluorescent (macro)molecules into polyacrylamide hydrogels was followed. The evolution of the concentration in the center of the hydrogel discs

(macro)molecule	r_h [nm]	D_{bulk} [$10^{-6}\text{cm}^2/\text{s}$]	D_{in} [$10^{-6}\text{cm}^2/\text{s}$]	D_{out} [$10^{-6}\text{cm}^2/\text{s}$]	
Fluorescein	0.54	3.97	3.42 ± 0.08	$*3.51 \pm 0.03$	6.48 ± 0.1
Dextran, 10 kDa	2.3	0.93	0.80 ± 0.04	2.66 ± 0.05	
Dextran, 70 kDa	6.0	0.36	0.101 ± 0.07	0.95 ± 0.1	

Tab. I. Bulk diffusion coefficients, D_{bulk} , were calculated from the hydrodynamic radii, r_h , via Stokes-Einstein equation. Influx diffusion coefficients, D_{in} , and release diffusion coefficients, D_{out} of fluorescent (macro)molecules were obtained by fitting Model 1 (influx and release with $*c_i = 100 \mu\text{M}$) or Model 2 (release with $c_i = 25 \mu\text{M}$) to the temporal change in concentration in the hydrogel center.

for different (macro)molecules is shown in Figure 1. Differences in hydrogel disc size were accounted for by normalizing the time axis with the squared radius, a^2 . The hydrogel radius $a(t)$ was monitored by bright-field transmission imaging. As expected, with increasing molecule size the increase in concentration is slower. This reflects the smaller diffusion coefficient of larger molecules. The diffusion coefficients, D , were quantitatively determined using the models described in Sec. III A. It was found that only Model 1 provides a good fit to the data while Model 2 results in a more gradual approach towards the equilibrium concentration and thus the distinctive plateau at long times can not be reproduced. Model 1 yielded diffusion coefficients, D_{in} (Tab. I), which are slightly lower than the bulk values, D_{bulk} , for fluorescein and D10, but significantly lower for D70 as expected due to the obstruction by the hydrogel with an estimated network correlation length of about 6 nm.¹⁵ In addition to the temporal evolution of the concentration in the hydrogel center, transient concentration profiles were determined (Fig. 2). The concentration inside the hydrogel was also fitted by Model 1 to yield a diffusion coefficient which is consistent with the values in Tab. I. The concentration at the interface was fitted to the experimentally observed value because scattering from the possibly rough and tilted hydrogel edge led to an increased fluorescence intensity close to the hydrogel-solution interface

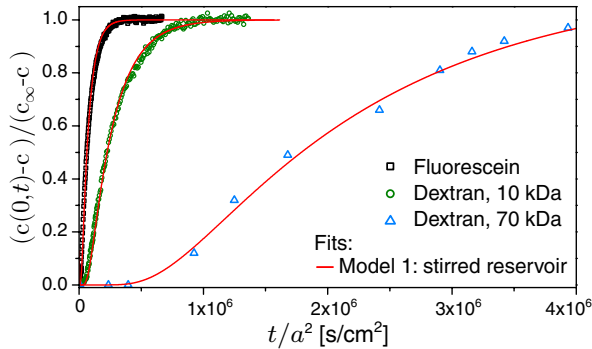


Fig. 1. Normalized concentration, $c(0, t)$, in the center of the hydrogel with radius a as a function of time t after the hydrogels has been contacted with solutions containing different fluorescent solutes (as indicated). Lines represent fits based on Model 1.

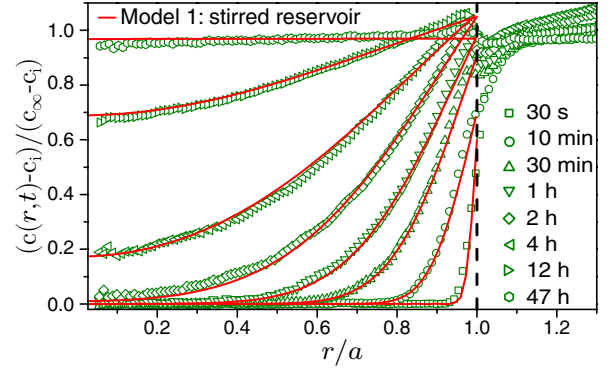


Fig. 2. Exemplary normalized D10 concentration profiles, $c(r, t)$, for different times (as indicated) after the hydrogel has been contacted with an aqueous solution containing fluorescent dextran (10 kDa). Fits based on Model 1 (red lines) as well as the data are corrected for the time dependence of the hydrogel radius, $a(t)$.

($r/a = 1$).¹¹ Additionally, this procedure compensates for small changes in the reservoir concentration due to the finite size of the reservoir.

C. Release of (Macro)molecules from Polymer Hydrogels

1. High Initial Concentration

The reverse process, namely (macro)molecule release from polyacrylamide hydrogel discs, was also studied. In a first step, we consider a high initial concentration inside the hydrogel discs; $c_i = 100 \mu\text{M}$. Again, the evolution of the concentration in the center of the discs as well as of the transient concentration profiles were measured (Fig. 3). It should be noted that the concentration profiles were normalized with the initial concentrations in the hydrogel and in the reservoir, c_i and $c_{\text{res},i}$, respectively. Due to the release, the concentration in the center, $c(r = 0, t)$ decreases with time and the initially strong concentration gradient at the hydrogel-reservoir interface decreases with the concentration profile, $c(r, t)$, evolving towards a homogeneous distribution of the fluorescent dye. The data were again fitted based on Model 1. The analysis yielded a diffusion coefficient of fluorescein,

3.4 Release of macromolecules from polyacrylamide hydrogels

4

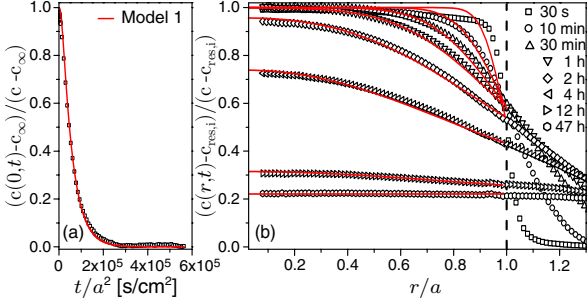


Fig. 3. Exemplary results for fluorescein diffusing out of a hydrogel disc with radius a : (a) normalized concentration, $c(r=0, t)$, in the center of the hydrogel as a function of time t and (b) normalized concentration profiles, $c(r, t)$, for different times t (as indicated) after the fluorescein-containing hydrogel has been contacted with pure water. The initial fluorescein concentration was $c_i = 100 \mu\text{M}$. Fits based on Model 1 (red lines) as well as the data are corrected for the time dependence of the hydrogel radius, $a(t)$.

$D_{\text{Fluo}} = 3.51 \pm 0.03 \times 10^{-6} \text{ cm}^2/\text{s}$, in agreement with the one determined in the influx measurements.

2. Low Initial Concentration

Decreasing the initial concentration to $c_i = 25 \mu\text{M}$ leads to a qualitatively different behavior. The decrease in concentration in the hydrogel center, $c(r=0, t)$, for all three molecules and for comparison the data of the fluorescein measurement with a four times higher start concentration, $c_i = 100 \mu\text{M}$, is shown in figure 4. In the case of the lower initial concentration, c_i , the concentration in the hydrogel, $c(r=0, t)$, saturates more gradually than predicted by Model 1. However, Model 2, i.e. a cylinder immersed in an unstirred infinite reservoir, ap-

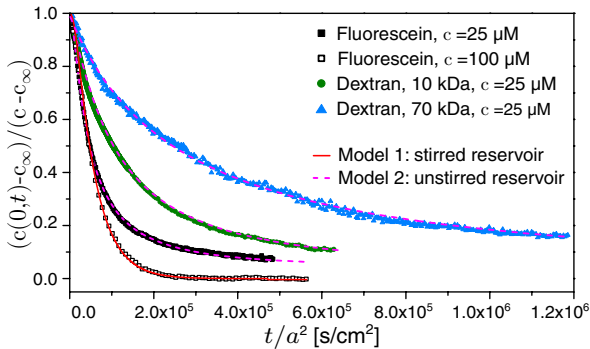


Fig. 4. Normalized concentration, $c(0, t)$, in the center of the hydrogel with radius a as a function of time t after the hydrogel that contained fluorescent solutes (as indicated) has been contacted with pure water. Solid and dashed lines represent fits based on Model 1 and 2, respectively.

pears to describe the data well (Fig. 4), but fitted values of the diffusion coefficients, D_{out} , averaged over five repeat measurements (Tab I) are markedly larger than the D_{in} values.

The concentration profiles, $c(r, t)$, were also determined. In Fig. 5 (a), normalized fluorescein release profiles for the two different initial concentrations $c_i = 100 \mu\text{M}$ and $25 \mu\text{M}$ are compared. The concentration profiles starting with $c_i = 25 \mu\text{M}$ show a decrease reaching further into the hydrogel and for late times, the concentration decreases homogeneously throughout the entire hydrogel. This is consistent with a larger diffusion coefficient $D_{\text{out}} > D_{\text{in}}$. However, by contrast to the concentration trace in the hydrogel center, the concentration profiles, $c(r, t)$, cannot be fitted based on Model 2. This suggests that the large D_{out} values for the low initial concentration are not reliable.

A qualitatively different behavior is observed for influx and release as well as for different initial concentrations, c_i . Since influx and release are the reverse processes and described by the same equations and also the initial concentration should not affect the evolution of the normalized concentration profiles, this should not affect the va-

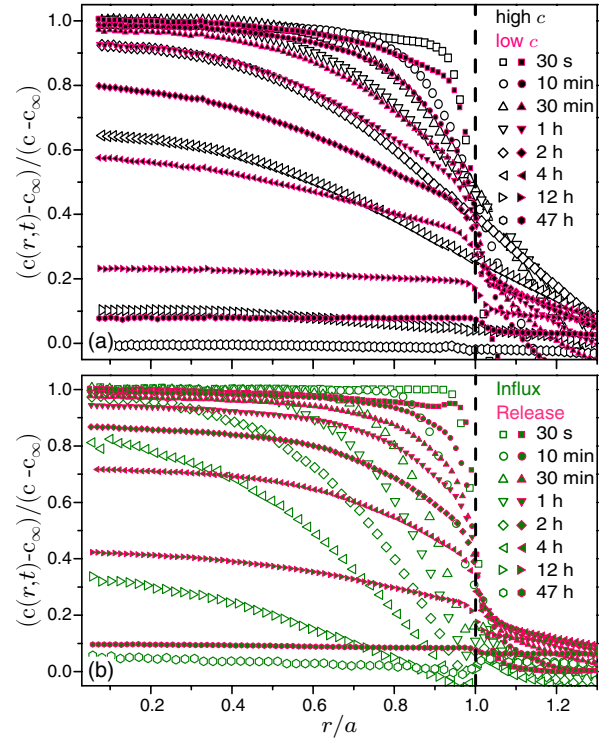


Fig. 5. Exemplary normalized concentration profiles, $c(r, t)$, for different times t (as indicated). For fluorescein, the release profiles for the two different initial concentrations, $c_i = 25 \mu\text{M}$ and $100 \mu\text{M}$, are compared (a) and for D10, influx and release profiles are displayed, whereas the influx profiles were mirrored horizontally to facilitate comparison (b).

lidity or the approximations involved in the two models. In particular, in all cases the reservoir volume is approximately 11 times the cylinder volume: $V_{\text{res}} = 11 V_{\text{cyl}}$. Model 1 considers a stirred and Model 2 an unstirred reservoir, which correspond to an infinite and finite diffusion coefficient in the reservoir, respectively. This enters only through the concentration at the hydrogel-reservoir interface, as only the concentration profiles inside the hydrogel are fitted. Interestingly, the normalized concentration at the interface hardly depends on the initial concentration (Fig. 5(a)). This suggests that also the validity of this assumption is hardly affected by c_i . However, there appears a large difference in the normalized concentration at the interface in the case of influx and release, respectively (Fig. 5(b)). In Fig. 5(b), the low c_i release profiles of 10 kDa dextrans are compared to influx profiles (Fig. 2) which were horizontally mirrored in order to facilitate direct comparison. A further aspect concerns a possible adsorption of the solute to the hydrogel. Its effects would be more pronounced at lower concentrations, as observed in the release experiments. Previously, a lower initial concentration, $c_i = 10 \mu\text{M}$, has been investigated in influx experiments.¹⁵ Also in this case, Model 2 resulted in a better fit than Model 1, consistent with the present observations. However, both models fail to completely describe the low c_i release data. Thus, a diffusion model including adsorption might be required

IV. CONCLUSION

Diffusion of three differently sized fluorescent molecules, a dye and dextrans, from and into polyacrylamide hydrogels was studied using fluorescence imaging. This yielded the evolution of the concentration profiles. They were quantitatively analyzed using different models describing diffusion with different boundary conditions. The obtained influx diffusion coefficients were smaller than in bulk with the decrease being more pronounced with increasing (macro)molecule size. While the concentration profiles in influx and release experiments

were consistent at high initial concentrations, a different behavior was observed at low concentrations, where markedly higher release diffusion coefficients were found. This can be attributed to adsorption of the solutes to the hydrogel which this significantly affects the validity of the different diffusion models.

ACKNOWLEDGEMENT

We acknowledge financial support from the Strategic Research Fund of the Heinrich Heine University and the International Helmholtz Research School of Biophysics and Soft Matter (IHRS BioSoft).

- ¹N. A. Peppas, *Curr. Opin. Colloid Interface Sci.* **2**, 531 (1997).
- ²S. Amin, S. Rajabnezhad, and K. Kohli, *Sci. Res. Essays* **3**, 1175 (2009).
- ³M. Bindu Sri, V. Ashok, and C. Arkendu, *Int. J. Pharm. Chem. Sci.* **1**, 642 (2012).
- ⁴T. R. Hoare and D. S. Kohane, *Polymer* **49**, 1993 (2008).
- ⁵M. Hamidi, A. Azadi, and P. Rafiei, *Adv. Drug Deliv. Rev.* **60**, 1638 (2008).
- ⁶G. W. Ashley, J. Henise, R. Reid, and D. V. Santi, *Proc. Natl. Acad. Sci. U.S.A.* **110**, 2318 (2013).
- ⁷A. S. Hoffman, *Adv. Drug Deliv. Rev.* **64**, 18 (2012).
- ⁸Y. Qiu and K. Park, *Adv. Drug Deliv. Rev.* **64**, 49 (2012).
- ⁹P. Gupta, K. Vermani, and S. Garg, *Drug Discov. Today* **7**, 569 (2002).
- ¹⁰P. I. Lee, *J. Control. Release* **2**, 277 (1985).
- ¹¹D. Wagner, J. Burbach, C. Grünzweig, S. Hartmann, E. Lehmann, S. U. Egelhaaf, and H. E. Hermes, "Solvent and solute ingress into hydrogels resolved by a combination of imaging techniques," (2016), accepted for publication.
- ¹²R. Messing, N. Frickel, L. Belkoura, R. Strey, H. Rahn, S. Odenbach, and A. M. Schmidt, *Macromol.* **44**, 2990 (2011).
- ¹³A. M. Mathur, S. K. Moorjani, and A. B. Scranton, *J. Macromol. Sci., Rev. Macromol. Chem. Phys.* **36**, 405 (1996).
- ¹⁴D. Wagner, M. Börgardt, C. Grünzweig, E. Lehmann, T. J. J. Müller, S. U. Egelhaaf, and H. E. Hermes, *Rev. Sci. Instrum.* **86**, 093706 (2015).
- ¹⁵D. Sandrin, D. Wagner, C. E. Sitta, R. Thoma, S. Felekyan, H. E. Hermes, C. Janiak, N. de Sousa Amadeu, R. Kühnemuth, H. Löwen, S. U. Egelhaaf, and C. A. M. Seidel, *Phys. Chem. Chem. Phys.* (2016).
- ¹⁶J. Crank, *The Mathematics of Diffusion* (Oxford University Press, New York, 1979).

This page has been left intentionally blank.

APPENDIX A

SOFTWARE

A.1 Display and save images of two cameras

This code was written in LabVIEW.

`DisplayCurrentView&Save_2cams.vi` is a program to control two firewire cameras. Live images are displayed and images are saved at defined time intervals. The number of images and the frame rate can be chosen and changed at any time during the measurement. Brightfield images are saved as jpg and fluorescence images as tiff files in a predefined file location. The date and a timestamp are written in the individual filenames.

The block-diagram shows the programming behind the graphical user interface.

DisplayCurrentView&Safe_2cams.vi

C:\Users\Dana\Dropbox\Arbeit\Appendix\Software\DisplayCurrentView&Safe_2cams.vi

Letzte Änderung am 26.04.2016 um 10:41

Gedruckt am 26.04.2016 um 11:23

Input values here before running (number and delay can be ammended)

Brightfield camera

Time between pictures (s) Beginning of filename Brightfield Camera Enter file path where BF images will be saved

Fluorescence camera

Number of pictures Beginning of filename Fluorescence Camera Enter file path where FI images will be saved

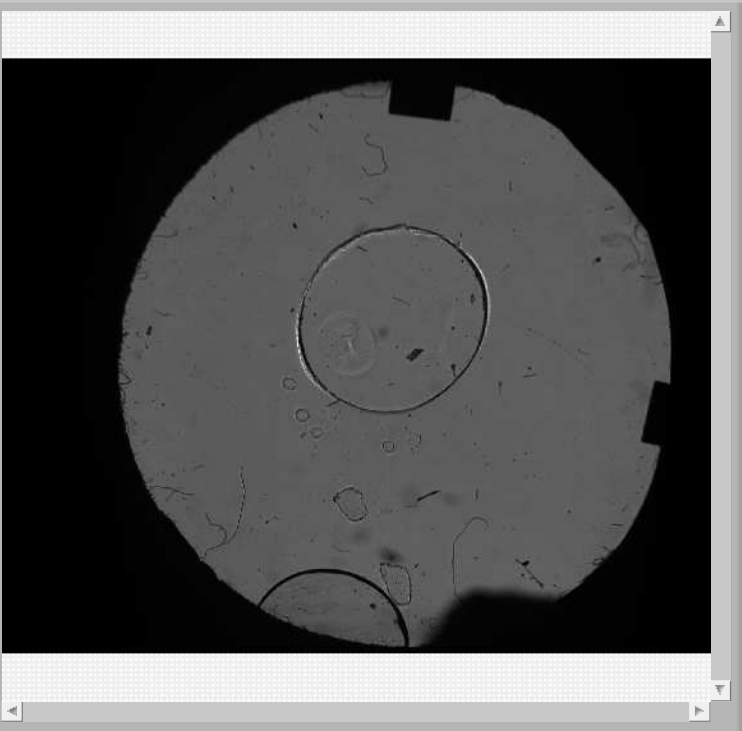
Details of last picture taken

File name BF cam

Number of pictures taken


File name FI cam

Brightfield



0 (0,0)

Fluorescence



0,0,0 (36,286)

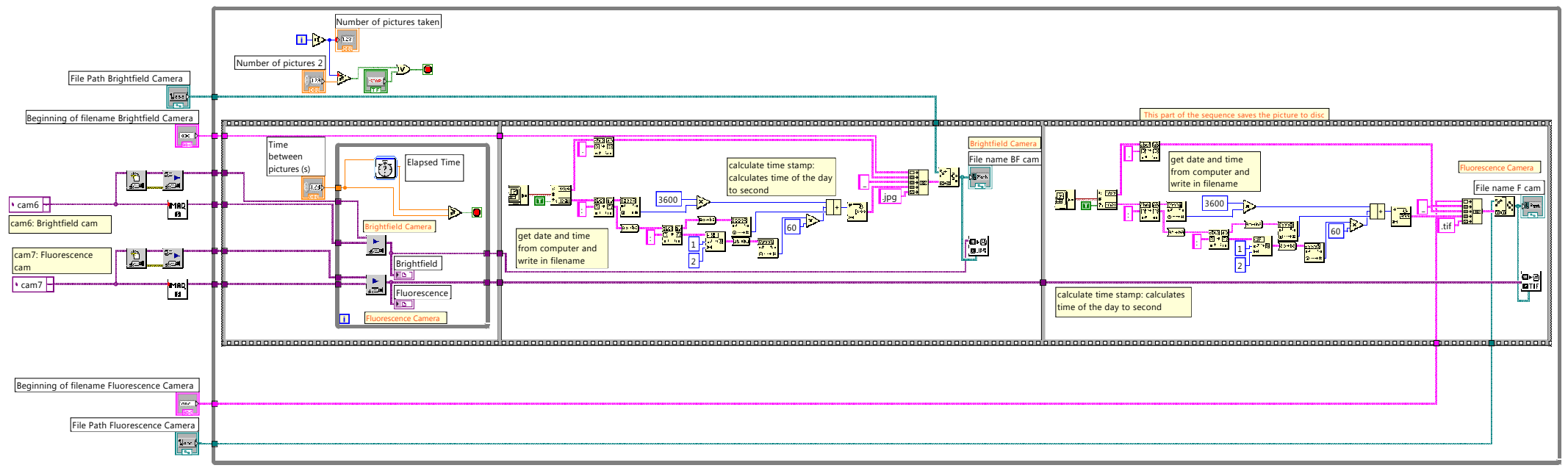
STOPP

DisplayCurrentView&Safe_2cams.vi

C:\Users\Dana\Dropbox\Arbeit\Appendix\Software\DisplayCurrentView&Safe_2cams.vi

Letzte Änderung am 26.04.2016 um 10:41

Gedruckt am 26.04.2016 um 10:41



A.2 Choose color plane, calculate average intensity in region of interest and export results to Origin

This code was written in LabVIEW.

Average_ChooseColorPlane_ExportOrigin.vi is a program that enables the user to read in several color images (for instance tiff, jpg or png files), select a color plane and a region of interest. The mean intensity recorded in the region of interest of the selected color plane is calculated for each image and the results are exported to an Origin file.

Before running the program, the user can already specify an existing Origin file and enter the names of subfolder, workbook and worksheet in this file, and select the first image to be analyzed. This image will be displayed after running the program. The user is then asked via a file dialog to choose all files to be analyzed. Then the user can specify a region of interest in the displayed image using two cursors. The averaging process begins after the button '*Area of interest chosen*' is pressed. The data path of the file that is currently analyzed and the according average pixel value is displayed. The timestamp read from the image filename and the average values are saved in the Origin file.

The block-diagram shows the programming behind the graphical user interface. Two subVIs are included: DisplayImageColor_chooseColorPlane_131101_subvi.vi and IntensNormArea_subvi.vi. The first subVI will be described in more detail in the next section. The second subVI merely reads in a fraction of a data array and calculates the mean value. It is thus not shown explicitly.



Average_ChooseColorPlane_ExportOrigin.vi

C:\Users\Dana\Dropbox\Arbeit\Appendix\Software\Average_ChooseColorPlane_ExportOrigin.vi

Letzte Änderung am 26.04.2016 um 10:19

Gedruckt am 26.04.2016 um 10:19

1) Choose existing Origin file where the results will be saved. Specify names of folder, book and sheet in origin file.
 2) Select first image file to be displayed and desired color plane.
 3) Press the button "Continue".
 4) Select all images to be processed and a folder where the images will be saved.
 5) Choose an Area of interest with the yellow and blue cursors. Make sure that the yellow cursor is below and to the left of the blue cursor.
 6) Press "Area of interest chosen".
 7) The timestamp read from the images and the mean pixel value of area of interest are stored in the origin file.

Choose Origin File to Save Data at
 % C:\phd\Auswertung\Test.opj

Enter Date of Measurement
 (name for Subfolder in Origin)
 20150308

Enter Sample Name
 (Name for Book in Origin)
 Messung8

Sheet Name in Origin
 Center

Enter filename of first image to analyze
 C:\phd\20150308\
 FL_Mrz15M08_11_53967.tif

Choose Color Plane
 Green

Display of first image

33 (868,111)

Continue

First image: choose area to average

2452
2200
2000
1800
1600
1400
1200
1000
800
600
400
200
0

0 200 400 600 800 1000 1200 1400 1600 1800 2056

50
25
0

Cursors	X	Y
1	860	1100
2	880	1120

Area of interest chosen

current data path
 % C:\phd\20150308\FL_Mrz15M08_11_53967.tif

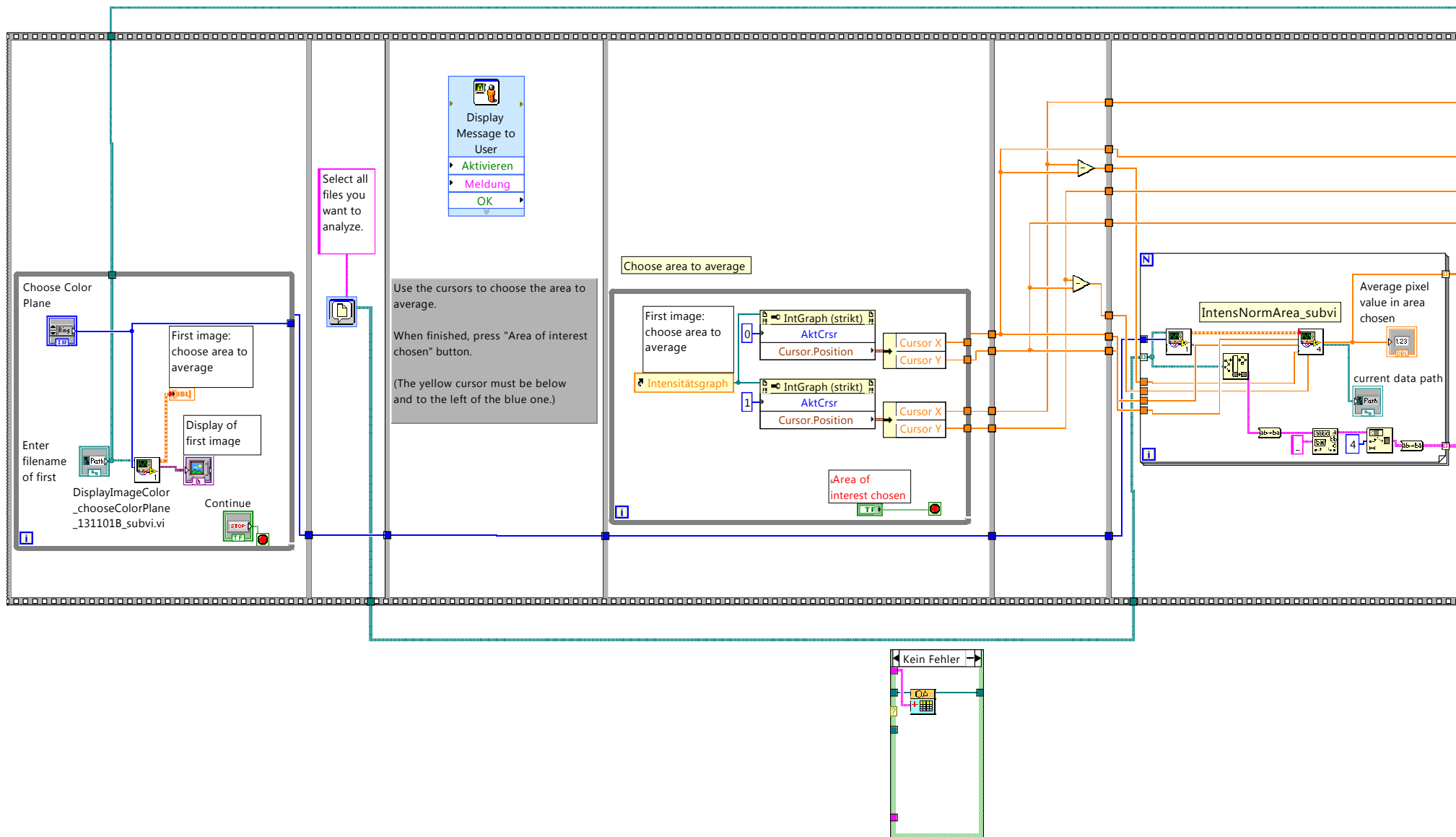
Average pixel value in area chosen 4.675

Average_ChoseColorPlane_ExportOrigin.vi

C:\Users\Dana\Dropbox\Arbeit\Appendix\Software\Average_ChoseColorPlane_ExportOrigin.vi

Letzte Änderung am 29.04.2016 um 12:58

Gedruckt am 29.04.2016 um 12:58

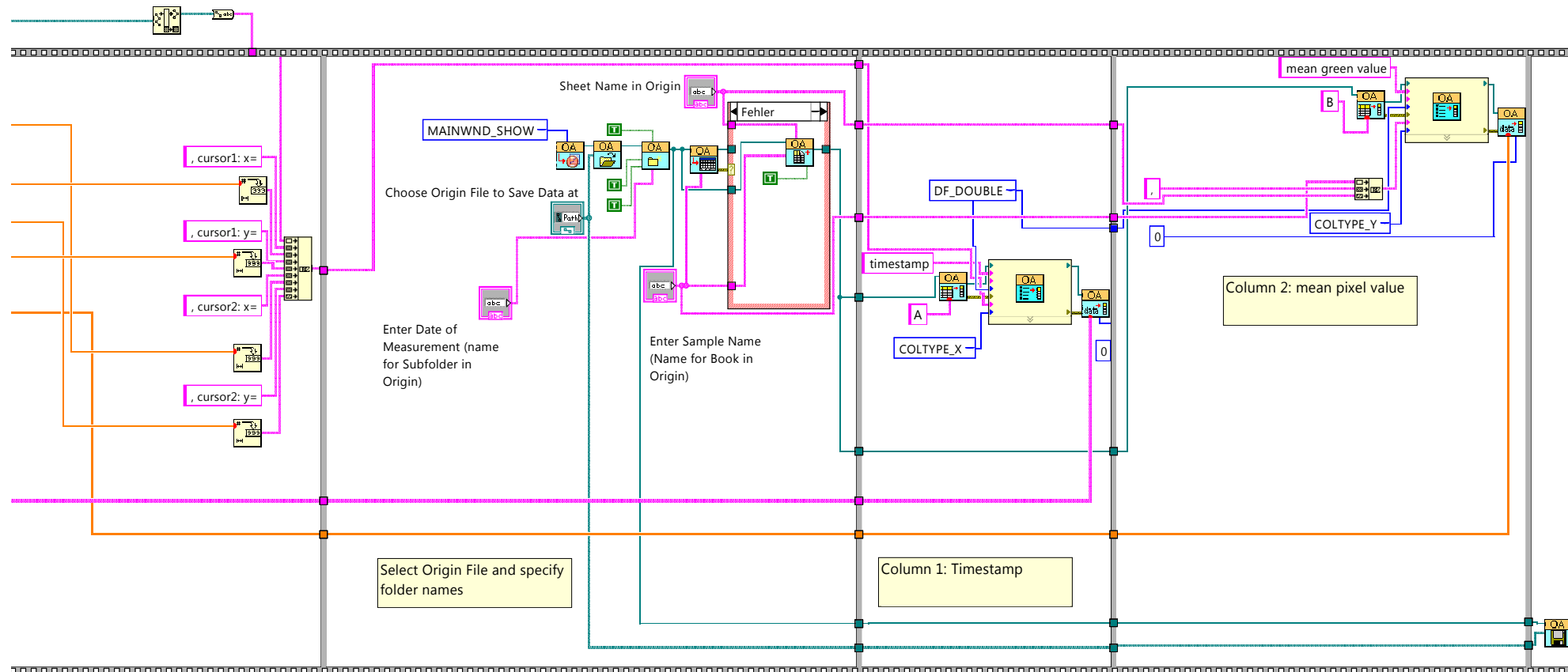


Average_ChoseColorPlane_ExportOrigin.vi

C:\Users\Dana\Dropbox\Arbeit\Appendix\Software\Average_ChoseColorPlane_ExportOrigin.vi

Letzte Änderung am 29.04.2016 um 12:58

Gedruckt am 29.04.2016 um 12:58

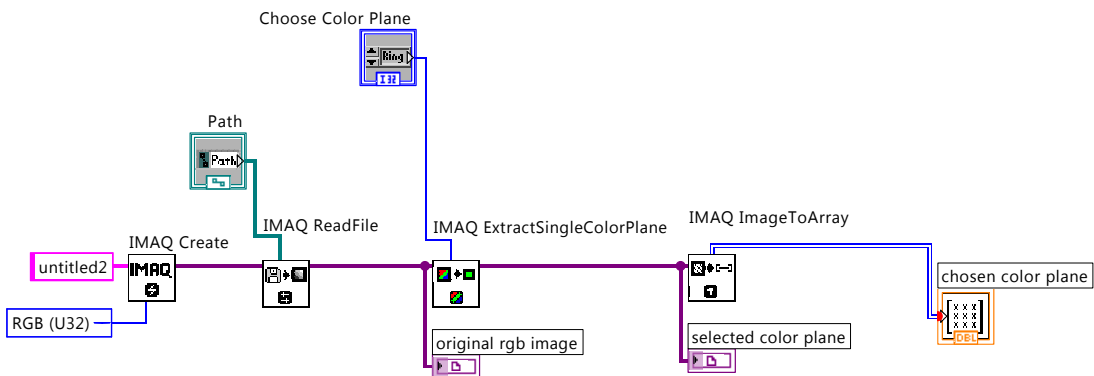


A.3 SubVI: Display color image and choose color plane

This code was written in LabVIEW.

This subVI was used in the previously shown program. Similar subVIs will be seen in the following sections, which are used to read in different image formats and display additional information such as an intensity histogram. These subVIs will not be shown in detail. Here, a color image is read in and displayed. A color plane is chosen and then only this color plane is displayed. The chosen color plane is transferred into an array which can be displayed and modified by the main program.

DisplayImageColor_chooseColorPlane_131101_subvi.vi
D:\phd\Labview\12NovAktuelleLabView\Auswertung\Fluorescence\
DisplayImageColor_chooseColorPlane_131101_subvi.vi
Last modified on 29.04.2016 at 11:19
Printed on 29.04.2016 at 12:28



A.4 Choose color plane and subtract background in area of interest in fluorescence images

This code was written in LabVIEW.

ChooseColorPlane_SubtractDark.vi is a program that enables the user to read in several color images (for instance tiff, jpg or png files), select a color plane and a region of interest. A background subtraction is performed and the pixel values of the chosen color plane are saved as a cropped text image. The background correction is optional and was found to have no influence on the results of the analysis of the fluorescence images.

The user is first asked to select an exemplary image, a dark image and the desired color plane. The original images and the resulting image after background subtraction are displayed and the contrast can be changed if necessary. Images and color plane can be changed until the *'Continue'* button is pressed. Afterwards, the user is asked via a file dialog to select all files to be analyzed and the folder where the cropped images will be saved. The area of interest can be chosen by moving the cursors on the displayed image or by inserting the x and y coordinates. The image manipulation is started after the button *'Area of interest chosen'* is pressed. All cropped images are briefly displayed.

The block-diagram shows the programming behind the graphical user interface.



ChooseColorPlane_subtractDarkinArea.vi

D:\phd\Labview\Software\ChooseColorPlane_subtractDarkinArea.vi

Last modified on 22.04.2016 at 15:01

Printed on 22.04.2016 at 15:10

- 1) Choose a test image, a dark image and the desired color plane. Both image and the result of the subtraction will be displayed. Change the contrast if necessary.
- 2) Press "Continue".
- 3) Select all images to be processed and a folder where the images will be saved.
- 4) Choose an Area of interest with the yellow and blue cursors. Make sure that the yellow cursor is below and to the left of the blue cursor.
- 5) Press "Area of interest chosen".
- 6) Text images will be saved with the filename extension "_sd".

Choose Color Plane

#Green

Enter filename of first image to analyze

D:\AKTUELL\Makroskop\2015Mrz\M03\FL\FL_Mrz15M03_04_56519.tif

dark

D:\AKTUELL\Makroskop\2015Mrz\M03\FL\FL_Mrz15M03_04_51890.tif

test image

dark image

Result: data-dark test

Continue

First Data File: choose area of interest

Cursors	X	Y
1	590	900
2	1740	2100

Cut Data

subtract dark

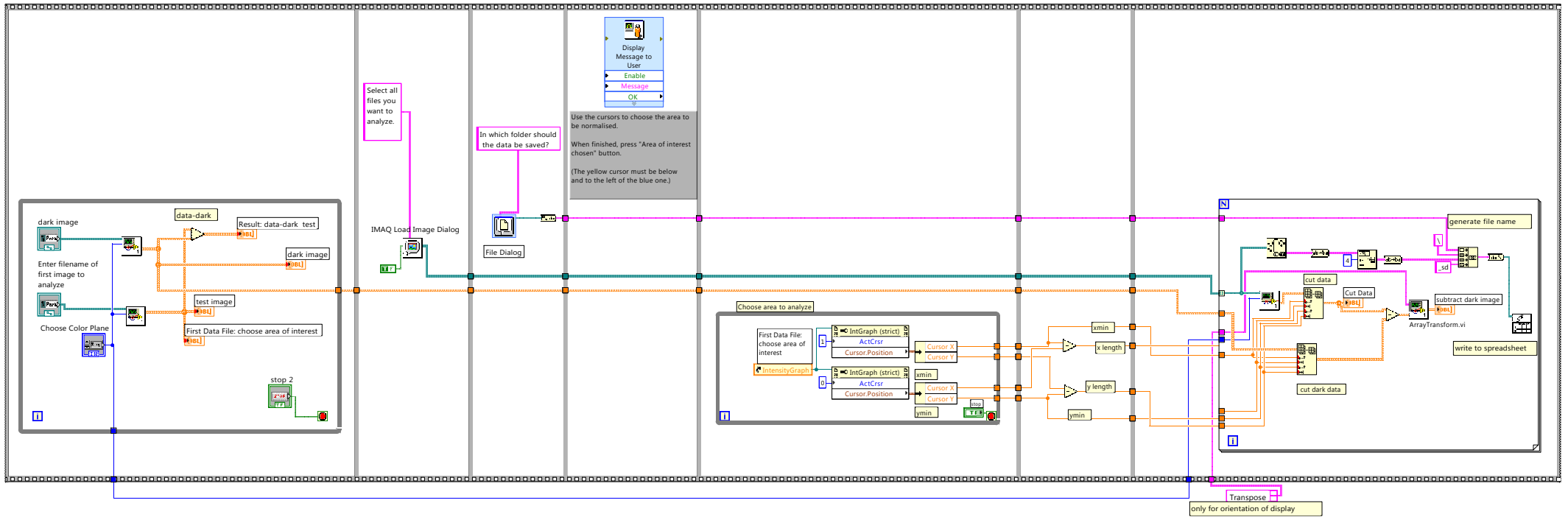


ChooseColorPlane_subtractDarkinArea.vi

D:\phd\Labview\Software\ChooseColorPlane_subtractDarkinArea.vi

Last modified on 29.04.2016 at 12:12

Printed on 29.04.2016 at 12:12



A.5 Normalize and scale neutron images

This code was written in LabVIEW.

NR_NormaliseScale.vi is a program that enables the user to correct neutron images (fits files) for spatial and temporal inhomogeneities in beam intensity and detector efficiency. This was done with all neutron images in a first step of the analysis. The user is supposed to select a dark, a bright and the first image to be analyzed before running the program. Dark and bright images were taken with all shutters closed or the sample removed from the beam, respectively. The median of a stack five dark and five bright images, which were previously saved as text images are used. The user is asked via a file dialog to select all files to be analyzed and the folder where the normalized images will be saved. Afterwards, a reference area in the first image is chosen where no change in intensity is expected during the measurement time using two cursors. The mean measured intensity in this reference area, $\langle I \rangle$, will be calculated for the dark, the bright and all sample images individually. To remove intensity peaks, which are an artifact caused by high intensity γ -particles directly hitting the CCD chip, the histograms of the reference areas of dark, bright and sample images are shown and the user is asked to review them and choose cut-off values. All values higher than the chosen cut-off values will be ignored in the averaging process. These mean intensities are used to calculate a scaling factor, S^* , for each image:

$$S^* = \frac{\langle I_{\text{bright}} \rangle - \langle I_{\text{dark}} \rangle}{\langle I_{\text{sample}} \rangle - \langle I_{\text{dark}} \rangle}$$

In the next step, the user is asked to choose the region of interest in the sample image using the same cursors as before. This region of interest can be the entire image or just a small fraction. The program crops the images according to the chosen region of interest and saves text images, where every original pixel intensity value is replaced by the transmission relative to the chosen reference area, T_{rel} :

$$T_{\text{rel}} = \frac{I_{\text{sample}}(x, y, t) - I_{\text{dark}}(x, y, t)}{I_{\text{bright}}(x, y, t) - I_{\text{dark}}(x, y, t)} \times S^{*-1}$$

The scaling factor is included in the new filename.

The block-diagram shows the programming behind the graphical user interface.



NR_NormaliseScale.vi

D:\phd\Labview\Software\NR_NormaliseScale.vi

Last modified on 25.04.2016 at 15:01

Printed on 25.04.2016 at 15:06

Analysis of neutron radiography images

- 1) Read in a dark image (taken when all shutters closed), a bright image (taken without a sample in the beam) and the first image to be analyzed. Here, the median of a stack five dark and five bright images, which were previously saved as text images are used.
- 2) File Dialog: Enter filename of last data set to analyze.
- 3) File Dialog: In which folder should the data be saved?
- 4) Choose an area to normalize the intensity to. This should be an area where no change in intensity is expected during the measurement. When finished, press "Area for intensity normalization chosen".
- 5) Look at the histograms and choose cut-off values for the calculation of the scaling factor. The cut-off removes intensity peaks.
- 6) Press "All parameters chosen".
- 7) Use the cursors to choose the area to be normalised. When finished, press "Area of interest chosen" button.
- 8) Normalized and scaled text images will be saved with the filename extension ".nor".

Select dark image: text image (.txt)

G:\Neutron Radiography\2012OktPSI_20120616_P12088\Messung10-Probe16\Median_dark_M10.txt

Select bright image: text image (.txt)

G:\Neutron Radiography\2012OktPSI_20120616_P12088\Messung10-Probe16\Median_bright_M10.txt

Select first image: original NR image (.fits)

G:\Neutron Radiography\2012OktPSI_20120616_P12088\Messung10-Probe16\N_1_60_D2O_D70K_H_0001.fits

Cut-off for gamma spots: dark Mean: dark 736.385

1200 Number of points removed: dark 106

Cut-off for gamma spots: bright Mean: bright 9474.82

13000 Number of points removed: bright 4

Cut-off for gamma spots in scaling area Number of points removed 2

13000

Histogram dark in area chosen histogram count

min value in area 642 max value in area 8130

Histogram bright in area chosen histogram count

min value in area 2 8490 max value in area 2 18133

Histogram Data histogram count

min value 521 max value 65535

All parameter chosen

G:\Neutron Radiography\2012OktPSI_20120616_P12088\Messung10-Probe16\normscale\N_1_60_D2O_D70K_H_85843_114_0001.nor

time of day 2012-11-01T23:50:43

timestamp (s) 85843

calculated Scaling factor 1.142

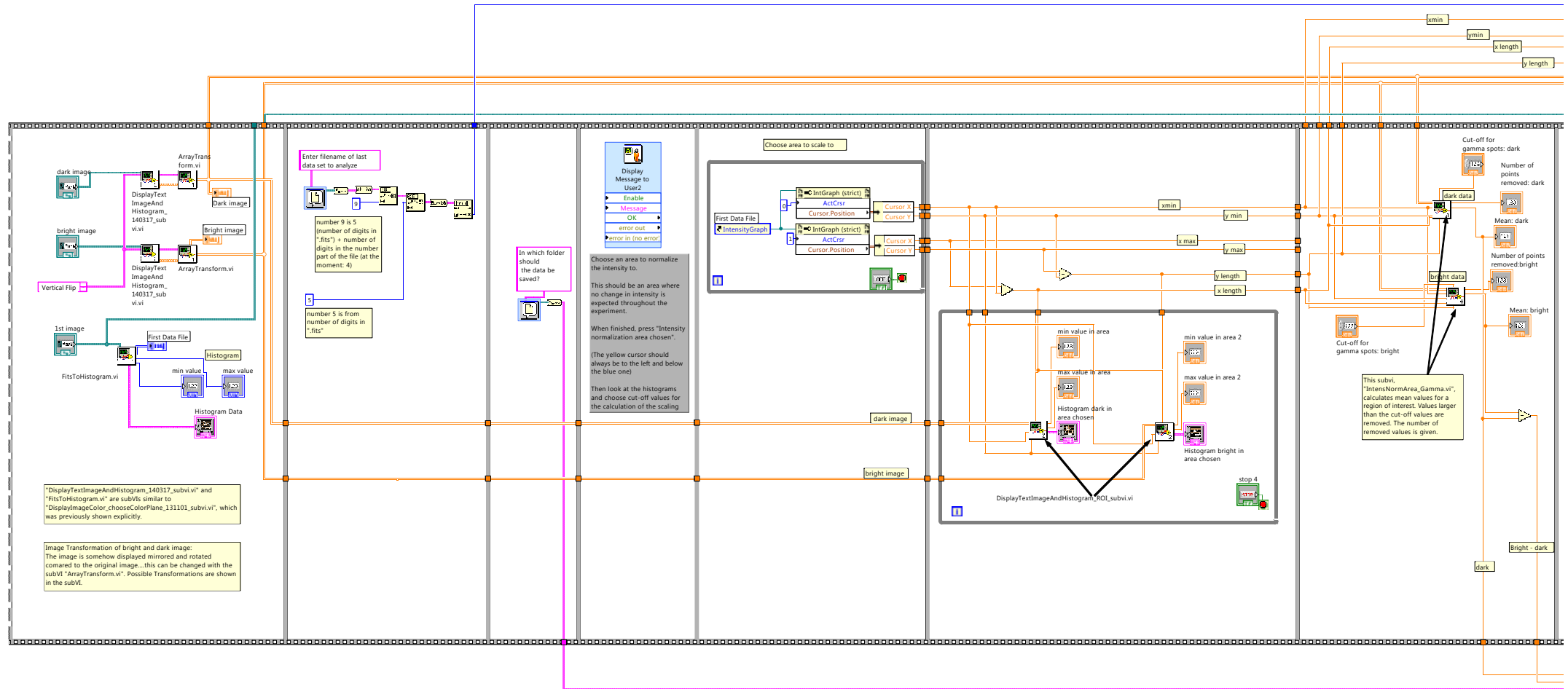


NR_NormaliseScale.vi

D:\phd\Labview\Software\NR_NormaliseScale.vi

Last modified on 29.04.2016 at 14:47

Printed on 29.04.2016 at 14:48



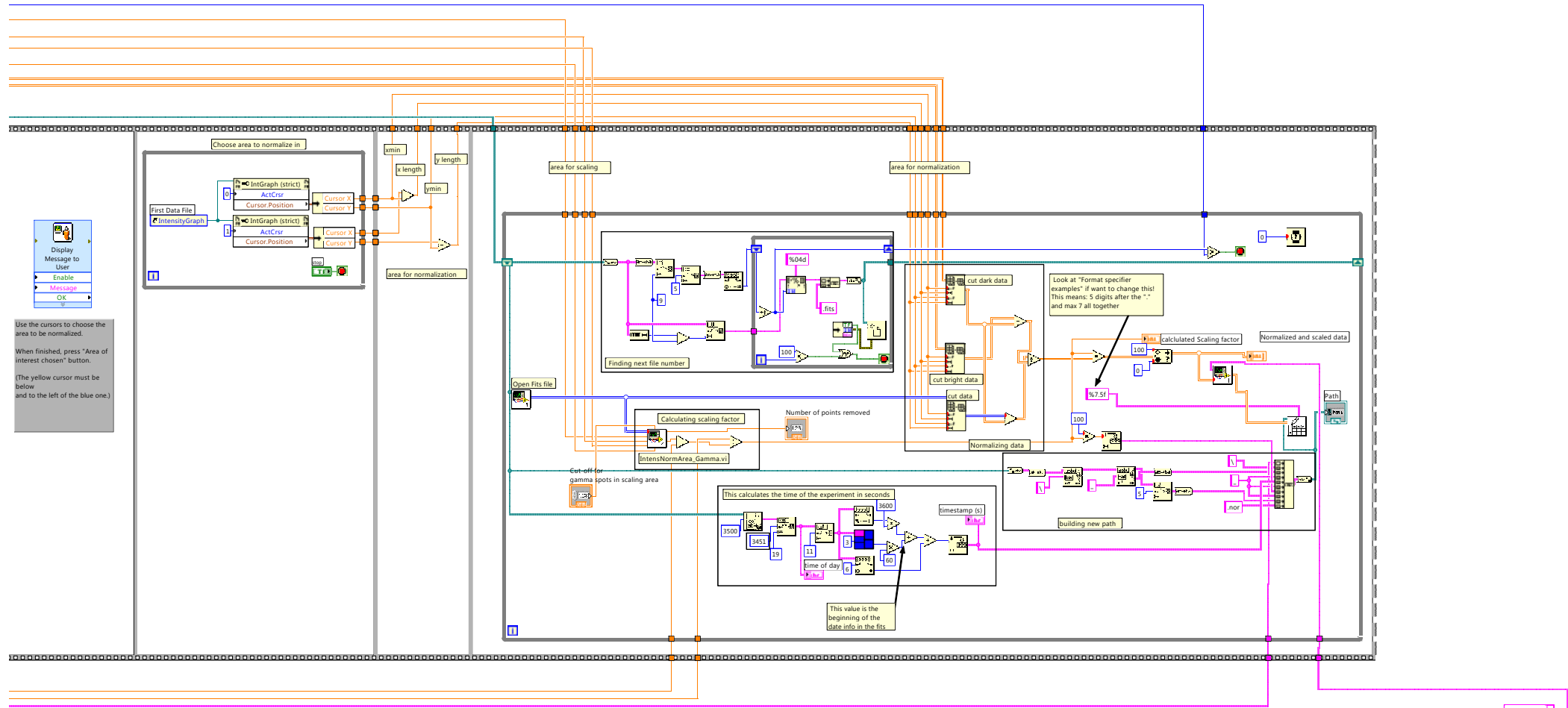


NR_NormaliseScale.vi

D:\phd\Labview\Software\NR_NormaliseScale.vi

Last modified on 29.04.2016 at 14:47

Printed on 29.04.2016 at 14:48



Use the cursors to choose the area to be normalized.
When finished, press "Area of interest chosen" button.
(The yellow cursor must be below and to the left of the blue one.)

Look at "Format specifier examples" if want to change this!
This means 5 digits after the "." and max 7 all together

This calculates the time of the experiment in seconds

This value is the beginning of the date info in the fits

A.6 Convert image to binary image

This code was written in LabVIEW.

`ConvertToBinary.vi` is a program that enables the user to create a binary image of the initial hydrogel. In the binary image, the hydrogel is recognized as 'particle' and all pixels belonging to this particle get the value 1, while all other pixels get the value 0. If additional parts of the source image such as parts of the sample cell are recognized as particle, filters can be used to solve this problem. One efficient way to remove small particles is the 'Waddel Disk Diameter' filter. The waddel disk diameter is the diameter of a disk with the same area as the particle. A lower and upper value of this diameter can be chosen and all particles in between this range are removed.

The shown program is optimized for neutron images but can also be used for fluorescence images after small modifications.

The block-diagram shows the programming behind the graphical user interface.

ConvertToBinary.vi

D:\phd\Labview\Software\ConvertToBinary.vi

Last modified on 25.04.2016 at 15:18

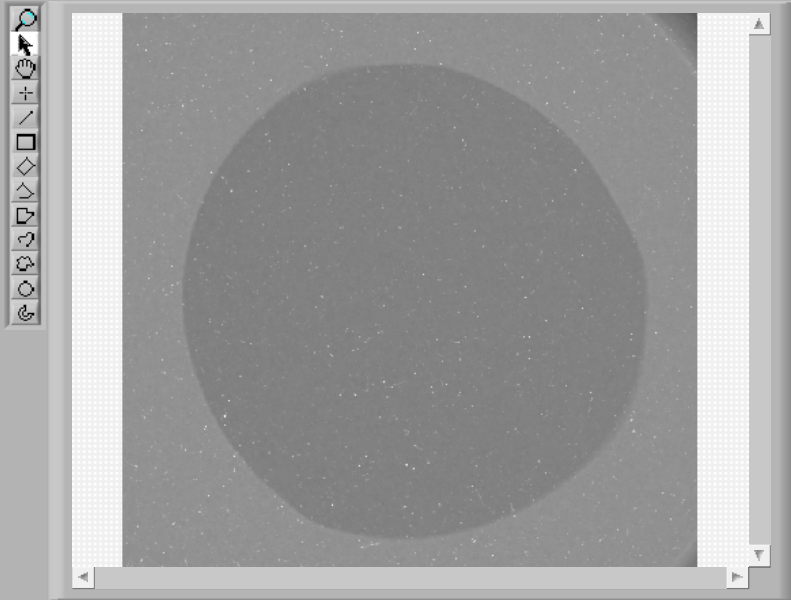
Printed on 25.04.2016 at 15:19

- 1) Read in normalized neutron image of initial hydrogel before contact with solvent. Change contrast if necessary
- 2) Adjust parameters until manipulated image as desired (hydrogel: red, rest: black).
- 3) Save File.

Normalized neutron radiograph

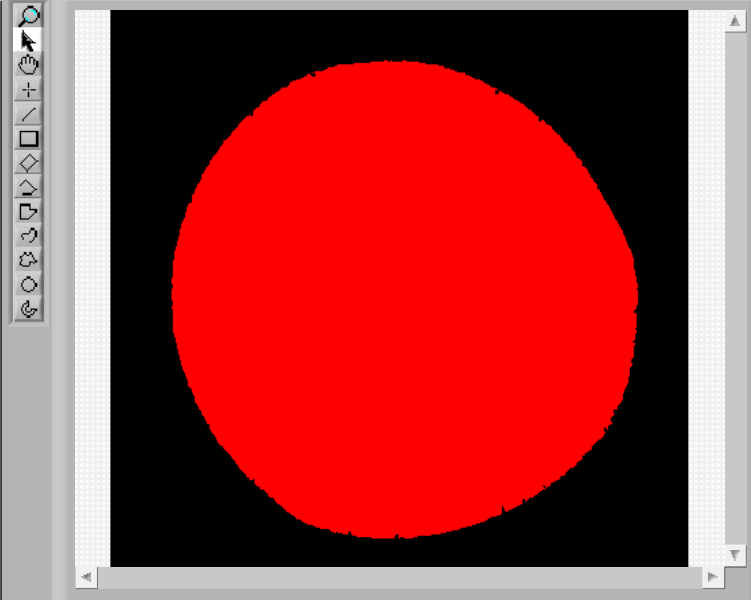
G:\Neutron Radiography\2012OktPSI_20120616_P12088\Messung10-Probe16\normscale\N_1_60_D2O_D70K_H_86107_114_0002.nor

Source Image



504x486 0.84X 8-bit image 144 (419,26)

Manipulated Image



504x486 0.84X 8-bit image 0 (0,0)

Change Contrast

Max Value: 2

Min Value: 0

Scale: 133.889

Save File

Filename Out

G:\Neutron Radiography\2012OktPSI_20120616_P12088\Messung10-Probe16\normscale\N_1_60_D2O_D70K_H_86107_114_0002_binary.tdms

Kernel Family: Smoothing 3
 Kernel Size (3,5,...): 3
 Kernel Number: 5

Adjust parameters:
 Choose Kernel Family from 1 to 4
 (3: Smoothing optimal)

Waddle Disk Diameter:
 makes sure that only hydrogel is detected as "particle"

Selection Values

Waddle Disk Diameter: 0

Range Lower Value: 0.00

Range Upper Value: 70.00

Include

Measurement Type: Pixel

Threshold Data out

Lower value: 0.00

Upper value: 117.00

Replace Value: 0.00

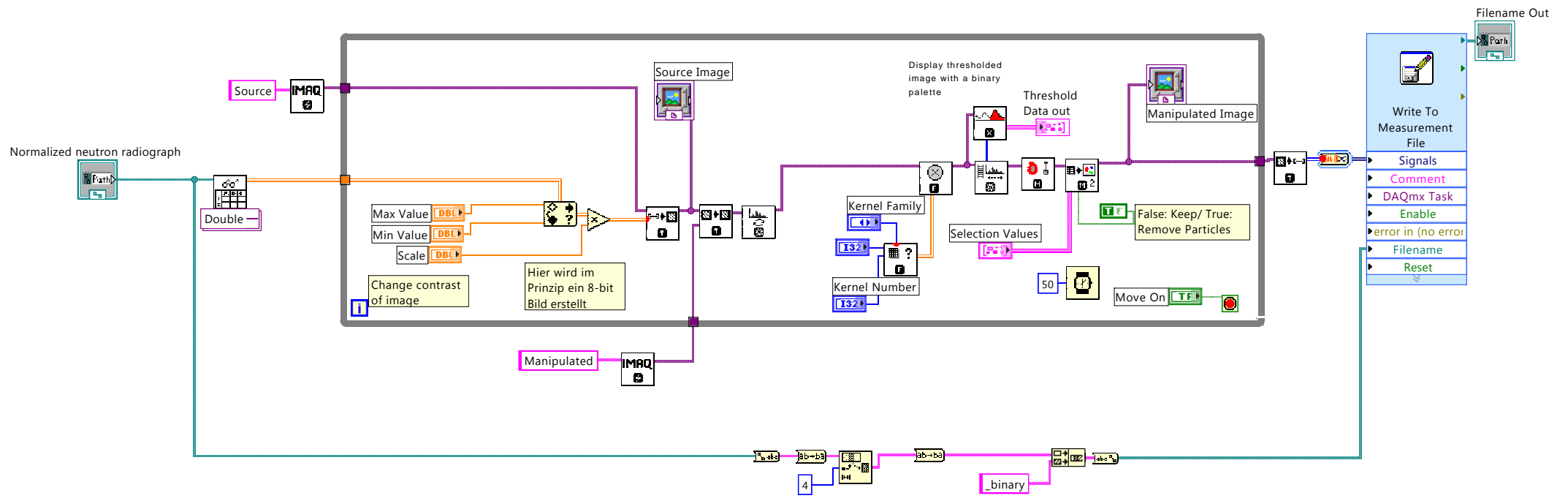
Keep/Replace Value (Replace): Replace

ConvertToBinary.vi

D:\phd\Labview\Software\ConvertToBinary.vi

Last modified on 25.04.2016 at 15:18

Printed on 25.04.2016 at 15:20



A.7 Find contour of the hydrogel

This code was written in LabVIEW.

`FindContour.vi` is a program that enables the user to calculate a contour map of a binary image based on the algorithms of Danielsson. This is done using the National Instruments VI IMAQ `Danielsson.vi`. The binary image of the hydrogel is read in and displayed. The inverse of this image is also displayed, where everything but the hydrogel belongs to the particle (value 1). A contour map is calculated for both images. Every pixel value of the particle (either the hydrogel or the region around the hydrogel) is encoded as a function of the location of that pixel in relation to the distance to the border of the particle. All distances greater than 255 are rounded down to 255. The values of the inside contour map are negated and all values are saved in one spreadsheet file. The resulting spreadsheet is basically a text image where every pixel has a value between -255 and 255 depending on the distance to the hydrogel border. Locations inside the hydrogel have negative values, locations outside the hydrogel have positive values and the border itself has the value 0. The block-diagram shows the programming behind the graphical user interface.



FindContour.vi

D:\phd\Labview\Software\FindContour.vi

Last modified on 25.04.2016 at 16:59

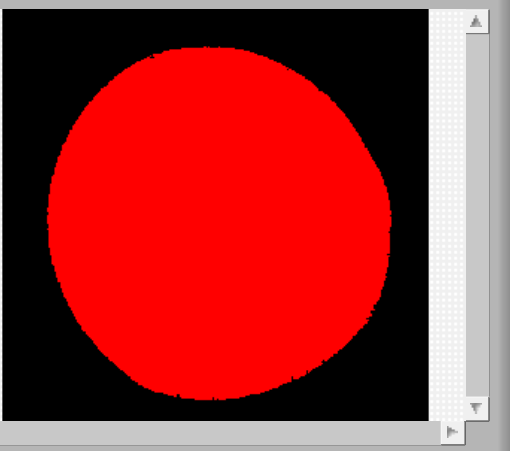
Printed on 25.04.2016 at 17:02

Input path of binary image before running

G:\Neutron Radiography\2012OktPSI_20120616_P12088\Messung10-Probe16\normscale\N_1_60_D2O_D70K_H_86107_114_0002_binary.tdms

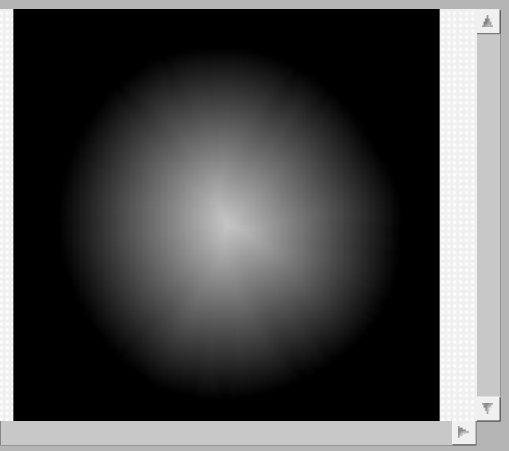
Write Output to File

Inside Image



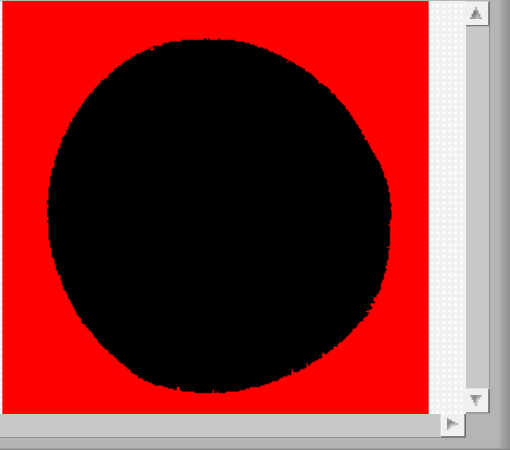
504x486 0.57X 8-bit image 0 (250,35)

Inside Contour Map



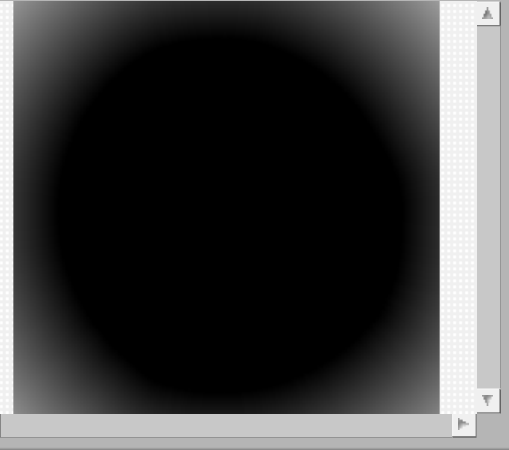
504x486 0.57X 8-bit image 0 (0,0)

Outside Image



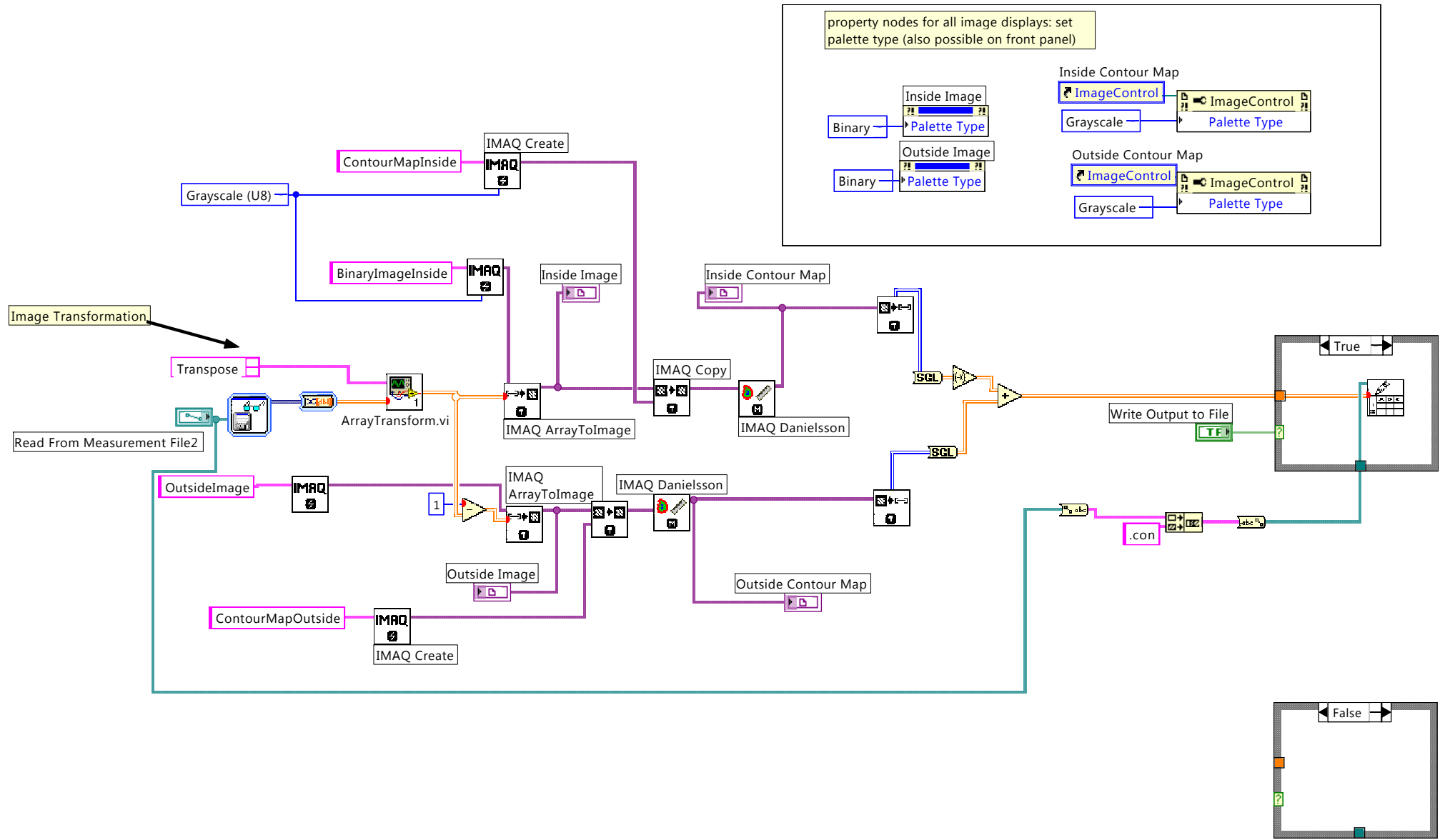
504x486 0.57X 8-bit image 1 (28,334)

Outside Contour Map



504x486 0.57X 8-bit image 149 (0,0)

FindContour.vi
 D:\phd\Labview\Software\FindContour.vi
 Last modified on 25.04.2016 at 16:59
 Printed on 25.04.2016 at 17:02



property nodes for all image displays: set palette type (also possible on front panel)

Binary	Inside Image	ImageControl
	Palette Type	ImageControl
Grayscale	Outside Image	ImageControl
	Palette Type	ImageControl

Inside Contour Map

Grayscale	ImageControl
	Palette Type

Outside Contour Map

Grayscale	ImageControl
	Palette Type

A.8 Calculate intensity profile

This code was written in LabVIEW.

NR_IntensityProfile_ExportOrigin.vi is a program that enables the user to calculate an intensity-distance profile for an image of choice and directly export the results to an Origin file. This is done by comparing an image and the corresponding contour map that was generated using the FindContour.vi program. The size of the image thus has to be identical to that of the contour map. The program basically averages all pixel values that belong to the same value of the contour map (i.e. a certain distance to the hydrogel border) and saves the results in a predefined Origin file. The program reads in the timestamp of the image from its filename and the timestamp of the contour map (t_0 : time when hydrogel was contacted with solution) and calculates the lag time ($\Delta t = t - t_0$). If the contour map was not calculated from the t_0 -image, an alternative t_0 -value can be entered before running the program. After choosing the image file to analyze, the user is asked to review the displayed image and decide if an area of the image should be omitted in the averaging process. This is useful in the case of air bubbles or if pieces of the sample cell are visible in the image. These areas are chosen with two cursors. The program replaces the pixel values of these areas with the value -10, which will be ignored later on in the averaging process by applying a lower threshold. Additionally, bright spots in the neutron images are removed by applying an upper threshold.

The shown program is optimized for neutron images but can also be used for fluorescence images after small modifications.

The block-diagram shows the programming behind the graphical user interface.

NR_IntensityProfile_ExportOrigin.vi
 D:\phd\Labview\Software\NR_IntensityProfile_ExportOrigin.vi
 Last modified on 25.04.2016 at 19:28
 Printed on 25.04.2016 at 19:30

t0 different to contour file?

Put in t0:

Choose Origin File to Save Data at:

Enter Date of Measurement (name for Subfolder in Origin):

Enter Sample Name (Name for Book in Origin):

Path to .con file:

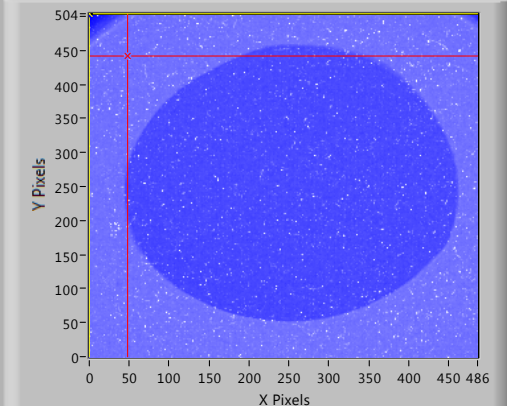
Current file being averaged:

Cursors:

	X	Y
Cursor 0	0	504
Cursor 1	48	442

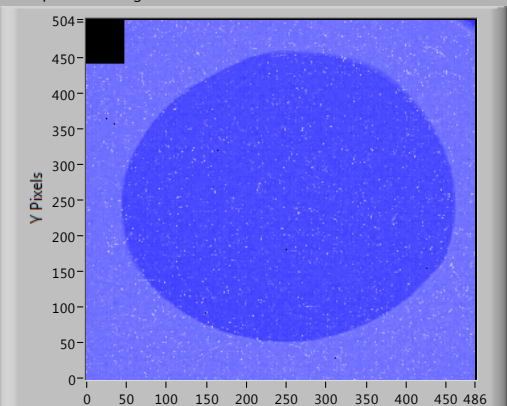
Yellow = Top Left
Red = Bottom Right

Original Image



X Pixels: 0 to 486
Y Pixels: 0 to 504

Manipulated Image



X Pixels: 0 to 486
Y Pixels: 0 to 504

No. of spots removed:

Manipulated Image

Width	Height
486	504

Contour Map

Width	Height
486	504

sizes of images and contour map must be identical

Data Array Size

Data Array Size:
 Data Array Overflow?

Bin Size (pixels)

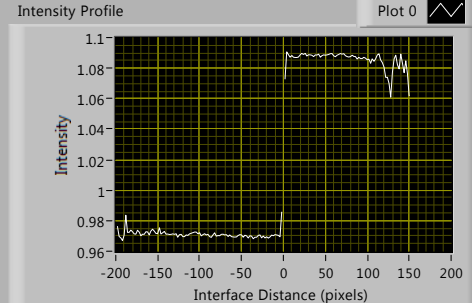
Desired	Actual	No of Bins
2	2	177

Histogram Size

Width	Height
177	20000

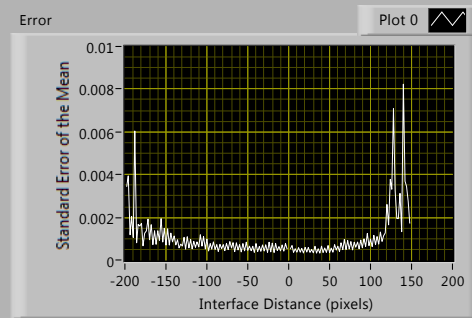
The Data Array Size Controls how big the histogram array is on initialisation. I have to initialise it first and 'guess' how many points will be in it. If one of the bins gets full, the led will light up and you will need to make it bigger.

Intensity Profile



Intensity: 0.96 to 1.1
Interface Distance (pixels): -200 to 200

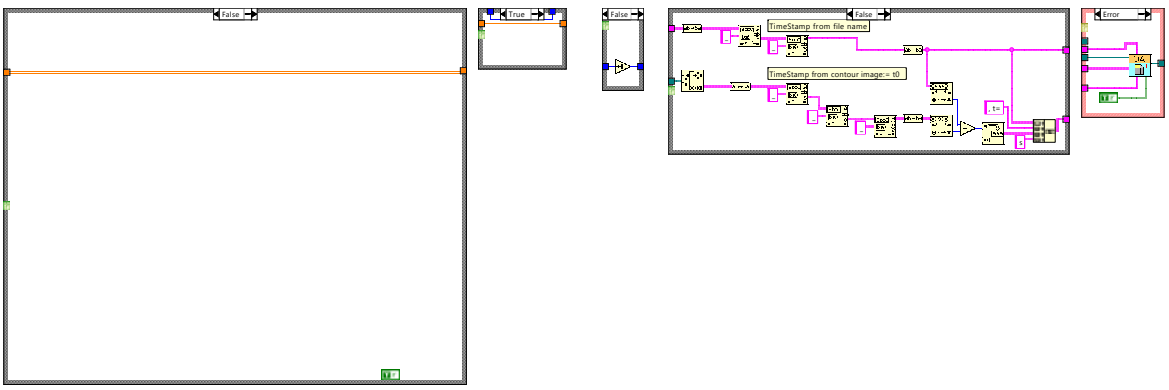
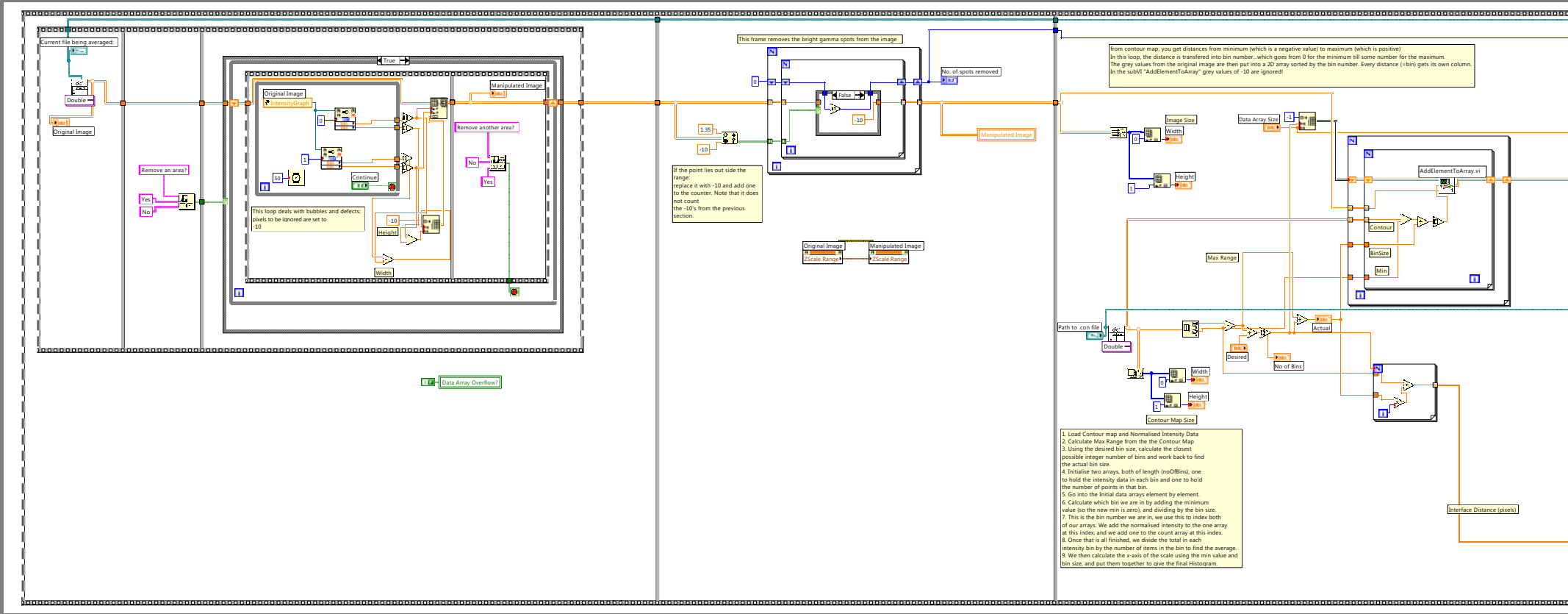
Error



Standard Error of the Mean: 0 to 0.01
Interface Distance (pixels): -200 to 200



NR_IntensityProfile_ExportOrigin.vi
 D:\phd\Labview\Software\NR_IntensityProfile_ExportOrigin.vi
 Last modified on 25.04.2016 at 19:28
 Printed on 25.04.2016 at 19:32



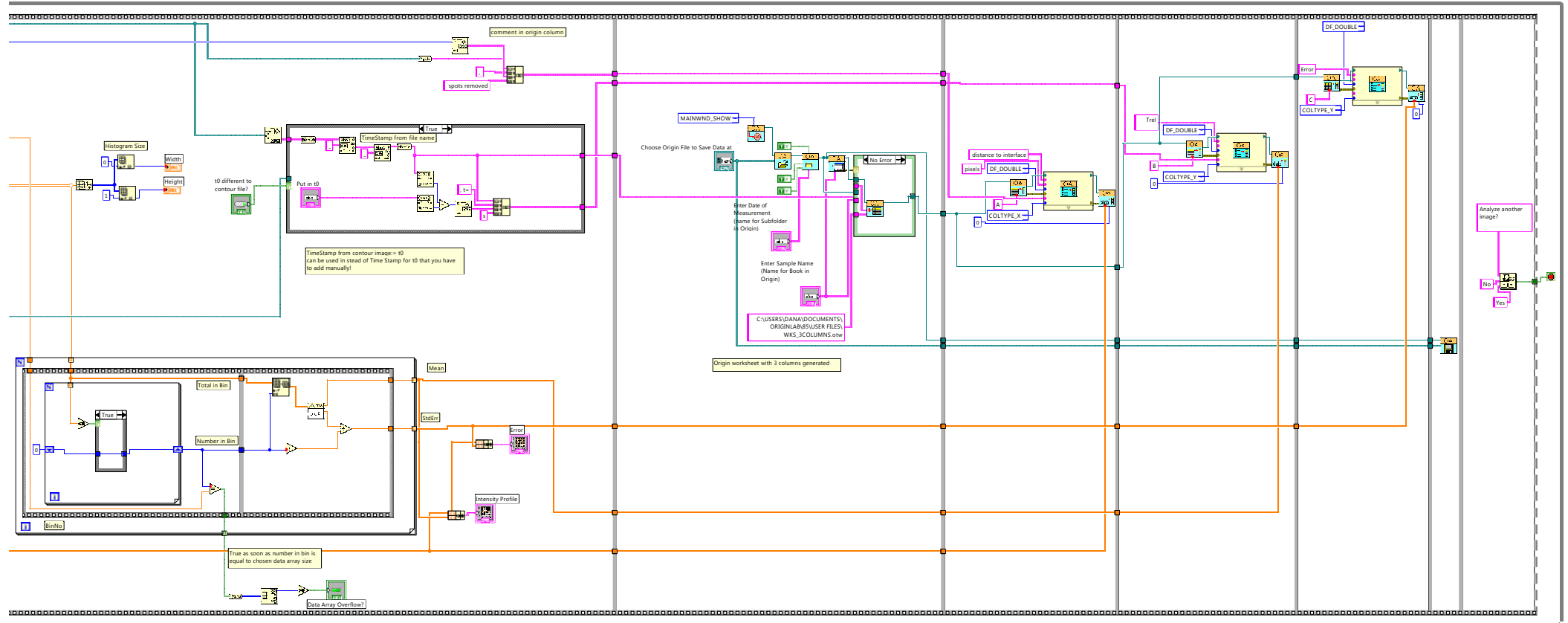


NR_IntensityProfile_ExportOrigin.vi

D:\phd\Labview\Software\NR_IntensityProfile_ExportOrigin.vi

Last modified on 25.04.2016 at 19:28

Printed on 25.04.2016 at 19:32



This page has been left intentionally blank.

PUBLICATIONS: PROTEIN PHASE BEHAVIOR

In the course of this PhD thesis, I contributed to four additional publications about protein phase behavior. Chapter B.1 deals with the effects of salt, glycerol, and dimethyl sulfoxide on the phase behavior of lysozyme solutions. Fluid-solid transitions, gas-liquid coexistence curves, and second virial coefficients were determined experimentally and interpreted theoretically based on the thermodynamic perturbation theory and the Derjaguin-Landau-Verwey-Overbeek model. Additionally, the fluid-solid transition temperatures of lysozyme solutions in the presence of two salts (NaCl and GuHCl) were compared (Chapter B.2). It was shown that both salts seem to affect the transition temperatures through electrostatic screening and salt-specific contributions, which were found to be additive in mixtures of the two salts. The specific effects of ionic and non-ionic additives on the phase behavior of lysozyme solutions were further elaborated and described in terms of effective colloidal interaction models (Chapter B.3). Finally, the macroscopic phase behavior of protein solutions in presence of all previously investigated cosolvents was quantitatively linked to protein-protein interactions based on a coarse-grained, simplified colloidal approach (Chapter B.4).

This page has been left intentionally blank.

B.1 Effect of glycerol and dimethyl sulfoxide on the phase behavior of lysozyme: Theory and experiments

Journal: The Journal of Chemical Physics

Reference: *J. Chem. Phys* **136**, 015105 (2012), DOI: 10.1063/1.3673442

Impact factor: 2.952

Authors: Christoph Gögelein, **Dana Wagner**, Frédéric Cardinaux, Gerhardt Nägele, and Stefan U. Egelhaaf

joint 1st author

DW performed phase diagram and light scattering measurements, calculated the second virial coefficients and analyzed the experimental data. CG did the theoretical calculations and the comparison between theory and experiment. All authors conceived and discussed the project and SUE and GN supervised the project. All authors contributed to the writing of the manuscript.

45% contribution of DW

This page has been left intentionally blank.

B.2 Additivity of the Specific Effects of Additives on Protein Phase Behavior

Journal: The Journal of Physical Chemistry. B

Reference: *J. Phys. Chem. B* 2015, 119, 14986–14993, DOI: 10.1021/acs.jpcc.5b08078

Impact factor: 3.302

Authors: Florian Platten, Jan Hansen, Johanna Milius, **Dana Wagner**, and Stefan U. Egelhaaf

4th author

DW, JH and JM performed the cloudpoint temperature measurements. FP performed CD measurements, analyzed and interpreted the data. FP and SUE conceived, discussed and supervised the project. All authors contributed to the writing of the manuscript.

20% contribution of DW

This page has been left intentionally blank.

B.3 Tuning protein-protein interactions by cosolvents: specific effects of ionic and non-ionic additives on protein phase behavior

Journal: Physical Chemistry Chemical Physics

Reference: *Phys. Chem. Chem. Phys.* 2016, **18**, 10270–10280, DOI: 10.1039/C5CP07285A

Impact factor: 4.493

Authors: Florian Platten, Jan Hansen, **Dana Wagner**, and Stefan U. Egelhaaf

3rd author

DW, and JH performed the cloudpoint temperature measurements. FP analyzed the data. FP and SUE conceived, discussed and supervised the project. All authors contributed to the writing of the manuscript.

25% contribution of DW

This page has been left intentionally blank.

B.4 Cosolvent-Induced Changes of Protein-Protein Interactions: From Phase Behavior to Second Virial Coefficient

Journal: The Journal of Physical Chemistry Letters

Status: In Preparation

Impact factor: 8.539

Authors: Florian Platten, Jan Hansen, **Dana Wagner**, and Stefan U. Egelhaaf

3rd author

DW, and JH performed phase diagram and light scattering measurements. DW, FP and JH analyzed the data. FP and SUE conceived, discussed and supervised the project. All authors contributed to the writing of the manuscript.

25% contribution of DW

This page has been left intentionally blank.

Cosolvent-Induced Changes of Protein–Protein Interactions: From Phase Behavior to Second Virial Coefficient

Florian Platten,* Jan Hansen, Dana Wagner, and Stefan U. Egelhaaf

*Condensed Matter Physics Laboratory, Heinrich Heine University, 40225 Düsseldorf,
Germany*

E-mail: Florian.Platten@hhu.de

*To whom correspondence should be addressed

B.4 Cosolvent-Induced Changes of Protein-Protein Interactions: From Phase Behavior to Second Virial Coefficient

Abstract

Protein stabilizing and destabilizing cosolvents are routinely used in biochemistry. However, probably due to experimental limitations and the molecular complexity of the systems, only little is known about their effects on protein–protein interactions, which govern the pathways of protein self-assembly into ordered and amorphous structures. We quantitatively link the macroscopic phase behavior of protein solutions in the presence of cosolvents to protein–protein interactions based on a coarse-grained, simplified colloidal approach. The Derjaguin-Landau-Verwey-Overbeek (DLVO) theory is applied in order to infer the second virial coefficient b_2 , an integral measure of the interaction potential, from the phase behaviour, namely cloud-point temperature (CPT) measurements under conditions favoring protein crystallization. Model calculations of b_2 quantitatively agree with those of another approach exploiting the extended law of corresponding states as well as the results of static light scattering (SLS) experiments. The strength of the attractions is quantified in terms of an effective Hamaker constant, which accounts for van der Waals attractions as well as non-DLVO forces, such as hydration and hydrophobic interactions. While sodium chloride reduces repulsions between proteins, both protein stabilizing and destabilizing cosolvents (glycerol, guanidine hydrochloride and dimethyl sulfoxide) can reduce attractions. These counterintuitive effects are explained qualitatively by preferential interactions and changes of the solution conditions. Our approach based on simple lab experiments to determine the CPT in combination with the DLVO theory is expected to facilitate further biophysical research on protein–protein interactions in complex solution environments.

Introduction

Solvent additives, also known as cosolvents, osmolytes, or excipients, are frequently used to modulate biochemical reactions or processes.^{1,2} For example, glycerol acts as a stabilizer in biosystems,³ while guanidine hydrochloride and urea are denaturants,⁴ which solubilize or unfold biomolecules. Their effects on protein stability are often ascribed to preferential

interactions⁵ and in many cases result in a linear dependence of the protein free energy on cosolvent concentration.^{6–9} Cosolvent molecules can preferentially be excluded from or bind to the surface of proteins, altering protein hydration. The relative effectiveness of ions to alter protein stability is ranked in the so-called Hofmeister series. The effects of kosmotropic ions, such as sulfate, and chaotropes, like thiocyanate, have initially been related to the making and breaking of water structure, i.e. to strengthen or weaken the network of hydrogen bonds in bulk water. Yet, recent experiments have questioned this explanation.¹⁰ Our molecular understanding of cosolvent effects on protein stability, i.e. keeping a single molecule in its native state, is still far from complete with many mechanisms for protein denaturation being discussed.

In contrast, the stability of protein solutions, which contain many proteins, against aggregation depends on protein–protein interactions, i.e. intermolecular interactions, which are even less investigated. Intermolecular interactions comprise, among others, electrostatic interactions, van der Waals attractions, the hydrophobic effect, hydrogen bonding and hydration.¹¹ The delicate balance of these forces, which can be tuned by the addition of cosolvents, determines the pathways of protein self-assembly. It thus controls protein solubility, which is related to protein homeostasis.¹² It also controls protein crystal growth, amorphous aggregation and fibril formation.^{13–15} These protein self-assembly processes are of interest in medicine, pharmaceutical industry and food engineering, e.g., in the context of diseases, such as cataract formation and diabetes,^{16,17} drug formulations¹ and food gels, such as yoghurt or cheese.¹⁸ Moreover, cosolvents and protein–protein interactions have recently been shown to strongly affect protein adsorption.^{19–21}

A realistic description of the complex phase behaviour of proteins requires a detailed and highly specific treatment, starting with the microscopic interactions on the level of atoms, including at least the asymmetric protein shape as well as the patchiness and directionality of the interactions, and extending to the bulk behaviour. Due to the complexity of the various forces contributing to the collective behavior of protein solutions and the large range of

B.4 Cosolvent-Induced Changes of Protein-Protein Interactions: From Phase Behavior to Second Virial Coefficient

length scales involved, descriptions starting from the atomic level are extremely challenging. Therefore, coarse-grained colloidal models, which, e.g., treat the solvent as a continuum, are applied and provide an effective description of protein–protein interactions. Similar coarse-graining arguments have already been successfully applied to, e.g., colloid-polymer mixtures,²² small molecules and nanoparticles.²³ Despite its simplicity, the colloidal approach can provide generic insights into protein interactions (see ref.²⁴ for a recent review).

In this context, the extended law of corresponding states (ELCS), as proposed by Noro and Frenkel,²⁵ deserves special attention. According to the ELCS, systems with sufficiently short-ranged attractions can be mapped onto equivalent square-well fluids using simulations and theory. The validity and applicability of the ELCS has been tested for many model potentials, such as Baxter’s model, the hard-core Yukawa potential and patchy interactions.^{26–29} These model potentials have also been applied to describe protein interactions.^{26,30–33} Based on comprehensive experimental studies,^{34,35} in which both the phase behavior and the second virial coefficient have been determined, it has been shown that the ELCS is applicable to the complex interactions underlying the phase behavior of protein solutions.³⁶ Therefore, the specific shape of the potential appears less crucial for an effective description of protein–protein interactions. Here, we choose the Derjaguin-Verwey-Landau-Overbeek (DLVO) theory, which separates the interactions into short-range van der Waals attractions and long-range electrostatic repulsions. It has been shown to account for the dependence of protein interactions and protein phase behavior on salt concentration, e.g. NaCl, or solvent composition, e.g. water-glycerol mixtures.^{35,37–43} In particular, repulsive interactions are readily parametrized in the DLVO potential by macroscopic solution properties, such as salt concentration and dielectric permittivity. Nevertheless, it is debated whether the DLVO theory can be applied to protein solutions and, if so, how the obtained parameters should be interpreted.^{44,45}

Since the phase behaviour appears not to depend on the specific shape of the protein–protein interactions but only on its overall repulsive or attractive nature, we focus on this

overall property when quantifying the potential. Although this approach neglects all atomistic details, it allows us to quantitatively link the macroscopic phase behaviour to the coarse-grained protein–protein interactions. Irrespective of the specific shape of the interaction potential, its overall repulsive or attractive properties are quantified by the second virial coefficient B_2 , a frequently applied integral parameter: Positive (negative) values of B_2 indicate net repulsive (attractive) interactions. For spherically symmetric interaction potentials, $U(r)$, B_2 is given by

$$B_2 = 2\pi \int_0^\infty \left(1 - \exp \left[-\frac{U(r)}{k_{\text{B}}T} \right] \right) r^2 dr, \quad (1)$$

where r denotes the center-to-center particle distance and k_{B} and T are Boltzmann’s constant and the absolute temperature, respectively. The normalized second virial coefficient b_2 is defined as

$$b_2 = \frac{B_2}{B_2^{\text{HS}}}, \quad (2)$$

where $B_2^{\text{HS}} = (2\pi/3)\sigma^3$ is the second virial coefficient of a hard sphere system with a particle diameter σ . In particular, b_2 turned out to be a predictor of the propensity of protein solutions to form ordered or amorphous aggregates. For a number of proteins, optimum solution conditions for crystallization are characterized by a window of b_2 values: $-10 \lesssim b_2 \lesssim -1$.⁴⁶ For even lower values of b_2 , amorphous aggregation takes place. Moreover, b_2 is correlated with protein solubility.^{47,48}

Several methods have been devised to experimentally study protein–protein interactions and determine the second virial coefficient. Small-angle X-ray and neutron scattering (SAXS and SANS) involve the use of large-scale facilities or specialized instruments.^{18,49,50} Traditional lab methods to determine b_2 , such as static light scattering (SLS) and osmometry,^{37,51,52} suffer from experimental difficulties.⁵³ For example, due to their small size, proteins scatter light only weakly and scattering signals hence are very sensitive to spurious

B.4 Cosolvent-Induced Changes of Protein-Protein Interactions: From Phase Behavior to Second Virial Coefficient

effects by, e.g., dust. Therefore, very careful scattering experiments and meticulous cleaning protocols are necessary and render comprehensive SLS experiments time and material consuming. New methods, such as self-interaction and size-exclusion chromatography, provide alternatives.^{54–57} Here, we propose another method to determine b_2 based on cloud-point temperature measurements.

The phase diagram of protein solutions usually comprises a liquidus (or solubility) line. This crystallization boundary separates a region of homogeneous solution from the region in which crystals and homogeneous solution coexist. Below the liquidus line, at the so-called cloud-point temperature (CPT), a metastable liquid–liquid phase separation (LLPS) into a protein-rich and a protein-poor phase starts. The CPT is indicated by a high turbidity of the protein solution and hence can be easily accessed in lab experiments using optical microscopy, visual inspection, or light scattering.^{35,58–60} It depends on the protein concentration and composition of the protein solution. Recently, the specific effects of additives on protein phase behavior have been characterized in terms of molar temperature increments, which quantify cosolvent effects on CPTs and liquidus lines.^{60,61} The location of the CPT depends on and hence characterizes the protein–protein interactions; the stronger the attractions between protein molecules, the higher the CPT. Changes of the protein phase behavior can also be linked to changes of b_2 ,^{30,39,42} but have hardly been exploited to determine b_2 values.^{36,62}

In this work, we use the links between phase behaviour and interactions as well as phase behaviour and b_2 , to relate protein–protein interactions and b_2 via the phase behaviour. In particular, we study the effects of commonly used solvent additives on lysozyme solutions under conditions favoring protein crystallization. Lysozyme is a globular protein with a roughly spherical shape and a high conformational stability, representing an ideal model system for biophysical studies.^{63,64} A broad range of cosolvents is analyzed: salts (NaCl, GuHCl) and solvents (glycerol and DMSO) of both kosmotropic (glycerol) and chaotropic (GuHCl) character. Their effect is quantified by the second virial coefficient b_2 . The b_2 values are inferred

from CPT data which are analyzed based on either the DLVO theory or the extended law of corresponding states, or they are experimentally determined using SLS. Within the DLVO framework, cosolvent-induced changes of the attraction strength are quantified in terms of an effective Hamaker constant, which is linked to the molar temperature increments of the phase boundaries. The quantitative agreement of b_2 values based on CPT measurements and SLS experiments supports the strategy to infer second virial coefficients from phase behavior. This approach is expected to facilitate further research on protein interactions in complex solution environments, where the application of conventional measurement techniques faces experimental difficulties.

Materials & Methods

Sample preparation

Hen egg-white lysozyme powder (Roche Diagnostics; Sigma Aldrich, prod. no. L6876), sodium chloride (NaCl; Fisher Chemicals, purity $\geq 99.8\%$), guanidine hydrochloride (GuHCl; Sigma, prod. no. G4505, purity $\geq 99\%$) and sodium acetate (NaAc; Merck, prod. no. 1.06268, p.a.) were used without further purification.¹ Ultrapure water with a minimum resistivity of 18 M Ω cm was used to prepare buffer and cosolvent stock solutions, which were filtered thoroughly (nylon membrane, pore size 0.2 μ m). The protein powder was dissolved in a 50 mM NaAc buffer solution, which was adjusted to pH 4 by adding small amounts of hydrochloric acid. At this pH value, lysozyme carries a positive net charge $Q = +11.4 e$,⁶⁵ where e is the elementary charge. The protein solution with an initial protein concentration $c_p \approx 40 - 70$ mg/mL was passed several times through an Acrodisc syringe filter with low protein binding (pore size 0.1 μ m; Pall, prod. no. 4611) in order to remove impurities and undissolved proteins. Its protein concentration was determined by refractometry⁶⁰ and UV

¹For light scattering experiments in the presence of GuHCl, a protein sample with much higher purity (Roche Diagnostics) than required for the CPT experiments (Sigma Aldrich)^{35,60} had to be used.

B.4 Cosolvent-Induced Changes of Protein-Protein Interactions: From Phase Behavior to Second Virial Coefficient

absorption spectroscopy. Samples were prepared by mixing appropriate amounts of buffer, protein and cosolvent stock solutions.

Cloud-point temperature (CPT) measurement

Metastable liquid–liquid coexistence curves were determined by CPT measurements. Samples were analyzed immediately after preparation, before protein crystals were formed.¹⁵ Samples with a typical volume of 0.1 mL were filled into thoroughly cleaned NMR tubes with 5 mm diameter, sealed, and placed into a thermostated water bath at a temperature well above the CPT. For an accurate determination of the temperature of the sample solution, a wire thermometer (Dostmann electronic P650, Wertheim, Germany) with a precision of 0.01 °C was mounted in a separate, but closely placed NMR tube filled with 0.1 mL water. Then, the temperature of the water bath was lowered at a low cooling rate (typically less than 0.3 °C/min), during which the sample solution was visually observed. The CPT was identified by the sample becoming turbid. Further details have been given previously.^{35,60}

Determination of the refractive index

The refractive indices of sample solutions and the solvents, n and n_s , respectively, were measured with a temperature-controlled Abbe refractometer (Model 60L/R, Bellingham & Stanley) operated with a HeNe laser at a wavelength of 632.8 nm and a temperature of 20.0 °C. The refractive index increments, dn/dc_p , were obtained from linear fits to the dependence of n on protein concentration c_p .

Static light scattering (SLS)

SLS experiments were performed with a 3D light scattering instrument (LS-Instruments) using only one beam with a wavelength $\lambda = 632.8$ nm. The samples were filled into cylindrical glass cuvettes (diameter 10 mm), centrifuged at least 40 min at typically 2500 g prior to

the measurements, and placed into the temperature-controlled vat of the instrument which was filled with decalin. Measurements were conducted at a constant temperature of 20.0 °C. We studied samples with dilute protein concentrations 3 – 21 mg/mL corresponding to volume fractions of 0.002 – 0.010. For each concentration, at least four independent samples were prepared and the scattering intensity recorded for typically 100 s with count rates of 5 – 220 kHz in the presence of proteins and about 4 kHz for buffer solutions. In order to check sample quality, dynamic light scattering (DLS) experiments were performed on the same samples which did not indicate the presence of aggregates.

The absolute scattering intensity, i.e. the excess Rayleigh ratio R , was determined using toluene as a reference according to

$$R(c_p) = \frac{\langle I_p(c_p) \rangle - \langle I_s \rangle}{\langle I_t \rangle} \frac{n^2}{n_t^2} R_t \quad (3)$$

with the time averaged scattered intensities of sample, solvent and toluene, $\langle I_p \rangle$, $\langle I_s \rangle$, and $\langle I_t \rangle$, respectively, the Rayleigh ratio of toluene, $R_t = 1.40 \times 10^{-5} \text{ cm}^{-1}$ (at $T = 35^\circ\text{C}$),⁶⁶⁻⁶⁸² and the refractive indices of the sample and toluene, n and n_t , determined at the temperature and wavelength of the SLS experiment.

Due to its small size with a particle diameter $\sigma = 3.4 \text{ nm}$, in our experiments lysozyme acts as a point scatterer because $\sigma \ll Q^{-1}$, where $Q = (4\pi n/\lambda) \sin(\theta/2) \approx 0.018 \text{ nm}^{-1}$ is the magnitude of the scattering vector with the scattering angle θ . Indeed, the scattered intensity is found to be independent of θ . Hence, SLS experiments were performed at a single scattering angle, $\theta = 90^\circ$. For dilute solutions, $R(c_p)$ is related to the second virial coefficient, B_2 , by

$$\frac{K c_p}{R(c_p)} = \frac{1}{M^{(0)}} \left(1 + \frac{2N_A B_2}{M^{(1)}} c_p \right), \quad (4)$$

²In previous experiments,³⁵ the temperature dependence of R_t was determined from the temperature dependence of the intensity scattered by a toluene sample.

B.4 Cosolvent-Induced Changes of Protein-Protein Interactions: From Phase Behavior to Second Virial Coefficient

where $M^{(0)}$ and $M^{(1)}$ represent the molar mass, N_A is Avogadro's number and K an optical constant given by

$$K = \frac{4\pi^2 n_s^2}{N_A \lambda^4} \left(\frac{dn}{dc_p} \right)^2. \quad (5)$$

Based on a measurement series with different protein concentrations c_p , the apparent molar mass, $M^{(0)}$, and the second virial coefficient, B_2 , can be determined, according to Eq. (4). We take $M^{(1)} = 14320$ g/mol, so that experimental errors in the apparent molar mass $M^{(0)}$ do not affect the determination of B_2 .³⁵ For $M^{(0)}$, we obtain values in the range $0.8 \lesssim M^{(0)}/M^{(1)} \lesssim 1.0$. The differences between $M^{(0)}$ and $M^{(1)}$ are mainly due to the low scattered intensity of the protein solutions, solvents and toluene and uncertainties in dn/dc_p and R_t ³⁵ and might reflect protein-solvent interactions.⁶⁹

Results and Discussion

Reference system: the universal phase behaviour

Fig. 1A shows the binodal line of a lysozyme solution, i.e. the dependence of the cloud-point temperature (CPT) on the protein volume fraction ϕ , in the presence of 0.9 M NaCl. This salt concentration is chosen as a reference in order to effectively screen electrostatic interactions⁶⁰ and to have conditions favoring protein crystallization.¹⁵ To quantitatively link the CPT to the protein-protein interaction potential, we use a coarse-grained colloidal approach, in which molecular details are neglected, and model the protein-protein interactions by the DLVO potential. This allows us to quantitatively determine the second virial coefficient b_2 as a function of temperature and thus parametrize the temperature axis by b_2 , which hence serves as an effective temperature. According to the ELCS,^{25,60} the resulting phase diagram is universal, as long as repulsive interactions are constant and attractions are short-ranged. Once this is established, it is applied to solutions containing cosolvents.

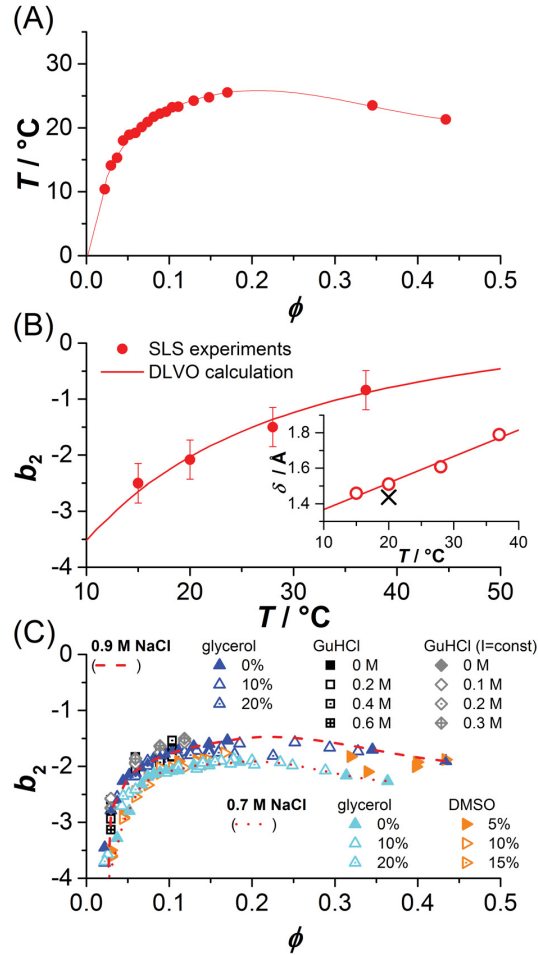


Figure 1: (A) Binodal of a lysozyme solution, i.e. the cloud-point temperatures (CPT) as a function of the lysozyme volume fraction ϕ , in the presence of 0.9 M NaCl (symbols: CPT measurements,³⁵ line: guide to the eye) and (B) corresponding normalized second virial coefficient, b_2 , as a function of temperature T as obtained by static light scattering (full symbols)³⁵ and DLVO calculations (Eq. (11), line). (Inset) Cut-off length δ as a function of temperature T , as obtained from the data in the main figure (open symbols), typical value at room temperature (cross),^{36,39,42} and linear fit to data (line). (C) Binodals of lysozyme solutions with the CPT parametrized by b_2 for various solution conditions, as indicated (symbols). Reference conditions, i.e. binodals in the presence of 0.7 M and 0.9 M NaCl without any further cosolvent added, are indicated by dotted and dashed lines, respectively.

B.4 Cosolvent-Induced Changes of Protein-Protein Interactions: From Phase Behavior to Second Virial Coefficient

The DLVO potential, $U_{\text{DLVO}}(r)$,³⁵ is written as

$$U_{\text{DLVO}}(r) = U_{\text{HS}}(r) + U_{\text{SC}}(r) + U_{\text{VDW}}(r). \quad (6)$$

The hard-sphere contribution $U_{\text{HS}}(r)$ is given by

$$U_{\text{HS}}(r) = \begin{cases} \infty, & r < \sigma \\ 0, & r \geq \sigma \end{cases}. \quad (7)$$

For $r > \sigma$, the screened Coulomb contribution $U_{\text{SC}}(r)$ reads

$$U_{\text{SC}}(r) = \frac{(Qe)^2 \exp[-\kappa(r - \sigma)]}{4\pi\epsilon_0\epsilon_s (1 + \kappa\sigma/2)^2 r}, \quad (8)$$

where ϵ_0 and ϵ_s are the permittivity of the vacuum and the solvent, respectively. The permittivity of water has a weak temperature dependence, which we describe by $\epsilon_s = \epsilon_{s,0} - \epsilon_{s,1} \cdot (T - 273.15 \text{ K})$ with $\epsilon_{s,0} = 87.62$ and $\epsilon_{s,1} = 0.36 \text{ K}^{-1}$ for $270 \text{ K} \lesssim T \lesssim 330 \text{ K}$, in agreement with previous work.³⁶ (Similar relations have been found for water-glycerol and water-DMSO mixtures.³⁵) The Debye screening length κ^{-1} is given by

$$\kappa^2 = \frac{e^2}{\epsilon_0\epsilon_s k_B T} \sum_i z_i^2 n_i, \quad (9)$$

where z_i and n_i are the valence and number density of the i -th ionic species, respectively.

The van der Waals contribution $U_{\text{VDW}}(r)$ is approximated by

$$U_{\text{VDW}}(r) = -\frac{A_{\text{eff}}}{12} \left(\frac{\sigma^2}{r^2 - \sigma^2} + \frac{\sigma^2}{r^2} + 2 \ln \left[1 - \frac{\sigma^2}{r^2} \right] \right). \quad (10)$$

The strength of the van der Waals contribution is determined by the effective Hamaker constant, A_{eff} ,⁷⁰ which is set to $A_{\text{eff}} = 8.3 k_B T$ in brine in agreement with previous studies^{36,39,42} and light scattering data.³⁷ Thus, the value of A_{eff} is larger than expected for van der Waals

attractions between typical proteins ($1-2 k_B T$, cf. ref.³⁸) and also accounts for non-DLVO forces, such as hydration, the hydrophobic effect and hydrogen bonding.⁷¹

The normalized second virial coefficient, b_2 , can be computed based on the DLVO potential by

$$b_2 = 1 + \frac{3}{(\sigma + \delta)^3} \int_{\sigma+\delta}^{\infty} (1 - \exp[-(U_{SC}(r) + U_{VDW}(r))/(k_B T)]) r^2 dr, \quad (11)$$

where δ represents a cut-off length, which is related to the Stern layer and the solvation shell around the proteins and avoids divergence of the integral in Eq. (11).

The second virial coefficient b_2 in the presence of 0.9 M NaCl has previously been inferred from SLS experiments at different temperatures T (Fig. 1B, full symbols).³⁵ Based on these data and Eq. (11), we have determined the optimum values of $\delta(T)$ (Fig. 1B, inset, open symbols). The value at room temperature is slightly larger than the previously cited value $\delta = 0.1437$ nm (cross), which has been applied to various solution conditions.^{36,39,42} A linear dependence of δ on T has been fitted to the data (dashed line) and used to calculate $b_2(T)$. The DLVO model (Fig. 1B, solid line) agrees with the experimental data, as expected, and thus provides a reasonable coarse-grained description of the underlying interaction potential.

Now, b_2 can be used as an effective temperature and the binodal line (Fig. 1A) scaled by b_2 (Fig. 1C, dashed line). As long as the repulsive contributions to the interaction potential are unchanged, the ELCS predicts that this binodal line is universal to all systems with sufficiently short-ranged attractions.^{25-29,34-36} Thus, the value of the second virial coefficient at the CPT is expected to be independent of the type and concentration of the cosolvent, but depends on the repulsive contribution to the interactions and hence, according to the DLVO theory (Eq. 8,9), on the charge Q , the total salt concentration, or rather the ionic strength, and the dielectric solution properties, i.e. ϵ_s . Therefore, this binodal line can serve as a reference for the cosolvent effects discussed in the following.

B.4 Cosolvent-Induced Changes of Protein-Protein Interactions: From Phase Behavior to Second Virial Coefficient

Cosolvents: from phase behavior to b_2

Protein phase behavior reflects the underlying interactions between protein molecules. In fact, the stronger the net attractions between proteins are, the higher the CPT. Zhang and Cremer⁷² have proposed a model for the effects of salts on CPTs. It comprises two contributions, a Langmuir-like term accounting for charge screening and a linear term related to salt-specific effects caused by non-electrostatic ion dispersion forces.⁷³ For various ionic and non-ionic cosolvents, both the CPT and crystallization boundary are strikingly linear functions of the cosolvent concentration, [cosolvent], if electrostatic interactions are essentially screened and short-ranged protein attraction dominates.^{60,61} This trend is illustrated in Fig. 2A, which shows the change of the CPT, $\Delta T = T - T_{\text{ref}}$, relative to the CPT of a reference system, T_{ref} , as a function of [cosolvent]. The linear dependence $\Delta T = \sigma[\text{cosolvent}]$ is indicated by dashed lines and the fitted cosolvent-specific slopes σ presented as inset. In order to cover a broad range of cosolvents, we investigate the effect of salts (NaCl, GuHCl) and solvents (glycerol, DMSO) of both kosmotropic (glycerol) and chaotropic character (GuHCl) on the phase behavior. Their effects are studied at various protein concentrations in the presence of 0.9 M NaCl (0.7 M NaCl in the case of DMSO).^{35,60}

In order to gain more quantitative insight into the cosolvent effects, we exploit the universality of the binodal line of the reference system (Fig. 1C, dashed line). This provides the values of b_2 at the CPT. For the different cosolvents, the salt concentrations and dielectric properties are taken into account through the repulsive screened Coulomb contributions (Eqs. 8,9). Attractive interactions are effectively parametrized by the values of A_{eff} and δ (Eqs. 10,11). Since a single value of δ was sufficient to reproduce the experimental b_2 values at room temperature for various solution conditions,^{36,42} we assume that the $\delta(T)$ relation obtained for the reference system also holds in the presence of cosolvents. Hence, A_{eff} is the only free parameter and adjusted (for each solution condition) so that b_2 at the CPT in the presence of cosolvents matches the respective b_2 of the reference system. Following this procedure, the binodals for all solution conditions studied here (Fig. 1C, symbols) collapse

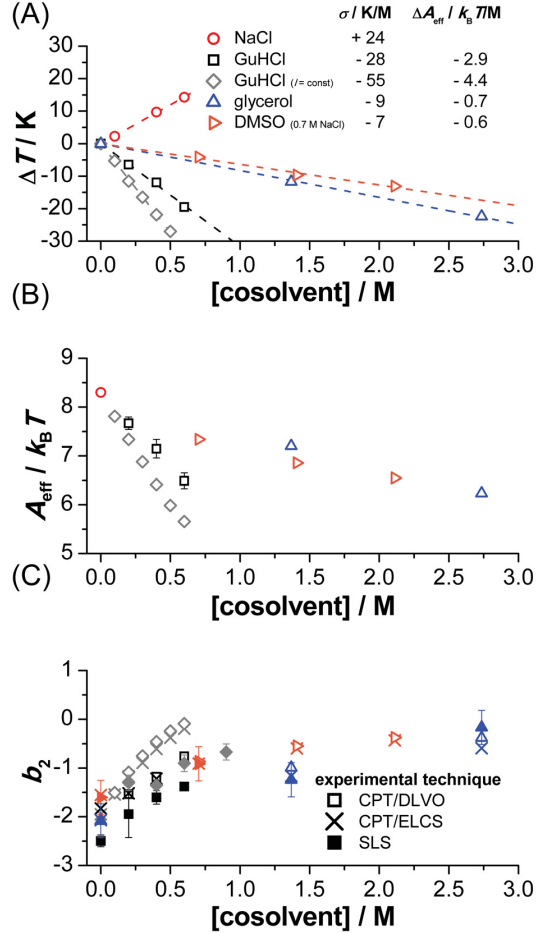


Figure 2: (A) Change of the cloud-point temperature (CPT), $\Delta T = T - T_{\text{ref}}$, relative to the CPT of a reference system, T_{ref} , as a function of cosolvent concentration for various additives as indicated (symbols) and linear fits (dashed lines). All solutions contain 50 mM NaAc buffer (pH 4) and 0.9 M NaCl, except in the case of DMSO (right triangle, 0.7 M NaCl) and the second GuHCl data set (rhombs) where the ionic strength is kept constant. Note that also in the case of NaCl, 0.9 M NaCl are present in addition to the indicated amount of NaCl. Symbols represent experimental values of ΔT obtained by averaging over different protein concentrations ranging from 30 to 180 mg/mL, which hardly affects ΔT .^{35,60} Next to the symbols, the slope σ and the molar change of the effective Hamaker constant ΔA_{eff} are listed. (B) Effective Hamaker constant, A_{eff} , as a function of cosolvent concentration for various cosolvents (as indicated in A), deduced from their effects on the CPTs. Error bars are shown in case they are larger than the symbol size, essentially reflecting statistical errors of the CPT as input parameter. (C) Normalized second virial coefficient b_2 for various cosolvent compositions (as indicated in A) at room temperature: CPT-based data analyzed using DLVO theory (open symbols) and ELCS (crosses³⁶), respectively, and data from static light scattering (SLS) experiments (full symbols).³⁵

B.4 Cosolvent-Induced Changes of Protein-Protein Interactions: From Phase Behavior to Second Virial Coefficient

onto those of the reference conditions of similar repulsive interactions (Fig. 1C, dashed and dotted lines). Fig. 2B shows the effective Hamaker constant A_{eff} for various solution conditions. Values for A_{eff} have been determined for different protein concentrations (and hence CPTs)^{35,60} and averaged. The decrease of A_{eff} (Fig. 2B) corresponds to the decrease of the CPT (Fig. 2A). The molar change of the Hamaker constant, ΔA_{eff} , (inset in Fig. 2A) seems linearly correlated with the slope σ of the CPTs. It thus can be regarded as a measure of the cosolvent effects on protein–protein attractions.

Based on the DLVO theory (Eq. 6-11) and the determined values of $\delta(T)$ (Fig. 1B) and A_{eff} (Fig. 2B), b_2 is calculated at room temperature (Fig. 2C, open symbols). These values agree with values obtained using a previously proposed method (Fig. 2C, crosses). It is also based on the experimentally determined CPTs, but exploits the extended law of corresponding states (ELCS).³⁶ In order to assess these two similar methods, their results are compared to values of b_2 determined by previous³⁵ and new static light scattering (SLS) experiments (Fig. 2C, full symbols).³ The values from light scattering and those based on the CPT, respectively, show the same trends and quantitatively agree for glycerol and DMSO. The discrepancy observed for the GuHCl samples is attributed to the different protein supplies (see Materials and Methods). The observed agreement between b_2 values determined based on SLS measurements and CPT measurements combined with arguments using DLVO theory, respectively, suggests that the DLVO model represents an efficient coarse-grained description of protein–protein interaction and, in particular, it provides a way to determine b_2 from CPTs.

Cosolvents effects on protein–protein interactions

While the specific effect of NaCl is to increase the attractions between proteins (Fig. 2A, circles, positive slope), the effects of DMSO (right triangles), glycerol (upward triangles) and GuHCl (squares and rhombs) are to reduce protein–protein attractions (negative slopes).

³In addition, the DLVO model also reproduces the temperature dependence of b_2 in the presence of cosolvents (data not shown).

The amount of the reduction increases from DMSO to glycerol and GuHCl. The latter shows an even stronger reduction if the total salt concentration or ionic strength I is kept constant (rhombs), i.e. $[\text{NaCl}] + [\text{GuHCl}] = 0.9 \text{ M}$, since in this case the increase of $[\text{GuHCl}]$ is accompanied by a decrease of $[\text{NaCl}]$ that further reduces ΔT . Mirroring the cosolvent-specific decrease of the CPT (Fig. 2A) and of the Hamaker constant A_{eff} (Fig. 2B), an increase of b_2 is observed (Fig. 2C) upon addition of GuHCl, glycerol and DMSO. These cosolvent-induced changes reflect changes of the protein–protein interactions. Stabilizers (glycerol) and denaturants (guanidine) are found to have qualitatively the same effect and hence both reduce protein–protein attractions. These trends are discussed in the following.

If GuHCl is added to the solution, b_2 increases (Fig. 2C). Differences between values obtained based on CPT and SLS experiments, respectively, are largely ascribed to the different protein samples. Moreover, if the ionic strength was kept constant and hence the NaCl concentration reduced as the GuHCl concentration is increased, the increase is even stronger. These pronounced increases of b_2 indicate a strong reduction of the attractions due to the guanidine ions. This is consistent with an increased solubility upon addition of GuHCl,⁴⁸ which is indeed observed in experiments on the crystallization boundary.⁶¹ Guanidine ions are known to preferentially bind to the protein surface, due to electrostatic interactions with charged and polar residues, hydrogen bonding and hydrophobic interactions.^{74,75} This preferential binding strongly reduces hydrophobic attractions between proteins and, consequently, b_2 increases. Similarly, also based on light scattering data, Liu et al.⁷⁶ concluded that the addition of GuHCl reduces hydrophobic attractions and results in charge screening. Note that for protein denaturation considerably higher GuHCl concentrations are necessary and different mechanisms might be responsible.

If glycerol is added to the reference system, b_2 increases, again indicating a significant reduction of the attractions. Reduced protein attractions in the presence of glycerol have previously been found by SAXS and SANS experiments^{77,78} This furthermore agrees with light scattering experiments,^{38,76} from which an increased hydration layer in the presence

B.4 Cosolvent-Induced Changes of Protein-Protein Interactions: From Phase Behavior to Second Virial Coefficient

of glycerol was deduced. It is also consistent with an increased protein solubility.^{61,79–81} In previous experiments,⁴² the effect of glycerol on the protein crystallization boundary could largely be explained by DLVO theory, consistent with the strong electrostatic contributions found in simulations.³ In this study,⁴² using Lifshitz theory the Hamaker constant was obtained directly from the solution properties; $\Delta A_{\text{eff}} \approx -0.5 k_B T/M$, which is slightly lower than the value found here. The effect of glycerol on protein solubility has also been related to the different solvation of protein surface groups by glycerol.⁸¹ This seems in contradiction to its role as protein stabilizer, that is preferentially excluded from the protein surface.⁸² It induces preferential hydration of the protein, which is probably due to heterogeneous electrostatic interactions³ and glycerol's ability to also interact with hydrophobic protein patches and hence provide an amphiphilic bridge to the polar system.³ We presume that the protein hydration induced by glycerol reduces the net attractions and leads to the increase of b_2 . Interestingly, glycerol also strongly affects adsorbed protein films;^{20,21,83} it reduces the protein surface excess at different hydrophilic and hydrophobic interfaces, which might also be due to the decreased protein–protein attractions in the presence of glycerol.

Upon addition of DMSO, b_2 increases and the molar change of the effective Hamaker constant $\Delta A_{\text{eff}} = -0.6 k_B T/M$, which agrees with previous findings based on phase boundaries and DLVO theory.⁴² Thus, an increased protein solubility is expected and indeed observed.^{61,80} DMSO, which acts as a denaturant at higher concentrations,⁸⁴ shows favorable interactions with hydrophobic side chains.⁸⁵ Therefore, the hydrophobic effect and hence protein attractions are reduced and b_2 increased in the presence of DMSO.

Conclusion

We proposed a method to relate the second virial coefficient b_2 to CPT measurements. Since b_2 is an integral parameter of the interaction potential, this implies some coarse-graining of the potential. This coarse-graining is guided by concepts developed in colloid physics, in

particular DLVO theory and the extended law of corresponding states (ELCS). The obtained b_2 values quantitatively agree with results from static light scattering (SLS) experiments as well as with results from CPT measurements and the application of the ELCS. This supports the proposed approach. Since it is based on relatively simple experiments, we expect it to stimulate further research on protein–protein interactions in complex solution environments.

The application of this approach is illustrated for the effects of cosolvents on the phase behaviour and protein–protein interactions. We determined b_2 and an effective Hamaker constant A_{eff} as a function of cosolvent composition and temperature based on the DLVO theory. The results suggest that while sodium chloride decreases repulsions between proteins, all investigated protein stabilizing and destabilizing cosolvents (glycerol, guanidine hydrochloride and dimethyl sulfoxide) are found to reduce protein–protein attractions. This is consistent with previous observations and contributes additional quantitative information on protein–protein interactions.

Author Contributions

F.P. and S.U.E. designed the research and wrote the manuscript; F.P., J.H., and D.W. conducted experiments; F.P. performed model calculations; F.P., J.H., D.W., and S.U.E. analyzed and interpreted the data.

Acknowledgement

We thank W.C.K. Poon (The University of Edinburgh, UK) and R. Castañeda-Priego (University of Guanajuato, Mexico) for very helpful discussions. We gratefully acknowledge support by the International Helmholtz Research School “BioSoft”.

B.4 Cosolvent-Induced Changes of Protein-Protein Interactions: From Phase Behavior to Second Virial Coefficient

References

- (1) Shukla, D.; Schneider, C. P.; Trout, B. L. Molecular level insight into intra-solvent interaction effects on protein stability and aggregation. *Adv. Drug Del. Rev* **2011**, *63*, 1074–1085.
- (2) Canchi, D. R.; García, A. E. Cosolvent effects on protein stability. *Ann. Rev. Phys. Chem.* **2013**, *64*, 273–293.
- (3) Vagenende, V.; Yap, M. G. S.; Trout, B. L. Mechanisms of protein stabilization and prevention of protein aggregation by glycerol. *Biochem.* **2009**, *48*, 11084–11096.
- (4) Pace, C. N.; Laurents, D. V.; Thomson, J. A. pH dependence of the urea and guanidine hydrochloride denaturation of ribonuclease A and ribonuclease T1. *Biochem.* **1990**, *29*, 2564–2572.
- (5) Timasheff, S. N. Protein-solvent preferential interactions, protein hydration, and the modulation of biochemical reactions by solvent components. *Proc. Natl. Acad. Sci. USA* **2002**, *99*, 9721–9726.
- (6) Greene, R. F.; Pace, C. N. Urea and guanidine hydrochloride denaturation of ribonuclease, lysozyme, α -chymotrypsin, and β -lactoglobulin. *J. Biol. Chem.* **1974**, *249*, 5388–5393.
- (7) Makhatadze, G. I. Thermodynamics of Protein Interactions with Urea and Guanidinium Hydrochloride. *J. Phys. Chem. B* **1999**, *103*, 4781–4785.
- (8) Timasheff, S. N.; Xie, G. Preferential interactions of urea with lysozyme and their linkage to protein denaturation. *Biophys. Chem.* **2003**, *105*, 421–448.
- (9) Holthauzen, L. M. F.; Auton, M.; Sinev, M.; Rösgen, J. Chapter Three - Protein Stability in the Presence of Cosolutes. *Methods Enzymol.* **2011**, *492*, 61–125.

- (10) Zhang, Y.; Cremer, P. S. Chemistry of Hofmeister anions and osmolytes. *Ann. Rev. Phys. Chem.* **2010**, *61*, 63–83.
- (11) Chi, E.; Krishnan, S.; Randolph, T.; Carpenter, J. Physical stability of proteins in aqueous solution: mechanism and driving forces in nonnative protein aggregation. *Pharm. Res.* **2003**, *20*, 1325–1336.
- (12) Knowles, T.; Vendruscolo, M.; Dobson, C. The amyloid state and its association with protein misfolding diseases. *Nat. Rev. Mol. Cell Biol.* **2014**, *15*, 384–396.
- (13) Vekilov, P. G. Phase diagrams and kinetics of phase transitions in protein solutions. *J. Phys.: Condens. Matter* **2012**, *24*, 193101.
- (14) Mezzenga, R.; Fischer, P. The self-assembly, aggregation and phase transitions of food protein systems in one, two and three dimensions. *Rep. Prog. Phys.* **2013**, *76*, 046601.
- (15) Sedgwick, H.; Kroy, K.; Salonen, A.; Robertson, M. B.; Egelhaaf, S. U.; Poon, W. C. K. Non-equilibrium behavior of sticky colloidal particles: beads, clusters and gels. *Eur. Phys. J. E* **2005**, *16*, 77–80.
- (16) Siezen, R. J.; Fisch, M. R.; Slingsby, C.; Benedek, G. B. Opacification of gamma-crystallin solutions from calf lens in relation to cold cataract formation. *Proc. Natl. Acad. Sci. USA* **1985**, *82*, 1701–1705.
- (17) Chiti, F.; Dobson, C. M. Protein misfolding, functional amyloid, and human disease. *Ann. Rev. Biochem.* **2006**, *75*, 333–366.
- (18) Gibaud, T.; Mahmoudi, N.; Oberdisse, J.; Lindner, P.; Pedersen, J. S.; Oliveira, C. L. P.; Stradner, A.; Schurtenberger, P. New routes to food gels and glasses. *Faraday Discuss.* **2012**, *158*, 267–284.
- (19) Evers, F.; Steitz, R.; Tolan, M.; Czeslik, C. Analysis of Hofmeister effects on the density

B.4 Cosolvent-Induced Changes of Protein-Protein Interactions: From Phase Behavior to Second Virial Coefficient

- profile of protein adsorbates: a neutron reflectivity study. *J. Phys. Chem. B* **2009**, *113*, 8462–8465.
- (20) Hüsecken, A. K.; Evers, F.; Czeslik, C.; Tolan, M. Effect of urea and glycerol on the adsorption of ribonuclease A at the air–water interface. *Langmuir* **2010**, *26*, 13429–13435.
- (21) Evers, F.; Steitz, R.; Tolan, M.; Czeslik, C. Reduced protein adsorption by osmolytes. *Langmuir* **2011**, *27*, 6995–7001.
- (22) Poon, W. C. K. Crystallization of globular proteins. *Phys. Rev. E* **1997**, *55*, 3762–3764.
- (23) He, G.; Tan, R. B. H.; Kenis, P. J. A.; Zukoski, C. F. Generalized phase behavior of small molecules and nanoparticles. *J. Phys. Chem. B* **2007**, *111*, 12494–12499.
- (24) Fusco, D.; Charbonneau, P. Soft matter perspective on protein crystal assembly. *Coll. Surf. B* **2016**, *137*, 22–31.
- (25) Noro, M. G.; Frenkel, D. Extended corresponding-states behavior for particles with variable range attractions. *J. Chem. Phys.* **2000**, *113*, 2941–2944.
- (26) Valadez-Pérez, N. E.; Benavides, A. L.; Schöll-Paschinger, E.; Castañeda-Priego, R. Phase behavior of colloids and proteins in aqueous suspensions: Theory and computer simulations. *J. Chem. Phys.* **2012**, *137*, 084905.
- (27) Katsonis, P.; Brandon, S.; Vekilov, P. G. Corresponding-states laws for protein solutions. *J. Phys. Chem. B* **2006**, *110*, 17638–17644.
- (28) Gazzillo, D.; Pini, D. Self-Consistent Ornstein-Zernike Approximation (SCOZA) and exact second virial coefficients and their relationship with critical temperature for colloidal or protein suspensions with short-ranged attractive interactions. *J. Chem. Phys.* **2013**, *139*, 164501.

- (29) Foffi, G.; Sciortino, F. On the possibility of extending the Noro–Frenkel generalized law of correspondent states to nonisotropic patchy interactions. *J. Phys. Chem. B* **2007**, *111*, 9702–9705.
- (30) Rosenbaum, D. F.; Kulkarni, A.; Ramakrishnan, S.; Zukoski, C. F. Protein interactions and phase behavior: Sensitivity to the form of the pair potential. *J. Chem. Phys.* **1999**, *111*, 9882–9890.
- (31) Pellicane, G.; Costa, D.; Caccamo, C. Theory and simulation of short-range models of globular protein solutions. *J. Phys.: Condens. Matter* **2004**, *16*, S4923.
- (32) Sear, R. P. Phase behavior of a simple model of globular proteins. *J. Chem. Phys.* **1999**, *111*, 4800–4806.
- (33) Gögelein, C.; Nägele, G.; Tuinier, R.; Gibaud, T.; Stradner, A.; Schurtenberger, P. A simple patchy colloid model for the phase behavior of lysozyme dispersions. *J. Chem. Phys.* **2008**, *129*, 085102.
- (34) Gibaud, T.; Cardinaux, F.; Bergenholtz, J.; Stradner, A.; Schurtenberger, P. Phase separation and dynamical arrest for particles interacting with mixed potentials—the case of globular proteins revisited. *Soft Matter* **2011**, *7*, 857–860.
- (35) Gögelein, C.; Wagner, D.; Cardinaux, F.; Nägele, G.; Egelhaaf, S. U. Effect of glycerol and dimethyl sulfoxide on the phase behavior of lysozyme: Theory and experiments. *J. Chem. Phys.* **2012**, *136*, 015102.
- (36) Platten, F.; Valadez-Pérez, N. E.; Castañeda Priego, R.; Egelhaaf, S. U. Extended law of corresponding states for protein solutions. *J. Chem. Phys.* **2015**, *142*, 174905.
- (37) Muschol, M.; Rosenberger, F. Interactions in undersaturated and supersaturated lysozyme solutions: Static and dynamic light scattering results. *J. Chem. Phys.* **1995**, *103*, 10424–10432.

B.4 Cosolvent-Induced Changes of Protein-Protein Interactions: From Phase Behavior to Second Virial Coefficient

- (38) Farnum, M.; Zukoski, C. Effect of glycerol on the interactions and solubility of bovine pancreatic trypsin inhibitor. *Biophys. J.* **1999**, *76*, 2716–2726.
- (39) Poon, W. C. K.; Egelhaaf, S. U.; Beales, P. A.; Salonen, A.; Sawyer, L. Protein crystallization: scaling of charge and salt concentration in lysozyme solutions. *J. Phys.: Condens. Matter* **2000**, *12*, L569.
- (40) Beretta, S.; Chirico, G.; Baldini, G. Short-range interactions of globular proteins at high ionic strengths. *Macromolecules* **2000**, *33*, 8663–8670.
- (41) Pellicane, G.; Costa, D.; Caccamo, C. Cloud and solubility temperatures versus ionic strength in model lysozyme solutions. *J. Phys.: Condens. Matter* **2003**, *15*, S3485.
- (42) Sedgwick, H.; Cameron, J. E.; Poon, W. C. K.; Egelhaaf, S. U. Protein phase behavior and crystallization: Effect of glycerol. *J. Chem. Phys.* **2007**, *127*, 125102.
- (43) Pellicane, G. Colloidal model of lysozyme aqueous solutions: A computer simulation and theoretical study. *J. Phys. Chem. B* **2012**, *116*, 2114–2120.
- (44) Piazza, R. Interactions in protein solutions near crystallisation: a colloid physics approach. *J. Cryst. Growth* **1999**, *196*, 415–423.
- (45) Ninham, B. On progress in forces since the DLVO theory. *Adv. Coll. Interf. Sci.* **1999**, *83*, 1–17.
- (46) George, A.; Wilson, W. W. Predicting protein crystallization from a dilute solution property. *Acta Cryst. Sec. D* **1994**, *50*, 361–365.
- (47) Rosenbaum, D.; Zamora, P. C.; Zukoski, C. F. Phase behavior of small attractive colloidal particles. *Phys. Rev. Lett.* **1996**, *76*, 150–153.
- (48) Guo, B.; Kao, S.; McDonald, H.; Asanov, A.; Combs, L.; Wilson, W. W. Correlation of second virial coefficients and solubilities useful in protein crystal growth. *J. Cryst. Growth* **1999**, *196*, 424 – 433.

- (49) Zhang, F.; Skoda, M. W. A.; Jacobs, R. M. J.; Martin, R. A.; Martin, C. M.; Schreiber, F. Protein interactions studied by SAXS: Effect of ionic strength and protein concentration for BSA in aqueous solutions. *J. Phys. Chem. B* **2007**, *111*, 251–259.
- (50) Möller, J.; Schroer, M.; Erlkamp, M.; Grobelny, S.; Paulus, M.; Tiemeyer, S.; Wierkert, F.; Tolan, M.; Winter, R. The effect of ionic strength, temperature, and pressure on the interaction potential of dense protein solutions: From nonlinear pressure response to protein crystallization. *Biophys. J.* **2012**, *102*, 2641–2648.
- (51) Haynes, C. A.; Tamura, K.; Korfer, H. R.; Blanch, H. W.; Prausnitz, J. M. Thermodynamic properties of aqueous alpha-chymotrypsin solution from membrane osmometry measurements. *J. Phys. Chem.* **1992**, *96*, 905–912.
- (52) Parmar, A. S.; Muschol, M. Hydration and hydrodynamic interactions of lysozyme: Effects of chaotropic versus kosmotropic ions. *Biophys. J.* **2009**, *97*, 590–598.
- (53) Tessier, P. M.; Lenhoff, A. M. Measurements of protein self-association as a guide to crystallization. *Curr. Opin. Biotechnol.* **2003**, *14*, 512–516.
- (54) Tessier, P. M.; Lenhoff, A. M.; Sandler, S. I. Rapid measurement of protein osmotic second virial coefficients by self-interaction chromatography. *Biophys. J.* **2002**, *82*, 1620–1631.
- (55) Bloustone, J.; Berejnov, V.; Fraden, S. Measurements of protein-protein interactions by size exclusion chromatography. *Biophys. J.* **2003**, *85*, 2619–2623.
- (56) Valente, J. J.; Verma, K. S.; Manning, M. C.; Wilson, W. W.; Henry, C. S. Second virial coefficient studies of cosolvent-induced protein self-interaction. *Biophys. J.* **2005**, *89*, 4211–4218.
- (57) Saluja, A.; Fesinmeyer, R. M.; Hogan, S.; Brems, D. N.; Gokarn, Y. R. Diffusion and

B.4 Cosolvent-Induced Changes of Protein-Protein Interactions: From Phase Behavior to Second Virial Coefficient

- sedimentation interaction parameters for measuring the second virial coefficient and their utility as predictors of protein aggregation. *Biophys. J.* **2010**, *99*, 2657–2665.
- (58) Broide, M. L.; Tominc, T. M.; Saxowsky, M. D. Using phase transitions to investigate the effect of salts on protein interactions. *Phys. Rev. E* **1996**, *53*, 6325–6335.
- (59) Muschol, M.; Rosenberger, F. Liquid–liquid phase separation in supersaturated lysozyme solutions and associated precipitate formation/crystallization. *J. Chem. Phys.* **1997**, *107*, 1953–1962.
- (60) Platten, F.; Hansen, J.; Milius, J.; Wagner, D.; Egelhaaf, S. U. Additivity of the specific effects of additives on protein phase behavior. *J. Phys. Chem. B* **2015**, *119*, 14986–14993.
- (61) Hansen, J.; Platten, F.; Wagner, D.; Egelhaaf, S. U. Tuning protein-protein interactions by cosolvents: specific effects of ionic and non-ionic additives on protein phase behavior. *Phys. Chem. Chem. Phys.* **2016**, *18*, 10270–10280.
- (62) Kastelic, M.; Kalyuzhnyi, Y. V.; Hribar-Lee, B.; Dill, K. A.; Vlachy, V. Protein aggregation in salt solutions. *Proc. Nat. Acad. Sci. USA* **2015**, *112*, 6766–6770.
- (63) Dumetz, A. C.; Chockla, A. M.; Kaler, E. W.; Lenhoff, A. M. Protein phase behavior in aqueous solutions: crystallization, liquid-liquid phase separation, gels, and aggregates. *Biophys. J.* **2008**, *94*, 570–583.
- (64) Evers, F.; Shokuie, K.; Paulus, M.; Sternemann, C.; Czeslik, C.; Tolan, M. Exploring the interfacial structure of protein adsorbates and the kinetics of protein adsorption: an in situ high-energy x-ray reflectivity study. *Langmuir* **2008**, *24*, 10216–10221.
- (65) Tanford, C.; Roxby, R. Interpretation of protein titration curves. Application to lysozyme. *Biochem.* **1972**, *11*, 2192–2198.

- (66) Bender, T. M.; Lewis, R. J.; Pecora, R. Absolute Rayleigh ratios of four solvents at 488 nm. *Macromol.* **1986**, *19*, 244–245.
- (67) Narayanan, J.; Liu, X. Protein interactions in undersaturated and supersaturated solutions: A study using light and X-ray scattering. *Biophys. J.* **2003**, *84*, 523–532.
- (68) Itakura, M.; Shimada, K.; Matsuyama, S.; Saito, T.; Kinugasa, S. A convenient method to determine the Rayleigh ratio with uniform polystyrene oligomers. *J. Appl. Polym. Sci.* **2006**, *99*, 1953–1959.
- (69) Blanco, M. A.; Sahin, E.; Li, Y.; Roberts, C. J. Reexamining protein–protein and protein–solvent interactions from Kirkwood-Buff analysis of light scattering in multi-component solutions. *J. Chem. Phys.* **2011**, *134*, 225103.
- (70) Leckband, D.; Israelachvili, J. Intermolecular forces in biology. *Q. Rev. Biophys.* **2001**, *34*, 105–267.
- (71) Pellicane, G.; Costa, D.; Caccamo, C. Microscopic determination of the phase diagrams of lysozyme and γ -crystallin solutions. *J. Phys. Chem. B* **2004**, *108*, 7538–7541.
- (72) Zhang, Y.; Cremer, P. S. The inverse and direct Hofmeister series for lysozyme. *Proc. Natl. Acad. Sci. USA* **2009**, *106*, 15249–15253.
- (73) Boström, M.; Parsons, D. F.; Salis, A.; Ninham, B. W.; Monduzzi, M. Possible origin of the inverse and direct Hofmeister series for lysozyme at low and high salt concentrations. *Langmuir* **2011**, *27*, 9504–9511.
- (74) Mason, P. E.; Brady, J. W.; Neilson, G. W.; Dempsey, C. E. The interaction of guanidinium ions with a model peptide. *Biophys. J.* **2007**, *93*, L04–L06.
- (75) Cooper, R. J.; Heiles, S.; DiTucci, M. J.; Williams, E. R. Hydration of guanidinium: second shell formation at small cluster size. *J. Phys. Chem. A* **2014**, *118*, 5657–5666.

B.4 Cosolvent-Induced Changes of Protein-Protein Interactions: From Phase Behavior to Second Virial Coefficient

- (76) Liu, W.; Bratko, D.; Prausnitz, J. M.; Blanch, H. W. Effect of alcohols on aqueous lysozyme-lysozyme interactions from static light-scattering measurements. *Biophys. Chem.* **2004**, *107*, 289–298.
- (77) Javid, N.; Vogtt, K.; Krywka, C.; Tolan, M.; Winter, R. Protein-protein interactions in complex cosolvent solutions. *ChemPhysChem* **2007**, *8*, 679–689.
- (78) Sinibaldi, R.; Ortore, M. G.; Spinozzi, F.; Carsughi, F.; Frielinghaus, H.; Cinelli, S.; Onori, G.; Mariani, P. Preferential hydration of lysozyme in water/glycerol mixtures: A small-angle neutron scattering study. *J. Chem. Phys.* **2007**, *126*, 235101.
- (79) Kulkarni, A. M.; ; Zukoski, C. F. Nanoparticle crystal nucleation: influence of solution conditions. *Langmuir* **2002**, *18*, 3090–3099.
- (80) Lu, J.; Wang, X.-J.; Ching, C.-B. Effect of additives on the crystallization of lysozyme and chymotrypsinogen A. *Cryst. Growth Des.* **2003**, *3*, 83–87.
- (81) Auton, M.; Rösgen, J.; Sinev, M.; Holthauzen, L. M. F.; Bolen, D. W. Osmolyte effects on protein stability and solubility: A balancing act between backbone and side-chains. *Biophys. Chem.* **2011**, *159*, 90–99.
- (82) Gekko, K.; Timasheff, S. N. Mechanism of protein stabilization by glycerol: preferential hydration in glycerol-water mixtures. *Biochem.* **1981**, *20*, 4667–4676.
- (83) Evers, F.; Reichhart, C.; Steitz, R.; Tolan, M.; Czeslik, C. Probing adsorption and aggregation of insulin at a poly(acrylic acid) brush. *Phys. Chem. Chem. Phys.* **2010**, *12*, 4375–4382.
- (84) Voets, I. K.; Cruz, W. A.; Moitzi, C.; Lindner, P.; Areâs, E. P. G.; Schurtenberger, P. DMSO-induced denaturation of hen egg white lysozyme. *J. Phys. Chem. B* **2010**, *114*, 11875–11883.

Appendix B. Publications: Protein Phase Behavior

- (85) Arakawa, T.; Kita, Y.; Timasheff, S. N. Protein precipitation and denaturation by dimethyl sulfoxide. *Biophys. Chem.* **2007**, *131*, 62–70.